UAB
Universitat Autònoma de Barcelona

Development of PocketABLE Devices
The next generation of Point-Of-Care Biosensors

GABRIEL MAROLI

ADVERTIMENT. L'accés als continguts d'aquesta tesi doctoral i la seva utilització ha de respectar els drets de la persona autora. Pot ser utilitzada per a consulta o estudi personal, així com en activitats o materials d'investigació i docència en els termes establerts a l'art. 32 del Text Refós de la Llei de Propietat Intel·lectual (RDL 1/1996). Per altres utilitzacions es requereix l'autorització prèvia i expressa de la persona autora. En qualsevol cas, en la utilització dels seus continguts caldrà indicar de forma clara el nom i cognoms de la persona autora i el títol de la tesi doctoral. No s'autoritza la seva reproducció o altres formes d'explotació efectuades amb finalitats de lucre ni la seva comunicació pública des d'un lloc aliè al servei TDX. Tampoc s'autoritza la presentació del seu contingut en una finestra o marc aliè a TDX (framing). Aquesta reserva de drets afecta tant als continguts de la tesi com als seus resums i índexs.

ADVERTENCIA. El acceso a los contenidos de esta tesis doctoral y su utilización debe respetar los derechos de la persona autora. Puede ser utilizada para consulta o estudio personal, así como en actividades o materiales de investigación y docencia en los términos establecidos en el art. 32 del Texto Refundido de la Ley de Propiedad Intelectual (RDL 1/1996). Para otros usos se requiere la autorización previa y expresa de la persona autora. En cualquier caso, en la utilización de sus contenidos se deberá indicar de forma clara el nombre y apellidos de la persona autora y el título de la tesis doctoral. No se autoriza su reproducción u otras formas de explotación efectuadas con fines lucrativos ni su comunicación pública desde un sitio ajeno al servicio TDR. Tampoco se autoriza la presentación de su contenido en una ventana o marco ajeno a TDR (framing). Esta reserva de derechos afecta tanto al contenido de la tesis como a sus resúmenes e índices.

WARNING. The access to the contents of this doctoral thesis and its use must respect the rights of the author. It can be used for reference or private study, as well as research and learning activities or materials in the terms established by the 32nd article of the Spanish Consolidated Copyright Act (RDL 1/1996). Express and previous authorization of the author is required for any other uses. In any case, when using its content, full name of the author and title of the thesis must be clearly indicated. Reproduction or other forms of for profit use or public communication from outside TDX service is not allowed. Presentation of its content in a window or frame external to TDX (framing) is not authorized either. These rights affect both the content of the thesis and its abstracts and indexes.

Development of PocketABLE Devices

The next generation of Point-Of-Care Biosensors

By

GABRIEL MAROLI



Department of Chemistry
Universitat Autònoma de Barcelona
&
Catalan Institute of Nanoscience and Nanotechnology (ICN2)

A PhD dissertation submitted to the Autonomous University
of Barcelona in accordance with the requirements of the
degree of DOCTOR IN PHILOSOPHY in Chemistry.

DIRECTORS:
PROF. ARBEN MERKOÇI
&
DR. RUSLAN ALVAREZ DIDUK

JULY 2024

AUTHOR'S DECLARATION

The present thesis, entitled "Development of PocketABLE Devices: The next generation of Point-Of-Care Biosensors", is submitted by Gabriel Maroli for the Doctoral Degree in chemistry of the Universitat Autònoma de Barcelona. This work was conducted within the Nanobioelectronics and Biosensors Group at the Institut Català de Nanociencia i Nanotecnología (ICN2), under the supervision of Prof. Arben Merkoçi, ICREA professor and group leader, and Dr Ruslan Álvarez-Diduk.

Gabriel Maroli

SIGNED: ..... DATE: .....

The supervisors

Prof. Arben Merkoçi

Dr. Ruslan Álvarez-Diduk

This Thesis was performed also under the doctoral program studies “Doctorado en Química” at the Department of Chemistry, Universitat Autònoma de Barcelona, under the cordination of Professor Xavier Sala Roman.

Xavier Sala Roman

Bellaterra, July 2024

Always keep these 3 pillars in mind. Think correctly about your questions, interesting questions will lead you to interesting paths and answers. Don't always do the same thing, be creative, remember that the wheel has already been invented. Try to work for yourself, always collaborate and help, but don't focus on working for someone else.

"Great discoveries are made not by those who know all the answers, but by those who are asking the right questions."
By W.I.B. Beveridge.

"Insanity is doing the same thing over and over again and expecting different results."
By Albert Einstein.

"Poor dad believed in being a good, hardworking man. He would say, 'Find a job and work your way up the ladder. Remember that companies do not like people who move around a lot. Companies reward people for seniority and loyalty.' But Rich dad always said, 'Mind your own business.' Financial struggle is often the direct result of people working all their lives for someone else. Many people have nothing to show for all their efforts at the end of their working days."
By Robert Kiyosaki

Acknowledgements for the financial and logistic support:







UAB
Universitat Autònoma
de Barcelona



Fundación
Carolina



Dedication and acknowledgements

I would like to begin by formally acknowledging the Autonomous University of Barcelona and the Catalan Institute of Nanoscience and Nanotechnology for providing me with the opportunity to pursue my PhD at these esteemed institutions. I am deeply grateful to the Carolina Foundation for awarding me the Doctorate 2020 scholarship, which enabled my journey to Spain. Lastly, I extend my sincere thanks to Prof. Merkoci and Dr. Alvarez Diduk for their invaluable supervision and guidance throughout my thesis.

It is known, and there are several studies on this subject, that when we express ourselves in a foreign language we are more rational, while in our own language we are more emotional. That is why the rest of my acknowledgements will be in Spanish.

Decir que sólo agradezco la supervisión y la guía seria quedarme corto. Arben, realmente te agradezco la confianza ciega desde el día que simplemente envíe un mail diciendo “hola quiero estar en tu grupo”, espero que tu apuesta haya salido como esperabas. También te agradezco la confianza y todas las libertades que me has dado durante el doctorado.

Ruslan, gracias por la sincera amistad, la posibilidad de tratarnos de igual a igual sin poner títulos por delante. Por lo aprendido dentro del lab, pero por sobre todo fuera del mismo. Por nuestras interminables charlas que me han enriquecido mucho, me llevo grandes enseñanzas de tu parte. Se que no te gusta que te lo recuerde, pero si hoy estoy redactando esta tesis, mucho tiene que ver nuestra conversación allá por el 2021 en Tirana cuando por mi cabeza estaba la idea de dejar el grupo.

Otra persona que merece párrafo aparte en mis agradecimientos en Anna, una de las mejores amistades que me llevo. Me llevo nuestros cafés, nuestras charlas, tus consejos y al menos algunas fotos por Girona. Todo grupo necesita una mama como vos.

Alla por el 2021 conocí gente increíble, con quien tuve el gusto de arrancar el doctorado. Lei, Liming, Qiuyue gracias por introducirme una nueva cultura, sobre todo platos que nunca hubiese probado. El doctorado también es eso, el intercambio cultural.

Xiky! Gracias por la bienvenida al grupo, me llevo interminables charlas, risas y llantos, pero sobre todo sonrisas. Lograste enseñarle a un ing. la importancia de la unión estreptavidina-biotina y como hacer mis primeros LFA competitivos. Aún más recuerdos me llevo fuera del lab. Cuando llegué me hiciste creer que los catalanes eran todos Miss simpatía como vos, resulto ser que en verdad era el toque valenciano de Celia Fuentes Chust.

En cambio, el catalán es otra cosa, es lucha, empoderamiento, empatía, todo eso y más,

personificado en Nere. No siempre compartimos el pensamiento, bueno diría que pocas veces, pero eso es lo que hace interesante nuestras conversaciones. Sentite realizada de que he aprendido más de lo que te voy a reconocer. Nunca pierdas la esencia, pero recordá que no todas las batallas merecen ser luchadas.

Sin duda el 2021 fue uno de los mejores años del doctorado, y mucho se lo debo a las 2 muchas de antes, a Anna, Ane, Ele, Granit, Andrea, nuestro presidente, Massimo, Jose y Enric. No solo por los momentos compartidos dentro del ICN2, pero sobre todo puertas afuera. Anna y Ane gracias por la locura de organizar viajes increíbles incluso abriéndonos las puertas de sus casas. Hacer group meetings on line medio borrachos desde la tierra Vasca o llegar trasnochado desde la terraza de Jose después de alguna despedida, bueno la de Granit. Como dije antes, el doctorado también es eso.

Para la segunda mitad del 2021, llegó Greg, gran incorporación al team, quedarán en el recuerdo las noches en urbalucho, el partido de champions y el viaje por Bruselas.

Aunque te nombre un poquito antes, Massimo, también mereces tu párrafo aparte. Comenzamos casi juntos y hemos pasado por muchas cosas a la par, momentos muy buenos y otros quizás no tanto. A pesar de que creo que por momentos desde afuera intentaban ponernos a competir en lugar de colaborar. Tengo la seguridad de que siempre hemos tenido un respeto mutuo y sabemos que contábamos con el otro.

Vern, disfrute mucho trabajar con vos, sigo pensando que hicimos un buen equipo y logramos cosas más que interesantes. Quizás nos faltó un poco más de dialogo interno pero siempre digo que el tiempo acomoda todo. Seguramente a futuro tendremos otra nanocolaboración.

Anna gracias por leerte la tesis, el feedback y las palabras de aliento.

Bombos y platillos, todos de pie, voy a hablar del Dr. Eric Calucho Palma y el Dr. Jose Alfonso Marrugo Ramírez (para cuando leas esto ya va a ser una realidad). Simplemente gracias. No pude haber sido más afortunado de compartir el doctorado con ustedes. Por todo lo que aprendí, por el sostén anímico mutuo que siempre es tan necesario. Por las discusiones científicas y las no tanto. Y por dejarme los mejores recuerdos de estos 3 años. Can only be described as a brotherhood [Calucho, E. (2024)].

La ofi 2004 me dio otras grandes amistades, Andy, me cuesta creer que llegaste hace poco más de un año, fueron muchos viajes compartidos y sobre todo charlas que no dejan tema sin tocar. Pau y Duygu gracias por renovar las energías de la ofi, por las risas y sonrisas cómplices e incluso por ordenarme el escritorio (contra mi voluntad).

Gracias Brasil por Cecilia, Matheus, Patricia, Gustavo y Davi, de todos ellos me llevo excelentes recuerdos. He aprendido mucho con ustedes, ya sea escuchándolos o intentando enseñar algo. Matheus, espero que la guía de diseño de antenas aun te sirva.

Ni hablar de Italia, además de la people nombrada, Italia nos dio a las Chiaras, Emilia, Gianluca, Daniele, Martina, Angela, Valentina, Giulia... Me doy el gusto de decir que con todos he compartido las 2 cosas mas importaste, una charla científica en donde he aprendido algo e

intentado aportar algo. Y una charla de la vida con cerveza incluida (a veces sin gluten).

He visto pasar infinidad de gente por este grupo, estudiantes de todos los niveles, Laura, Manasi, Ana, Entea, Zaheer, Linham, Cristian, Mayla, David, Ivan, Gamme, Abby, Jose, Rene, Adriá, Maria y seguro estoy siendo injusto porque se me escapa algún nombre, pero de todos he aprendido algo y he intentado portarles algo, espero haberlo logrado.

Antes de cerrar con los posdoc, mi último párrafo aparte es para Robert. Fue un placer compartir con vos tu estancia en el grupo, cada vez que veo una de tus publicaciones con la frase "my friend and mentor" no podría sentir mas orgullo. Estoy seguro de que la vas a romper en el grupo de Wang, sos crack, y espero que pronto estemos colaborando juntos nuevamente.

Sinan, gracias por los findes encerrados en el lab y "our fantastic science".

Giulio, Andrew, gracias por la supervisión en dos interesantes proyectos y por enseñarme las diferentes caras de la academia. Giulio, extendele mi agradecimiento a Kata por la idea de Artivive.

Dani, gracias por la buena predisposición de siempre, por los minipuntos, aunque el premio no haya sido el solicitado y sobre todo los supuestos datos facticos sin saber nunca cuándo nos estabas engañando.

Marianna!! Sobran las palabras.. he aprendido muchísimo de vos, desde aptámeros e hibridación de ADN hasta cuestiones de la vida misma. Solo espero que sea cual sea el camino que siga, nos encuentre trabajando en algún proyecto juntos.

Esta última parte es un poco mas personal y sentida. Ruslan, Enric, Danilo, Andy, Carlos y Lara, gracias. Gracias por el gran trabajo y el aporte que han hecho en GLEBioassay. Saben lo que ese proyecto significa para mi y espero que podamos llevarlo a donde tiene que estar, en un hospital haciendo su pequeño aporte.

No me queda más que agradecerle a mi familia por el apoyo incondicional de siempre. A Vivi, por tener que soportarme en este último tiempo. Y a mis amigos de toda la vida por siempre estar incluso a la distancia.

PREFACE

The research presented in this PhD thesis has been carried out in the Nanobioelectronics and Biosensors group of the Catalan Institute of Nanoscience and Nanotechnology (ICN2), under the supervision of Prof. Arben Merkoçi and Dr. Ruslan Álvarez-Diduk.

As a result of the experimental work carried out, several articles have been published in high impact journals or are under review at the time of submission:

- **Maroli, G.**; Abarintos, V.; Piper, A.; Merkoçi, A. The Cleanroom-Free, Cheap, and Rapid Fabrication of Nanoelectrodes with Low zM Limits of Detection. Small 2023, 19 (51), 2302136, DOI:10.1002/smll.202302136.
- **Maroli, G.**; Rosati, G.; Suárez-García, S.; Bedmar-Romero, D.; Kobrin, R.; González-Laredo, A.; Urban, M.; Alvárez-Diduk, R.; Ruiz-Molina, D.; Merkoçi, A. Wearable, battery-free, wireless multiplexed printed sensors for heat stroke prevention with mussel-inspired bio-adhesive membranes,Biosensors and Bioelectronics,260, 2024, 116421, Doi.org/10.1016/j.bios.2024.116421.
- Uzunçar, S; **Maroli, G.**; Urban, M; Merkoçi, A. Stable Prussian-Blue-Infused Catalytic Interface Architecture for Battery-Free Wireless Urine Glucose Monitoring via Smartphone. (submitted)
- **Maroli, G.**;...Alvárez-Diduk, R.; Merkoçi, A. From the Bench to the Point-of-Care: Develompent of a Smartphone-Based Portable Electrophoretic Power Supply with Electrochemical Readout. (Manuscript in preparation).

In addition, the collaborations carried out during the PhD led to participation in several review publications that were not part of the thesis:

- M. Urban, G. Rosati, **G. Maroli**, F.D. Pelle, A. Bonini, L. Sajti, M. Fedel, A. Merkoçi. Nanostructure tuning of gold nanoparticles films via click sintering, Small, 2023, 2306167, Doi.org/10.1002/smll.202306167.
- Rossetti, M; Srisomwat, C.; Urban, M.; Rosati, G.; **Maroli, G.**; Yaman Akbay, H. G.; Chailapakul, O.; Merkoçi, A. Unleashing inkjet-printed nanostructured electrodes and battery-free potentiostat for the DNA-based multiplexed detection of SARS-CoV-2 genes, Biosensors and Bioelectronics, 250, 2024, 116079, Doi.org/10.1016/j.bios.2024.116079.

- Le Brun, G.; Calucho, E.; Hauwaert, M.; Moumneh, R.; **Maroli, G.**; Yunus, S.; Rosati, G.; Álvarez-Diduk, R.; Piper, A.; Merkoçi, A.; Raskin, J. Studying ion transport dynamics in electrochemical measurements of lateral flow assays, Journal of Electroanalytical Chemistry, 2024, 118399, Doi.org/10.1016/j.jelechem.2024.118399.

- Minervini, G.; Panniello, A.; Quesada-González, D.; **Maroli, G.**; Fanizza, E.; Striccoli, M.; Álvarez-Diduk, R.; Curri, M.L.; Merkoçi, A. High Resolution Portable Platform for pH sensing via Colorimetric Fluorescence Response of Carbon Dots. (submitted).

- Rosati, G.; Deroco, P.; Bonando, M.; Dalkiranis, G.; Cordero-Edwards, K.; **Maroli, G.**; Kubota, L.; Novais Oliveira, J.; Saito, L.; Silva, C.; Merkoci, A. Introducing fully-inkjet-printed metal microneedles (submitted).

Throughout this thesis, the reader will come across some figures with the VR logo, these figures are interactive and have an associated video, which can be accessed using the Artivive app or with the URL indicated in the caption.

Chapter 1: Introduction - FUNDAMENTALS OF PORTABLE DIAGNOSTIC DEVICES
The introduction lays the groundwork for the thesis by discussing the fundamentals of sensor technology and the role of near-field communication (NFC) in biosensors. It reviews the existing literature on smartphone-assisted optical biosensors and the integration of NFC in sensor applications, highlighting the potential and challenges of these technologies in real-world scenarios.

Chapter 2: Objectives
The objectives of the thesis are presented

Chapter 3: DEVELOPMENT OF POCKETABLE SENSOR INTERFACES (READOUT)
This chapter introduces two microchips of high relevance to this thesis: the SIC4340 and the SIC4341. The first one is a generic sensor interface, capable of performing resistance and capacitance measurements. The second is a potentiostat sensor interface, capable of electrochemical measurements. Both integrated circuits are powered through the Near Field Communication (NFC) protocol, so, in addition to characterising the chips, this chapter consists of the design and characterisation of antennas suitable for NFC communication.

Chapter 4: PRINTED SENSORS FOR WEARABLES
This chapter examines the potential of wireless and battery-free platforms, based on the SIC4340 and SIC4341 chips, for the development of wearable devices. This chapter will focus on the fabrication, characterisation and implementation of humidity and temperature sensors based on silver mender resistor and rGO resistors. Furthermore, we demonstrate the advanced capabilities of these platforms by developing a simplified device for surface electromyography, thereby illustrating the potential of these innovative technologies in enhancing wearable sensor functionalities.

Chapter 5: TRANSDUCERS FOR DIAGNOSTIC DEVICES AND APPLICATIONS
This chapter presents an in-depth analysis of the development of various electrochemical transducers, including nanoband electrodes, laser-induced graphene electrodes, and PCB electrodes. Each type of transducer is subjected to an examination of its fabrication challenges, performance metrics, and potential applications in diagnostic devices. The chapter emphasises the sensitivity,

affordability, and practicality of these transducers in point-of-care diagnostics.

Chapter 6: ELECTROPHORETIC DEVICE FOR PORTABLE DIAGNOSTICS
This chapter outlines the design, development and validation of a portable electrophoretic device focusing on diagnostic applications. This chapter examines the integration of electrophoretic and electrochemical techniques within a single platform, with the use of NFC technology for energy harvesting and data transmission. This chapter covers the fabrication process, the creation of user-friendly software interfaces, and the comprehensive performance validation through experimental runs. The resulting device is demonstrated to have significant potential for use in medical diagnostics and environmental monitoring, emphasising its portability, ease of use, and efficiency in diverse diagnostic scenarios.

Chapter 7: Conclusion and Future Direction
The final chapter summarizes the key findings of the research, emphasizing the contributions to the field of wearable and portable diagnostics. It discusses the broader implications of the work and outlines potential future research directions, including advancements in sensor technology, integration techniques, and application areas.

TABLE OF CONTENTS

Page

List of Tables **xix**

List of Figures **xxi**

1 Introduction - Fundamentals of Portable Diagnostic Devices **1**

1.1 Overview of Portable Diagnostics . . . 3
1.2 Smartphone-Based Biosensors . . . 3
1.2.1 Optical Sensors . . . 5
1.2.2 Electrochemical Sensors . . . 10
1.3 Wire Interface: USB-C Port . . . 12
1.4 Wireless interface . . . 13
1.4.1 Bluetooth . . . 13
1.4.2 Wi-FI . . . 13
1.4.3 LoRa . . . 14
1.4.4 RFID . . . 14
1.4.5 NFC . . . 15
1.5 Delving deeper into NFC (Bio)sensing . . . 17

2 Objectives **25**

3 Development of pocketable Sensor Interfaces (readout) **27**

3.1 Wireless Sensing Using NFC . . . 28
3.1.1 Analog Sensor Interface – SIC4340 . . . 28
3.1.2 Potentiostat Sensor Interface – SIC4341 . . . 34
3.2 Inkjet Printed Antenna Design . . . 38
3.2.1 Inductance . . . 39
3.2.2 Resistance . . . 40
3.2.3 Capacitance . . . 42
3.2.4 Final design . . . 43
3.2.5 Inkjet Printed Limitations . . . 44

3.3 Voltera Printed Antenna . . . 46
3.4 Commercially Manufactured Antenna . . . 51
3.5 Comparison of antennas performance . . . 52
3.6 Conclusions of the chapter . . . 53

4 Printed Sensors for Wearables 55
4.1 Application: wearable wireless printed sensors . . . 55
4.2 Fabrication of the Wearable . . . 57
4.3 Device performance . . . 58
4.3.1 Humidity Sensor . . . 58
4.3.2 Temperature Sensor . . . 61
4.3.3 Muscle contraction simplified sensing . . . 66
4.4 Conclusions of the chapter . . . 72

5 Transducers for Diagnostic Devices and applications 73
5.1 Nanoband Electrodes . . . 74
5.1.1 Fabrication and Characteristics . . . 75
5.1.2 Characterization . . . 76
5.1.3 Different Electrode Designs - “LEGO-brick” concept . . . 83
5.1.4 DNA Detection . . . 86
5.1.5 Nanoband Electrodes in combination with NFC . . . 89
5.2 Laser-induced Graphene Electrodes . . . 90
5.2.1 Fabrication and Characteristics . . . 90
5.2.2 Characterization . . . 91
5.2.3 Microfluidic cell with LIG-Electrodes and NFC . . . 92
5.3 PCB-Electrodes . . . 96
5.3.1 PCB: Introduction . . . 96
5.3.2 PCB: Fabrication . . . 96
5.3.3 PCB: Flexible . . . 98
5.3.4 PCB - Electrodes Fabrication . . . 99
5.3.5 Cleaning and Characterization . . . 102
5.4 Conclusions of the chapter . . . 111

6 Electrophoretic Device for Portable Diagnostics 113
6.1 Fundamentals of electrophoresis . . . 113
6.1.1 Electrophoretic mobility . . . 117
6.1.2 Isoelectric point . . . 119
6.1.3 Electroendosmotic flow . . . 119
6.2 Electrophoresis device for Point Of Care applications . . . 121

6.3 Electronic design of the Power Supply . . . 121
6.3.1 First version of the device . . . 124
6.3.2 Second version of the device . . . 129
6.4 Development and Implementation of Arduino Code . . . 135
6.5 Smartphone Application Development . . . 137
6.5.1 MIT App Inventor . . . 137
6.5.2 User Interface . . . 138
6.6 Housing Development . . . 141
6.7 Characterization . . . 144
6.8 Electrochemical Readout . . . 151
6.9 Conclusions of the chapter . . . 154

7 Conclusion and Future Directions **157**

Bibliography **159**

Appendix A - Matlab Code for Inductance Design **171**

Appendix B - SIC434X Chip Characterisation **175**

Appendix C - Electrophoresis Codes **181**
Arduino Code . . . 181
Smartphone APP Code . . . 188

Appendix D - Conferences & Congresses **197**

Appendix E - Published Papers **205**

List of Tables

Table **Page**

1.1 The table was extracted with the permission of [5] Copyright ©(2017) Licensee MDPI, Basel, Switzerland. The study of smartphone-assisted optical biosensors can be traced back to the early 2000s. 6

1.2 Applications of NFC in Sensors and Biosensors (Part 1) 17

1.3 Applications of NFC in Sensors and Biosensors (Part 2) 18

3.1 Comparison of the quality factor of the antennas built by the different methods, using Voltera Printer, Inkjet Printer and PCB. 52

4.1 This table summarises the values obtained from the temperature sensors at 3 points in time: when the sensor is placed on the skin, without the membrane, after the membrane has been placed on the skin and when the membrane has dried. The temperature changes obtained can be observed. 64

4.2 The table presents a summary of the results obtained for gel impedance at different frequencies. The resistance(R), phase angle(θ), and impedance (Z) were obtained by the LCR-meter, while the capacitive impedance (Xc), was calculated with the expression $Xc = -\sqrt{Z^2 - R^2}$. 67

4.3 The table presents a summary of the results obtained for carbon tape impedance at different frequencies. The resistance(R), phase angle(θ), and impedance (Z) were obtained by the LCR-meter, while the capacitive impedance (Xc), was calculated with the expression $Xc = -\sqrt{Z^2 - R^2}$. 68

5.1 This table presents the results of electrode measurements with a copper thickness of 17.4 μm, which demonstrated resistance to the cleaning process at varying concentrations of ferro-ferricyanide. This analysis focuses on the oxidation and reduction current peaks, which determine the reversibility of the process and the separation between peaks that determines the formal potential (E_0). 104

5.2 This table presents the results of electrode measurements with a copper thickness of 17.4 μm, without the cleaning process at varying concentrations of ferro-ferricyanide. This analysis focuses on the oxidation and reduction current peaks, which determine the reversibility of the process and the separation between peaks that determines the formal potential (E_0). 105
5.3 This table presents the results of electrode measurements with a copper thickness of 34.8 μm, without the cleaning process at varying concentrations of ferro-ferricyanide. This analysis focuses on the oxidation and reduction current peaks, which determine the reversibility of the process and the separation between peaks that determines the formal potential (E_0). 105
5.4 Comparative table of Nanoband Electrodes, Laser-Induced Graphene Electrodes , and PCB-electrodes. 112

6.1 Table of component costs for the Electrophoretic Power Supply circuit. 134

List of Figures

Figure **Page**

1.1 The evolutionary trajectory of mobile communication devices, from the bulky Motorola DynaTAC of 1984 to today's compact, high-capacity smartphones, which are paving the way for an increasingly integrated future. It highlights the major milestones in this evolution, including the first colour screen, the incorporation of cameras, the first iPhone and the introduction of the Android operating system. 2

1.2 Schematic representation of (a) preparation and functionalization of the $ReSe_2$ nanosheet; (b) detection scheme of photothermal LFIA for human anti-SARS-CoV-2 S protein IgG antibodies.Reprinted with permission from [41]. Copyright ©2022 American Chemical Society. 8

1.3 (i) NFC interface to a smartphone and image processing approaches. (A) Pictures demonstrating NFC between a sweat monitoring device and a smartphone to launch software for image capture and analysis. (B) Images of the epidermal microfluidic biosensor (left) before and (right) after injecting artificial sweat (C) polar co-ordinate of captured volume sweat. Reprinted with permission from Ref. [42] Copyright ©2016, The American Association for the Advancement of Science. (ii) (A) 3D model and (B) assembly setup of multichannel smartphone spectrometer. Reprinted with permission from Ref. [43]. Copyright ©2017, Elsevier 9

1.4 Comparison of several common methods for wireless transmission. a) RFID (active and passive RFID). b) NFC. c) Bluetooth. d) Wi-Fi. e) LoRa. Wireless technologies each possess distinct features and associated constraints. For instance, Bluetooth and Zigbee are characterized by their low power consumption, but they suffer from a low data rate and typically necessitate a battery for power. Conversely, RFID and NFC are battery-free technologies, but this results in a relatively low transmission rate. Wi-Fi offers a high transmission rate, while LoRa, despite its low data rate and complex deployment, is a relatively recent technology that provides the benefits of long transmission distance and low power consumption. 16

1.5 A comprehensive overview of the versatility of NFC technology in wearable devices. (I) In vivo diabetic diagnosis and therapy of the smart contact lens. Adapted with permission from [85]. Copyright ©2020, Science Advances. (II) Wireless sensor system for real-time posture monitoring. Battery- free strain sensors mounted on cervical (S1), thoracic (S2), and lumbar (S3) sections are simultaneously interconnected to an NFC hub device. Adapted with permission from [91]. Copyright ©2020, Springer Nature. (III) Dental patch system for caries lesion detection by monitoring the topical oral microenvironment pH fluctuation. Adapted with permission from [86]. Copyright ©2022, npj Flexible Electronics. (IV) Glucose monitoring system operating on increasing concentration of glucose. Adapted with permission from [81]. Copyright ©2022, Scientific Reports. (V) Sensor network for the determination of skin temperature and humidity and muscle contractions. Adapted with permission from [87]. Copyright ©2024, Elsevier. (VI) Miniaturized flexible pulse oximeter built on silicone elastomer and equipped with a near-field wireless chip. Reproduced with permission from ref. 157. Copyright ©2017 Wiley 19

1.6 (I) NFC system adhered to a diaper, and several screens of the mobile APP designed to interface with the user. Adapted with permission from [88]. Copyright ©2019, IEEE. (II) Overview of the NFC-based smart facemask for wireless CO2 real-time determination. Adapted with permission from [90]. Copyright ©2022, Springer Nature. (III) NFC strain sensor tag attached to a food package for meat spoilage detection. The LED will be ON if the product is suitable for consumption. Adapted with permission from [93]. Copyright ©2021, IEEE.) 21

1.7 (I) Lin et al. report the development of near-field-enabled clothing that can establish wireless power and data connectivity between multiple distant points around the body, creating a network of battery-free sensors interconnected by proximity to functional textile patterns. Adapted with permission from [91]. Copyright ©2020, Springer Nature. (II) Oh et al. present a soft, skin-mountable sensor system that includes a pressure-responsive element based on membrane deflection and a battery-free, wireless mode of operation capable of multi-site measurements at strategic locations across the body. The sensors yield continuous, simultaneous readings of pressure and temperature in a sequential readout scheme from a pair of primary antennas mounted under the bedding and connected to a wireless reader and a multiplexer located at the bedside. Adapted with permission from [82]. Copyright ©2021, Springer Nature. . . . 23

3.1 SIC4340 Integrated Circuit Block Diagram depicts the analog section where the information is extracted and energy is harvested, as well as the digital block, where the system logic is located, and ADC block with the sensor driver. 29

3.2 A simple device that consists of a PCB to which the chip has been soldered and is attached to a silver printed antenna, manufactured for the measurement of commercial resistors and capacitors in order to verify the operation of the SIC4340 IC. 30
3.3 Comparison of four resistors measured with the NFC system and the Keithley DMM6500 Digital Multimeter. A wide range of resistors up to 220K can be found in the SIC434X Chip Characterisation Appendix. 31
3.4 (I) Screenshots of the App provided by Silicon Craft where the parameters can be set: bias current (A), limit voltage (B), apply a low-pass filter (C), implement a buffer (D), Sampling Frequency (Fs) (E), Sampling Delay Times (Ts-Dly) (F) and Warm Up Times (Twarm-up) (G). (II) Scheme for the measurement of capacitors by DC charging and discharging. (III) PCB containing the SIC4341 chip, attached to an antenna printed with silver ink for the measurement of two capacitors in parallel. 32
3.5 Comparison of two capacitors and two in parallel measured with the NFC system and the Keithley DMM6500 Digital Multimeter. Other capacitor measurements can be found in the SIC434X Chip Characterisation Appendix. 33
3.6 SIC4341 Integrated Circuit Block Diagram depicts the analog section where the information is extracted and energy is harvested, as well as the digital block, where the system logic is located, and the electrochemical interface. 35
3.7 Ferro/Ferricyanide voltagrams at three different concentrations of 2mM, 1mM and 0.5mM and two different Scan Rates of 0.1 V/s and 0.05V/s. The measurements were performed with the SIC4341 IC and an Autolab potentiostat for comparison. 37
3.8 Lumped circuit of the inductor and the capacitance of the chip. 39
3.9 Scheme of a planar square coil, where its most relevant design parameters are indicated. 40
3.10 Traces printed with silver ink using Epson X15000 printer on PET substrate from Mitsubishi.A change in color tonality can be seen in the traces that have more layers of ink deposited 41
3.11 Reduction of sheet resistivity due to the printing of a greater number of layers. The decrease in resistance is indicated in percentage, relative to the resistance of a single layer. 41
3.12 On the left, shift of the resonance frequency of the inductor when designing as the seed value of the iteration. On the right, the new design that consider the parasitic capacitance. 43
3.13 Measurement of the series resistance of the inductor. 44
3.14 Top: Printing on the MIASkin membrane using the CD holder. Below: sintering of the membrane, which resulted in a change in colour. Despite the heat treatment, the conductivity remained below the expected level. 46
3.15 SEM images obtained from the traces printed with the Voltera show the width and thickness of the trace, as well as the microparticles that compose it. 47

3.16 Antenna design made in Altium Designer Summer 09 and the antenna printed with the Voltera on the bio-inspired membrane. Dimensions expressed in [mm]. 48

3.17 Measurement of the series resistance with both the digital multimeter and the LCR meter. The resistance obtained is much lower than inkjet antennas, which improves the quality factor of the antenna. 48

3.18 Measurement of the inductance with both LCR meter. Theoretical inductance of $2.5\mu H$ and a measured inductance of $2.39\mu H$. 49

3.19 Pictures of the fabrication phases of the printed sensorised bioadhesive membranes. a) Free-standing membrane on water. b) Transfer on the plastic temporary substrate for printing. c) Silver paste deposition with Voltera equipment to form the NFC antenna. d) Attachment of the flexible PCB integrating the NFC chip on the printed membrane. e) Release of the printed membrane from the temporary substrate. f) Testing of the NFC connection on the free-standing membrane on water. g) Adhesion of the membrane to the forearm skin. h) Testing of the NFC connection on the adhered membrane. i) Close-up of the printed membrane. The membrane has been placed with the antenna, chip and ssEMG contacts on top only for illustrative purposes. (https://youtu.be/tssbd9i0iLg) 50

3.20 Design of the flexible PCBs made with Altium Designer Summer 09, both small PCBs as chip interface, as well as PBCs with integrated antenna. Dimensions expressed in [mm]. 51

4.1 a) Schematic of the sensor network. The rGO temperature sensor is connected between pads A and B and exhibits a decrease in resistance value with increasing temperature, as indicated by the arrows. The silver sensor between pads B and D exhibits an increase in resistance value with increasing temperature. The humidity sensor, consisting of a silver interdigitate, between pads C and D evaluates the change in conductivity of the substrate. As the humidity increases, the resistance decreases. The electrodes used for motion and seizure detection are located between pads E and F. b) Schematic of the sensor placement on the forearm. 56

4.2 Fabrication steps of the inkjet-printed sensors network on Mitsubishi substrate. a) The sensor network is printed on the A4-sized Mitsubishi substrate. To enhance the conductivity of the traces, the design is printed twice. b) The wax printer is then employed to print a coating of wax, which adheres to the substrate and the silver traces. This step is also carried out in duplicate. c) To allow the wax to permeate the substrate and to remove it from the silver traces, the sensor is passed through a laminator, covering the devices with a sheet of paper. The wax diffuses into the substrate, and any excess is absorbed by the paper. d) In this step, the devices are cut and manipulated one by one. The rGO sensor is transferred using a press. e) Carbon tape circles are placed on the printed electrodes. f) Anisotropic conductive tape is placed on the connection pads between the antennas and the device. g) Finally, the antennas are connected. 57

4.3 a. 3D part for the manufacture of the humidity sensors with different shapes. b. GO-N films once dried. c. Response of the GO-N sensor on the Mitsubishi substrate, values of the same order of magnitude as the humidity sensor interdigitated on the same substrate are observed. d. Response of the GO-N sensor on PET to avoid interferences, in this case the resistance measured is an order of magnitude higher.. 59

4.4 a. Linear response of the interdigitated humidity sensor printed with silver on Mitsubishi substrate, 94 % saturation is observed. b. GO-N sensor on MIASkin substrate, by reducing the size of the sensor the range of resistive value of response was reduced. c. Temporal response of the interdigitated humidity sensor when exposed to breath. . 60

4.5 Calibration curves of rGO temperature sensors with different shapes, in all cases the response is linear and thermal coefficient is negative. The bottom right shows the calibration of the mender resistor, which, being silver, has a positive coefficient. . . . 61

4.6 Resistive response of the silver ink resistor in series with the rGO transfered resistor over a wide temperature range. On the right is the device that uses copper tape to interconnect the two resistors. 62

4.7 Top: Image of the sensor placed on the forearm. Bottom: thermographic image of the sensor and the reading made with the smartphone through NFC both at room temperature and applying hot air. 63

4.8 The sensor is first placed on the skin, and a reading is taken after a while. The recorded temperature is that of the skin at rest, at time 0. As the skin is dry, the humidity sensor is out of range. Next, the wet membrane is placed, causing the temperature of the skin to decrease and the value measured by the sensors to decrease as well. In this step, a variation of 5 degrees was recorded, which is consistent with the thermographic images. Finally, after 30 minutes and with the user in motion, the membrane dries and the temperature rises to approximately 36-37 degrees Celsius. 65

4.9 Two silver electrodes printed on mitsubishi substrate, the same as those used for ssEMG measurements, have been interconnected using gel. 67

4.10 Frequency response of the Gel contact.It can be observed that even the resistive component of this gel was frequency dependent, due to the electrolytic nature of the gel. Furthermore, it can be observed that the phase shift reached up to 40 degrees, indicating that the capacitive component had an impedance almost equal to the resistive component. 67

4.11 Two silver electrodes printed on mitsubishi substrate, the same as those used for ssEMG measurements, have been interconnected using carbon tape. 68

4.12 Frequency response of the Carbon Tape contact.It is observed that the carbon tape did not exhibit a variation in frequency and that the capacitive component was practically null. As a disadvantage, the resistance was an order of magnitude higher than that of the conductive gel. 68

4.13 ssEMG normalized measurement on the forearm for the dection of the fingers muscle contraction (a). SsEMG normalized measurements on the tricep muscle (b) and on the bicep muscle (c). The red arrows indicate the contraction and the blue ones the rest phases in all the plots. 70

4.14 Measurement of bicep muscle contraction during physical exercise. A drop in the signal has been detected during each contraction starting from the second one, which may be correlated with fatigue. The reduction in muscle signal intensity observed during consecutive bicep isometric contractions when lifting a dead weight was indicative of muscle fatigue. In contrast, the decrease was not observed in the case of the tricep, where only one muscle contraction was performed without weight lifting. 71

5.1 Cyclic voltammogramms (CVs) of the 27 possible combinations of substrate (Kapton, PET or PEN) with each of the different capping layers (Kapton tape, acrylic and laminate), cut by each of the three cutting methods tested (precision cutter, scissors or scalpel). CVs were recorded in a 10 mM phosphate buffered saline solution solution containing 5 mM potassium ferricyanide, 5 mM potassium ferrocyanide, at 10 mV/s vs a formal Ag/AgCl reference electrode and Pt wire counter electrode. 76

5.2 Square Wave Voltammograms (SWVs) of the 27 possible combinations of substrate (Kapton, PET or PEN) with each of the different capping layers (Kapton tape, acrylic and laminate), cut by each of the three cutting methods tested (precision cutter, scissors or scalpel). SWVs were recorded in a 10 mM phosphate buffered saline solution solution containing 5 mM potassium ferricyanide, 5 mM potassium ferrocyanide vs a formal Ag/AgCl reference electrode and Pt wire counter electrode. 77

5.3 Scanning electron microscope images of nanoband electrodes made from Au sputtered onto Kapton and covered with Kapton tape, cut with surgical scissors. 78

5.4 On the right: AFM image of the edge of one of the sputtered Au devices on Kapton (uncapped) with five corresponding step height measurements from left to right across the ridge. On the left it can be seen that the Au thickness is $\approx 30-40nm$ and the roughness of the Au surface is the same as that of the Kapton (single nanometres). . 78

5.5 CycloVoltammetric (CV) measurements of Ferro/Ferricyanide at different concentrations from 5 mM to 39.06 μM. The calibration curve, with an R > 0.999, is shown at the bottom left. 80

5.6 Squarewave voltammetry (SWV) measurements of Ferro/Ferricyanide at different concentrations from 5 mM to 39.06 μM. The calibration curve, with an R > 0.999, is shown at the bottom left. 81

5.7 Comparative Cyclovoltammetry and SquareWaveVoltametry measurements of Macro Electrodes, ScreenPrinted Electrodes and Nanoband Electrodes. The average detection limit is lower for the nanobands than for the other electrode types, which is in line with previous reports on nanoelectrodes. 82

5.8 Schematics (not to scale), photographs and SEM images of the different LEGO brick designs fabricated and tested in this project. A) Bonding finished devices together. B) Sputtering directly onto the capping layers. C) 2D Devices.(https://youtu.be/8iuDemUqiwc) 84

5.9 Electrochemical responses of the three electrode systems put together in the Lego brick design. (A) Overlayed cyclic voltammogramms and square wave voltammograms (SWV) of the completed three electrode device using the sputtered working nanoband electrode with an external Pt wire as a counter electrode (CE) and a comercial double junction Ag/AgCl reference electrode (RE), at a scan rate of $10mV/s$, in a solution of $5mM$ potassium ferricyanide and $5mM$ potassium ferrocyanide in $1xPBS$. In (B) the potential vs ΔI transients were recorded from $-0.15V to +0.6V$ vs the open circuit potential with a $9mV$ step, a modulation amplitude of $20mV$ and a frequency of $2.5Hz$. 85

5.10 A) Schematic illustration of how the DNA sensing mechanism works. B) Overlayed CVs of the DNA sensing system response to different target DNA concentrations on a macroelectrode. Overlayed with Square Wave Voltammetry (SWV) data from the experiments, shown in (C). The results of the same experiment, with lower DNA target concentrations on nanoband electrodes are shown in (D) and (E). F) The calibration curves from the macro and nanoelectrode repeats with corresponding fits to the Langmuir isotherm. 87

5.11 Cyclic voltammetry of a bare nanoband electrode, functionalized with the DNA probe sensing film, that was exposed to ultrapure DNA free water rather than different DNA target concentrations. 88

5.12 Top: Device obtained by combining the nanoband and the SIC4341 potentiostat with the PBC antenna. Bottom: Ferro/ferricyanide measurements at 5mM and 2.5mM. . . 89

5.13 Dimensions of the three-electrode compartment on Polyimide substrate. a) Cutting edges (red), working electrode (pink), counter electrode and neck (cyan), Ag/AgCl ink (dark green), and Ag ink-made tracks (violet). b) Dashed blue line indicates the region to be covered with dielectric material. Dimensions expressed in [mm]. 91

5.14 Optimal LIG-based three-electrode platform selection. a) Various bare LIG designs, b) their CV-redox signals in PBS and b1) in ferric solution, c) PB-CHIA-modified LIGs' CV-redox signals in PBS and c1) in ferric solution. d) EIS assays of bare and PB-CHIA-modified LIGs (LIG*) in PBS. e) Amperometric response of PB-CHIA-modified LIGs to H2O2 and f) corresponding charge density and sensitivity values. g) Surface morphology of $2-LIG_{\%60}$. 93

5.15 Quantification of LIG-F-based three-electrode platform and the fluidic cell. Prototype fabrication and validation. (a-b) LIG-F-based platform [LIG-F/(PEDOT:PB)G-GOx] and fluidic cell [LIG-FFC/(PEDOT:PB)G-GOx], (c-d) amperometric responses to successive glucose injections (Inset: magnified view of the first two injections, $10\mu M$ and $20\mu M$), and (e-f) corresponding calibration plots between $10\mu M$ and $4000\mu M$ glucose. g) Fabrication of fluidic cell and h) assembly of the NFC potentiostat read mode with a smartphone and its real-time glucose readout (inset curve showing amperometric signals of the four consecutive additions of the same sample containing glucose and intermittent rinsing with PBS) in synthetic urine-spiked samples.https://youtu.be/fIgEifUkSXE 94

5.16 TOP: 2D view of the electrodes designed using Altium Designer Summer 09 and the dimensions of the most representative values of the design. Middle: 2D view of the electrodes designed in Altium Designer Summer 09 for both the top and bottom layers. Bottom: real images of the resulting flexible PBCs manufactured in polyamide. Note how the electrodes and pads are plated with gold. 101

5.17 Cyclic voltammograms of PCB-electrodes subjected to a cleaning process using sulfuric acid. The voltammograms for the electrodes with copper thicknesses of $17.4\mu m$ (top) and $34.8\mu m$ (bottom) are shown.In both cases, it can be observed that despite 25 cycles, not only is stability not achieved, but also the current increases with each cycle, resulting in further damage to the electrode. The inset image clearly demonstrates that the working electrode has sustained damage, resulting in the detachment of the gold coating. 103

5.18 Cyclic voltammograms of the electrode, with a copper thickness of $17.4\mu m$, that withstood the cleaning process at different concentrations of Ferro-FerriCyanide ($5\ mM$,$2.5\ mM$ and $1.25\ mM$) and at different ScanRates ($2.5\ mV/s$, $5\ mV/s$, $7.5\ mV/s$, $10\ mV/s$ and $12.5\ mV/s$). The graphs on the left show the linearity obtained between the peak currents and the square root of the ScanRate. While the graphs on the bottom show the linearity with respect to Ferro-FerriCyanide concentration. 107

5.19 Cyclic voltammograms of the electrode, with a copper thickness of 17.4μm, without the cleaning process at different concentrations of Ferro-FerriCyanide (5 mM,2.5 mM and 1.25 mM) and at different ScanRates (2.5 mV/s, 5 mV/s, 7.5 mV/s, 10 mV/s and 12.5 mV/s). The graphs on the left show the linearity obtained between the peak currents and the square root of the ScanRate. While the graphs on the bottom show the linearity with respect to Ferro-FerriCyanide concentration. 108

5.20 Cyclic voltammograms of the electrode, with a copper thickness of 34.8μm, without the cleaning process at different concentrations of Ferro-FerriCyanide (5 mM,2.5 mM and 1.25 mM) and at different ScanRates (2.5 mV/s, 5 mV/s, 7.5 mV/s, 10 mV/s and 12.5 mV/s). The graphs on the left show the linearity obtained between the peak currents and the square root of the ScanRate. While the graphs on the bottom show the linearity with respect to Ferro-FerriCyanide concentration. 109

6.1 Charges in a uniform electric field. $|\vec{E}|$: electric field vector; : $|\vec{F}_e|$: electric force vector; $|\vec{F}_r|$: frictional force vector; + : positive pole or anode; - : negative pole or cathode. A - Charges experience an electric force directed towards the opposite pole of the charge. B - When the charged particles begin to move, they experience a frictional force in the opposite direction. The arrows indicate the direction and sense of the vectors, and the lengths of the force vectors are proportional to their respective moduli. C- An equilibrium is quickly reached where the moduli of the forces are equal, $|\vec{F}_e|$ = $|\vec{F}_r|$. At this point, the acceleration is zero and the displacement velocity is constant. D- The particles continue to move at a constant velocity towards the opposite poles. 115

6.2 Effect of ionic strength on the migration of a charged particle in a solution, under the influence of an electric field $|\vec{E}|$, is significant. A higher ionic strength results in a lower migration speed due to the particle's need to counteract the movement of its counterions in the opposite direction. Conversely, when the charge concentration is lower, the particle can move more freely through the medium. The diagram shows the velocity vector $|\vec{v}|$ in each case, with the length of the vector being proportional to its modulus. The direction and sense of the electric field vector $|\vec{E}|$ are indicated by the lower arrow. 116

6.3 Example of an electrophoretic run of a substance. A strip of paper - support - is shown, where a potential difference was established between the points A and B (ΔV_{AB}), $|\vec{E}|$: Vector electric field; L: length of the support; d: distance run by the sample. 118

6.4 Electroendosmotic Effect. In part A), the polarization of the solution is illustrated when the support medium is ionized. Positively charged ions, or cations, gather around the negatively charged anions that are fixed to the paper. B) When a potential difference is applied, the cations will migrate towards the cathode, bringing their hydration sphere along with them. The anions, being fixed to the paper, do not migrate. 120

6.5 Block diagram of the DC-DC converter. The pin assignment can be observed. Diagram taken from the manufacturer's data-sheet. 122

6.6 Output voltage as input voltage under the condition that the control pin is short-circuited to the input pin. It can be seen that the output voltage also depends on the load. Graph taken from the manufacturer's data-sheet. 123

6.7 Wiring diagram for the $A03P-12$ DC-DC converter. It shows the resistive divider made up of $R1$, $R1p$, and $R2$, as well as the headers used to change the output polarity.124

6.8 Schematic of some of the main components of Version 1 of the electrophoretic source. It shows the Arduino Nano; the Bluetooth Module HC-06, the DAC MCP4725 and the buffer formed by the LM324N op amps. 125

6.9 Complete overview of Version 1 of the Electrophoretic Power Supply (EPS) schematic. 126

6.10 2D and 3D views of the PCB design for the first version of the device, created using Altium Designer Summer 09. The 2D view details the layout of the components and their connections, while the 3D view offers a realistic depiction of the final printed circuit. Dimensions expressed in [mm]. 127

6.11 Left: final device, which was fabricated using the Voltera V-one printer, with all components mounted on the board. Right: The voltage displayed on the device is compared with the voltage measured by a multimeter at the output of the electrophoretic source, providing a comparative analysis of the device's performance and accuracy. 128

6.12 Left: Wiring diagram for the $AGH03P-5$ DC-DC converter. It shows the resistive divider made up of $R5$ and $R6$, as well as the solid-state relays used to change the output polarity. Right: Schematic of the Arduino Nano 33 BLE and pinout used. . . . 129

6.13 Left: Connection diagram of the USC-C port, with the charging resistors necessary to activate the USB OTG or host mode. Right: wiring diagram for the MCP4725 DAC, which is connected to an Arduino microcontroller through a level shifter to ensure compatibility between the two devices. 130

6.14 Complete overview of Version 2 of the Electrophoretic Power Supply schematic. 131

6.15 2D and 3D views of the PCB design for the second version of the device, created using Altium Designer Summer 09. The 2D view details the layout of the components and their connections, while the 3D view offers a realistic depiction of the final printed circuit. Dimensions expressed in [mm]. 132

6.16 The images depict the PCB prototype created with the Voltera V-One (top), the PCB manufactured by PCB-Way, and the final EPS after all components have been assembled (bottom). 133

6.17 Flowchart of the code running inside the Arduino. It shows the different stages of initialisation and the section that runs in loop while the device is connected.. 135

6.18 Screenshot of the App developed to control the electrophoretic Power Supply. At the top, the device can be connected and disconnected. In the middle is the manual control of the source and at the bottom the Shaker mode and the redirection to the Electrochemistry App. 138

6.19 Flowchart of the Smartphone App developed with MIT App Inventor. 140

6.20 On the left, the housing with plastic Eppendorf where the nitrocellulose strip was not flat. On the right, one of the first proposed solutions where a lateral flow cassette was used to keep the strip flat. 141

6.21 Next improvement of the housing where the plastic eppendors were replaced by stainless steel eppendors to connect the director to the source. The top of the housing was modified to fit the side flow case. 142

6.22 a) Bromophenol Blue drop on the sample holder before starting the electrophoresis. b) After 15 minutes the drop reaches the detection window (in this case there is no recognition element) and the colour of the drop has changed to yellow due to the pH change. c) Shaker mode is implemented and 2 zones of acidic and alkaline pH are well defined.https://youtu.be/aDAqDQ2kfI4 143

6.23 The Final Electrophoretic device. On the right the 3D printed device in PLA. The buffer reservoirs were coated with varnish to make them waterproof. On the left, the machined device. The reservoirs are made of methacrylate and a platinum wire goes through the reservoirs and contacts the source with magnets. The nitrocellulose support was 3D printed with resin. 144

6.24 Electrophoretic runs of 1 μl of 1 mM Bromophenol Blue in 10 mM Borate Buffer at five different voltages. The displacement distance vs. time has been plotted. It can be seen that for all cases the response is linear. 145

6.25 Electrophoretic runs of 1 μl of 1 mM Bromophenol Blue in 100 mM Borate Buffer at five different voltages. The displacement distance vs. time has been plotted. It can be seen that only for voltages of 99 V and 150 V the response is linear, while for higher voltages it becomes logarithmic. 146

6.26 Electrophoretic runs of 1 μl of 1 mM Bromophenol Blue in 10 mM Phophate Buffer at five different voltages. The displacement distance vs. time has been plotted. It can be seen that for all cases the response is linear. However for 300 V slope is lower than expected 147

6.27 Electrophoretic runs of 1 μl of 1 mM Bromophenol Blue in 100 mM Phosphate Buffer at five different voltages. The displacement distance vs. time has been plotted. It can be seen that only for voltages of 99 V and 150 V the response is linear, while for higher voltages it becomes logarithmic. 148

6.28 a) A droplet of TriTrack 6X is placed on the nitrocellulose at 0 on the scale. b) After 15 minutes the sample reaches 2 cm displacement and begins to separate. c) After 30 minutes, the sample is separated, but dispersed. d) Shaker mode is implemented by applying 200 V to each side for 10 seconds. The separation is better defined after 30 minutes.https://youtu.be/D0MFp07oTIg 149
6.29 Separation of TriTrack 1X, in Borate Buffer 10 mM applying 200 V. a) After 15 minutes the dyes are already separated. b) After 30 minutes the separated dyes begin to diffuse in the nitro. c) 30 minutes of shaking is applied to reconcentrate the dyes with the drawback that the dyes tend to move towards the centre of the strip.https://youtu.be/9l1v-xUeFCc 150
6.30 Separation of TriTrack 6X, in $TRIS \cdot HCl$ Buffer 100 mM applying 200 V. a) After 15 minutes, a channel was observed in the centre of the dye, which corresponded to the migration of the cations towards the negative pole, the cathode. b) After 30 minutes, the flow front is partially homogenised, and two colours are visible, due to the turning of the bromophenol blue from blue to yellow. c) Shaker mode is applied for 30 minutes at 200 V for 5 seconds per side. d) It is shown how the anode is left with a basic solution while the cathode is left with an acidic solution.https://youtu.be/KVHKFqHjOX8 . . . 151
6.31 a) Chronoamperometry of the separation of Ascorbic Acid and Dopamine. The mixture was added twice to the system, so that two peaks of each component appear. b) The setup used was that of screen-printed electrodes, with the antenna printed with silver ink. 152
6.32 On the left, the nitrocellulose support with the PCB electrode and antenna system is shown. At the bottom, with the nitrocellulose already wet, it can be seen how it is added to the electrode. On the right, a screenshot of the chronoamperometry performed for the detection of ascorbic acid is displayed. 153

CHAPTER 1

INTRODUCTION - FUNDAMENTALS OF PORTABLE DIAGNOSTIC DEVICES

As of 2024, approximately 4.88 billion people worldwide use smartphones, representing 60.42% of the global population[1]. This is a significant leap from 1973, when Martin Cooper made the first mobile phone call on his DynaTAC 8000X3. This device, which took a decade to bring to market after its first call, cost $3,995, weighed 1.1 kg, measured 33 x 4.5 x 8.9 cm, and offered just 30 minutes of communication after 10 hours of charging[2].

As illustrated in Figure 1.1, the evolution of mobile phones has been marked by a series of significant milestones. In 1994, IBM introduced the Simon, the first device that could be considered a smartphone, featuring applications and a touchscreen[3]. However, it did not gain widespread popularity. This period also saw the emergence of sliding phones like the Motorola StarTAC.In 1998, Siemens launched the S10, the first mobile phone with a color screen. The following year, the Japanese company Kyocera introduced the first smartphone with a camera, the Kyocera VP-210[4], featuring a 0.11-megapixel front camera, a capability essential for smartphone sensing[5].

A major shift occurred in January 2007 when Steve Jobs introduced the first iPhone, marking a disruptive milestone in mobile technology. Until then, mobile devices were designed for specific functions. However, the launch of Android 1.0 on September 23, 2008, developed by Google and the Open Handset Alliance, fundamentally changed this paradigm[6]. Android, an open-source software based on the Linux kernel, operates across multiple platforms and allows millions of users to develop their own applications.

The evolution of mobile phones has transformed not only how we communicate but also how we interact with the world. Modern smartphones are equipped with a variety of sensors that enable functionalities ranging from navigation and gaming to health monitoring and scientific

research[7]. This transformation underscores the remarkable journey of mobile phones from a luxury item to an indispensable tool, shaping our lives in ways that were unimaginable when the first call was made on a DynaTAC 8000X.



Figure 1.1: The evolutionary trajectory of mobile communication devices, from the bulky Motorola DynaTAC of 1984 to today's compact, high-capacity smartphones, which are paving the way for an increasingly integrated future. It highlights the major milestones in this evolution, including the first colour screen, the incorporation of cameras, the first iPhone and the introduction of the Android operating system.

1.1 Overview of Portable Diagnostics

Portable diagnostics represents a significant advancement in healthcare, providing rapid, accurate, and user-friendly diagnostic solutions. These compact devices have revolutionized medical diagnostics, allowing tests and results to be obtained in real-time, even in remote or resource-limited settings[7–10].The development of portable point-of-care (PoC) diagnostic devices has had a profound impact on global health[11–14], contributing significantly to clinical management in various fields such as pathology, drug discovery, and food safety[15–17].

Previously, diagnostic tests in isolated or remote areas were time-consuming, costly, and labor-intensive. However, the advent of miniaturized biosensor technologies for PoC testing has made detection processes more sensitive, reliable, rapid, and cost-effective without the need for sophisticated instruments[13, 18].

1.2 Smartphone-Based Biosensors

In the early 21st century, the rise of mobile phones, particularly smartphones, revolutionized PoC diagnostics. These devices, equipped with various tools and applications such as cameras, USB interfaces, audio ports, and wireless technologies like Wi-Fi, Bluetooth, and NFC, ushered in a new era of biosensing technologies. Over the past two decades, research has focused on integrating these analytical tools into smartphone systems for data processing and communication[14, 19].

Biosensors, as bioanalytical instruments, use biological recognition elements known as bioreceptors, including antibodies, enzymes, and nucleic acids. These bioreceptors interact with physical or physicochemical transducers, which measure real-time changes upon interaction between the substrate and the bioreceptor, converting it into an electrical signal. One possible classification, frequently cited in the literature, categorizes biosensors into six groups based on their signal transduction methods: electrochemical, thermal, optical, mass, magnetic, and micromechanical.

The integration of smartphones in biosensing has made real-time monitoring portable and affordable, reducing the cost and complexity of sensing systems. These platforms have found applications in healthcare, such as clinical diagnosis and self-diagnosis, transforming patient care into a self-monitoring platform for various physiological conditions like blood pressure, pulse rate, and body weight. Additionally, patients can now monitor various biomarkers, antibodies, enzymes, pathogens, and metabolites without needing a healthcare professional.

The accessibility of data is a crucial factor for smart diagnostic devices. Integrating technologies like artificial intelligence and machine learning into sensing platforms enhances the capabilities of smartphone-based devices. Designing and developing mobile diagnostic devices offers versatility and measurable benefits in diagnosis and medical treatment costs.

To address the complexity and cost of bulky readout devices in miniaturized biosensors, the scientific community has merged mobile phone technology with biosensor technology. This merger

reduces the overall size, complexity, and cost of detection systems. Modern smartphones, akin to mini-computers with state-of-the-art components, serve as effective biosensor devices. With almost 5 billion smartphone users worldwide, smartphones have the potential to be more ubiquitous, accessible, and cost-effective than conventional analytical devices. They offer a portable, cost-efficient, real-time, and PoC detection platform for disease diagnostics and environmental monitoring, especially in low-income countries with limited resources.

In the rapidly evolving field of smartphone-based sensing, numerous reviews have been conducted, categorizing detection methods into optical and electrochemical types and classifying devices by their data transmission modes—Wi-Fi, Bluetooth, or NFC. This thesis will explore this landscape, providing a brief overview of optical sensors while emphasizing electrochemical sensors, which have shown immense promise in various applications. In addition, a crucial yet often overlooked aspect of biosensor functionality and efficiency, powering methods, will be discussed.

In the rapidly evolving field of smartphone-based sensing, a plethora of reviews have been conducted, including those by Quesada-Gonzales et al., Beduk et al., and others[7, 11, 13, 16]. These reviews typically categorize detection methods into two primary types: optical and electrochemical. Furthermore, they often the devices on their mode of data transmission, Wi-Fi, Bluetooth, or Near Field Communication (NFC).

In this thesis, we will delve into this landscape, providing a brief overview of optical sensors while emphasizing electrochemical sensors. The latter has shown immense promise in various applications, warranting a more in-depth exploration. We will also discuss various power supply methods for biosensors, an aspect that is often overlooked but is crucial for the functionality and efficiency of these devices. The transmission of data, a vital component in the utility and effectiveness of these sensors, will be another focal point of our discussion. One of the key elements that will be given special attention in this thesis is NFC communication. As a central component of modern smartphone technology, NFC plays a pivotal role in the operation of these sensors. In addition to enabling communication between the sensor and the mobile phone, NFC also allows for wireless powering of the sensor, thus facilitating the development of battery-free sensors.

By investigating these areas, we aim to provide a comprehensive understanding of the current state of smartphone-based sensing technologies, their operation, and their potential for future applications. This thesis will serve as a valuable resource for those interested in the intersection of mobile technology and biosensing, offering insights that could guide future research and development in this field.

1.2.1 Optical Sensors

Optical sensing technology facilitates the instantaneous, label-independent identification of a broad spectrum of biological and chemical entities. The fundamental mechanism of optical sensing involves the observation of color alterations in various mediums such as tubes, capillaries, microfluidic chips, filter papers, and nitrocellulose strips, contingent on the concentration of the analyte. Its notable attributes include high sensitivity, biocompatibility, and seamless incorporation into portable platforms[20]. The integration of optical sensors with smartphones has gained traction in recent times, attributed to the convenient image analysis capabilities of smartphones[11, 21, 22]. Applications like FLASK station and ImageJ are frequently employed for data interpretation[23, 24].

Given that the photographic camera was one of the first features to be incorporated into mobile phones, it is not surprising that biosensors utilizing this capability have been under development for over 20 years. It is interesting to observe the Table 1.1 extracted from Geng et al.'s review [5], where smartphones such as the Nokia N73 or the Sony-Ericsson Aino, phones from the early 2000s, are reported.

During the recent COVID-19 pandemic, antigen tests, a type of Lateral Flow Assay (LFA), became crucial optical biosensors. These tests typically provide a visual indication of a positive result through the appearance of a test line[25]. While commonly used to distinguish between positive and negative results, the intensity of the test line in LFAs can also be utilized for quantitative measurements in various diseases. For example, LFAs used for detecting dengue fever, malaria, or HIV can be adapted to provide not only a binary result but also quantitative information based on the intensity of the test line, which correlates with the concentration of the target antigen. This versatility depends on the specific capture antibody or aptamer used in the test line, allowing LFAs to be tailored for different diagnostic applications[26]. This is where the smartphone camera contributes to the quantification of the assay, as reported in several studies[27].

For example, Bergua et al. developed colorimetric lateral flow strips that can detect and quantify Escherichia coli species in tap, river, and sewage water samples as indicators of fecal pollution [36]. By combining this LFA with a simple water filtration unit and a commercially available colorimetric reader, they enhanced the assay's sensitivity and enabled more accurate quantification of bacterial concentration. This approach illustrates how smartphone integration can transform LFAs into powerful tools for precise quantitative measurements across various applications.

The performance of the biosensor is crucial, but equally important is the program that reads, interprets, and analyzes the signal. The importance of digital solutions in enhancing the quantitative capabilities of LFA cannot be overstated. Schary et al. presented an open-source, all-in-one smartphone-based system for the quantitative analysis of LFAs[37]. This system includes a 3D-printed photo box for consistent image capture, a smartphone for image acquisition, and

Sensing Mechanism	**Detect Target**	**Limit of Detection**	**Smartphone Model**	**Accessory**	**Reference**
Brightfield and fluorescence	Red blood cells (brighfield), sputum (fluorescence)	$\geq 1.2\mu m$	Nokia N73 3.2 megapixel	LED, filter(for fluorescence), lenses, eyepiece, objective	[28]
Contact microscope	White blood cells	$\geq 1.6\mu m$ (Samsung), $\geq 1.5\mu m$ (Sony-Ericsson)	Samsung Galaxy S2, 8 megapixel; Sony-Ericsson Aino, 8 megapixel	LED, lenses, rotater, fiber-optic taper	[29]
Brightfield	CD4+ T-cells	> 60 cells per μL	MotoX-XT1575, Motorola	Functionalized microfluidic chip, light source, lenses	[30]
Fluorescent	White blood cells	$\sim 2\mu m$	Sony-Erickson U10i Aino, 8 megapixel	Microfluidic chip, LED, plastic color filter, batteries, lens	[31]
Quantitative phase microscope	Red blood cells, pap smear, monocot root, broad bean epidermis	-	Nubia Z9 mini	3D printed shell, eyepiece, micro-objective, LED, precision translation stage	[32]
Lensfree microscopy	Red blood cells, white blood cells, platelets, Giardia lamblia cysts	$\geq 2.2\mu m$	Moto Zine ZN5, 5 megapixel	LED, plastic components, battery	[33]
Lensfree Shadow imaging	Blood cells, microorganisms	≥ 500 nm	Samsung galaxy S4, 13 megapixels	-	[34]
Lensfree Image recognition	Paper-based blood typing device	-	Google Nexus 5	-	[35]

Table 1.1: The table was extracted with the permission of [5] Copyright ©(2017) Licensee MDPI, Basel, Switzerland. The study of smartphone-assisted optical biosensors can be traced back to the early 2000s.

an R Shiny application with a modular and customizable workflow. This platform allows for image editing, analysis, data extraction, calibration, and quantification of the assays, significantly improving the accuracy and ease of data interpretation.

Additionally, Can Dincer's team introduced a light-controlled dynamic bioassay (OptoAssay) that enables bi-directional movement of biomolecules. This innovation allows for wash-free signal readout of bioassays, eliminating the need for external flow control devices[38]. These advancements highlight how integrating advanced programs and innovative technologies can transform LFAs into powerful tools for precise quantitative measurements, further expanding their applicability across various diagnostic fields.

Another study by Colombo et al. [39] introduced a real-time, smartphone-based processing method for LFAs that can detect signal intensity at the test line, control line, and background, and employs statistical comparison of these values to predictively categorize tests as "positive", "negative", or "failed".

Moreover, a smartphone-based automated reader for drug-of-abuse LFA tests was developed, consisting of an inexpensive light box and a smartphone device [40]. Test images captured with the smartphone camera are processed in the device using computer vision and machine learning techniques to perform automatic extraction. Not only is the built-in camera of the mobile device employed for detection, but other researchers, such as Hao et al. [41], have also integrated a thermal camera into the mobile device to enhance the sensitivity of the LFA, as is shown in Figure 1.2. The photothermal LFA, due to its superior photothermal conversion efficiency and stability, was introduced for the rapid, on-site, and highly sensitive assay of human anti-severe acute respiratory syndrome coronavirus 2 (SARS-CoV-2) Spike (S) protein IgG antibodies.

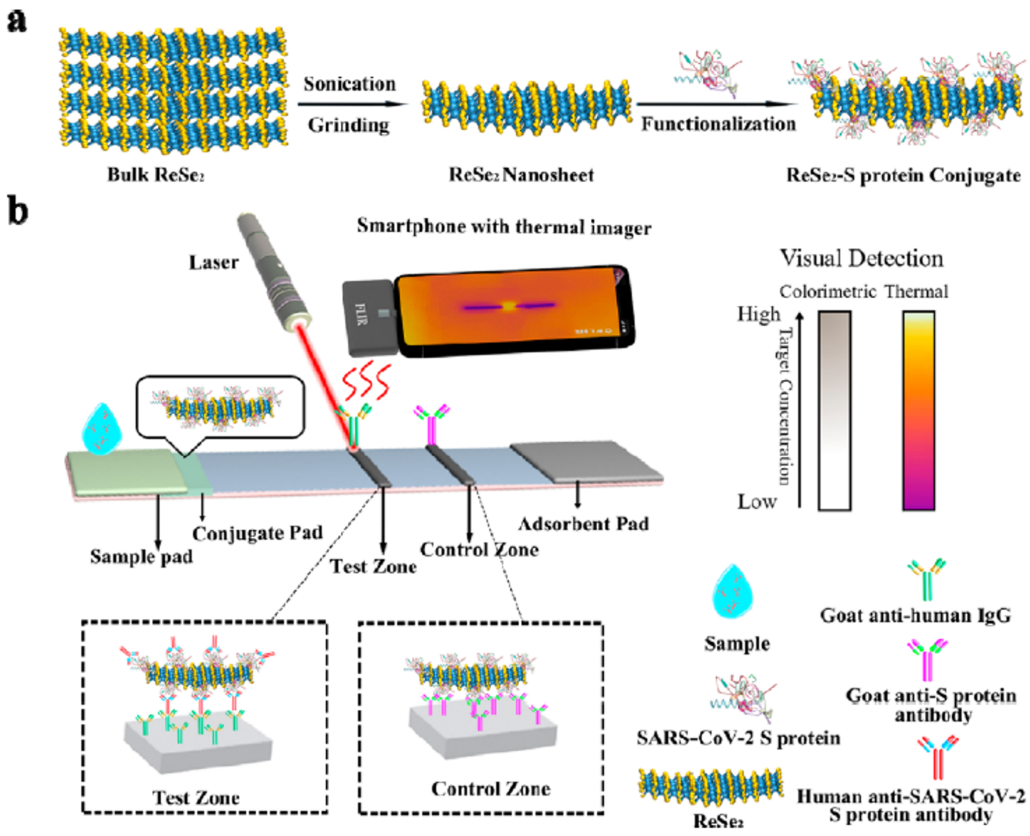


Figure 1.2: Schematic representation of (a) preparation and functionalization of the $ReSe_2$ nanosheet; (b) detection scheme of photothermal LFIA for human anti-SARS-CoV-2 S protein IgG antibodies.Reprinted with permission from [41]. Copyright ©2022 American Chemical Society.

Optical sensors are not restricted to paper-based or LFA. There have been advancements in the field of wearable technologies, one of which has been introduced by Koh et al.[42]. The development of a soft, wearable microfluidic device that is capable of capturing, storing, and colorimetrically sensing sweat is ilustrated in Figure 1.3 . This innovative device, which is thin and soft, houses a closed microfluidic system that can efficiently collect sweat directly from the skin pores. The collected sweat is then directed to various channels and reservoirs within the device for multiparametric analysis of different markers. The device also offers the possibility of wireless connectivity to external devices, enabling image capture and subsequent analysis. These examples illustrate how smartphones, combined with advanced software and sensor technologies, have enhanced the accuracy, sensitivity, and convenience of optical biosensors, broadening their applications across various diagnostic fields.

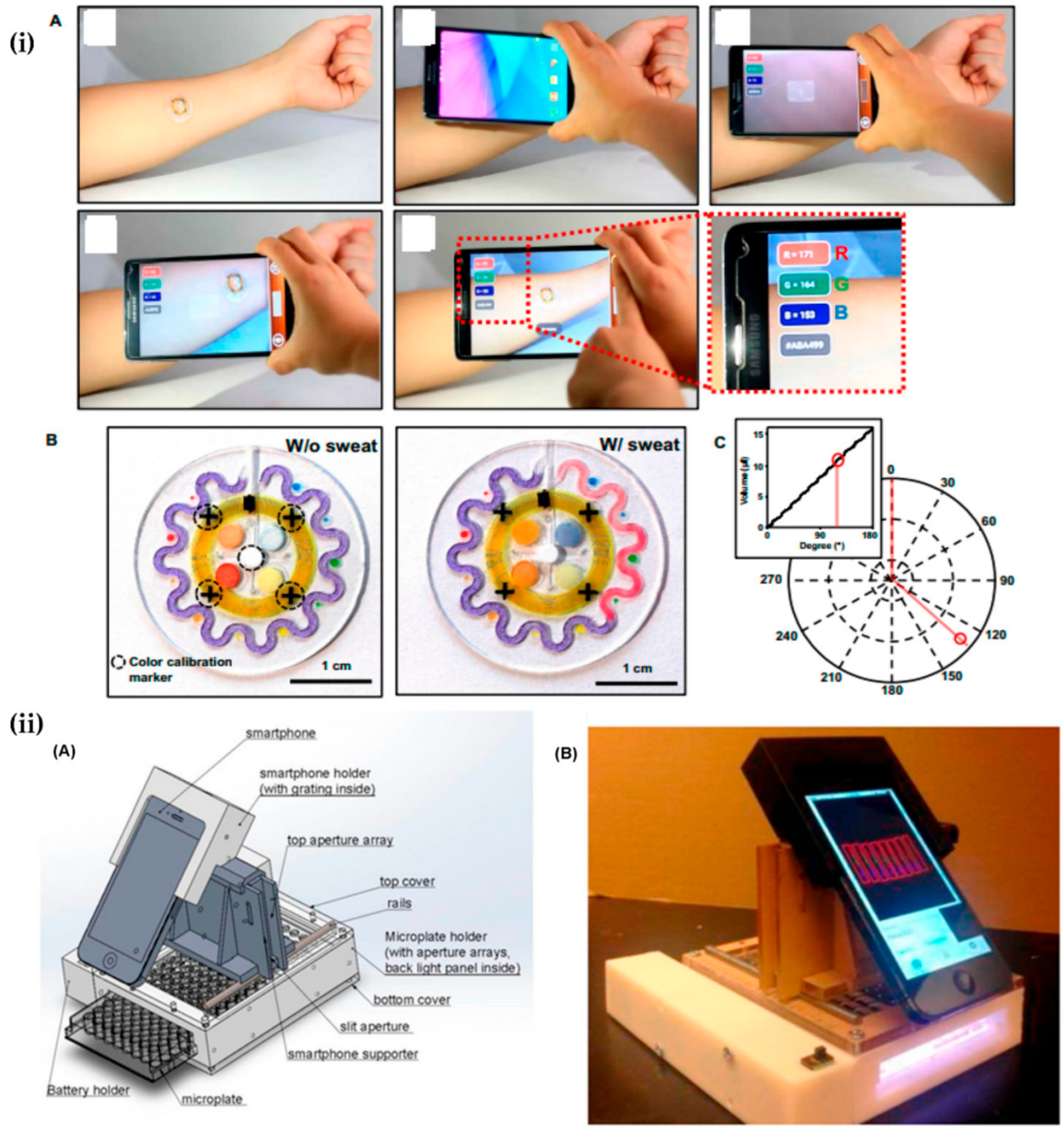


Figure 1.3: (i) NFC interface to a smartphone and image processing approaches. (A) Pictures demonstrating NFC between a sweat monitoring device and a smartphone to launch software for image capture and analysis. (B) Images of the epidermal microfluidic biosensor (left) before and (right) after injecting artificial sweat (C) polar co-ordinate of captured volume sweat. Reprinted with permission from Ref. [42] Copyright ©2016, The American Association for the Advancement of Science. (ii) (A) 3D model and (B) assembly setup of multichannel smartphone spectrometer. Reprinted with permission from Ref. [43]. Copyright ©2017, Elsevier

1.2.2 Electrochemical Sensors

The integration of electrochemical point-of-care (POC) devices with smartphones presents a highly promising approach, combining the strengths of both technologies to enhance diagnostic capabilities. Electrochemical biosensors are known for their high sensitivity and specificity, and their ability to provide rapid and straightforward quantitative measurements. These advantages are significantly amplified when paired with smartphone technology[13, 44–46].

Various strategies are employed to create these devices,with smartphones serving either as the electrochemical analyser or as a source of power for external peripherals. A significant consideration is the manner in which the measurement module is connected to the smartphone. Among the wired connections, the Micro-USB or the USB-C port with the OTG (on-the-go) protocol may be employed for the purposes of powering and data communication[47, 48]. Aditionally,the headphone and microphone ports of smartphones are particularly versatile, as they can be used for both powering the devices and performing Electrochemical Impedance Spectroscopy (EIS) measurements in the audio range (20 - 20 kHz). This dual functionality allows for greater flexibility in designing electrochemical sensing systems[49].

On the other hand, wireless peripherals, utilizing Bluetooth or NFC, provide significant advantages in biosensing applications. These technologies enable the integration of measurement electrodes in close proximity to the patient, including wearable formats[50]. Smartphones can function as power sources, signal processors, and convenient data readout devices for these wearable sensors[51–53].

Another method of integration with the smartphone is the incorporation of internal dedicated hardware. While there are instances of this occurring, the primary challenge is that such developments are designed for a specific type of smartphone and hence are limited only to that particular type and brand of phone. For example, if we develop a sensor that uses MagSafe technology, which is used by the iPhone to attract magnetic particles, even though many phones have wireless charging, our approach will only work on this brand of smartphone.

As previously discussed, the integration of smartphones with micro-USB and, currently, with USB-C ports has emerged as a significant avenue for facilitating the transmission of both digital data and analog voltage to and from the device. This capability holds particular significance in electrochemical sensing applications, where the application of analog voltage to the sensor and the subsequent collection of voltage, current, and resistance signals are imperative for accurate measurements. Electrochemical sensors, integral to biosensing, can be broadly classified into three categories: conductometric, potentiometric, and amperometric sensors. Each of these sensor types operates based on fundamental principles of electrical circuitry and Ohm's law, which establishes the relationship between voltage, current, and resistance.

1.2.2.1 Conductive Sensor

Conductive sensors, also known as resistive chemosensors, directly detect changes in the sensor's resistance. These sensors, a subset of electrochemical sensors, determine the concentration of target analytes by measuring changes in electrical conductivity. Conductive sensors detect alterations in conductivity induced by the introduction of specific analytes or fluctuations in ion concentration within the sample. Additionally, resistive chemosensors can be constructed using nanocomposite nanomaterials that change resistance in the presence of target analytes. For example, carbon nanotube-based sensors can detect gas molecules such as ammonia, demonstrating significant changes in resistance upon exposure[54]. Notably, certain lateral flow assays (LFAs) incorporate conductive principles, where changes in the resistance of the test line indicate a positive result.[55].

1.2.2.2 Potentiometric Sensor

Potentiometric sensors, which function based on resistance changes that cause voltage output variations, are widely used in various applications. These sensors measure the output voltage and correlate it with the target variable under test. A common example of a potentiometric sensor is the ion-selective electrode. This electrode measures the potential difference between two electrodes when there is no current flow. The measured potential is closely related to the concentration of the analyte of interest, as dictated by the Nernst equation.

Among the various types of potentiometric sensors, membrane-based ion-selective electrodes are especially common in biosensing applications. These electrodes are composed of a glass tube that contains a reference electrolyte solution and an ion-selective membrane. The membrane allows the selective passage of specific ions, which in turn modulates the potential difference.

As an additional example, consider pH meters, which are a type of potentiometric sensor. They measure the hydrogen ion activity in water-based solutions, indicating its acidity or alkalinity. The pH meter has a voltmeter that measures the potential difference between a pH electrode and a reference electrode, and then converts this potential into a pH value as per the Nernst equation. This is a crucial tool in many industries, including food processing, water treatment, and pharmaceuticals.

1.2.2.3 Amperometric Sensor

Amperometric sensors are characterized by the maintenance of constant resistance while varying the flow of current through the circuit. These sensors, termed amperometric sensors, measure the resulting electric current generated under these conditions. In this configuration, a constant potential is applied to the sensor electrodes to facilitate detection of target analytes in a sample through the electrical current produced by oxidation or reduction reactions.

Typically, amperometric sensors comprise a working electrode, a reference electrode, a counter electrode, and an electrolyte solution. The working electrode, composed of a suitable material, initiates the desired electrochemical reaction with the target analyte. As the analyte undergoes oxidation or reduction at the working electrode, an electric current proportional to its concentration is generated. The reference electrode maintains a stable potential at the working electrode, while the counter electrode completes the current flow. The electrolyte solution facilitates the exchange of ions between the electrodes, enabling the electrochemical reaction to proceed effectively. An example of such a biosensor is the device presented in Chapter 5 for the detection of glucose in urine.

1.3 Wire Interface: USB-C Port

The voltage, current, and conductance signals generated by electrochemical detection methods are initially converted into analog voltage signals. For instance, by measuring the voltage drop across a known resistor, a current signal can be transformed into a voltage signal. Similarly, a Wheatstone bridge can be used to convert a conductance signal into voltage. However, before these analog voltage signals can undergo further processing, such as with a microcontroller, they must be converted into digital signals using an analog-to-digital converter.

Microcontrollers are compact computers capable of receiving and processing both analog and digital signals across multiple channels. Among the most widely used customizable microcontrollers is the Arduino, equipped with numerous pins for receiving analog and digital signals. The Arduino board features an integrated analog-to-digital converter, essential for processing analog signals. Additionally, it includes a microprocessor and modest memory, enabling the uploading of compiled code via its USB port for digital data processing.

The processed results can be transmitted to other devices, such as mobile phones, via the USB port. In modern times, USB-C ports are commonly integrated into smartphones, providing a compact version of the standard USB port. These ports facilitate high-speed digital data transfer between a mobile phone and a computer, as well as between devices. Smartphone applications utilize these processed digital signals to present assay outcomes to users.

Moreover, the USB-C port serves as a charging interface for a phone's battery via an AC-to-DC adapter. It also enables powering external devices by drawing from the phone's battery, particularly advantageous with adapters and microcontrollers that can utilize the phone's power source. Chapter 6 of this thesis will present an illustrative application that demonstrates this concept.

1.4 Wireless interface

Unlike traditional wired devices, which offer limited flexibility for prolonged health surveillance, wireless wearable sensors present a distinctive solution for the continuous observation of various physiological signals. These signals range from those on the surface of human skin to those within the body, all while minimally disrupting everyday movements. A crucial component of this system, wireless modules, are instrumental in transmitting data from wearable sensors to external devices and cloud servers without the need for physical connections. This section will delve into notable wireless technologies utilized in wearable sensors, with an emphasis on their operational principles, attributes, benefits, and limitations. The key points are shown in the infographic in Figure 1.4.

1.4.1 Bluetooth

Bluetooth, a wireless communication technology characterized by low power consumption, cost-effectiveness, and high speed, enables the wireless exchange of information between devices through the transmission of data via high-frequency short waves. Due to its user-friendly operation and maturity, Bluetooth technology has found widespread applications in various aspects of our daily lives, including healthcare, asset tracking, and robot navigation.

Recently, Bluetooth tags have been integrated with innovative wearable sensors to enhance wearable electronics . For instance, a wearable humidity sensor was developed by integrating a highly flexible, stretchable, and transparent polyacrylamide/Carrageenan hydrogel film with a Bluetooth module, facilitating the wireless monitoring of respiratory interruptions. Despite the system's high adhesiveness to human skin, its bulkiness due to the requirement of batteries and a printed circuit board (PCB) is a major disadvantage.[56–59].

In contrast, a self-powered wireless wearable sweat analysis system, consisting of a multilayered sensor patch connected with a Bluetooth module, was able to effectively convert the mechanical energy of human movement into electrical energy via a hybrid nanogenerator module [60]. This system provided a platform for the real-time wireless monitoring of sodium (Na+) and potassium (K+) ions in sweat by transmitting the collected data via Bluetooth. However, several challenges hinder the expansion of Bluetooth technology into new domains. These include its relatively low transmission speed, the need for improved device compatibility, and the desirability of a flexible Bluetooth module for applications in wearable sensing systems.

1.4.2 Wi-FI

Wi-Fi, a traditional wireless communication technology, has rapidly evolved to meet the growing demand for wireless data transfer. Recently, Wi-Fi sensing has emerged as an innovative approach for data acquisition and transmission using Wi-Fi-based radio frequency (RF) signals. Leveraging modeling algorithms and machine learning-based algorithms, Wi-Fi sensing can utilize ubiquitous

Wi-Fi devices, thereby eliminating the need for additional hardware and facilitating wireless sensing of physical activities. Current applications of Wi-Fi sensing include human location tracking, environment or object detection, and respiration/heart rate estimation [61, 62].

However, Wi-Fi communication, due to its wireless data transmission over relatively long distances, faces several challenges, including relatively high power consumption. In contrast, Zigbee, a newer wireless technology, boasts low power consumption, large-scale expansion capability, and cost-effectiveness. But, due to its lower power consumption compared to Wi-Fi, Zigbee experiences slower transmission speed and greater performance loss [63, 64]. Despite these trade-offs, the choice between Wi-Fi and Zigbee ultimately depends on the specific requirements of the application, balancing factors such as range, power efficiency, and data transfer speed to achieve optimal performance.

1.4.3 LoRa

While the transmission distance of previously mentioned wireless techniques is relatively short due to the tradeoff between long distance and low power consumption, a wide area network based on the Internet of Things (IoT) can facilitate wireless data transmission over ultra-long distances with low power consumption. Long-Range Radio (LoRa), a proprietary spread spectrum modulation technology, offers a unique solution for remote and ultra-low power transmission. It exhibits versatile and robust characteristics, making it superior to other wireless technologies such as Wi-Fi, Bluetooth, Zigbee, and NFC. LoRa can achieve a coverage range of 5–15 kilometers.

The integration of a highly sensitive sensing system with the LoRa network enables the acquisition of various physiological signals. These signals can be stored in a cloud server and transmitted to remote hospitals for real-time health monitoring or diagnosis [65–67]. LoRa is anticipated to find potential applications in smart homes, industrial settings, and military fields. However, the data rate of LoRa is relatively low compared to other wireless technologies like Wi-Fi and Bluetooth. Furthermore, due to complex deployment and inevitable interference, the LoRa network often falls short of achieving the desired performance.

1.4.4 RFID

Radio Frequency Identification (RFID) is a contactless technology capable of automatic identification and wireless data transfer via electromagnetic waves, finding extensive applications in our daily lives. A typical RFID system consists of an electronic tag, a reader, and a computer network. The electronic tag, a key component, includes a microchip and a coupling antenna for wireless communication. When the antenna's frequency aligns with the input frequency of the electromagnetic wave, a conjugate impedance match occurs between the tag antenna and the RFID chip[68].

RFID tags are generally categorized into active, semi-active, and passive types based on their function and power consumption. Unlike active RFID that requires a battery for long-distance

signal transmission, passive RFID lacks an internal power source, simplifying the design and reducing costs. Furthermore, passive RFID does not require a chip, facilitating integration and miniaturization, making it a popular choice for integration with wearable sensors for wireless data transmission [69–71].

However, the inclusion of microchips in RFID tags increases fabrication complexity and generally results in rigidity. In contrast, chipless RFID tags can be fabricated using a relatively simple process [72], significantly reducing costs. Adjusting the dielectric property of the substrates or the electrical conductivity of the conductors can shift the tag response, making chipless RFID ideal for sensing various external stimuli such as humidity [73, 74], temperature [75, 76], and mechanical strain [77, 78].

Moreover, chipless tags can operate at higher temperatures or harsh conditions compared to their counterparts with chips and circuits due to the limited operating temperatures of Si-based chips. As a result, wearable chipless sensors have garnered significant interest in both industrial and fundamental research. The advent of various novel functional materials and manufacturing technologies has further propelled the development of chipless RFID-based flexible and wearable sensors.

Despite the small size of microchips, conventional RFID tags have limited mechanical flexibility, restricting their potential applications in flexible electronic devices. Additionally, the operation distance of RFID is relatively short, particularly for low-frequency and high-frequency tags. Privacy and security issues also persist due to the design concept of the RFID system.

1.4.5 NFC

Near Field Communication, a widely adopted RFID communication standard, has seen significant growth over the past decades, with extensive applications in access control retail and various other scenarios [53]. Data transmission between NFC devices is accomplished through magnetic or inductive coupling. When an NFC reader is positioned near an NFC chip, a magnetic field is generated, inducing a current in the NFC tag and resulting in a magnetic coupling between the reader and the NFC chip. The data detected are converted into digital values by a voltage rectifier and an analog-digital converter, and wirelessly transmitted to the NFC reader. NFC, a battery-free and contactless technology, offers key benefits such as high security, rapid speed, and easy connection[12, 79–84].

Given its extensive integration into smartphones, NFC has found widespread use in wearable devices and sensing systems. However, despite the rapid advancement of functional materials and novel manufacturing technologies for NFC tags and systems, several challenges impede the widespread adoption of NFC technology in wearable devices. Notably, the working distance of NFC is relatively short (approximately 5–20 cm), and the readout and data transmission between NFC devices are discontinuous, posing challenges for long-term and continuous monitoring. Furthermore, the biocompatibility of the conductive materials used for NFC tags and coils requires

further investigation for their application in wearable and implantable devices.

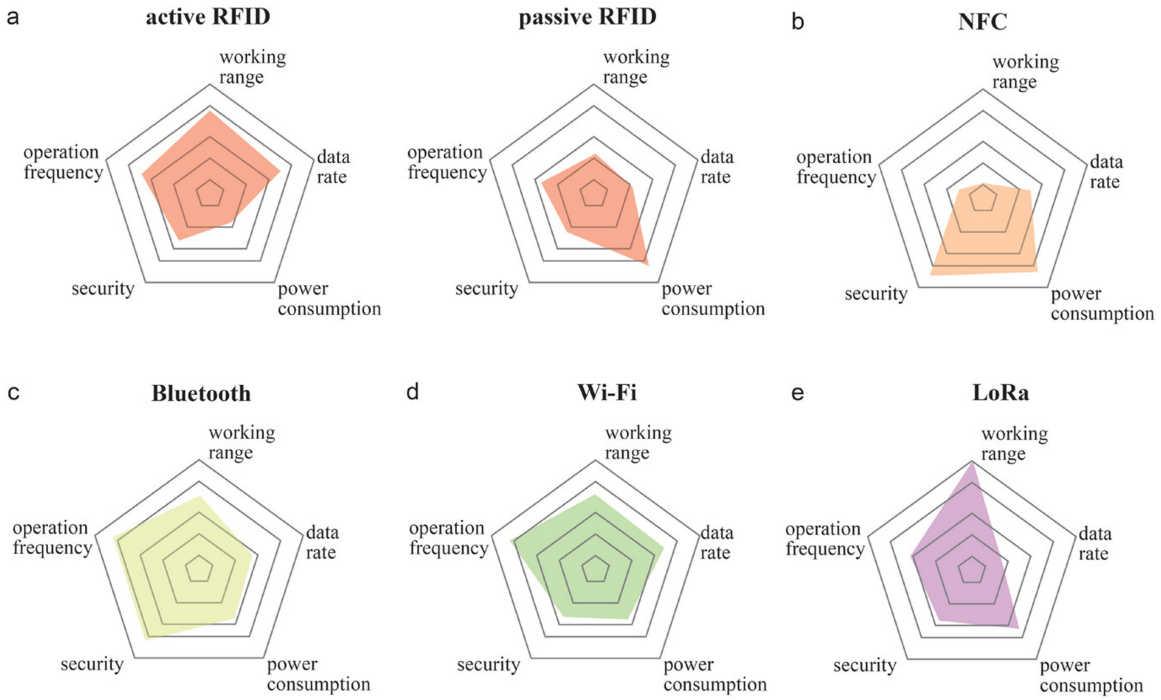


Figure 1.4: Comparison of several common methods for wireless transmission. a) RFID (active and passive RFID). b) NFC. c) Bluetooth. d) Wi-Fi. e) LoRa. Wireless technologies each possess distinct features and associated constraints. For instance, Bluetooth and Zigbee are characterized by their low power consumption, but they suffer from a low data rate and typically necessitate a battery for power. Conversely, RFID and NFC are battery-free technologies, but this results in a relatively low transmission rate. Wi-Fi offers a high transmission rate, while LoRa, despite its low data rate and complex deployment, is a relatively recent technology that provides the benefits of long transmission distance and low power consumption.

1.5 Delving deeper into NFC (Bio)sensing

Following an examination of various biosensors, including both colourimetric and electrochemical types, and an exploration of the different communication technologies available, including WiFi, LoRa and Bluetooth, it becomes evident that NFC offers distinct advantages for biosensing applications. One of the most significant benefits of NFC is its ability to operate without a battery, thereby reducing the cost and enhancing the portability of sensors.

This battery-free operation is particularly advantageous for creating inexpensive and lightweight devices that are easier to deploy and maintain. NFC technology facilitates real-time, non-invasive monitoring, rendering it particularly suitable for wearable devices.

As illustrated in Tables 1.2 and 1.3, NFC-enabled biosensors can detect various analytes, including glucose, lactate, pH, and electrolytes, in bodily fluids such as tears, saliva, sweat, and urine. For instance, NFC-integrated sensors can monitor glucose and lactate levels in tears, providing critical information for diabetes management without requiring invasive blood samples.

Table 1.2: Applications of NFC in Sensors and Biosensors (Part 1)

Application	**Parameter Type**	**Analyte**	**Wearable**	**Description and Reference**
Tear Analysis	Chemical	Glucose	Yes	Detects glucose levels in tears using NFC-enabled sensors integrated into smart contact lens - diagnosis and therapy. [85]
Saliva Analysis in Teeth	Chemical	Acidic environment fluctuation	Yes	Detection of the topical acidic environment fluctuation caused by oral microbial metabolism through electrical stimulation, fluorides are delivered to give feedback therapy. [86]
Skin Pressure and Stretching Points	Physical	Pressure, Strain	Yes	Measures skin pressure and stretching using NFC-integrated flexible sensors. [82]
Skin Humidity and Temperature	Physical	Humidity, Temperature	Yes	Tracks skin humidity and temperature with NFC-enabled patches. [87]
Smart Diapers	Physical	Volume of liquid	Yes	Moisture detector is based on a capacitive sensor. [88]
Glucometers	Chemical	Glucose	Yes	Continuously measures glucose levels using NFC-enabled glucometers. [81]
Electrochemical Measurements	Chemical	Various Electrolytes	No	Analyzes various electrolytes using NFC-enabled electrochemical sensors. [89]
COVID-19 Masks	Chemical	Gas CO_2	Yes	Non-invasive gas determination by means of wearable solutions with a high potential for clinical translation. [90]

Table 1.3: Applications of NFC in Sensors and Biosensors (Part 2)

Application	**Parameter Type**	**Analyte**	**Wearable**	**Description and Reference**
Motion Detection	Physical	Movement	Yes	Tracks physical movement with NFC-integrated motion sensors. [91]
EMG	Physical	Muscle Activity	Yes	Monitors muscle activity using NFC-enabled EMG sensors. [87]
ECG	Physical	Heart Activity	Yes	Tracks heart activity using NFC-integrated ECG sensors. [84]
Sweat Analysis	Chemical	Glucose, hydrogen, sodium, potassium	Yes	Real-time on-body sweat analysis for simultaneous quantitative detections of glucose, hydrogen, sodium, and potassium. [92]
Food Spoilage Detection	Physical	Strain, Temperature	No	Swollen food packages can be detected with the strain sensor, serving as beacons of microbial contamination. [93]
Water Quality Monitoring	Chemical	pH, Heavy Metals	No	Measures water quality parameters such as pH and heavy metals using NFC-enabled sensors. [94]
Soil Health Analysis	Chemical	Nutrients, pH	No	Monitors soil nutrients and pH using NFC-enabled sensors. [95]
Seaweed Monitoring	Physical	temperature, light intensity, depth, and motion	No	The device records and shares data on temperature, light, depth, and motion for seaweed farmers' decision-making. [96]
Blood Oxygen Levels	Physical	Oxygen Saturation	Yes	Measures blood oxygen saturation with NFC-integrated sensors. [97]
Respiratory Rate Monitoring	Physical	Breathing Rate	Yes	Tracks respiratory rate using NFC-enabled sensors. [98]
Wearable Hydration Sensors	Physical	Hydration Levels	Yes	Monitors hydration levels with NFC-integrated wearable sensors. [99]
pH Sensors	Chemical	pH	No	battery-less color sensor based on NFC. [100]
Lactate Monitoring	Chemical	Lactate	Yes	Tracks lactate levels using NFC-integrated sensors. [101]
Uric Acid Detection	Chemical	Uric Acid	Yes	Monitors uric acid levels with NFC-enabled sensors. [69]
Cortisol Measurement	Chemical	Cortisol	Yes	Tracks cortisol levels using NFC-integrated wearable sensors. [102]
Implantable Glucose Sensors	Chemical	Glucose	No	A Continuous Oral-fluid Monitoring of Glucose. [103]

Moreover, NFC sensors in dental devices can track pH and glucose levels in saliva, offering insights into oral and systemic health conditions. In wearable technology, NFC plays a crucial role in monitoring physiological parameters. For instance, flexible sensors integrated with NFC can measure skin pressure and stretching points, providing valuable data for applications ranging from rehabilitation to ergonomic assessments. Additionally, NFC-enabled patches can

track skin humidity and temperature, essential for managing conditions like hyperhidrosis and thermoregulatory disorders, as shown in the Figure 1.5.

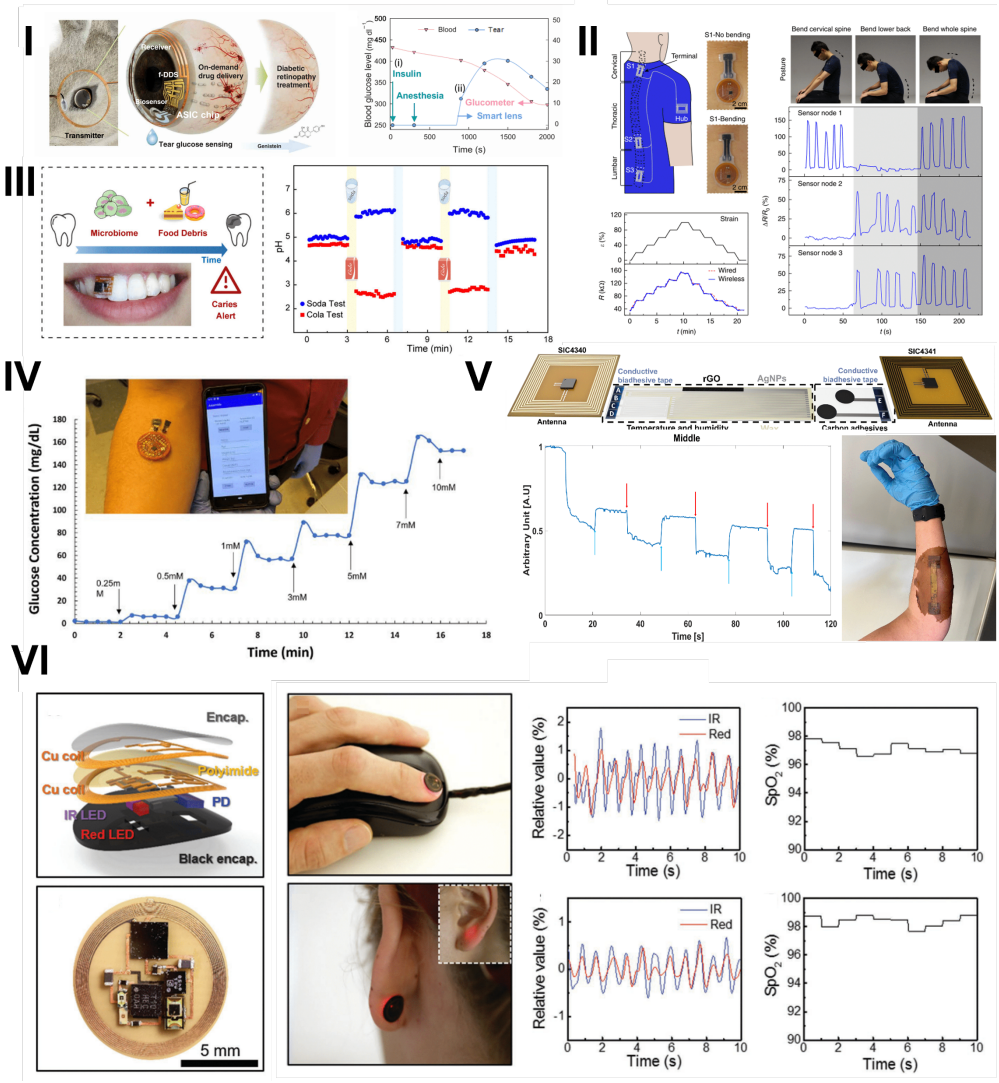


Figure 1.5: A comprehensive overview of the versatility of NFC technology in wearable devices. (I) In vivo diabetic diagnosis and therapy of the smart contact lens. Adapted with permission from [85]. Copyright ©2020, Science Advances. (II) Wireless sensor system for real-time posture monitoring. Battery- free strain sensors mounted on cervical (S1), thoracic (S2), and lumbar (S3) sections are simultaneously interconnected to an NFC hub device. Adapted with permission from [91]. Copyright ©2020, Springer Nature. (III) Dental patch system for caries lesion detection by monitoring the topical oral microenvironment pH fluctuation. Adapted with permission from [86]. Copyright ©2022, npj Flexible Electronics. (IV) Glucose monitoring system operating on increasing concentration of glucose. Adapted with permission from [81]. Copyright ©2022, Scientific Reports. (V) Sensor network for the determination of skin temperature and humidity and muscle contractions. Adapted with permission from [87]. Copyright ©2024, Elsevier. (VI) Miniaturized flexible pulse oximeter built on silicone elastomer and equipped with a near-field wireless chip. Reproduced with permission from ref. 157. Copyright ©2017 Wiley

The utility of NFC extends to infant health management, where smart diapers equipped with NFC sensors can monitor glucose and pH levels in urine. NFC-enabled glucometers provide continuous glucose monitoring, which improves diabetes management by delivering timely and accurate data. Electrochemical sensors utilising NFC technology enhance diagnostic capabilities by precisely measuring various electrolytes, which is critical for both clinical and home settings.

NFC-enabled face masks have emerged as a significant advancement in public health, particularly during the COVID-19 pandemic[104], by detecting viral particles in exhaled breath. Wearable NFC sensors also facilitate the monitoring of physical activities and physiological signals. For instance, NFC technology is employed in motion detection sensors, electromyography (EMG) sensors, and electrocardiography (ECG) sensors to track movement, muscle activity, and heart activity, respectively. Furthermore, NFC-enabled sensors can monitor sweat electrolytes, pH, and blood oxygen levels, exemplifying their versatility and significance in personal health monitoring.

In addition to its applications in health monitoring, NFC technology is also instrumental in environmental applications. NFC sensors can be used to measure pH and heavy metals in water, soil nutrients, and gases in food packaging, thereby improving environmental health and safety, as shown in the Figure 1.6.

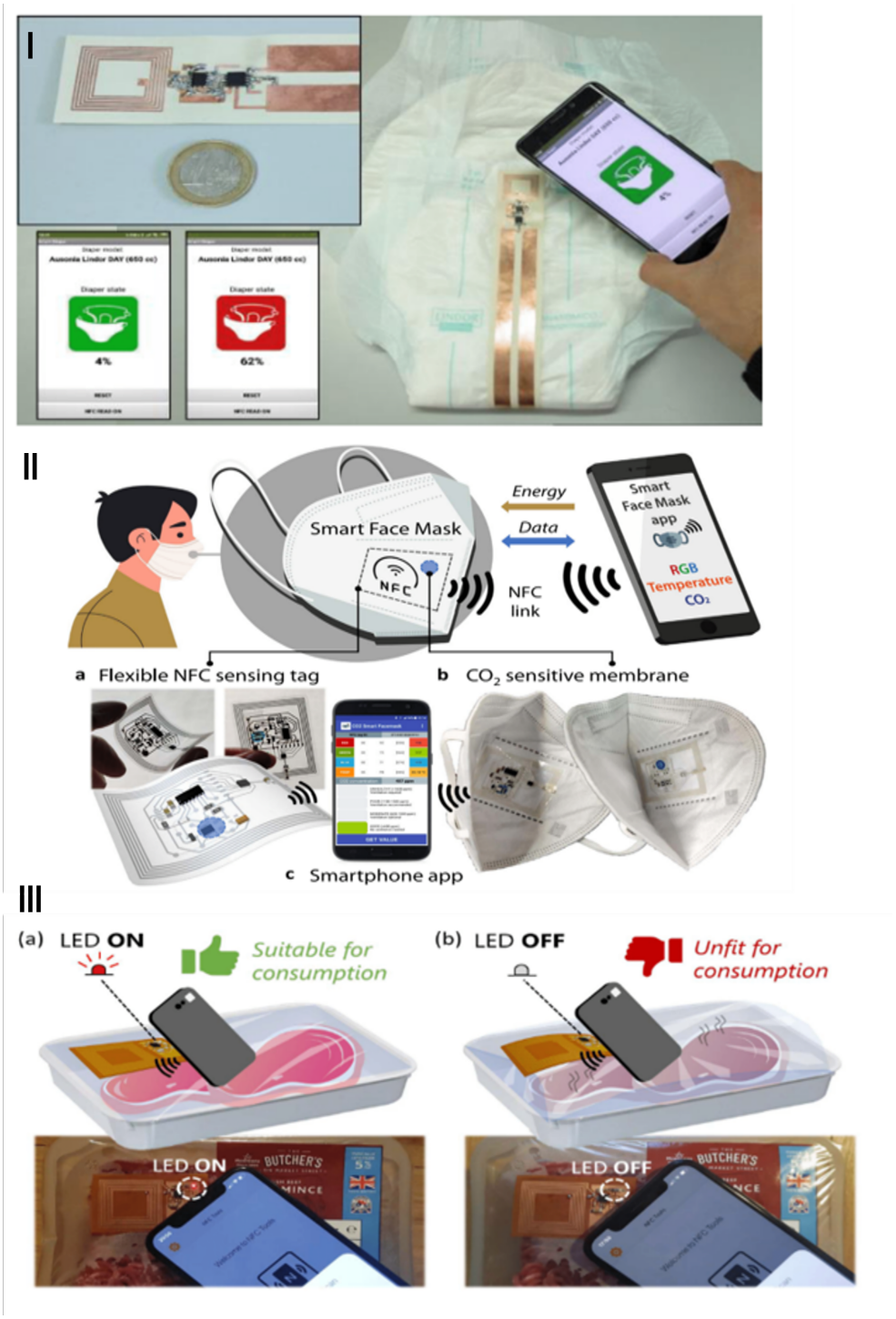


Figure 1.6: (I) NFC system adhered to a diaper, and several screens of the mobile APP designed to interface with the user. Adapted with permission from [88]. Copyright ©2019, IEEE. (II) Overview of the NFC-based smart facemask for wireless CO2 real-time determination. Adapted with permission from [90]. Copyright ©2022, Springer Nature. (III) NFC strain sensor tag attached to a food package for meat spoilage detection. The LED will be ON if the product is suitable for consumption. Adapted with permission from [93]. Copyright ©2021, IEEE.)

Ultimately, the interconnection and simultaneous reading of NFC biosensors can be discussed. Two recent studies provide the groundwork for this analysis: one on near-field-enabled clothing and the other on battery-free, wireless soft sensors for continuous multi-site measurements of pressure and temperature.

The first study focuses on the development of clothing with near-field technology that enables wireless connection of energy and data between various distant points on the body. The integration of conductive threads into fabric patterns enables the creation of a battery-free sensor network that enables simultaneous measurements at strategic locations, such as spine posture, temperature and gait during exercise. This approach demonstrates real-time multi-node measurement capability and maintains long-term stability, which is crucial for continuous monitoring.

The second study presents a soft sensor system that mounts on the skin to continuously measure pressure and temperature. This system operates wirelessly without batteries, relies on membrane deflection to measure pressure, and provides simultaneous readings. The configuration includes primary antennas mounted under the bedding, connected to a wireless reader, with a multiplexer allowing sequential reading of multiple sensors. The clinical trials validate the functionality and long-term stability of this technology in hospital settings. The findings of both studies, shown in Figure 1.7, indicate that the feasibility of simultaneously interfacing and reading NFC biosensors is supported by several rationales. NFC wearables demonstrate the scalability of the network, proving that a network of interconnected sensors is feasible.

Extending this concept, multiple soft sensors could be strategically placed throughout the body, enabling simultaneous readings. This approach is resource efficient, as simultaneous readings reduce the need for repeated scans, which minimises patient discomfort and saves energy. From a clinical perspective, the integration of interconnected NFC biosensors can enhance patient care by facilitating the acquisition of comprehensive data for the prevention of pressure injuries, postural analysis and temperature monitoring. As can be seen the interconnection and simultaneous reading of NFC biosensors hold significant promise for advancing wearable healthcare technology.

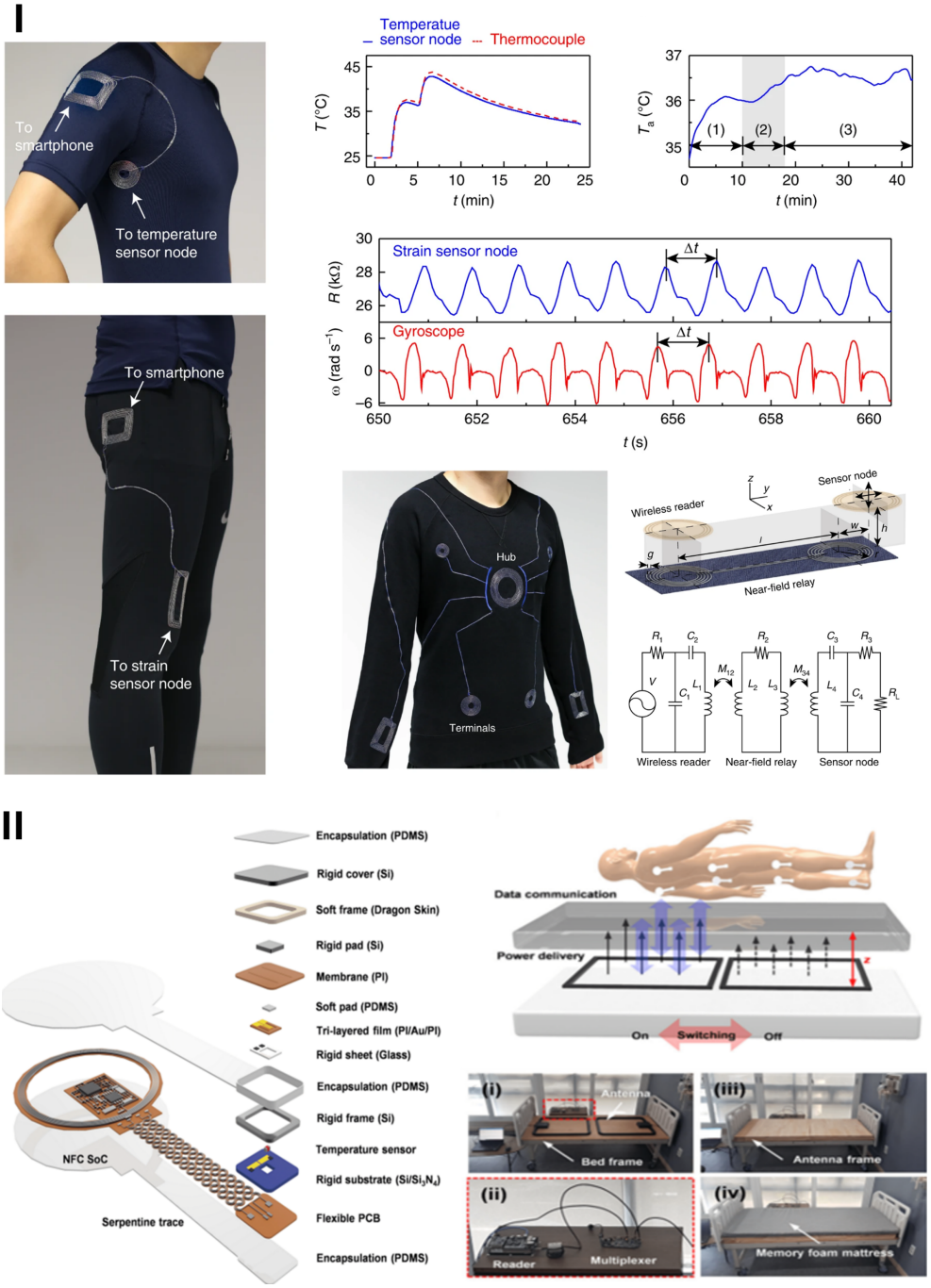


Figure 1.7: (I) Lin et al. report the development of near-field-enabled clothing that can establish wireless power and data connectivity between multiple distant points around the body, creating a network of battery-free sensors interconnected by proximity to functional textile patterns. Adapted with permission from [91]. Copyright ©2020, Springer Nature. (II) Oh et al. present a soft, skin-mountable sensor system that includes a pressure-responsive element based on membrane deflection and a battery-free, wireless mode of operation capable of multi-site measurements at strategic locations across the body. The sensors yield continuous, simultaneous readings of pressure and temperature in a sequential readout scheme from a pair of primary antennas mounted under the bedding and connected to a wireless reader and a multiplexer located at the bedside. Adapted with permission from [82]. Copyright ©2021, Springer Nature.

This chapter has provided an overview of the fundamental principles and advancements in smartphone-based biosensors for portable diagnostics. The integration of various sensor technologies with smartphones has been explored, with particular attention paid to their impact on PoC diagnostics.

Optical sensors, which leverage smartphone image analysis, have enabled real-time identification of biological and chemical entities. During the global pandemic caused by the SARS-CoV-2 virus, LFAs exemplified the utility of these technologies, demonstrating the potential for smartphones to provide both qualitative and quantitative data.

Electrochemical sensors have shown great promise due to their sensitivity and versatility. The integration of these sensors with smartphones has reduced detection system costs and complexity, enhancing real-time monitoring. The combination of advances in sensor technology and smartphone computational power has transformed mobile devices into powerful diagnostic tools.

The incorporation of NFC technology has further enhanced portability and usability. NFC-enabled, battery-free sensors simplify the design and operation of portable biosensors, facilitating seamless communication between the sensor and the smartphone.

In summary, the convergence of sensor technologies with smartphones represents a significant advancement in portable diagnostics. This integration enables real-time, accurate, and cost-effective diagnostics using widely available mobile devices. The ongoing advancement of sensor integration, data analysis, and wireless communication will facilitate further innovations, expanding the scope of applications and enhancing the accessibility of portable diagnostic solutions.

Given the numerous benefits and applications of NFC technology in biosensors and wearables, it is evident that NFC is a cornerstone of modern health diagnostics and monitoring. The ability of NFC technology to provide accurate, real-time data in a non-invasive and cost-effective manner renders it invaluable for both personal and public health. For these reasons, NFC technology has been chosen as the focal point for the development of this thesis, with the objective of exploring and enhancing its capabilities in the field of biosensing.

CHAPTER 2

OBJECTIVES

The principal aim of this doctoral thesis is to develop smartphone-based portable sensors and biosensors, with a particular focus on using NFC technology to measure physical and electrochemical parameters.

More in detail, the objectives of this thesis can be summarized as follows:

1. Study of commercially available integrated circuits(ICs) for resistance and capacitance measurements (for physical parameters) and electrochemical measurements.
    - To verify the functionality of the ICs against a standard instrument (multimeter/potentiostat).
    - Design of antennas compatible with the NFC protocol and their manufacture using different construction techniques.
2. Development of a battery-free wearable device that can measure skin temperature and humidity, as well as muscle contraction signals.
3. Development of electrodes of varying types for electrochemical sensors, with applications in the measurement of DNA, glucose, and compound identification.
    - Fabrication and characterization of low-cost nanoband electrodes using sputter coater.
    - Fabrication and characterization of laser-induced graphene electrodes modified with a gelatine and Prussian-blue compound.
    - Design and characterization of PCB-electrodes, which are easily mass-producible by PCB manufacturers.

4. Development of a portable electrophoretic source, which can be powered by a mobile phone and which allows simultaneous electrochemical readings.

    - This last project integrates most of the concepts seen throughout the thesis.

CHAPTER 3

DEVELOPMENT OF POCKETABLE SENSOR INTERFACES (READOUT)

Recent investigations have underscored the progressive advancement of affordable, compact potentiostats. There has been a notable development of cost-effective, open-source potentiostats that serve as complements to the more expensive, conventional laboratory-grade devices [52, 105]. However, these alternatives often necessitate a computer for operation, hindering their utility in home-testing scenarios and environments with limited resources. Additionally, these systems lack the capability for direct data transmission to cloud services, which restricts their functionality in sharing information with healthcare providers for clinical uses.

With the worldwide surge in smartphone ownership, exceeding more than 5,000 million by 2025,integrating smartphones with potentiostats is becoming increasingly prevalent in electrochemical sensing applications. Through interfaces such as Bluetooth, Wi-Fi, USB, or audio ports, smartphones serve as versatile tools for powering potentiostats, as well as for processing, displaying, and disseminating data[106–108].

Existing literature details various implementations of smartphone-based potentiostats. For instance, Ainla et al. introduced a "universal wireless electrochemical detector" (UWED) that utilises Bluetooth connectivity to pair with smartphones[51]. Similarly, Cai et al. demonstrated the xenSTAT device, capable of performing a broad spectrum of electrochemical methods and connecting via Bluetooth[109]. Jenkins et al. developed the ABE-Stat, which conducts a range of electrochemical analyses and connects to smartphones wirelessly using Wi-Fi[110]. Nonetheless, such devices often rely on external batteries, complicating their design and increasing both cost and maintenance needs[111].

As previously stated in the introduction, NFC represents a highly promising alternative to portable potentiostats. NFC's value as a wireless sensor platform is increasingly recognised, offering cost-effective, portable, and real-time monitoring solutions in diverse fields, including

food safety[17], environmental monitoring[112], and healthcare[82, 90]. NFC's superiority lies in its capacity for passive power transfer, enabling sensor operations that are either battery-free or boast extended battery life[108].

Several studies have integrated NFC with electrochemical sensing systems. Kassal et al. utilized an RFID/NFC wireless sensor tag for potentiometric readings with pH and ion-selective electrodes[113]. Steinberg et al. demonstrated a semi-autonomous wireless potentiostat for amperometric measurements that communicates via NFC, capable of storing and externally processing chronoamperometric data on a smartphone[114]. NFC-enabled chemical sensors have also been used to quantify biomolecules such as uric acid and glucose. The "smart bandage" developed by Kassal et al. is a biosensor interface for a wearable potentiostat that wirelessly communicates uric acid levels pertinent to wound monitoring to various smart devices[69]. Fedtschenko et al. showcased a wireless system for glucose detection in tear fluid, employing NFC for data transmission to a portable reader[115]. In cyclic voltammetry applications, Siegl et al. described a sensor strip with an integrated NFC-powered circuit featuring components such as an antenna, a chip, and an electrode connector for real-time analysis[116].

This chapter introduces two integrated circuits (ICs): an NFC-enabled potentiostat (SIC4341) and an NFC-analog sensor interface (SIC4340). Both ICs operate without batteries and connect to smartphones using NFC technology. In this chapter, it will be shown how to design antennas compatible with this communication protocol, how to fabricate them with different methodologies and what to consider between each fabrication method. As well as the performance of both ICs.

3.1 Wireless Sensing Using NFC

3.1.1 Analog Sensor Interface – SIC4340

The SIC4340, engineered by Silicon Craft Technology PLC, is a sophisticated integration circuit designed for utilisation within the high-frequency (HF) RFID domain, specifically targeting NFC technologies. Operating within the 13.56 MHz bandwidth and conforming to NFC Forum Type 2 Tag standards, the chip guarantees compatibility with an extensive range of NFC-enabled devices[117].

A cornerstone of the SIC4340's operational paradigm is its intrinsic low-power design. It derives active energy via electromagnetic induction from proximal NFC devices, circumventing the need for an embedded power source. This energy-harvesting feature is especially critical for sensor and biosensor applications where persistent, autonomous operation is necessary, particularly in settings requiring biocompatibility and minimal maintenance[71].

The integrated circuit is adept at resistance measurement across an expansive spectrum. It is worth mentioning that for the measurement to be valid, the bias current must be set in such a way that the voltage measured by the chip is between $0.2V$ and $1.2V$. The resistance value will be given by the equation $R = V_{sen}/I_{sen}$. Where I_{sen} is the bias current that takes values ranging

from $1\mu A$ to $504\mu A$, with the exception that placing a current lower than $10\mu A$ can cause too high error due to the least significant bit (LSB). Therefore, we will take as valid values of current $10\mu A$ to $504\mu A$ and voltage of $0.2V$ to $1.2V$. Taking into account these limitations, the resistance limit values will be $R_{min} = 0.2V/500\mu A = 400\Omega$ and $R_{max} = 1.2V/10\mu A = 120K\Omega$.

This gives us the possibility of measuring variations of 300 times, as long as the bias current is adapted to each measurement; if the bias current is kept fixed, the variation that we can measure is six times. On the other hand, the SIC4340 Chip has three channels, so the bias current values can be adapted to have three measurement ranges, thus achieving a variation of 216 times.

As shown in Figure 3.1 of the block diagram of the SIC4340, the onboard analog front-end (AFE) provides a versatile interface with multiple sensor outputs. It delivers analog-to-digital conversion and supports the collection and interpretation of data from external stimuli. This AFE is compatible with a broad array of sensor modalities, enabling the translation of various physical, chemical, or biological signals into computable digital information.

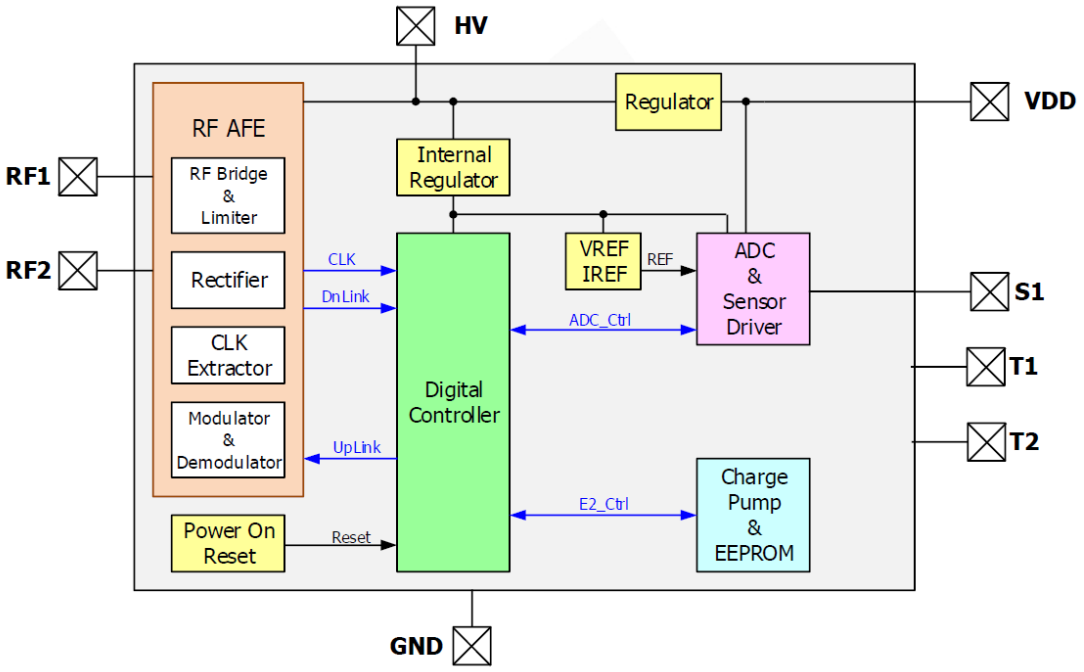


Figure 3.1: SIC4340 Integrated Circuit Block Diagram depicts the analog section where the information is extracted and energy is harvested, as well as the digital block, where the system logic is located, and ADC block with the sensor driver.

Biosensor applications, in particular, reap significant benefits from the SIC4340's functional architecture. The chip directly transduces biological interactions into electronic signals, subsequently conveying this information wirelessly to NFC-capable readers. Such functionality is increasingly sought after in health diagnostics, environmental surveillance, and biological

research, where the expeditious gathering of data is of essence[118].

To rigorously evaluate the chip's performance in measuring resistive and capacitive elements and to understand the influence of bias current, a device was developed. This device features four terminals—two parallel pairs—to facilitate the interchange of commercial resistors and capacitors. The obtained values were then cross-referenced with readings from a precision Digital Multimeter, the Keithley DMM6500, to confirm accuracy.

For interfacing with the SIC4340 chip, a compact PCB was specifically engineered and produced. The designed board was sent to be fabricated by PCBway, a Chinese manufacturing service. Its design incorporates a dedicated space on the top layer for mounting the chip and situating two tuning capacitors for fine adjustments. The bottom layer of the PCB is minimalistic, comprising merely six contact pads: two for antenna connections, three for interfacing with the chip's measurement channels, and one for the ground connection(GND).

The antenna required for NFC functionality was crafted using Inkjet printing technology, the specifics of which are laid out in the next section. To affix the antenna to the PCB, we employed a unique Electrically Conductive Adhesive Transfer Tape (ECATT), specifically the 3M Electrically Conductive Adhesive Transfer Tape 9703. This ECATT boasts anisotropic electrical conductivity, meaning it facilitates current flow exclusively through the thickness of the adhesive ('Z-axis') and not along its plane. This selective conductivity is achieved by embedding the adhesive matrix with conductive particles positioned to create point-to-point connections across the adhesive layer while maintaining electrical insulation laterally. This characteristic is particularly advantageous in preventing short circuits among the closely spaced pads and ensures reliable, targeted electrical connections. The device obtained is shown in Figure 3.2.

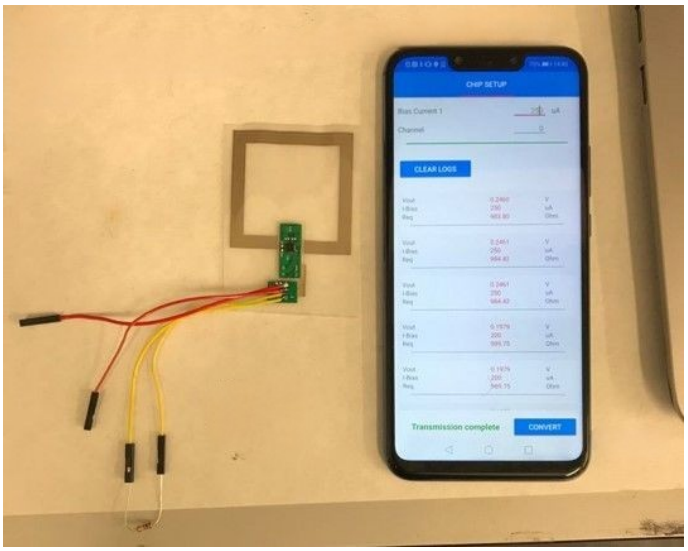


Figure 3.2: A simple device that consists of a PCB to which the chip has been soldered and is attached to a silver printed antenna, manufactured for the measurement of commercial resistors and capacitors in order to verify the operation of the SIC4340 IC.

In the empirical investigation of the SIC4340 chip's functionality, a comprehensive range of resistors from $1K\Omega$ to $220K\Omega$ was tested across its three channels, employing varied bias currents to elucidate the relationship between current and measured resistance. The data explains a notable trend: when measuring resistors at the lower end of the spectrum with insufficiently low bias currents, the resultant readings fall below the actual resistance values. This deviation from expected results is attributed to the measurements falling outside the chip's linear operational range, which commences at a threshold voltage of $0.2V$, as previously delineated.

Therefore, it is imperative to moderate the bias current when addressing high-value resistors to avoid overloading the chip's measurement capacity. During trials with resistors valued at $3.9K\Omega$, $4.7K\Omega$, $5.6K\Omega$, and $6.8K\Omega$, it was observed that an excessive bias current of $500\mu A$ invariably led to a saturation of the system. This phenomenon was consistently evidenced by a false reading of $2.56K\Omega$ across all resistors mentioned above values, thus underscoring the critical need for precise bias current calibration to ensure the accuracy and integrity of resistance measurements within the specified operational parameters of the chip. All measurements and their comparison with the Keithley DMM6500 Digital multimeter are shown in the bar graphs in Figure 3.3 and in the SIC434X Chip Characterisation Appendix.

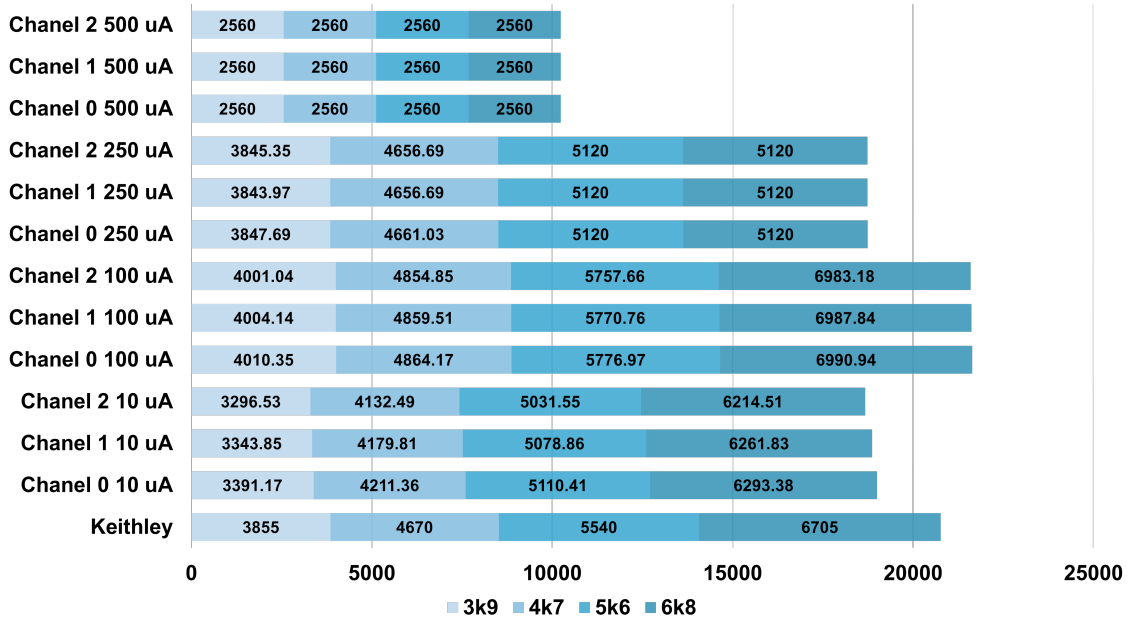


Figure 3.3: Comparison of four resistors measured with the NFC system and the Keithley DMM6500 Digital Multimeter. A wide range of resistors up to 220K can be found in the SIC434X Chip Characterisation Appendix.

For the characterisation of the SIC4340 chip's capacitive measurement capabilities, an analogous examination was conducted utilising an array of commercially available capacitors. Unlike resistance measurement, capacitive measurement necessitates a more complex configuration of parameters to ensure precision and reproducibility (Figure 3.4) .

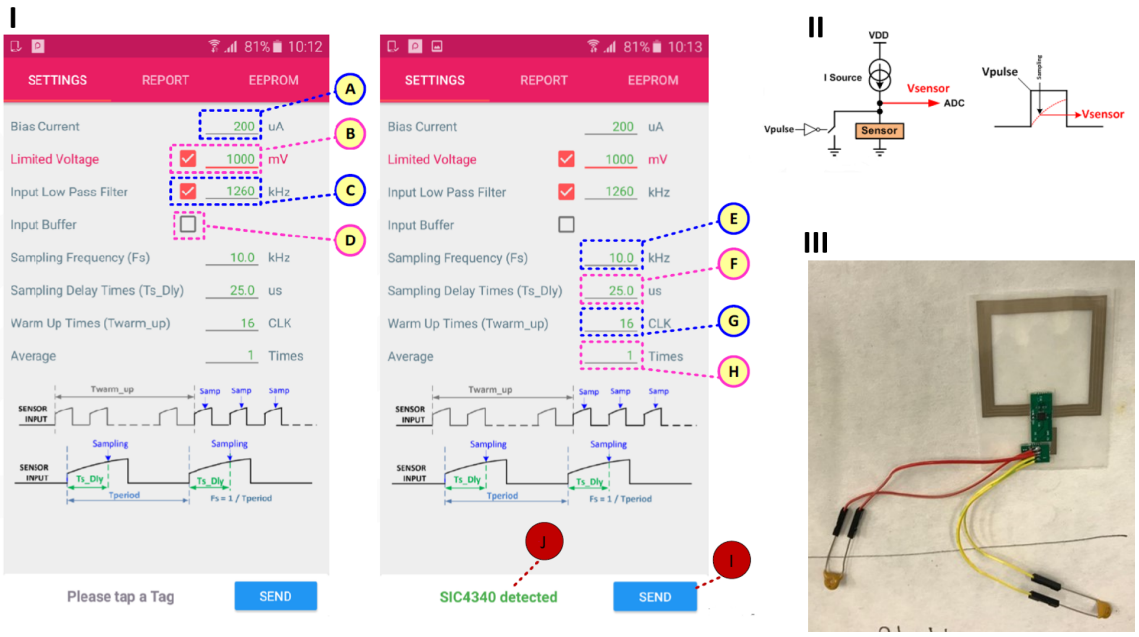


Figure 3.4: (I) Screenshots of the App provided by Silicon Craft where the parameters can be set: bias current (A), limit voltage (B), apply a low-pass filter (C), implement a buffer (D), Sampling Frequency (Fs) (E), Sampling Delay Times (Ts-Dly) (F) and Warm Up Times (Twarm-up) (G). (II) Scheme for the measurement of capacitors by DC charging and discharging. (III) PCB containing the SIC4341 chip, attached to an antenna printed with silver ink for the measurement of two capacitors in parallel.

The bias current (A), which was similarly adjusted in the resistance measurements, requires supplementing with a low-pass filter (C) to attenuate high-frequency noise that could otherwise compromise the measurement integrity. Furthermore, a buffer (D) is employed to accumulate a sequence of data points, as the assessment of capacitance is derived indirectly through the observation of the capacitor's charge and discharge cycles.

To accurately capture the charging and discharging behavior of the capacitor, several critical settings must be meticulously configured. These include the Sampling Frequency (Fs) (E), which dictates the rate at which the chip samples the charge state of the capacitor. The Sampling Delay Times (Ts-Dly) (F) establish the intervals between successive sampling events. The Warm Up Times (Twarm-up) (G) allow the system to stabilize before measurements commence. Lastly, the number of measurements to be averaged (H) is specified to mitigate transient variations and enhance the robustness of the capacitive value determination.

The quantification of capacitance is ultimately governed by the time constants derived from the charge/discharge curves, and the specific equation for capacitance calculation, which considers these dynamic parameters is presented below,

$$C = \frac{I_s \times T_s}{V_{sen}} \tag{3.1}$$

where I_s is the Bias Current, T_s is the Sampling Delay Times and V_{sen} is the voltage obtained from the measurement.

As with the resistor evaluations, the outcomes from the capacitive measurements underscore the reproducibility across the chip's channels and the significance of accurately calibrating the measurement parameters. For capacitance assessments, utilizing a bias current that is lower than the optimal value tends to yield an overestimation of the capacitance (Figure 3.5 and SIC434X Chip Characterisation Appendix). The feasible measurement spectrum extends from a minimum of $4pF$, achievable under conditions of a sampling delay time (Ts) of $5\mu s$ and a bias current (Is) of $1\mu A$, to a maximum of $2.5\mu F$, which can be measured with a Ts of $1ms$ and an Is of $504\mu A$. These ranges demonstrate the chip's versatility in capturing a wide expanse of capacitive values, provided the measurement settings are finely tuned to align with the specific characteristics of the capacitor under test.

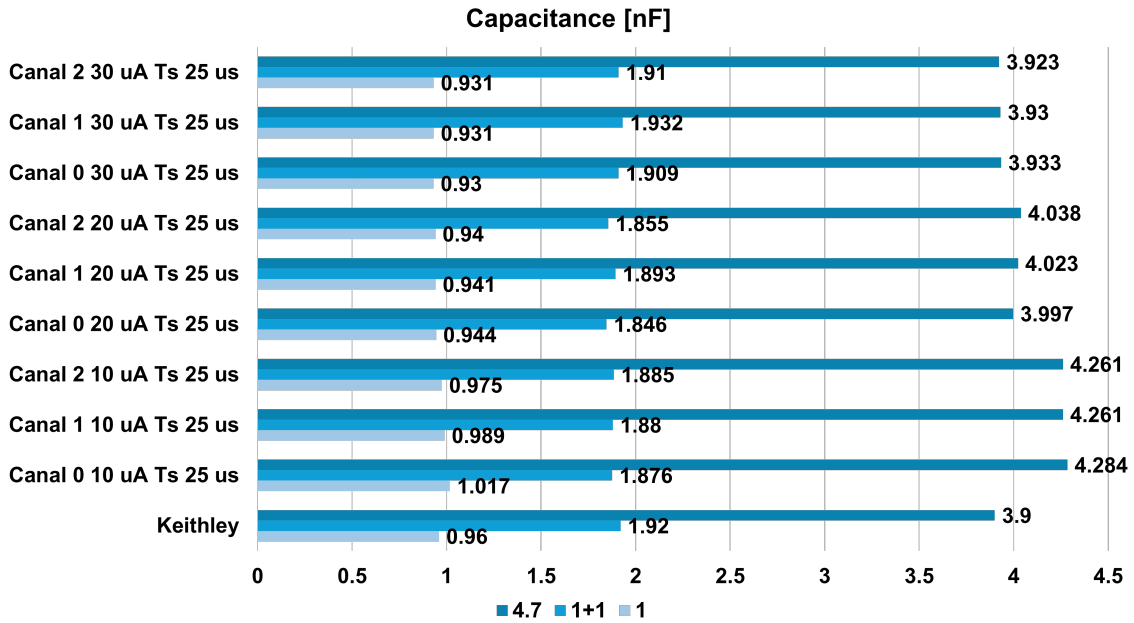


Figure 3.5: Comparison of two capacitors and two in parallel measured with the NFC system and the Keithley DMM6500 Digital Multimeter. Other capacitor measurements can be found in the SIC434X Chip Characterisation Appendix.

3.1.2 Potentiostat Sensor Interface – SIC4341

The integrated circuit depicted in Figure 3.6 is intricately designed, consisting of multiple components that facilitate its function. The first segment is the analog interface, which serves as a bridge between the RF signals and the digital controller. The second segment encompasses the digital controller paired with a memory unit. This duo orchestrates the operational responses of the integrated circuits, specifically tailored for data transmission at the high-frequency (HF) $13.56MHz$ radio band, maintaining compatibility with ISO1443A standards. Additionally, it integrates a subsystem for processing the chemical sensor's signals to capture sensor responses accurately.

Upon the close proximity of an NFC-enabled smartphone to the antenna, the dormant NFC microchip is energized through the magnetic field generated by the smartphone's RF output. Once the microchip detects a power influx above the threshold, it springs into action, initializing its system, activating peripheral devices, and awaiting commands from the smartphone to proceed with specific tasks.

The SIC4341 microchip is engineered with an embedded potentiostat adept at measuring currents up to $\pm 20\mu A$ from chemical sensors. It boasts the capability to modulate the bias voltage across the working and reference electrodes within a range of $-800mV$ to $+800mV$. This modulation is achieved through the precise operation of dual digital-to-analog converters (DACs), which offer a maximum voltage of $1.28V$, adjustable in $5mV$ increments.

Control over the bias voltage applied to the sensors is delegated to an smartphone application, which issues commands to fine-tune the DAC voltage as required. Concurrently, the sensor's physical current is processed by a 10-bit analog-to-digital converter (ADC) coupled with a digital signal processor, transforming the analog signal into digital data. This data is then stored within the microchip's internal memory, standing by for retrieval by the NFC smartphone.

The innovative application does not merely act as a control unit; it is also capable of sending periodic commands to the DACs, adhering to specified biasing profiles like cyclic voltammetry.

Following each command cycle, the smartphone reads the resultant conversion data, allowing the reconstruction of a voltammetry waveform on the application's graphical user interface (GUI). The application's timing parameters, including sweep rates ranging from $5mV/s$ to $1000mV/s$ for cyclic voltammetry, are user-configurable through the GUI, which also enables flexible arrangement of the three-electrode terminals to accommodate diverse electrode configurations.

The smartphone application, Chemister APP supplied by Silicon Craft Technology, is designed to be versatile, supporting a suite of electrochemical techniques beyond cyclic voltammetry. It adeptly facilitates the performance of chronoamperometry, where the current is measured over time at a fixed potential, providing insights into the kinetics of electrochemical processes.

Moreover, the GUI allows for the execution of Linear Sweep Voltammetry (LSV), where the potential is linearly scanned over a range, and the resulting current is recorded, thus aiding in the analysis of electrochemical reaction mechanisms. Differential Pulse Voltammetry (DPV) is

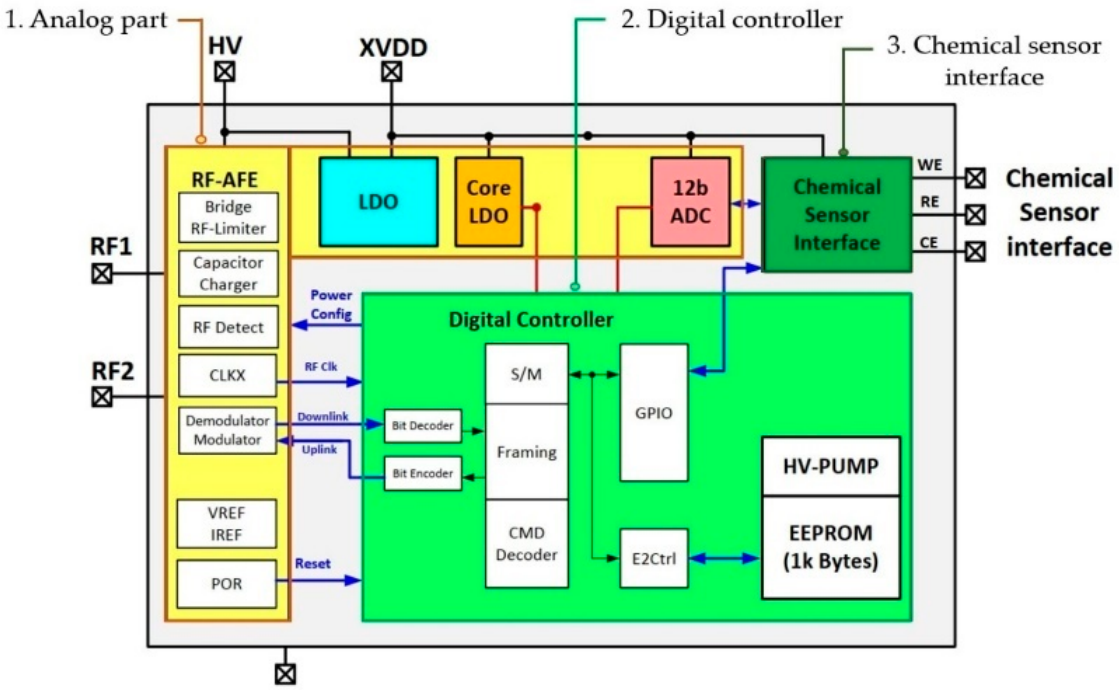


Figure 3.6: SIC4341 Integrated Circuit Block Diagram depicts the analog section where the information is extracted and energy is harvested, as well as the digital block, where the system logic is located, and the electrochemical interface.

another advanced technique available through the interface. DPV applies a series of potential steps with superimposed pulses, enabling the detection of substances with enhanced sensitivity and resolution. Additionally, the GUI encompasses Square Wave Voltammetry (SWV), a method where a square wave potential is applied, and the current is sampled at the end of each forward and reverse pulse. This technique is particularly beneficial for trace analysis due to its high sensitivity and fast scanning capabilities.

Each of these techniques is integral to various analytical applications, and the GUI has been thoughtfully constructed to provide an intuitive and user-friendly platform for researchers to select and customize parameters specific to their experimental needs. This versatility ensures that a broad range of electrochemical investigations can be conducted efficiently and effectively.

To confirm the proper functionality of the SIC4341 chip, a similar setup to the one used in the SIC4340 investigation was assembled. Rather than employing four discrete connectors, this device incorporated a flexible printed circuit (FPC) connector directly onto the PCB. This adjustment was made to facilitate the attachment of a screen-printed electrode, thereby enabling the execution of cyclic voltammetry assays. A range of Ferro-Ferricyanide concentrations and scan rates were tested to evaluate the system's performance.

The results gleaned (Figure 3.7) from these experiments were benchmarked against readings obtained from a Metrohm Autolab PGSTAT12, a standard in electrochemical analysis, to ensure accuracy and reliability in the chip's measurement capabilities.The voltammograms produced by both potentiostats exhibit significant similarity, with nearly identical current peaks. An exception is observed in the case of Ferro Ferricyanide at 0.5mM and a scan rate of 0.05 V/s, where the oxidation peak measured by the NFC potentiostat is a little lower than that of the Autolab. However, under the same conditions, the reduction peaks overlap. Additionally, at a 1mM concentration, both potentiostats display a shoulder effect near the oxidation peak. Furthermore, at a concentration of 0.5 mM and a scan rate of 0.1 V/s, both voltammograms exhibit a glitch or small peak at -0.4 V. These observations suggest that the NFC potentiostat performs comparably well to the Autolab for this type of application, demonstrating its suitability and reliability for electrochemical measurements.

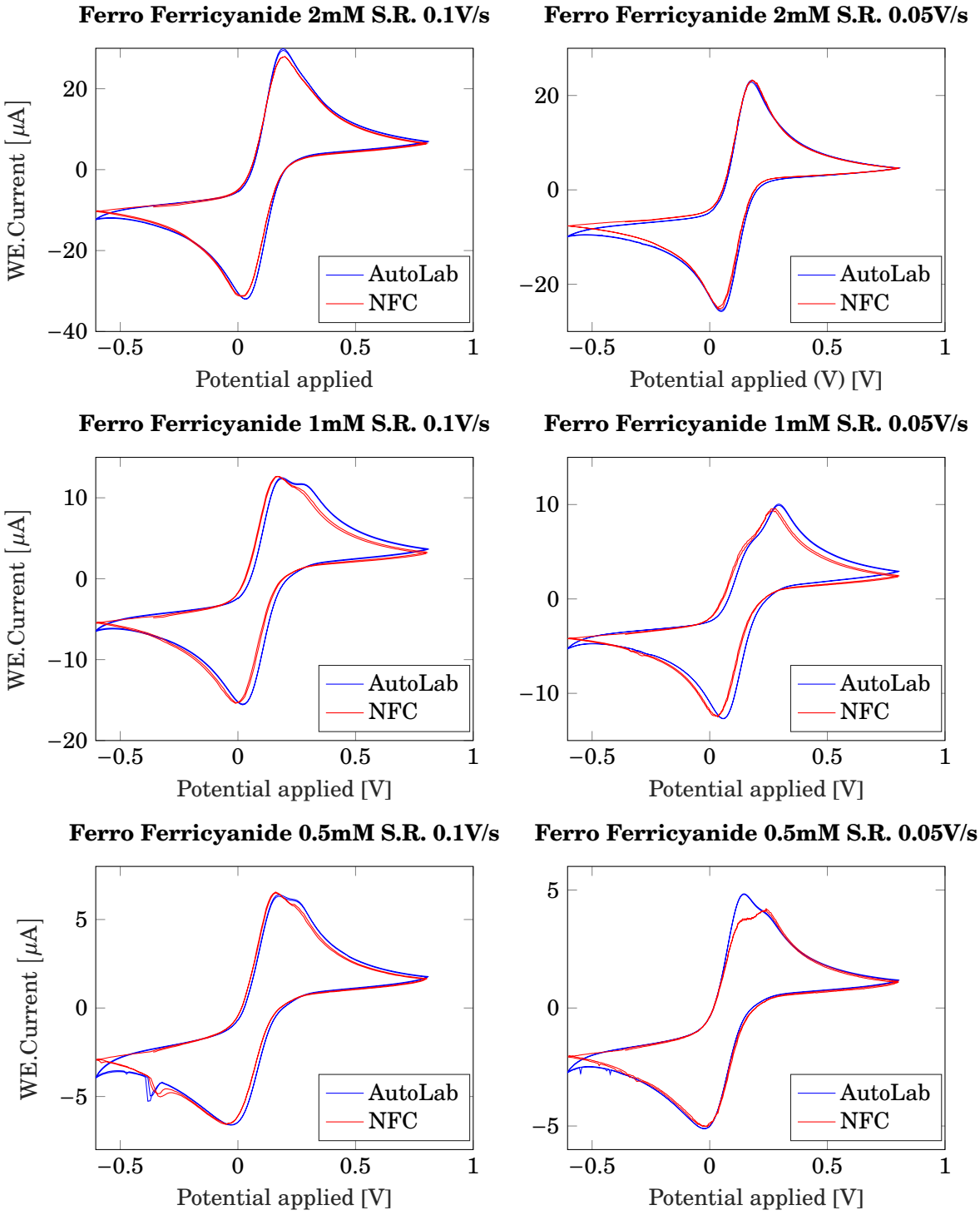


Figure 3.7: Ferro/Ferricyanide voltagrams at three different concentrations of 2mM, 1mM and 0.5mM and two different Scan Rates of 0.1 V/s and 0.05V/s. The measurements were performed with the SIC4341 IC and an Autolab potentiostat for comparison.

3.2 Inkjet Printed Antenna Design

As detailed in the introduction, NFC technology is a short distance communication protocol, in the order of 5 cm, and that operates at 13.56 MHz on ISO / IEC 18000-3 air interface and at rates ranging from 106 kbit / s to 424 kbit / s. NFC uses loop antennas, whose inductance value will be determined by the internal capacity of the chip to be used, in such a way that the resonance frequency between the designed antenna and the internal capacitor is 13.56MHz. It is also possible to incorporate external capacitors in order to reduce the value of the desired inductance. In addition, the parasitic capacitance presented by the inductor must be taken into account. A compact model of the concentrated components of the inductor and the capacitance of the chip can be seen in Figure 3.8. Based on this model, the resonance frequency of the antenna and chip set will be given by,

$$f_{resonance} = \frac{1}{2\pi\sqrt{L(C_{chip} + C_{parasitic})}} \tag{3.2}$$

Most of the chips for NFC communication have an internal capacitance of the order of 50 pF, this data will be the starting point for the design of the inductor, in particular, the chip used in this work from Silicon Craft has an internal capacitance of 51 pF.. Using Eq. 3.2, and neglecting the parasitic capacitance of the inductor, the required inductance value will be calculated. With the inductance value determined, the inductor is designed geometrically, then the parasitic capacitance is obtained and the model is iteratively adjusted. As the first iteration step, the required inductance will be $L = \frac{1}{(2\pi f_{res})^2 C_{chip}} = 2.75\mu H$. Another important parameter to take into account in this type of design is the series resistance that the inductor will have. Both its length, as well as the width and thickness of the traces will determine the resistance value. This parameter is very important since it will define the quality factor (Q) of the inductor, where $Q = wL/R$.

The Quality Factor of an antenna is a measure of its efficiency in transferring energy from delivered power to radiated power. It is used to assess how much energy is lost in the process of radiation compared to the initial power delivered to the antenna. In general, a high Quality Factor (high Q) signifies an efficient antenna, where most of the energy delivered to the antenna is converted into radiated electromagnetic waves. Conversely, a low Quality Factor (low Q) indicates a less efficient antenna with significant energy losses.

$$Q = \frac{RadiatedPower}{PowerLoss} \tag{3.3}$$

Where, Radiated Power is the amount of electromagnetic energy emitted by the antenna in the form of electromagnetic waves. And Power Loss is the amount of energy that dissipates or is lost within the antenna due to factors such as electrical resistance in the conductors and other forms of energy dissipation.

Also, the quality factor is entirely related to the distance at which the antenna will be able to transmit. This relationship can be seen in Ortego's work[119].

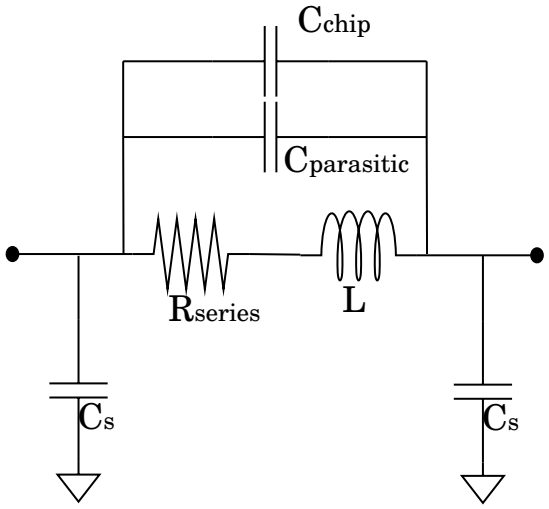


Figure 3.8: Lumped circuit of the inductor and the capacitance of the chip.

3.2.1 Inductance

In order to determine the inductance value for a square planar inductor, such as the one depicted in Figure 3.9, the equations proposed by Jenei et al..[120] have been utilised. These are described in detail below.

$$L_{self} = \frac{\mu_0}{2\pi} l \left(\ln \frac{l}{n(w+t)} - 0.2 \right) \tag{3.4}$$

$$M^{-}_{x/y} = 0.47n \times \frac{\mu_0}{2\pi} l \tag{3.5}$$

$$M^{+} = \frac{\mu_0}{2\pi} l(n-1) \times \left[\ln \left(\sqrt{1 + \left(\frac{l_{seg}}{d^{+}} \right)^2} + \frac{l_{seg}}{d^{+}} \right) - \sqrt{1 + \left(\frac{d^{+}}{l_{seg}} \right)^2} + \frac{d^{+}}{l_{seg}} \right] \tag{3.6}$$

$$d^{+} = (w+s) \times \frac{(3n - 2N - 1)(N+1)}{3(2n - N - 1)} \tag{3.7}$$

$$L = L_{self} - M^{-} + M^{+}. \tag{3.8}$$

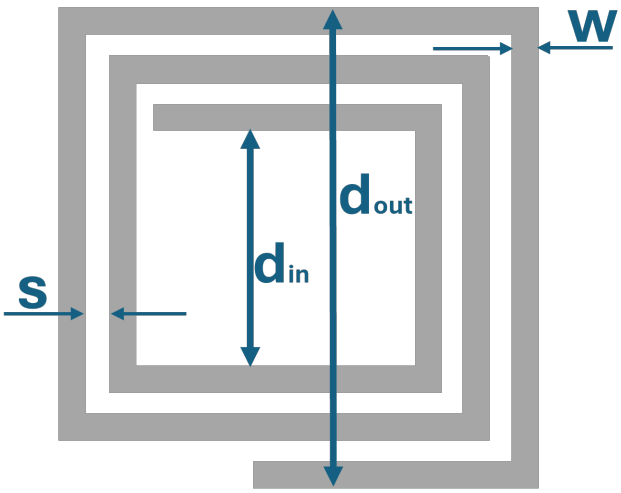


Figure 3.9: Scheme of a planar square coil, where its most relevant design parameters are indicated.

Where L_{self} is the sum of the inductance of each segment of the inductor, M^- is the negative mutual inductance because of the anti-parallel segments contribute and the M^+ is the total positive mutual inductance, to which contribute interactions between parallel segments on the same side of a square. From the application of these equations, it was arrived at the design of a square inductor with out diameter $Dout = 60mm$, trace width $w = 1.5mm$, a separation between traces $s = 0.25mm$, number of turns $n = 5$ and a theoretical inductance of $L = 2.69\mu H$.

3.2.2 Resistance

To obtain the resistance value, the first step is to calculate the total length of the inductor, for which the following eq is used,

$$l = 4.n.d_{out} - 4.n.w - (2n+1)^2(s+w) \tag{3.9}$$

to apply Eq. 3.9 we obtain that the total length of the designed inductor is $l = 1086.7mm$. As can be seen in Ortego et al., 2012[119], silver ink has a significantly lower conductivity than bulk silver, it is of the order of 12.5%. To study this phenomenon, we have made multiple prints of layers of silver ink as shown in Figure 3.10. , independent of the thickness and treating the resistivity as a sheet resistivity.

From the study it was obtained that the silver ink has a single layer resistance per square of 0.2 Ω/sq, 2 Layers 0.09Ω/sq, 3 Layers 0.06Ω/sq and 4 Layers 0.045Ω/sq (Figure 3.11).

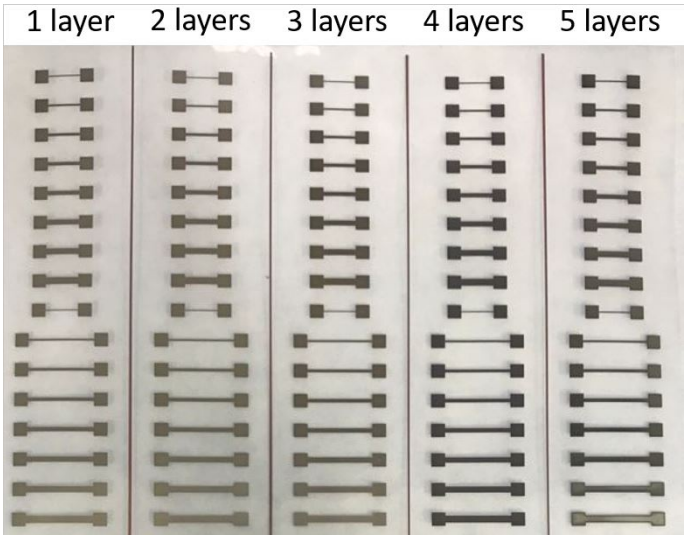


Figure 3.10: Traces printed with silver ink using Epson X15000 printer on PET substrate from Mitsubishi.A change in color tonality can be seen in the traces that have more layers of ink deposited

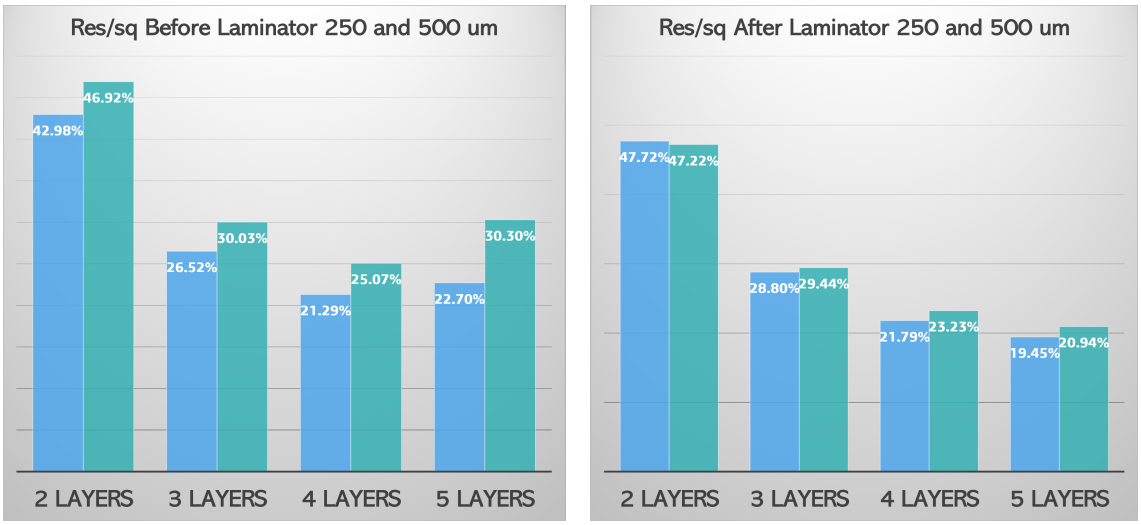


Figure 3.11: Reduction of sheet resistivity due to the printing of a greater number of layers. The decrease in resistance is indicated in percentage, relative to the resistance of a single layer.

Considering the proposed geometry and that 3 layers have been printed, it is possible to calculate the aspect ratio of the inductor as $l/w = 1086.7mm/1.5mm$, giving a total of 724.46 squares. So the series resistance of the inductor will be given by Eq,

$$R = \rho_{sq} \times n_{sq} \tag{3.10}$$

The calculated value is 43.47Ω, with the values obtained and for a frequency of $13.56MHz$, the Quality Factor (Q) will be 5.27.The value of Q is notably low. In an ideal inductor with zero

series resistance, it would be expected to approach infinity. In practice, copper wire inductors tend to have Q values greater than 100. For printed inductors, the value obtained is typical and, although low, allows for the transmission of energy and fulfils its function.

3.2.3 Capacitance

For the parasitic capacitance component, the analysis is based on the work presented by Pieters[121], which proposes to obtain the inductor capacitance through the effective relative permittivity ϵ_{eff} of the structure and the capacitance between the metal strips in free space C_0.

$$\epsilon_{eff} = \frac{C_{parasitic}}{C_0} \tag{3.11}$$

C_0 is obtained using conformal mapping and Schwartz transformations by

$$C_0 = \epsilon_0 \frac{K(k)}{K(k')}, \tag{3.12}$$

where $K(k)$ is the complete elliptic integral of the first kind and the equation for the effective relative permittivity between the coplanar strips is given by

$$\epsilon_{eff} = 1 + \frac{1}{2}(\epsilon_{PET} - 1)\frac{K(k)K(k_2')}{K(k')K(k_2)} \tag{3.13}$$

where,

$$k = \sqrt{1 - \left(\frac{\chi_a}{\chi_b}\right)^2} \tag{3.14}$$

where $\epsilon_{PET} = 3.1$ is the PET's dielectric constant, $\chi_a = s/2$, $\chi_b = \chi_a + w$. and $k' = \sqrt{1-k^2}$.

$$k_2 = \sqrt{1 - \frac{\sinh^2(\pi\chi_a/2h)}{\sinh^2(\pi\chi_b/2h)}} \tag{3.15}$$

The implementation of all these equations, via a Matlab code, for the design of planar antennas is presented in Appendix A. Having applied these equations, it was obtained that $C_{parasitic} = 16.6pF$ and $C_s = 2.3pF$. With the addition of the parasitic capacitance,there will be a shift in the resonant frequency. The new resonance value is given by Eq.3.2, and is $f_{resonance} = 11.87MHz$, which is consistent with the value obtained through the simulation Figure 3.12. Since the parasitic capacitance causes a shift of the resonant frequency, which impairs the antenna's functionality, it is necessary to modify the inductance to achieve a resonance as close as possible to 13.56 MHz. The new antenna will exhibit a distinct parasitic capacitance, necessitating an iterative process involving two or three turns to develop a functional design.

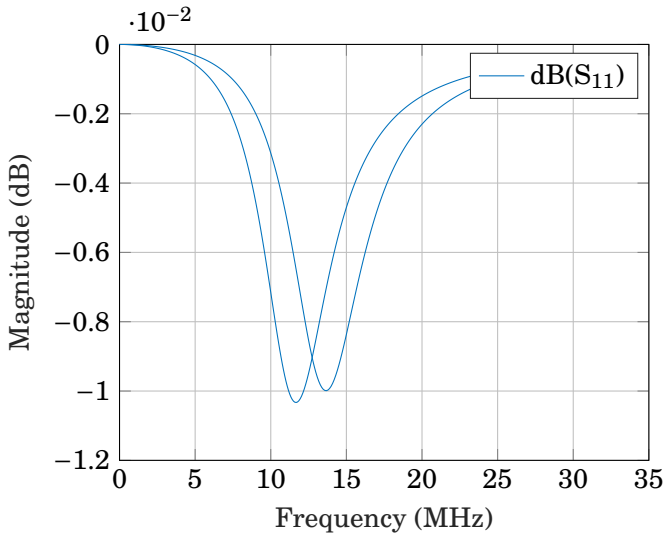


Figure 3.12: On the left, shift of the resonance frequency of the inductor when designing as the seed value of the iteration. On the right, the new design that consider the parasitic capacitance.

3.2.4 Final design

After multiple iterations, a final design was reached with the following characteristics: the values of trace width $w = 1.5mm$, the separation $s = 0.25mm$ and the number of turns $n = 5$ were left constant, the out diameter was modified to a final value of $Dout = 54mm$. The final length of the inductor is $897.8mm$, resulting in a resistance of 35.91Ω, which is very close to the measured value of 36.6Ω (Figure 3.13). This configuration yields an inductance of $L = 2.13\mu H$ and a quality factor Q of 5.67. The design was printed using commercial silver ink (Mitsubishi Paper Mills Silver Nano™ AgNP, NBSIJMU01) that was loaded into a rechargeable cartridge and printed with an Epson XP15000 printer on the Mitsubishi Paper Mills special substrate (NB-TP-3GU100).

This design has proven immensely valuable for numerous PoC device projects and applications, not only due to its battery-free nature but also for its ability to transmit signals through barriers. This capability opens doors for various sensor applications, such as gas sensors, enabling wireless readings through barriers. For instance, it facilitates the development of gas sensors that can wirelessly transmit readings from within a chamber containing gases.

Moreover, in scenarios like a Covid situation, this technology offers unique advantages. Healthcare professionals can stay protected behind a glass barrier while taking readings from a patient on the other side. The patient can possess the sensor, allowing seamless readings to be obtained without direct physical contact.



Figure 3.13: Measurement of the series resistance of the inductor.

3.2.5 Inkjet Printed Limitations

In wearable technology, achieving intimate skin-sensor contact is crucial. An innovative approach leverages nature-inspired bioadhesive membranes, drawing inspiration from mussel-like materials commonly used in biomedical applications.

However, these membranes present challenges for inkjet printing due to their fragility and specific material properties. Traditional inkjet printing methods are not suitable for the delicate, mussel-inspired free-standing membranes. Despite these challenges, integrating sensors into advanced materials like Mussel-Inspired free-standing films as Artificial biosensing Skin for tissue regeneration (MIaSkin) holds significant promise for wearable technology and point-of-care (PoC) devices [122, 123].

MIaSkin is designed to emulate natural skin and potentially facilitate tissue regeneration, offering a novel platform for sensor integration. Nonetheless, the delicate nature of these membranes complicates the printing of intricate components, such as antennas.

The attempt to print the designed antenna directly onto the MIaSkin membrane faced significant hurdles due to its fragile composition. The nature of traditional inkjet printing, reliant

on dry surfaces, rendered the membrane brittle and prone to breakage during the printing process. This fragility led to difficulties in successfully imprinting the antenna design onto the MIaSkin.

However, two different approaches were explored for printing the antenna on the MIASkin membrane. Figure 3.14 delineates the utilization of the Epson Printer for this purpose.As mentioned above a notable challenge emerged with the inherent need for these materials to be dry, resulting in their increased brittleness and fragility. This posed a risk to the internal components of the desktop printer, particularly the rollers and paper drive wheels. To mitigate this risk, we utilized the CD printing tool provided with the printer, allowing the substrate to remain flat with minimal movement. Nonetheless, this method presents a drawback: unlike conventional printing software that enables adjusting print quality based on DPI settings, the CD tool necessitates an image file. However, this image is compressed, resulting in significantly lower quality and compromised conductivity due to reduced deposition of silver ink. This limitation adversely impacts the final print quality. Although the printing of some patterns was possible, printing with silver ink requires a subsequent sintering process at high temperature to make the tracks conductive. This process not only damaged the membranes but also stick them to the CDs used as holders in such a way that it was impossible to remove them afterwards.

Having ruled out printing with the consumer printer, the possibility of printing the system with a Dimatix (Fujifilms DMP 2800 series) research-grade printer was studied. In this case, because the drop spacing and platform temperature can be adjusted to dry the ink as it is printed, among other parameters, we were able to print a functional antenna on the membrane. However, this process is very slow, since to avoid any short circuit between the antenna tracks it was necessary to print with only one nozzle, and to achieve a good conductivity it was still necessary to apply the thermal sintering process, so it was not possible to remove the membrane from the sacrificial substrate, in this case PET, after the sintering process.

In light of these challenges, transitioning from conventional inkjet printing to different technology, such as the Voltera Printer, became imperative.This equipment does not print inks, but rather dispenses screen printing pastes, such as silver paste, which does not require a subsequent sintering process. However, a softer heat treatment improves the conductivity of the traces. Additionally, this equipment offers precision and finesse, mitigating the risk of damage to delicate substrates like MIaSkin. Thus, the decision to switch to the Voltera Printer for printing the antenna, as elaborated in the subsequent section of this thesis, was necessitated by the fragility of the MIaSkin membranes, ensuring the successful integration of sensors without compromising their structural integrity.

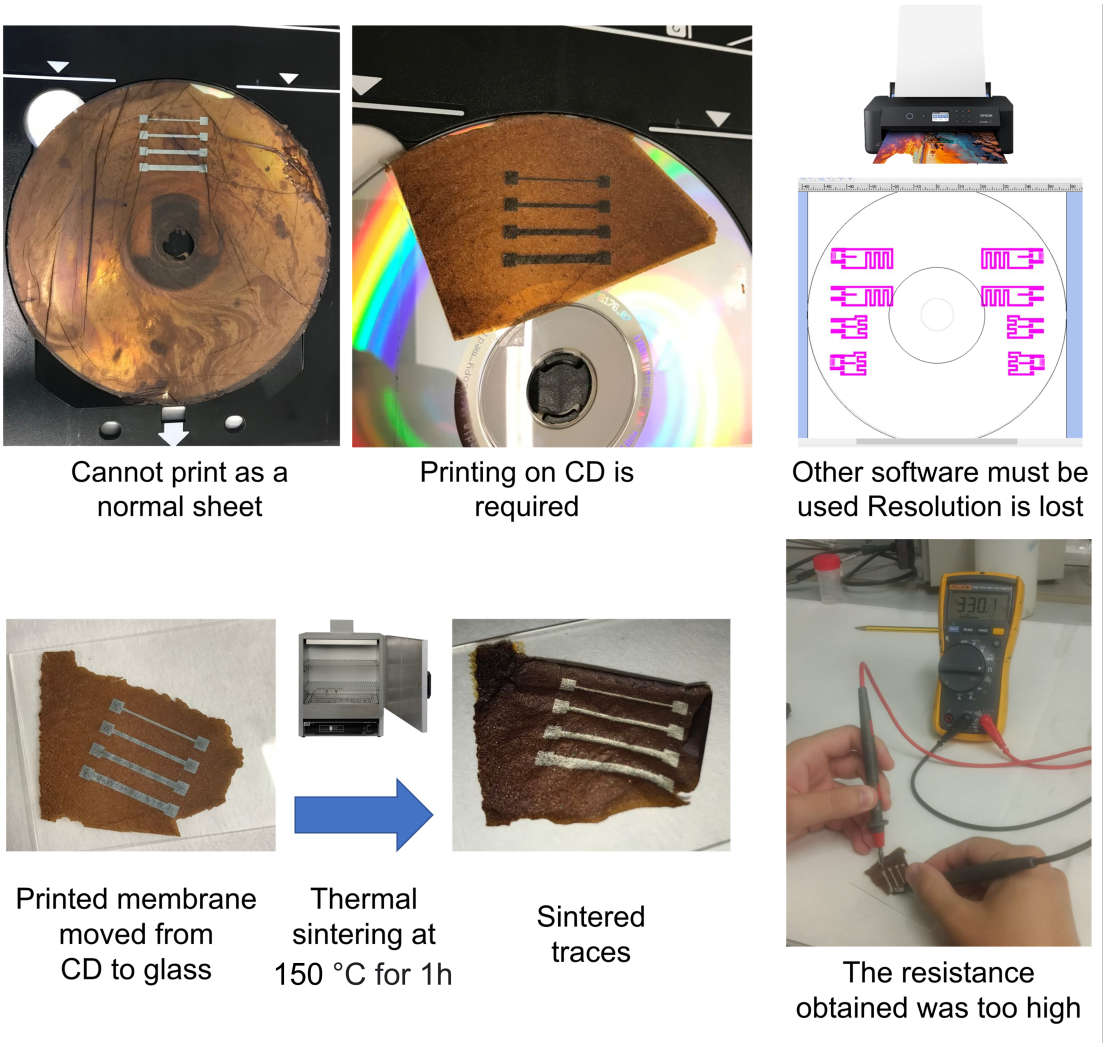


Figure 3.14: Top: Printing on the MIASkin membrane using the CD holder. Below: sintering of the membrane, which resulted in a change in colour. Despite the heat treatment, the conductivity remained below the expected level.

3.3 Voltera Printed Antenna

In order to be able to print on the membrane a V-One printer from Voltera was used, which is a paste dispenser instead of printing inks. Hybrid contactless printing techniques like the one proposed by Voltera allows deposition-on-demand of conductive pastes, making this machine suitable for printing on fragile substrates. The Voltera V-One is a multifunctional PCB printer that uses additive manufacturing to create electronic components such as sensors, connectors, antennas and PCBs in general, which are essential for most electronic devices, including wearables.

The V-One allows for greater design flexibility, enabling the creation of many different layers, geometries and shapes. This flexibility, combined with the ability to print different materials such as carbon, semiconductor materials, conductors or even resistive materials for heaters, opens up

new possibilities for wearable technology. For example, it is possible to design a rubber/stretch material that has the mechanical properties of a skin, or wearables that are integrated onto the user's body.

Printing with this system has two major advantages, the first is that the substrate is kept flat on a surface while the carriage that extrudes the silver paste moves over it. On the other hand, silver pastes, in addition to not requiring a sintering process, form a thicker and thus more conductive layer, so it has been possible to design a smaller antenna than the one printed with inkjet ink. The average track thickness obtained for traces with a width of $500\mu m$ was $50\mu m$, as shown in the SEM images in Figure 3.15. It should be noted that the trace width is irregular due to the printer's nature, resulting in a distribution where the thickness decreases at the edges of the tracks. The particles that make up the printed traces are also visible in this figure.

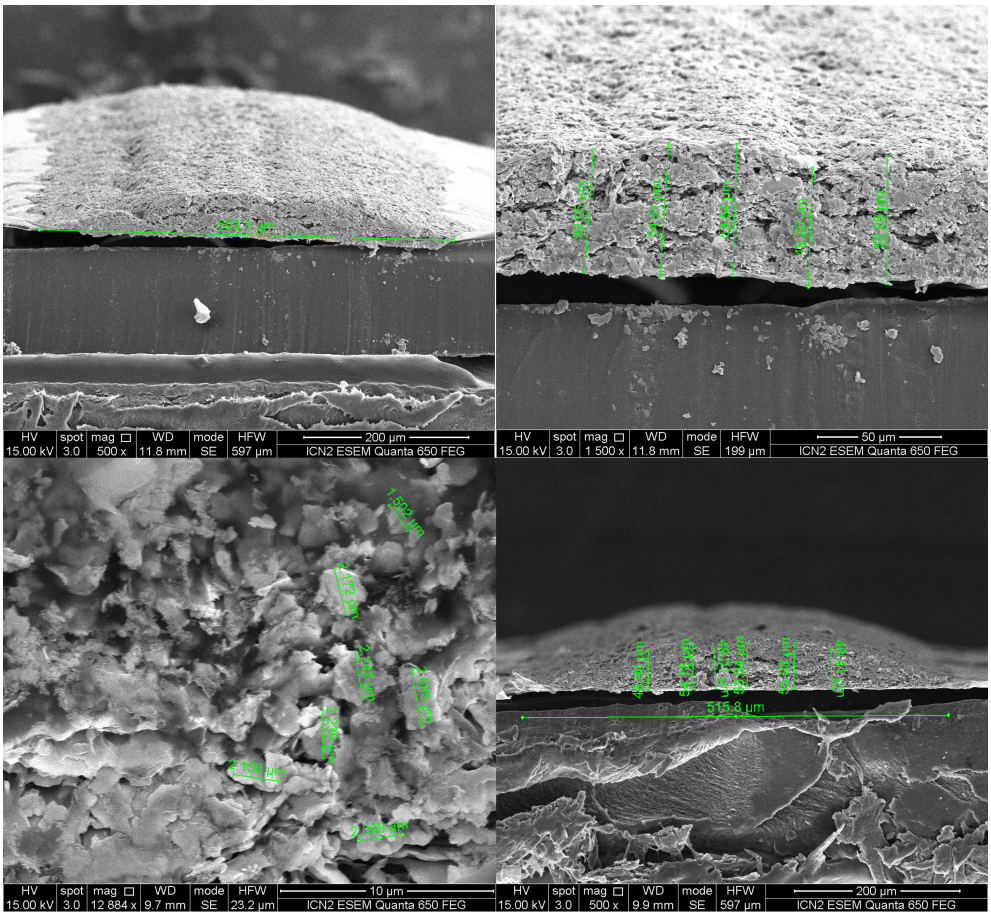


Figure 3.15: SEM images obtained from the traces printed with the Voltera show the width and thickness of the trace, as well as the microparticles that compose it.

In contrast to inkjet printed traces, which result in a nanoparticulated structure due to the use of silver nanoparticles in the ink, screenprinting pastes are composed of silver microparticles, making the thermal sintering process unnecessary. The new design was achieved with the

following characteristics, the trace width values were reduced three times $w = 0.5mm$, the spacing was increased three times $s = 0.75mm$, the number of turns was increased to $n = 7$, and despite this the out diameter was modified with a final value of $Dout = 35mm$ as is shown in Figure 3.16. Resistance and inductance measurements of the Voltera printed antenna are shown in Figure 3.17 and Figure 3.18 respectively.

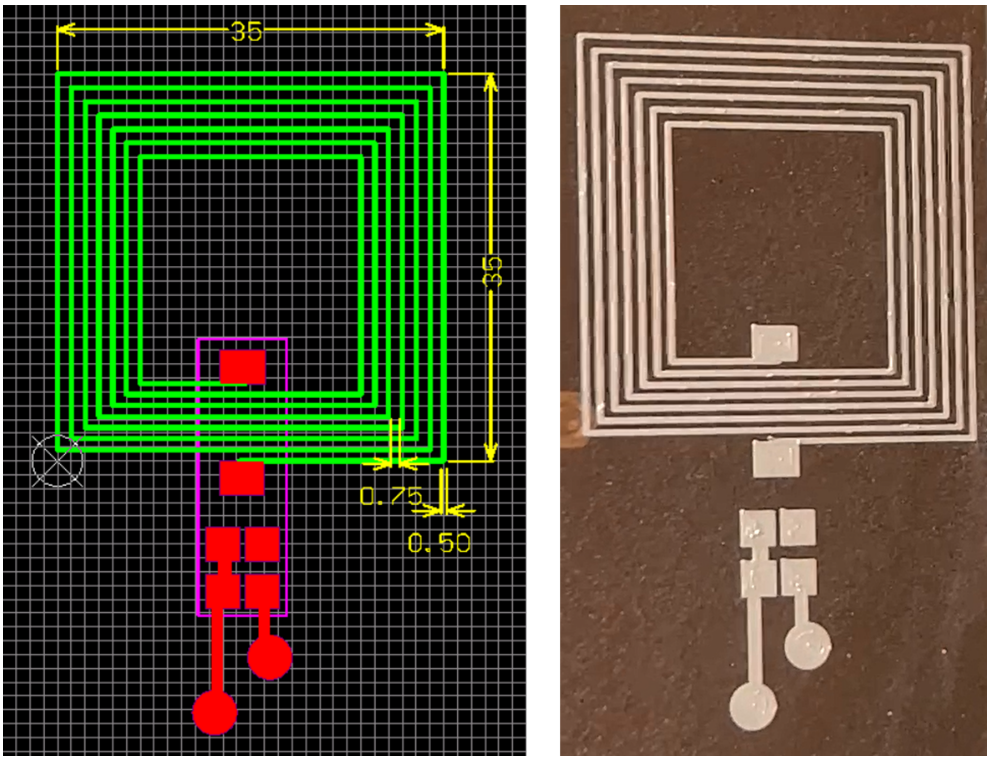


Figure 3.16: Antenna design made in Altium Designer Summer 09 and the antenna printed with the Voltera on the bio-inspired membrane. Dimensions expressed in [mm].

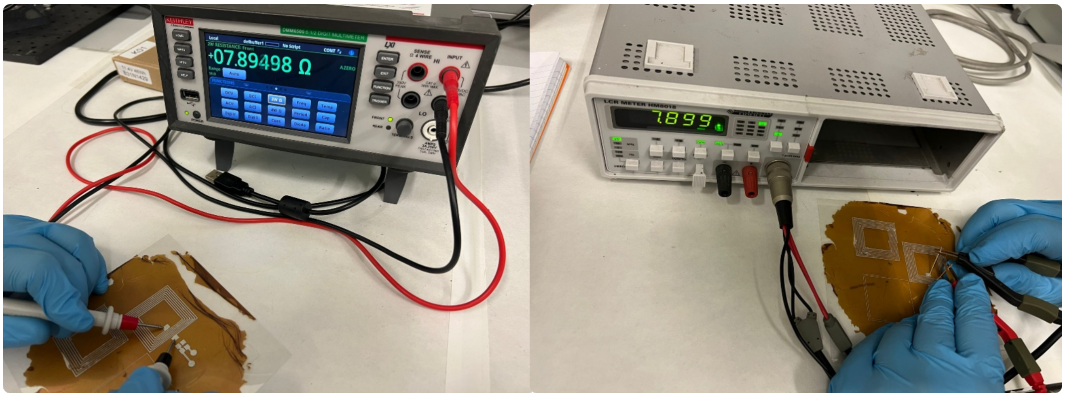


Figure 3.17: Measurement of the series resistance with both the digital multimeter and the LCR meter. The resistance obtained is much lower than inkjet antennas, which improves the quality factor of the antenna.

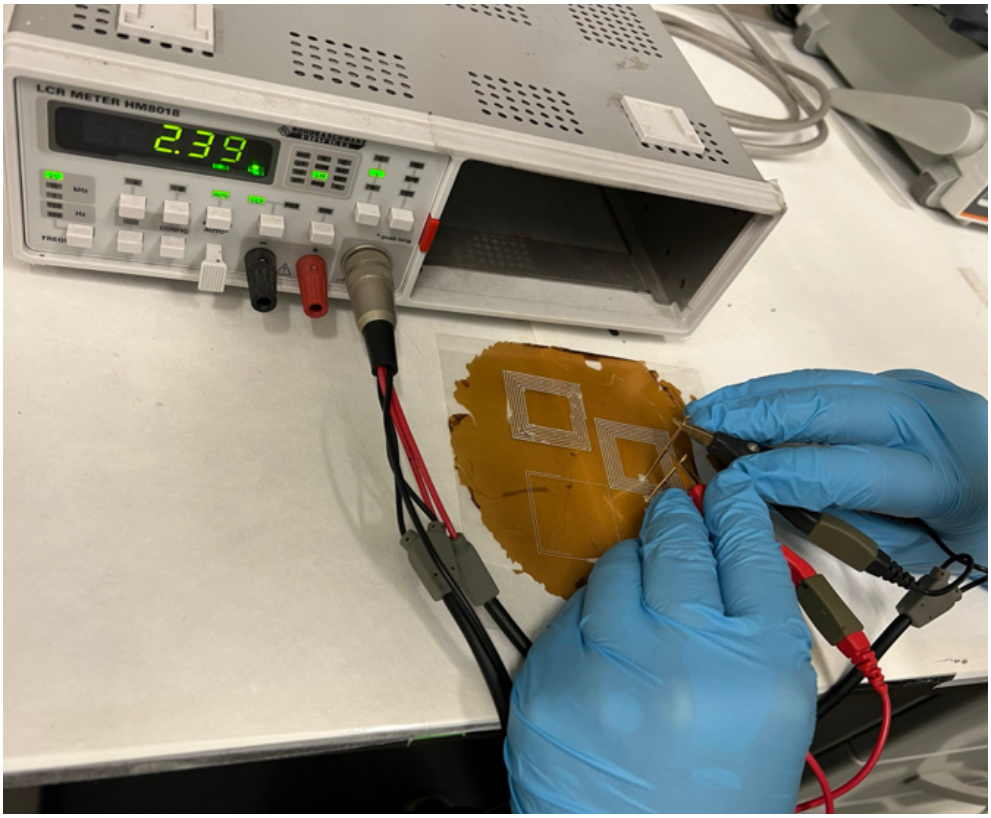


Figure 3.18: Measurement of the inductance with both LCR meter. Theoretical inductance of $2.5\mu H$ and a measured inductance of $2.39\mu H$.

As shown in Figure 3.19, the membrane is immersed in a water-containing vessel and delicately lifted using a PET piece. Subsequently, this PET, along with the membrane, is placed within the Voltera V-One system. Here, the desired design, sourced from the fabrication files (Gerber files), is precisely printed onto the membrane using silver paste.

Following the printing of the antenna and contact pads, the SIC-434X chip is positioned. Due to the chip pad's size, direct soldering onto the substrate proves challenging. Hence, a compact auxiliary PCB measuring 25 mm in length and 8 mm in width was devised to serve as an adapter. This not only facilitated easy attachment of the chip but also enabled its subsequent removal for reusability in new devices. This PCB was manufactured in flexible polyamide substrate, by the company PCB-Way. The chip was soldered onto the PCB using Voltera's solder paste and then the flexible PCB and chip assembly were stuck to the membrane by employing the ECATT.

In order to detach the device from the PET, the device is again immersed tangentially in water (Figure 3.19.e), the system is tested in water to verify that the membrane has not broken or that the PCB has not detached on contact with water (Figure 3.19.f). As a proof of concept for the development of wearables, the arm was then inserted into the container and the membrane sticks to the arm as it is taken out from the tank (Figure 3.19.g). Finally, the smart phone is brought close to the device for reading via NFC (Figure 3.19.h).

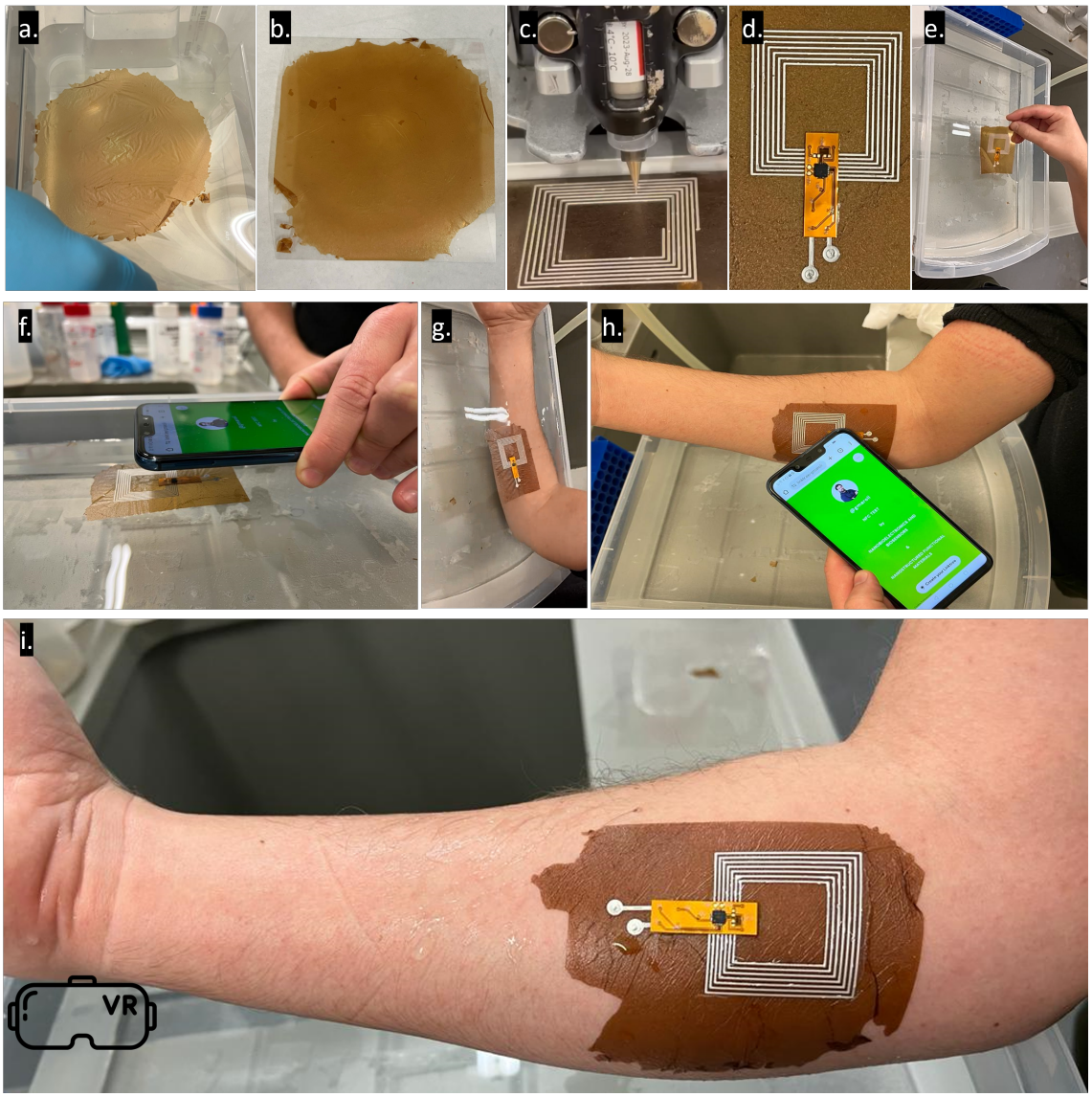


Figure 3.19: Pictures of the fabrication phases of the printed sensorised bioadhesive membranes. a) Free-standing membrane on water. b) Transfer on the plastic temporary substrate for printing. c) Silver paste deposition with Voltera equipment to form the NFC antenna. d) Attachment of the flexible PCB integrating the NFC chip on the printed membrane. e) Release of the printed membrane from the temporary substrate. f) Testing of the NFC connection on the free-standing membrane on water. g) Adhesion of the membrane to the forearm skin. h) Testing of the NFC connection on the adhered membrane. i) Close-up of the printed membrane. The membrane has been placed with the antenna, chip and ssEMG contacts on top only for illustrative purposes. (https://youtu.be/tssbd9i0iLg)

3.4 Commercially Manufactured Antenna

In certain applications, particularly in wearable technology, miniaturization is crucial. However, the existing printing methodologies we've discussed pose challenges in achieving this size reduction. The inherent issue lies in the intrinsic conductivity limitations of the printed materials, whether they are inks or pastes. Notably, when aiming for a smaller antenna size, the reduction in its external diameter leads to a decrease in inductance.

To offset this decrease in inductance, compensatory measures such as augmenting the number of loops, reducing the spacing, and narrowing the traces are necessary. Nevertheless, these alterations intended for size reduction augment the series resistance within the antenna. Consequently, this escalation leads to a decrement in the quality factor, eventually falling below the threshold of one. At this point, the component transitions from functioning as an inductor to exhibiting characteristics akin to a resistor. This shift in behavior significantly impacts the functionality and efficiency of the device in practical applications.

It is for this reason that we design and send to manufacture an antenna on kapton in the same way as the flexible PCB mentioned in the previous section. In this type of fabrication, copper is electrodeposited on the kapton and its conductivity is that of bulk copper. The antenna had the following characteristics, the trace width values were reduced to $w = 15mil = 381\mu m$, the spacing was reduced to $s = 8mil = 203\mu m$, the number of turns was increased to $n = 10$, and the output diameter was modified with a final value of $Dout = 800mil = 20.3mm$. The design was made with the CAD tool Altium Designer summer 09 as shown in Figure 3.20. A "mil" is a unit of length in the imperial and U.S. customary systems. It represents one-thousandth of an inch, which is equivalent to 0.001 inches or 0.0254 millimeters. In terms of fractions, a mil is expressed as 1/1000 of an inch. This measurement is commonly used in the electronic industry.

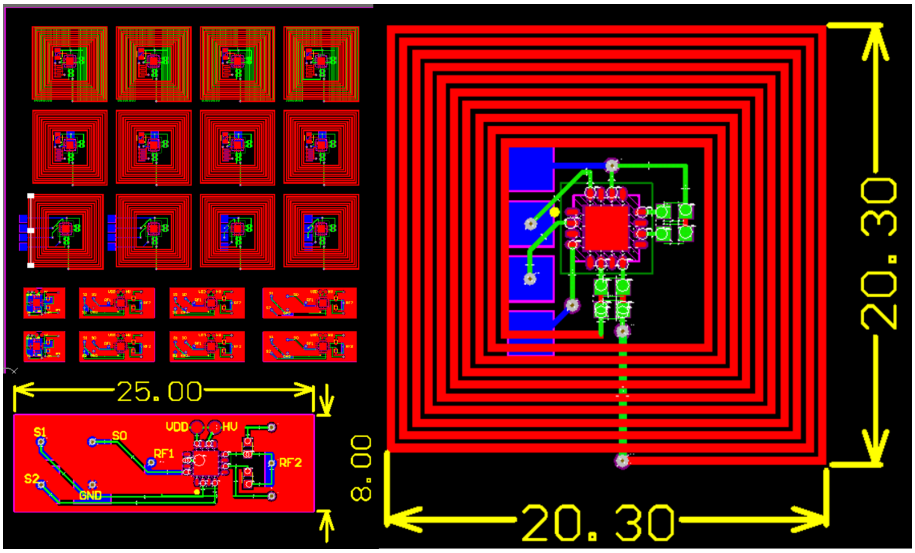


Figure 3.20: Design of the flexible PCBs made with Altium Designer Summer 09, both small PCBs as chip interface, as well as PBCs with integrated antenna. Dimensions expressed in [mm].

3.5 Comparison of antennas performance

The performance of an antenna is characterized by its quality factor (Q), which correlates the transmitted power to the dissipated power. The quality factor Q is also defined as the ratio of the reactance to the resistance in the circuit, i.e., $Q = X/R$. A higher Q factor results in a superior reading distance[124].

Since the antennas' inductances are very similar and are required to resonate with the chip capacity of 51 pF at 13.56MHz, the series resistance can be directly compared. The lower the resistance, the higher the Q, and the better the performance.

The resistance of the inkjet printed antenna, as well as that of the voltmeter, were measured using a digital multimeter. Due to the low value of the series resistance of the PCB antenna, it was calculated using the expression

$$R = \frac{\rho \times L}{w \times t} \tag{3.16}$$

where ρ is the resistivity of copper $1.68 \times 10^{-8}\Omega - m$, L is the antenna length = 0.61 m, w is the trace width = 381 μm, and t is the copper thickness = 34.8 μm. The copper thickness was a manufacturing condition while the length L is calculated using the expression

$$L = (4n+1).d_{in} + (4n+1).Ni.(w+s) \tag{3.17}$$

where n is the number of turns, d_{in} is the inner diameter of the antenna, Ni is the integer number of turns, in our case the same = 10, and s is the track spacing = 203.2μm.

	Voltera	Inkjet	Flex PCB
R [Ω]	7.89	36.6	0.77
L[μH]	2.39	2.13	2.12
Q	25.81	4.96	234.58

Table 3.1: Comparison of the quality factor of the antennas built by the different methods, using Voltera Printer, Inkjet Printer and PCB.

As shown in Table 3.1, the antenna, manufactured using standard PCB technology, exhibits superior performance. This is due to the method of deposition of the conductive material, copper, which results in compact traces. In contrast, inkjet methods produce porous traces, resulting in a conductivity that is ten times lower than that of the bulk material. This difference in conductivity has a significant impact on the performance of the antennas, with those produced using standard PCB technology showing a clear advantage.

3.6 Conclusions of the chapter

The development of pocketable sensor interfaces, especially in the context of electrochemical sensing, marks a significant advancement in portable diagnostics. This chapter has detailed the design and implementation of NFC enabled sensor interfaces, focusing on the SIC4340 and SIC4341 integrated circuits. These devices harness NFC technology to facilitate battery-free operation, enabling compact and efficient sensor systems that are ideal for real-time, on-the-go applications.

- **NFC Technology Integration:**
  - NFC technology is a powerful enabler for wireless, compact, and battery-free sensor interfaces. It allows the sensor devices to harvest energy from nearby NFC-enabled devices, eliminating the need for an internal power source. This innovation is crucial for applications where space, weight, and power consumption are critical constraints.
  - The SIC4340 and SIC4341 ICs demonstrate effective use of NFC for both analog and potentiostatic sensing. They convert biological, chemical, or physical signals into digital data, which is then transmitted wirelessly to NFC readers such as smartphones.
  - We have tested both chips with a series of resistances and capacitances, contrasting the values obtained with a desktop multimeter. In the case of the SIC4341, we have tested it with screen-printed electrodes using solutions of known concentrations of Ferro/FerriCyanide and contrasting the voltammograms obtained with those generated by the Autolab potentiostat.
- **Antenna Design and Fabrication:**
  - The design and fabrication of NFC-compatible antennas are critical to the performance of these sensor interfaces. Various methods, including inkjet printing and Voltera V-one printing, have been explored. Each method has its advantages and limitations in terms of manufacturing ease, cost, and performance characteristics.
  - The chapter provides a comparative analysis of antenna performance, highlighting the trade-offs between different fabrication techniques. Optimizing these designs is essential for achieving reliable and efficient NFC communication in compact sensor systems.
- **Application Potential:**
  - The integration of these sensor interfaces into portable devices opens up new possibilities for point-of-care diagnostics, environmental monitoring, and smart wearable technologies. Their ability to operate without batteries and communicate seamlessly with smartphones enhances their suitability for diverse applications, from home health testing to field-based environmental analysis.

CHAPTER 4

PRINTED SENSORS FOR WEARABLES

In this chapter we will study how we can use the wireless and battery-free platforms developed from the SIC4340 and SIC4341 chips to manufacture wearables. In particular we will look at the fabrication of humidity and temperature sensors, their characterization and implementation. Going a step further with this platform we have developed a device capable of performing simplified surface electromyography (ssEMG).

4.1 Application: wearable wireless printed sensors

This chapter shows practical applications of sensors, particularly wearable, using the platforms described in the previous chapter. The pervasive integration of wearable technologies in our society continues to evolve, promising further advancements in the near future[12, 50, 125]. The exploration of continuous and widespread sensing capabilities, coupled with the analysis and interpretation of large-scale data, has commenced its journey. Nevertheless, existing technologies remain encumbered by bulkiness, including batteries and electronics, and often exhibit challenges in establishing effective skin contact.

In this chapter, we will show the development of printed sensors on the Mitsubishi substrate to create circuits and NFC antennas for battery-free and wireless readout of a network of temperature, humidity, and ssEMG sensors that would be used in the prevention of heat stroke (Figure 4.1).

We will be delving into the design and implementation of a sensor network that aims to achieve the highest possible degree of integration for this type of fabrication method. We will introduce innovative solutions to address the most common challenges associated with temperature sensing by a meander resistor, humidity sensing by IDE electrodes, and ssEMG.

Our approach includes: i) the incorporation of a reduced graphene oxide resistor to offset the variations in the humidity sensor due to temperature fluctuations; ii) the utilization of the absorbing coating of the plastic substrate used for inkjet printing for humidity sensing with the IDE; iii) the application of simple amperometric measurements to capture the current associated with the muscle action potential, thereby obtaining the ssEMG envelope that identifies muscle contraction. Furthermore, we will discuss how we have linked this sensor network to two flexible antennas that incorporate NFC readout chips, enabling real-time, wireless, and battery-free data transmission to a smartphone.

We will also present the validation process of the entire platform, which includes lab testing under controlled temperature and humidity conditions, in-vivo testing on healthy volunteers during physical activity, and exposure to high-temperature air to simulate conditions similar to those faced by firefighters.

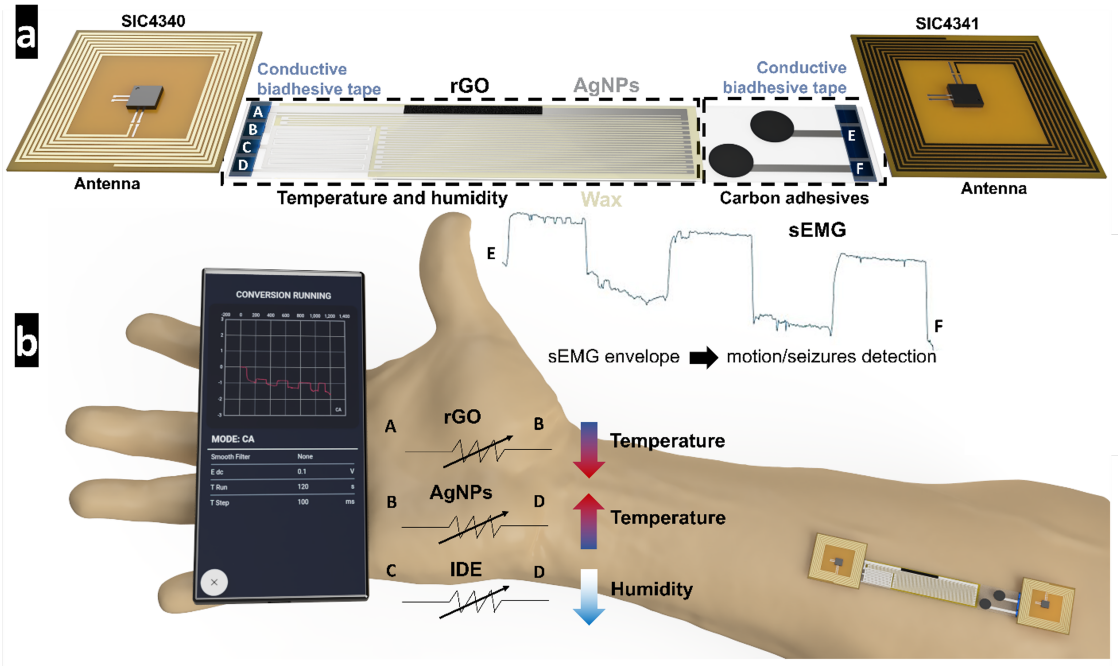


Figure 4.1: a) Schematic of the sensor network. The rGO temperature sensor is connected between pads A and B and exhibits a decrease in resistance value with increasing temperature, as indicated by the arrows. The silver sensor between pads B and D exhibits an increase in resistance value with increasing temperature. The humidity sensor, consisting of a silver interdigitate, between pads C and D evaluates the change in conductivity of the substrate. As the humidity increases, the resistance decreases. The electrodes used for motion and seizure detection are located between pads E and F. b) Schematic of the sensor placement on the forearm.

4.2 Fabrication of the Wearable

For the fabrication of the sensor network on the Mitsubishi substrate, the silver trace layout was first printed twice with the epson printer. This approach aimed to enhance conductivity by incorporating a higher volume of silver nanoparticles within the ink. In parallel, the Graphene Oxide(GO) is filtered and subsequently reduced by laser following the steps previously reported by our group[126].

Then, the trace of reduced Graphene Oxide (rGO) is transferred to the substrate by a press. Then the carbon conductive adhesives tabs are placed on the silver circles reserved to be the electrodes. Finally, using 3M 9703 conductive tape, the flexible PCBs are attached to the connection pads. The fabrication steps can be seen in Figure 4.2.

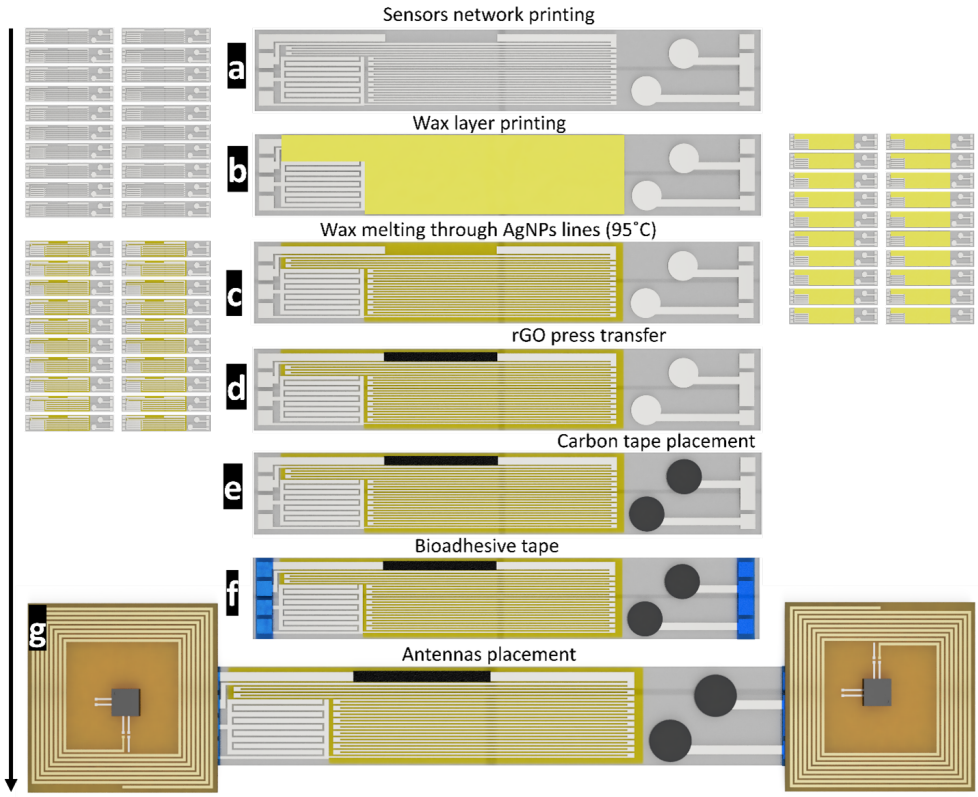


Figure 4.2: Fabrication steps of the inkjet-printed sensors network on Mitsubishi substrate. a) The sensor network is printed on the A4-sized Mitsubishi substrate. To enhance the conductivity of the traces, the design is printed twice. b) The wax printer is then employed to print a coating of wax, which adheres to the substrate and the silver traces. This step is also carried out in duplicate. c) To allow the wax to permeate the substrate and to remove it from the silver traces, the sensor is passed through a laminator, covering the devices with a sheet of paper. The wax diffuses into the substrate, and any excess is absorbed by the paper. d) In this step, the devices are cut and manipulated one by one. The rGO sensor is transferred using a press. e) Carbon tape circles are placed on the printed electrodes. f) Anisotropic conductive tape is placed on the connection pads between the antennas and the device. g) Finally, the antennas are connected.

4.3 Device performance

4.3.1 Humidity Sensor

The SIC-4340 chip, with its three measuring channels, was utilized to install three distinct sensors: a humidity sensor and two temperature sensors. The temperature sensors were designed with contrasting coefficients, one being negative and the other positive.

The humidity sensor is an interdigitated sensor, which operates not by measuring changes in capacitance, but by detecting changes in the resistance of the Mitsubishi substrate when it absorbs humidity. To characterize this humidity sensor, the interdigitated electrodes were placed inside a plastic beaker that maintained a constant relative humidity (RH). This was achieved by preparing saturated solutions of various salts. The salts used for this purpose included $LiCl$ (11%RH), $MgCl_2$ (33%RH), KCO_3 (4%RH), $NaNo_3$ (64%RH), $NaCl$ (75%RH), KCl (84%RH), and KNO_3 (94%RH).

The changes in resistance were measured using a digital multimeter. Figure 4.4 illustrates the linear region of the calibration curve of the interdigitated humidity sensor. At 11%RH) and 33%RH) relative humidity, the resistance values obtained were over 100 $M\Omega$ and 43 $M\Omega$, respectively. It was observed that at 94%RH) relative humidity, the sensor reached saturation. This implies that the Mitsubishi substrate was fully wet, having absorbed as much water as it could.

Given that this sensor operates based on the water absorption property of the Mitsubishi substrate and the corresponding change in conductivity, it was not feasible to transfer this concept to the MIASkin membrane. Therefore, a new sensor was developed for the MIASkin membrane, based on Graphene Oxide with Nafion(GON). The composite was created following the protocol reported by [127]. The initial testing involved applying the GO-N material onto the Mitsubishi substrate. Given the nature of GO-N as a solution, it required deposition onto the substrate and subsequent drying. To facilitate the creation of various shapes, a 3D piece was designed to adhere to the substrate using double-sided tape. The humidity sensors obtained from this process are depicted in Figure 4.3.

Results obtained from this compound on the Mitsubishi substrate closely resembled those obtained from the interdigitated silver sensor. This similarity led to the hypothesis that the observed response was more linked to the substrate properties rather than the compound itself. To test this assumption, the experiment was repeated directly on PET (Polyethylene Terephthalate). Here, a significant increase in the measured resistance was noted, indicating that the response was indeed attributed to the compound.

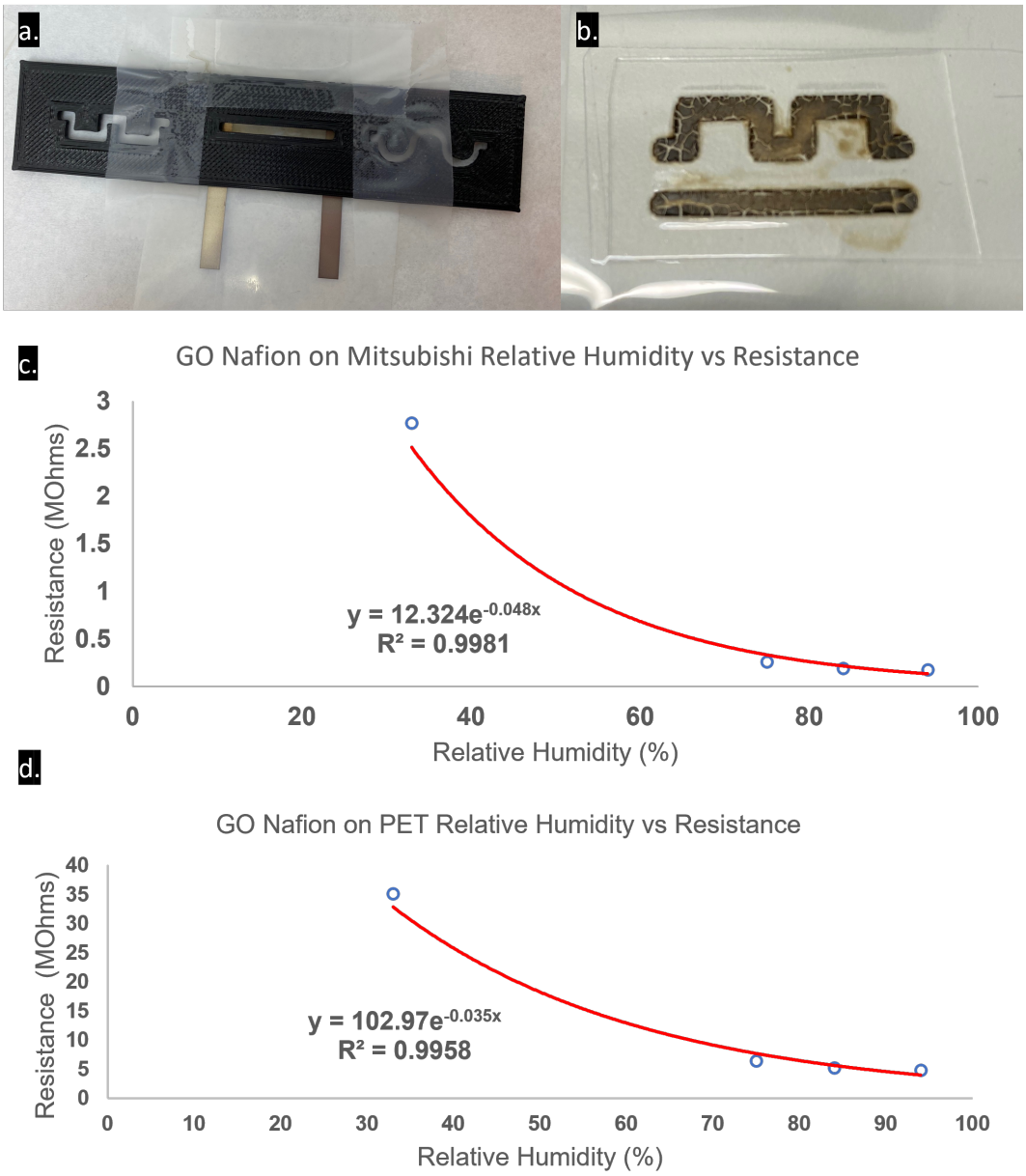


Figure 4.3: a. 3D part for the manufacture of the humidity sensors with different shapes. b. GO-N films once dried. c. Response of the GO-N sensor on the Mitsubishi substrate, values of the same order of magnitude as the humidity sensor interdigitated on the same substrate are observed. d. Response of the GO-N sensor on PET to avoid interferences, in this case the resistance measured is an order of magnitude higher..

Given the excessively high resistance values obtained, adjustments were made to the sensor's geometry to narrow the resistance range. As anticipated, an exponential response was achieved (as demonstrated in Figure 4.4). Notably, this method yielded the advantage of lower resistance values compared to those obtained from the interdigitated sensor on the Mitsubishi substrate.

It should be noted that many humidity sensors are slow to react to humidity fluctuations due

to the slow desorption of water from the sensor surface. Having a fast-responding sensor is crucial in wearables to ensure accurate and timely readings. This research contributes significantly to the development of such sensors, paving the way towards more efficient and reliable humidity and temperature monitoring systems.

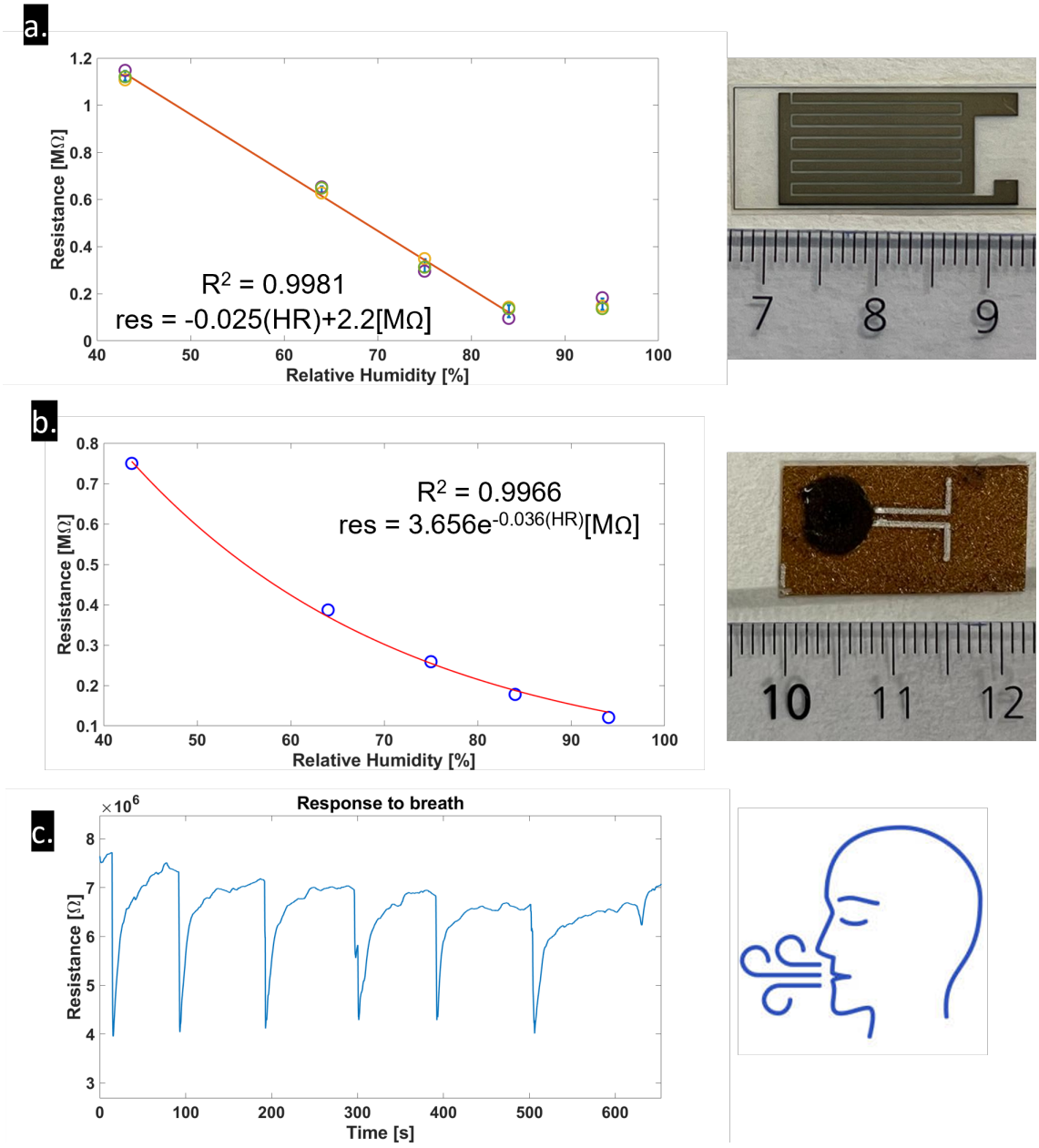


Figure 4.4: a. Linear response of the interdigitated humidity sensor printed with silver on Mitsubishi substrate, 94 % saturation is observed. b. GO-N sensor on MIASkin substrate, by reducing the size of the sensor the range of resistive value of response was reduced. c. Temporal response of the interdigitated humidity sensor when exposed to breath.

4.3.2 Temperature Sensor

It is known that metals change their resistance with temperature, and the case of the humidity sensor made with silver ink is not an exception. To compensate for this effect, temperature sensors of positive coefficient and negative coefficient were incorporated. The positive coefficient sensor consists of a silver-ink printed mender resistor, in the same way as the interdigitated one was printed. Silver traces are a porous material; this is why the resistivity of printed silver is usually 10 times higher than that of bulk silver. Similarly, the thermal coefficient of the printed silver is different from that of bulk silver.

The resistor was exposed to various temperatures and its thermal coefficient was calculated with the following equation $R = R_0.(1 + \alpha.\Delta T)$, it was determined that the alpha for the printed silver is $\alpha = 1.9110^{-3}\ 1/K$. In contrast to the behaviour of metals, carbon-based materials such as reduced Graphene Oxide (rGO) exhibit a unique property: a negative thermal coefficient. In practical terms, this means that the resistance of rGO decreases as the temperature increases. Figure 4.5 shows different configurations of temperature sensors made from stamped rGO. Through rigorous temperature evaluations, the thermal coefficient for these sensors was found to be $\alpha = -5.810^{-4}\ 1/K$.

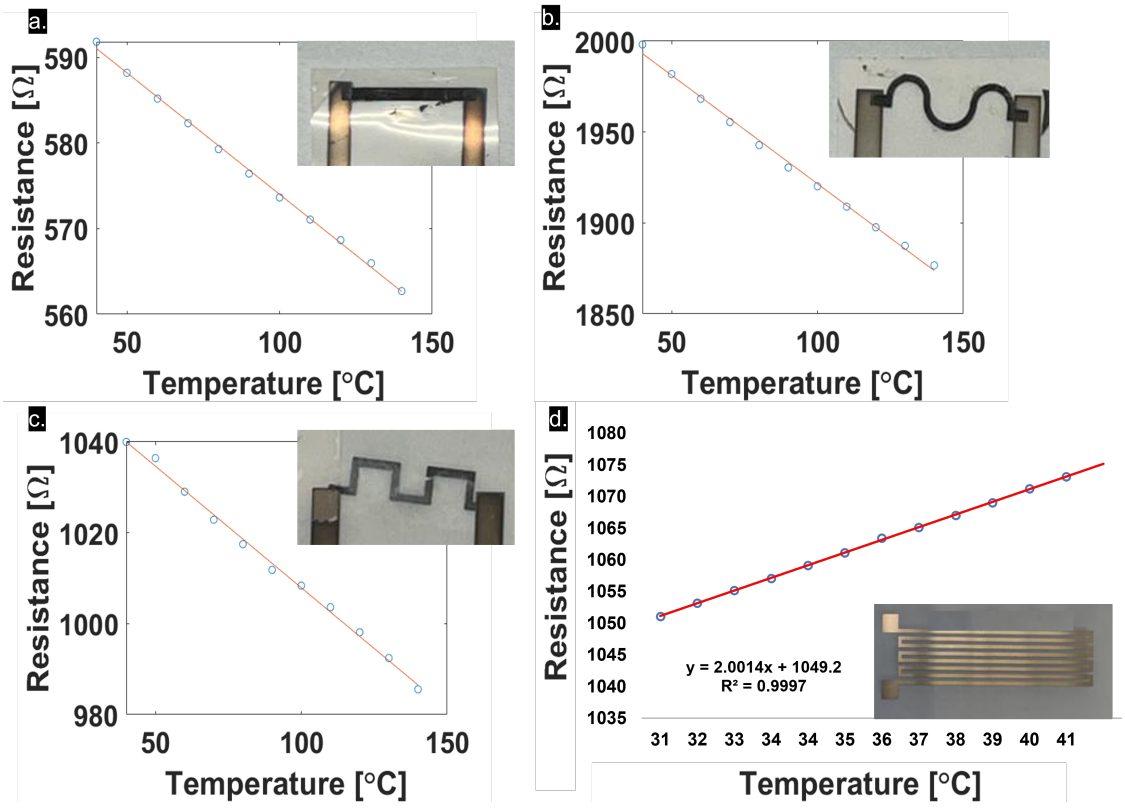


Figure 4.5: Calibration curves of rGO temperature sensors with different shapes, in all cases the response is linear and thermal coefficient is negative. The bottom right shows the calibration of the mender resistor, which, being silver, has a positive coefficient.

This intriguing property of rGO opens up the possibility of fabricating flexible resistors that maintain a constant performance over temperature changes. Figure 4.6 illustrates an innovative approach: the integration of a printed silver resistor with a positive thermal coefficient in series with a stamped rGO resistor with a negative coefficient. This combination creates a system where the resulting resistance is unaffected by temperature variations. Over a temperature range of $30 \circ C$ *to* $100 \circ C$, our tests showed a maximum resistance variation of just 0.22%. Such a marginal variation makes the impact negligible for a wide range of applications.

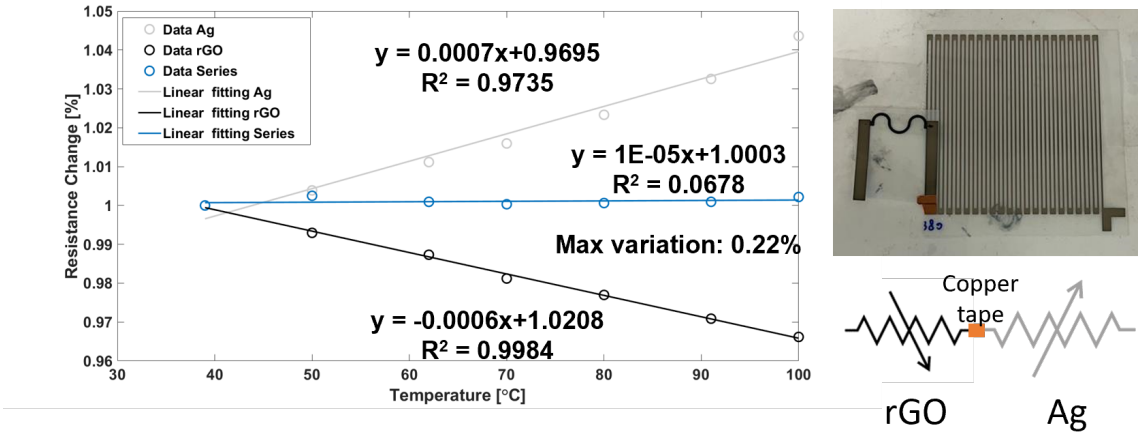


Figure 4.6: Resistive response of the silver ink resistor in series with the rGO transfered resistor over a wide temperature range. On the right is the device that uses copper tape to interconnect the two resistors.

Using this novel methodology, we applied this design strategy to the construction of our wearable technology. By combining these different materials with opposite thermal characteristics, we achieved a robust resistance value that remained virtually impervious to temperature changes, a critical feature for reliable performance in various real-world scenarios.

To verify its performance, the sensor was placed on the forearm and exposed to hot air. Figure 4.7 shows the thermal image of the arm with the sensor before and after exposure to heat, as well as the values obtained with the smartphone via NFC. The initial value with the skin at $30 \circ C$ is 1150.28 Ω for sensor 1, silver resistor, and 1710.94 Ω for sensor 2, silver in series with rGO. After exposing the arm to the hot air, measurements were taken again and 1188.31 Ω and 1743.53 Ω were obtained. Using the alpha values obtained during the characterisation of the sensors, it is possible to estimate the temperature at which the arm was exposed:

$$T = \frac{\frac{R}{R_0} - 1}{\alpha} + T_0 = \frac{\frac{1188.31}{1150.28} - 1}{1.9110^{-3}} + 30 = 47.31 \circ C \tag{4.1}$$

The rGO resistor value is determined by the difference between channel 1 and channel 2, as the resistors are in series. The obtained values are 560.66Ω and 555.22Ω, respectively. Applying again the equation 4.1. the temperature obtained by this sensor is:

$$T = \frac{\frac{555.25}{560.66} - 1}{-5.810^{-4}} + 30 = 46.73 \circ C \tag{4.2}$$

The calculated temperatures closely match those obtained through thermal imaging. Both measurements indicate that sensor 1 is 'Out of Range', indicating dry skin. If the skin were wet, as in physical activity, this sensor would register a value and the humidity would affect the temperature readings, resulting in lower reported values. To overcome this problem, the temperature sensor area is coated with wax. This prevents sweat absorption and interference with the resistance measurement.



Figure 4.7: Top: Image of the sensor placed on the forearm. Bottom: thermographic image of the sensor and the reading made with the smartphone through NFC both at room temperature and applying hot air.

During in vivo tests (Figure 4.8), sensor readings were taken to capture the skin's temperature upon application, which was measured at 31°C with the thermal camera. Once the membrane secured the sensor in place, a cooling effect was observed due to its moisture content. The experiment showed a 7-degree decrease in temperature in both temperature sensors and a significant change in the humidity sensor value. This was confirmed by a decrease in sensor resistance values and thermal imaging. As the person moved, their body temperature gradually increased, resulting in a subsequent increase in sensor readings. The recorded temperatures were approximately 13 degrees higher than the initial baseline temperature (Table 4.1), indicating the dynamic nature of sensor responses to physiological changes. This highlights the complex interplay between sensor placement, environmental conditions, and user activity.

In vivo temperature test				
	Time 0	Freshly applied membrane	Thermal Coefficient	Δ Temperature
Silver Series rGO	1100.23 Ω 1956.21 Ω 855.98 Ω	1084.35 Ω 1943.43 Ω 859.08 Ω	1.9110^{-3} $1/K$ -5.810^{-4} $1/K$	$-7.56 \circ C$ $-6.71 \circ C$
	Freshly applied membrane	Dry membrane	Thermal Coefficient	Δ Temperature
Silver Series rGO	1084.35 Ω 1943.43 Ω 859.08 Ω	1111.08 Ω 1963.96 Ω 852.88 Ω	1.9110^{-3} $1/K$ -5.810^{-4} $1/K$	$12.91 \circ C$ $12.44 \circ C$

Table 4.1: This table summarises the values obtained from the temperature sensors at 3 points in time: when the sensor is placed on the skin, without the membrane, after the membrane has been placed on the skin and when the membrane has dried. The temperature changes obtained can be observed.

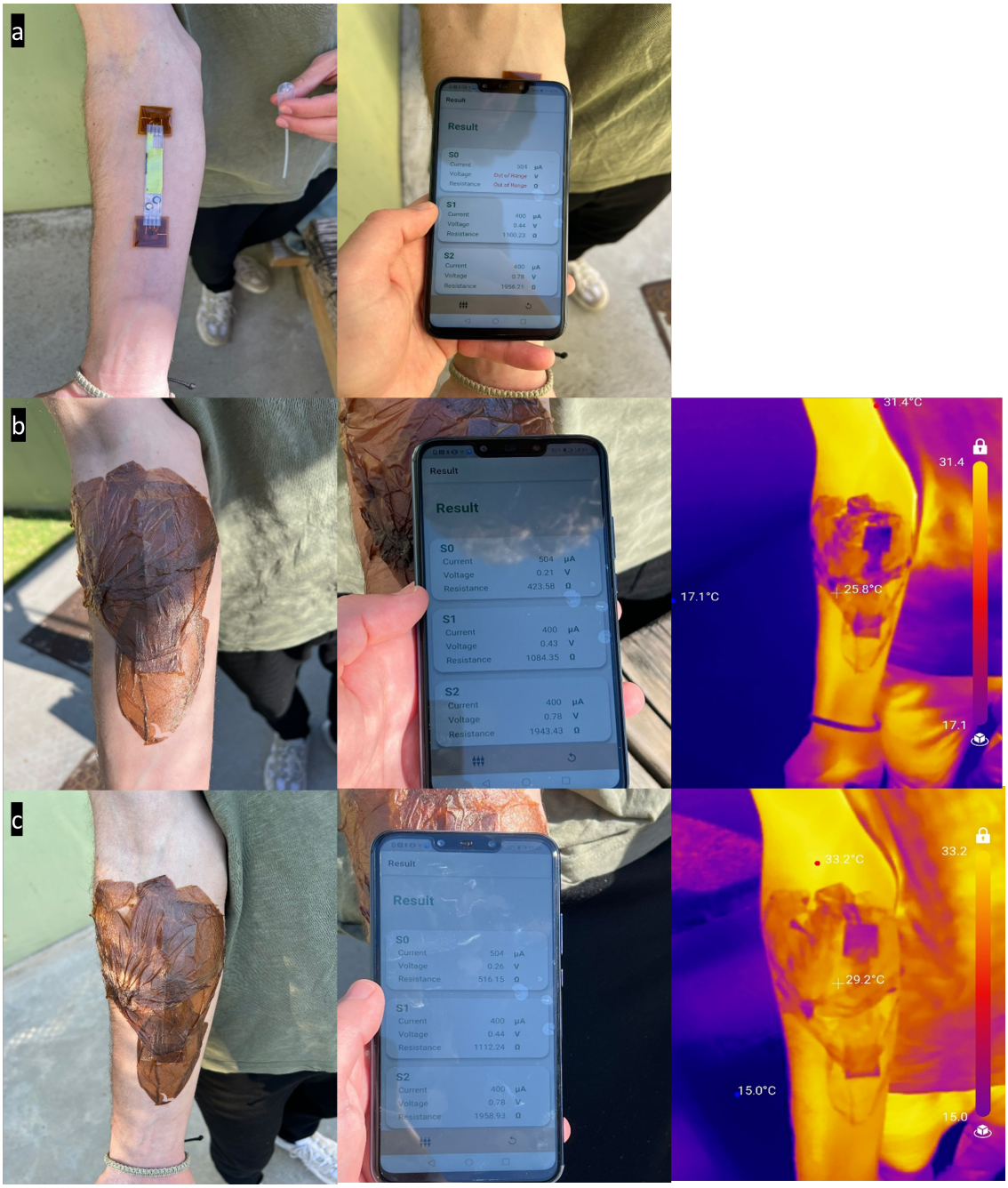


Figure 4.8: The sensor is first placed on the skin, and a reading is taken after a while. The recorded temperature is that of the skin at rest, at time 0. As the skin is dry, the humidity sensor is out of range. Next, the wet membrane is placed, causing the temperature of the skin to decrease and the value measured by the sensors to decrease as well. In this step, a variation of 5 degrees was recorded, which is consistent with the thermographic images. Finally, after 30 minutes and with the user in motion, the membrane dries and the temperature rises to approximately 36-37 degrees Celsius.

4.3.3 Muscle contraction simplified sensing

Surface myography, a non-invasive technique for recording muscle activity, is traditionally performed by placing two electrodes along the muscle fibers. These electrodes capture the electrical activity generated by the muscle fibers during contraction. A third electrode, known as the ground electrode, is placed in a zone that is not influenced by the muscle contraction, typically on the closest joint. This setup allows for the muscle action potential to be amplified and recorded over time. The data is collected at a sufficient sampling frequency, typically 1 KHz, to capture all the necessary information about the muscle's activity. However, this conventional setup has its limitations. The most significant of these is that it is wired, which can hinder the performance of natural movements. Additionally, it requires relatively bulky electronics to be placed next to the sensors, which can be inconvenient for the user.

In our work, we have developed a novel platform that addresses these issues. We have repurposed the SIC4341 NFC chip. This integrated circuit is intended for electrochemical measurements, but since it can perform chronoamperometry, it is suitable for this application. Like a potentiostat, the chip has a connection for 3 electrodes, Working, Counter and Reference. However, the APP provided by the manufacturer, gives the possibility to configure the system on 2 electrodes, only considering the Working and the Counter. This was the mode selected for the muscle contraction measurements. A voltage of $0.5V$, a run time of $300s$ and a measurement interval of $100ms$ were configured. To improve the connection between the printed pads and the skin, carbon conductive adhesives tabs, typically used for SEM samples, were used. Notably, this tape exhibits a higher impedance compared to conventional conductive gels.

However, these gels present two significant drawbacks for this specific application. Firstly, given the semi-permeable nature of our substrate, the gel tends to disperse across the substrate, thereby posing a risk of short-circuiting the electrodes. Secondly, these gels exhibit a capacitive response that can result in a phase shift of up to 40 degrees. The gel behaves like a resistor-capacitor filter that enhances some frequencies and mitigates others, deforming the signal. In contrast, the carbon tape, while being tenfold more resistive than the gel, maintains a consistent value across varying frequencies and does not exhibit a capacitive component. A comparative analysis of these two connection modalities is presented in the tables 4.2 and 4.3 and Figures 4.9 - 4.12. An LCR-meter at 5 different frequencies (100 Hz, 120 Hz, 1000 Hz, 10000 Hz, and 25000 Hz) was used in order to determine the frequency response of the contacts. The measurement model used was the series model, and the measurements taken were resistance (R), phase angle (θ), and impedance (Z)

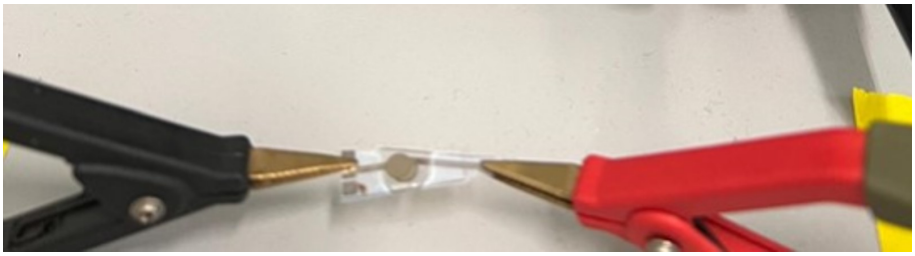


Figure 4.9: Two silver electrodes printed on mitsubishi substrate, the same as those used for ssEMG measurements, have been interconnected using gel.

Gel Contact				
Freq. [Hz]	Resistance [Ω]	Capacitive Impedance [Ω]	Impedance [Ω]	Phase [◦]
100	31.04	−16.98	35.38	−28.68
120	29.84	−17.03	34.36	−29.72
1000	14.68	−10.50	18.05	−35.58
10000	10.12	−2.44	10.41	−13.56
25000	9.29	−1.60	9.43	−9.78

Table 4.2: The table presents a summary of the results obtained for gel impedance at different frequencies. The resistance(R), phase angle(θ), and impedance (Z) were obtained by the LCR-meter, while the capacitive impedance (Xc), was calculated with the expression $Xc = -\sqrt{Z^2 - R^2}$.

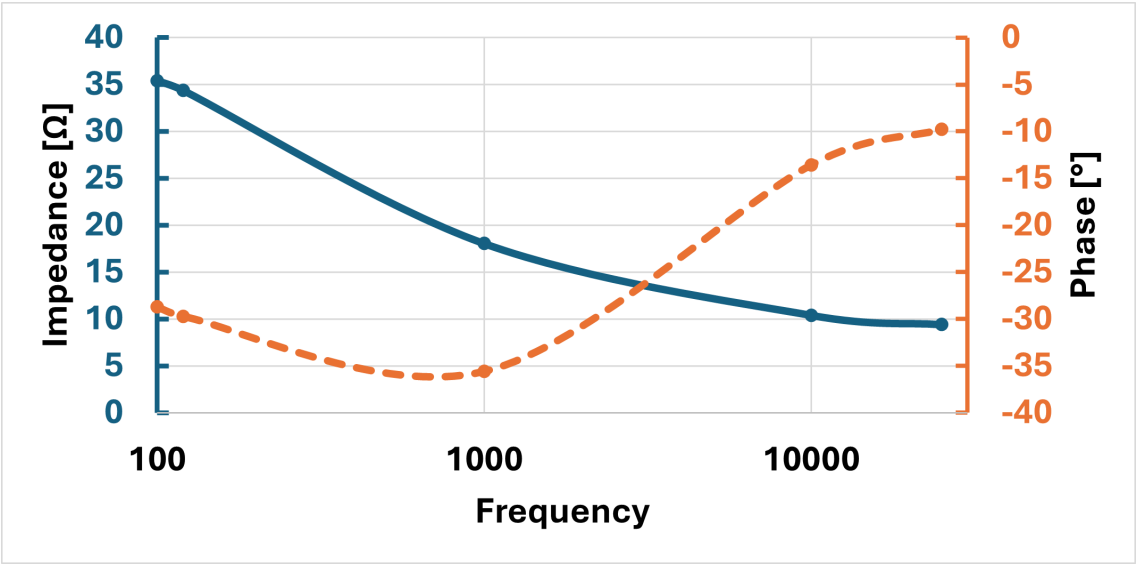


Figure 4.10: Frequency response of the Gel contact.It can be observed that even the resistive component of this gel was frequency dependent, due to the electrolytic nature of the gel. Furthermore, it can be observed that the phase shift reached up to 40 degrees, indicating that the capacitive component had an impedance almost equal to the resistive component.



Figure 4.11: Two silver electrodes printed on mitsubishi substrate, the same as those used for ssEMG measurements, have been interconnected using carbon tape.

Gel Contact				
Freq. [Hz]	Resistance [Ω]	Capacitive Impedance [Ω]	Impedance [Ω]	Phase [◦]
100	250.4	0	250.4	0
120	250.4	0	250.4	0
1000	250.3	−10.04	250.3	−0.01
10000	250.2	−0.35	10.41	−0.08
25000	250.2	−1.18	9.43	−0.27

Table 4.3: The table presents a summary of the results obtained for carbon tape impedance at different frequencies. The resistance(R), phase angle(θ), and impedance (Z) were obtained by the LCR-meter, while the capacitive impedance (Xc), was calculated with the expression $Xc = -\sqrt{Z^2 - R^2}$.

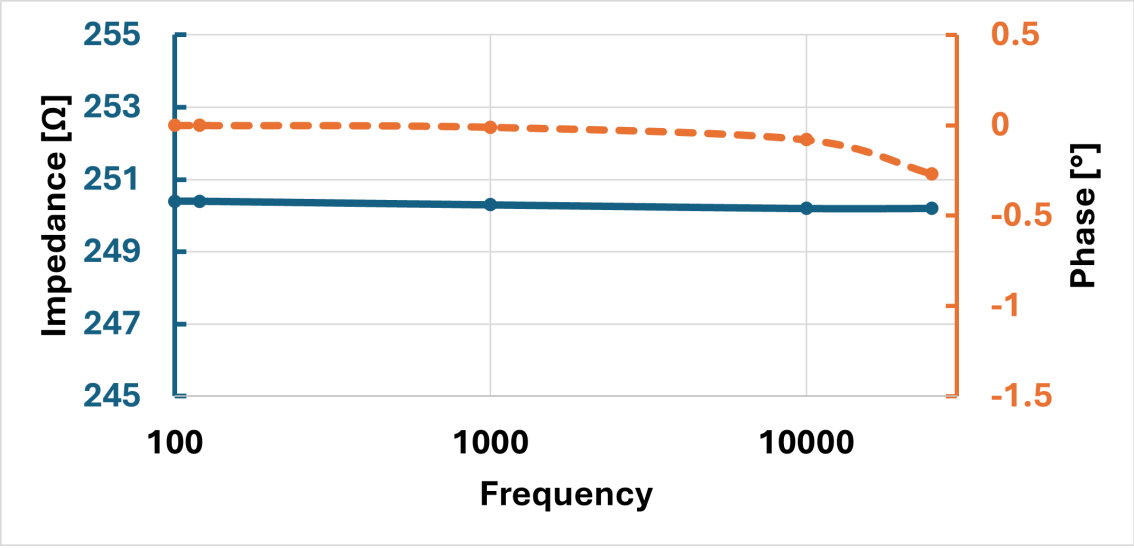


Figure 4.12: Frequency response of the Carbon Tape contact.It is observed that the carbon tape did not exhibit a variation in frequency and that the capacitive component was practically null. As a disadvantage, the resistance was an order of magnitude higher than that of the conductive gel.

For the larger muscles such as the bicep and tricep, the scale of $20\mu A$ was used, while for finger movement recording the scale selected was $2.5\mu A$.This innovative use of the NFC chip allows for a more streamlined and user-friendly setup.

Our configuration enables the direct measurement of the currents associated with muscle contraction. The system is powered wirelessly and the data is read in real-time by a smartphone, eliminating the need for batteries. Despite the relatively low sampling frequency of the device, which results in a poorer frequency content of the signal, and the partial drift of the signal due to the absence of a ground electrode, our results clearly indicate that muscle contractions were accurately detected.

We tested our system on various muscles and under different conditions. We performed tests on the fingers extension muscles located on the back of the forearm (as shown in Figure 4.13a), and on the triceps and biceps muscles in response to the extension (Figure 4.13b) and contraction of the forearm (Figure 4.13c), respectively. The red arrows in the figures signify the instances of action execution: finger movement, tricep contraction without load, and bicep contraction with load. Conversely, the light blue arrows denote the resting positions: fingers curled into a relaxed fist without exerting force, the tricep relaxed without weight resistance, and the extended arm position during the bicep exercise.

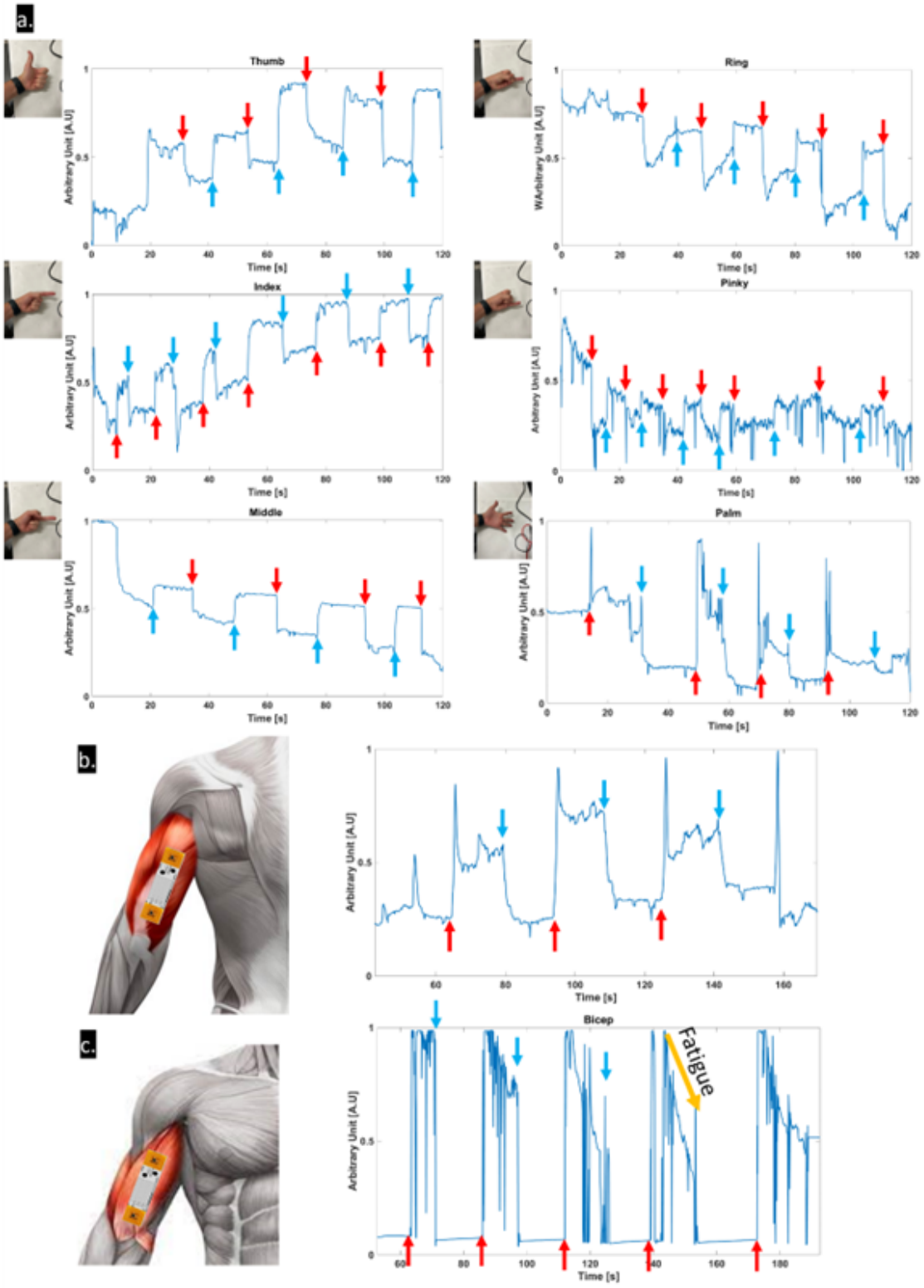
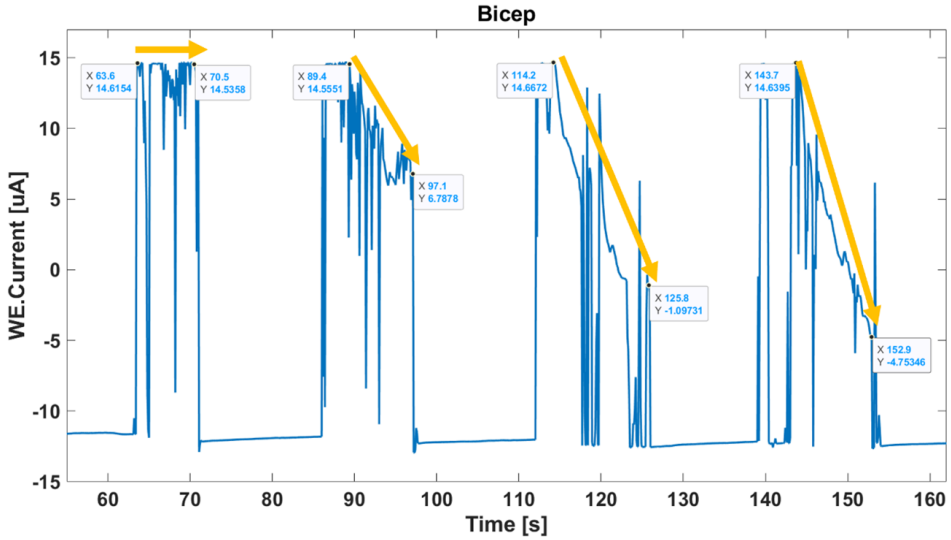


Figure 4.13: ssEMG normalized measurement on the forearm for the dection of the fingers muscle contraction (a). SsEMG normalized measurements on the tricep muscle (b) and on the bicep muscle (c). The red arrows indicate the contraction and the blue ones the rest phases in all the plots.

Figure 4.14 illustrates the occurrence of a reduction in signal intensity during each bicep contraction, commencing with the second contraction, during weight-bearing exercise. This reduction may be correlated with fatigue. The reduction in muscle signal intensity observed during consecutive isometric contractions of the biceps during dead weight lifting was indicative of muscle fatigue. In contrast, the decrease was not observed for the triceps, where only one muscle contraction was performed without lifting.

Our results demonstrate the potential of our platform for wireless, battery-free surface myography. We believe that our work represents a significant advancement in the field and has the potential to improve the convenience and effectiveness of muscle activity monitoring greatly.



Lifting	1	2	3	4
Time[s]	6.90	7.77	11.6	9.20
Signal Decrease [μA]	-0.10	-7.70	-15.76	-19.39
Slope [$\mu A/s$]	-0.01	-0.99	-1.36	-2.11

Figure 4.14: Measurement of bicep muscle contraction during physical exercise. A drop in the signal has been detected during each contraction starting from the second one, which may be correlated with fatigue. The reduction in muscle signal intensity observed during consecutive bicep isometric contractions when lifting a dead weight was indicative of muscle fatigue. In contrast, the decrease was not observed in the case of the tricep, where only one muscle contraction was performed without weight lifting.

4.4 Conclusions of the chapter

In this chapter we have seen how the platforms developed in Chapter 3 can be used as wearables. In particular, we have seen how we can take advantage of the 3 channels of the SIC4340 to implement humidity sensors and temperature sensors with positive and negative coefficients. The calibration curves of these sensors were presented. We have also seen how, although the SIC4341 is a potentiostat chip designed for electrochemical measurements, it can also be used to measure physical parameters such as muscle contraction using surface myography. In order to perform electrochemical measurements with the SIC4341, it would be necessary to develop transducers, i.e. electrodes, which will be discussed in the next chapter.

CHAPTER 5

TRANSDUCERS FOR DIAGNOSTIC DEVICES AND APPLICATIONS

Before delving into the intricacies of electrochemical measurements, it is important to first understand the fundamental components that form the basis of these processes. One such component is the set of electrodes.

An electrode is an electrical conductor that serves as a bridge for contact with a non-metallic part of a circuit, such as a semiconductor, an electrolyte, a vacuum, or even air. Electrodes play a key role in the functionality and efficiency of the system they are a part of, beyond just being a conduit for electrical currents[128]. It is important to recognise the significant contribution of electrodes in this field.

In biosensing, electrodes facilitate the detection and measurement of biological elements such as proteins, nucleic acids, enzymes, and other biomolecules[45]. Electrodes in biosensors are designed to interact with specific target molecules, leading to a change in electrical properties that can be measured and analyzed. They are an integral part of any electrochemical biosensing system, enabling the detection and quantification of a wide range of biological and chemical compounds.

A typical electrochemical cell consists of three electrodes[129]. The working electrode, where the electrochemical reaction of interest occurs. The reference electrode, which maintains a constant potential against which the working electrode's potential can be measured. Finally, the counter electrode serves to complete the circuit by providing a path for the current to flow from the working electrode. Together with the transducers, these electrodes form a robust and efficient system capable of performing precise and accurate electrochemical measurements. The transducers convert the biochemical reaction into an electrical signal, which can be amplified and read by the system.

Electrodes are not just components in a circuit; they are the essential components of biosensing

systems. Their significance cannot be overstated, and their role in advancing the field of biosensing is monumental. Moving forward, we will continue to explore and understand the fascinating world of electrodes and their numerous applications in biosensing. This chapter describes in detail the three types of electrodes developed and used in this thesis. The following sections discuss their particular characteristics, fabrication methods and applications for each.

5.1 Nanoband Electrodes

This section delves into the realm of nanoscale electrodes—a domain of intensive research spanning decades. Nanoelectrodes, owing to their heightened sensitivity derived from reduced dimensions, offer an ideal platform for developing analyte sensors detecting low concentrations[130–132]. Yet, their fabrication historically demanded costly equipment and laborious methods, hindering widespread use and commercialization. This section unveils a novel approach to fabricate nanoband electrodes utilizing affordable materials and commonplace lab equipment worldwide.

For years, electrochemists have grappled with limited electrode options. Traditional electrodes like gold, silver, and carbon necessitate time-consuming manual polishing and harsh cleaning processes before use[133, 134]. Contemporary alternatives like inkjet or screen-printed electrodes[135–137] offer rough surfaces and post-printing challenges, hindering reproducibility. Cleanroom-fabricated electrodes using advanced techniques like atomic layer deposition or electron beam evaporation ensure purity and precision but come with exorbitant costs, limiting accessibility.

Nanoelectrodes, defined by at least one nanoscale dimension, exhibit heightened sensitivity attributed to enhanced mass transport, smaller double layers, and reduced iR drops compared to macroscopic counterparts[132, 138]. Their rapid functionalization potential signifies accelerated sensor development. However, existing fabrication methods—expensive or unsuitable for mass production—pose significant hurdles.

This section introduces a cleanroom-free fabrication method employing a sputter coater to craft nanoelectrodes. The process deposits metallic thin films with sub-nanometer precision using inexpensive lab equipment, yielding cost-effective, high-performance electrodes. These nanoband electrodes, costing less than €0.10 each, exhibit electrochemical properties surpassing larger electrodes. Their superior performance in detecting DNA sequences highlights their potential for highly sensitive diagnostics.

These electrodes, affordable, easily manufacturable, and more sensitive than conventional counterparts, have the capacity to transform electrode-based research. Their rapid functionalization and cost-effectiveness promise accelerated assay development. They hold promise for developing highly sensitive PoC sensors for detecting biomarkers at low concentrations, enabling early disease diagnosis and potentially revolutionizing nucleic acid biomarker detection without

amplification.

5.1.1 Fabrication and Characteristics

The fabrication process of nanoelectrodes in this thesis involved sputtering gold onto flexible plastic substrates using a standard sputter coater (model SC7620, Quorum Technologies) and stencils. The chosen substrates—polyimide (Kapton), polyethylene terephthalate (PET), and polyethylene naphthalate (PEN)—were selected for their accessibility, flexibility, and ease of manipulation. Notably, this approach allows electrode formation on various substrates without specific fabrication optimisation, a key advantage over other methods. Stencils, made from aluminium or the same plastics as the substrates, were employed to ensure precise electrode dimensions during sputtering. The ability to rapidly design and utilise masks of varying layouts facilitated swift iterations in electrode design—a feat unattainable through photolithography.

Gold deposition via sputtering, a well-documented process, enabled controlled nanometer-thin metallic film deposition with sub-nanometer accuracy[139, 140]. Depositions ranged from 50–100 nm, ensuring robust device connections and uniform substrate coverage comparable to cleanroom-fabricated nanoelectrodes in literature[130, 141]. This process can be performed on multiple substrates. As will be seen in the next section, conductivity tests confirmed consistent sheet resistances among the sputtered gold films on different substrates, emphasising substrate insignificance in affecting device electrochemical performance.

To create nanoelectrodes, the sputtered metal required capping and cutting. Various capping methods—Kapton tape, acrylic spray coating, and lamination—were tested and proven effective, each potentially suitable for distinct applications. Kapton tape emerged as the favoured choice due to its efficiency and ease of use. Subsequent cutting using scalpels, scissors, or a paper guillotine yielded functional nanoband electrodes, demanding sharp and precise blades to avoid layer deformation. Cutting face-down prevented adhesive coverage over the electrodes.

This fabrication approach, leveraging commonplace laboratory equipment and versatile substrates, demonstrates a cost-effective and accessible means to produce nanoelectrodes with consistent performance across varied substrates—an essential step toward revolutionising electrode-based research. The fabrication process, including sputtering, capping, and cutting, required less than an hour for a single batch of electrodes. Once the devices were fabricated, creating fresh electrodes via cutting took mere seconds, a notable advancement compared to other cleanroom-free fabrication methods that demand considerably longer processing times. For instance, methods reported by the White group[142] involve resin encapsulation, requiring 24 hours to dry, followed by extensive mechanical polishing for hours to attain pristine electrodes. A comprehensive video illustrating our fabrication process accompanies our public in small journal related to this section, utilizing commonly available laboratory equipment with low upfront capital costs, as summarized in Table S2 of the Supplementary Information of this paper.

Excluding upfront equipment expenses, the per-electrode material cost remains below €0.01,

given the cutting of devices a minimum of ten times to yield at least ten electrodes per device. This cost-effectiveness renders these electrodes inherently disposable, favoring their recreation over cleaning and reusing. A distinctive advantage lies in the ability to cut a single device multiple times to generate several electrodes, enhancing cost efficiency. Though device fabrication may take up to an hour, the cutting and creation of a fresh nanoelectrode require mere seconds.

5.1.2 Characterization

Figure 5.1 displays the Cyclic Voltammograms (CVs) and Figure 5.2 displays the Square Wave Voltammograms (SWVs) for different substrate types, each with distinct capping layers and cutting methods. These curves exhibit characteristic wave-like shapes, indicative of nanoelectrodes, coupled with consistently low capacitances across all electrodes. Among the cutting methods employed, precision cutting displayed the highest reproducibility, followed by scissors and scalpel, aligning with the level of human error inherent in each method. The scalpel's variability in angle, pressure, and precision resulted in more inconsistent cuts, which impacted reproducibility.

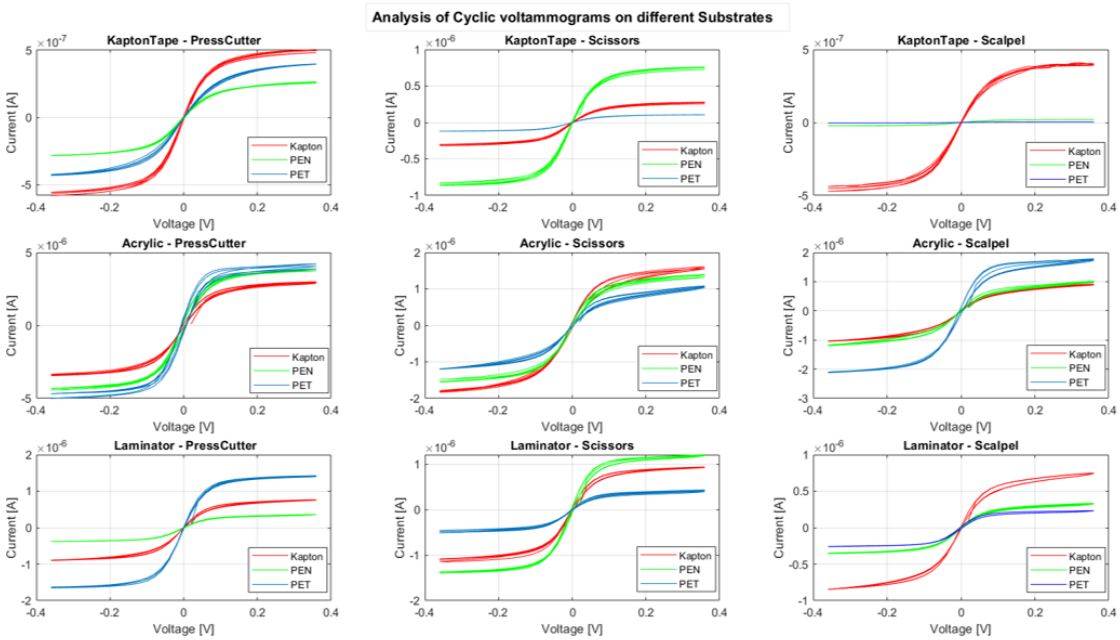


Figure 5.1: Cyclic voltammogramms (CVs) of the 27 possible combinations of substrate (Kapton, PET or PEN) with each of the different capping layers (Kapton tape, acrylic and laminate), cut by each of the three cutting methods tested (precision cutter, scissors or scalpel). CVs were recorded in a 10 mM phosphate buffered saline solution solution containing 5 mM potassium ferricyanide, 5 mM potassium ferrocyanide, at 10 mV/s vs a formal Ag/AgCl reference electrode and Pt wire counter electrode.

Concerning the capping layers, acrylic proved the most reproducible due to its robust setting. Conversely, softer adhesives like tape and the melt layer of the laminate often caused smearing

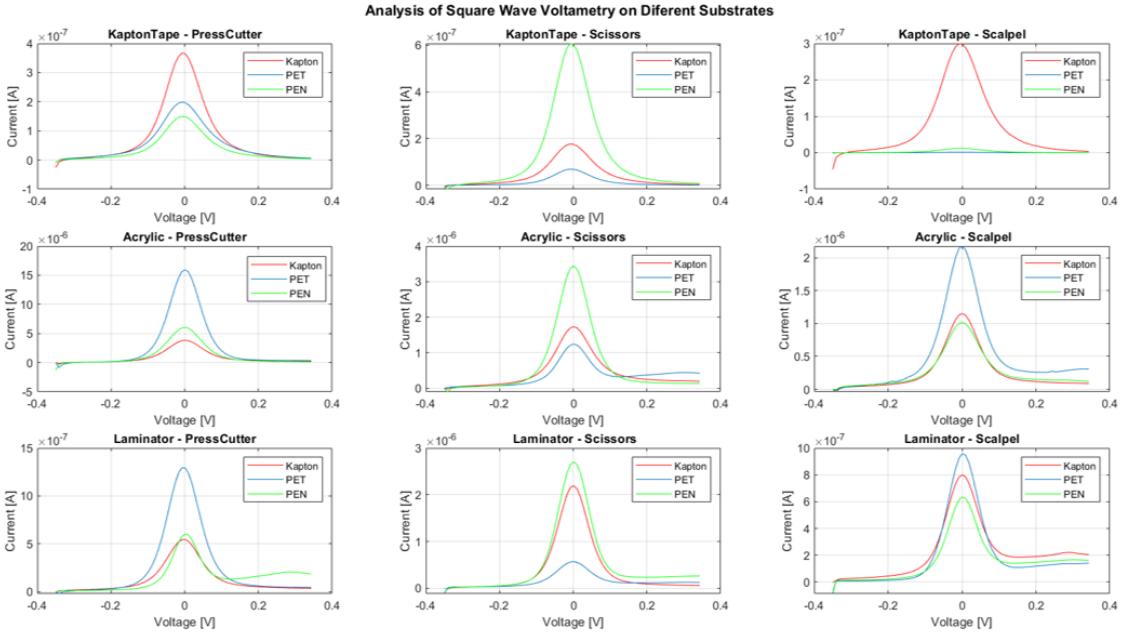


Figure 5.2: Square Wave Voltammograms (SWVs) of the 27 possible combinations of substrate (Kapton, PET or PEN) with each of the different capping layers (Kapton tape, acrylic and laminate), cut by each of the three cutting methods tested (precision cutter, scissors or scalpel). SWVs were recorded in a 10 mM phosphate buffered saline solution solution containing 5 mM potassium ferricyanide, 5 mM potassium ferrocyanide vs a formal Ag/AgCl reference electrode and Pt wire counter electrode.

on the electrodes during cutting. Achieving a clean cut that pulls the adhesive away from the electrode is critical. The precision cutter consistently produced reproducible cuts and larger electrode areas due to reduced adhesive residue. Notably, the choice of substrate did not significantly impact the final electrode quality in our experiments.

This was also confirmed by the measurements of the sheet resistances. The deposited Au was tested with a four-point probe to assess its conductivity. The results obtained were $3.51 \pm 0.70\ \Omega/sq$ (PEN), $3.07 \pm 0.15\ \Omega/sq$ (PET), $4.45 \pm 0.55\ \Omega/sq$ (Kapton). There was no significant difference between the resistances of the gold sputtered onto any of the different substrates, this is pleasing as it evidences that the substrate does not affect the electrochemical performance of the devices.

To confirm the nanoscale nature of the fabricated electrodes, SEM images (Figure 5.3) captured the bands, while atomic force microscopy (AFM) measurements (Figure 5.4) determined the uncapped sputtered metal edges' height. The SEM images distinctly illustrate a nanoscale conductive band between the substrate and capping layer. Analysis using SEM software estimated this band's height between 40 and 45 nm, slightly below the targeted 50 nm sputtering thickness, attributable to experimental errors in the sputtering process. AFM measurements on uncapped Au layers sputtered onto Kapton revealed a comparable step height of about 40 nm.

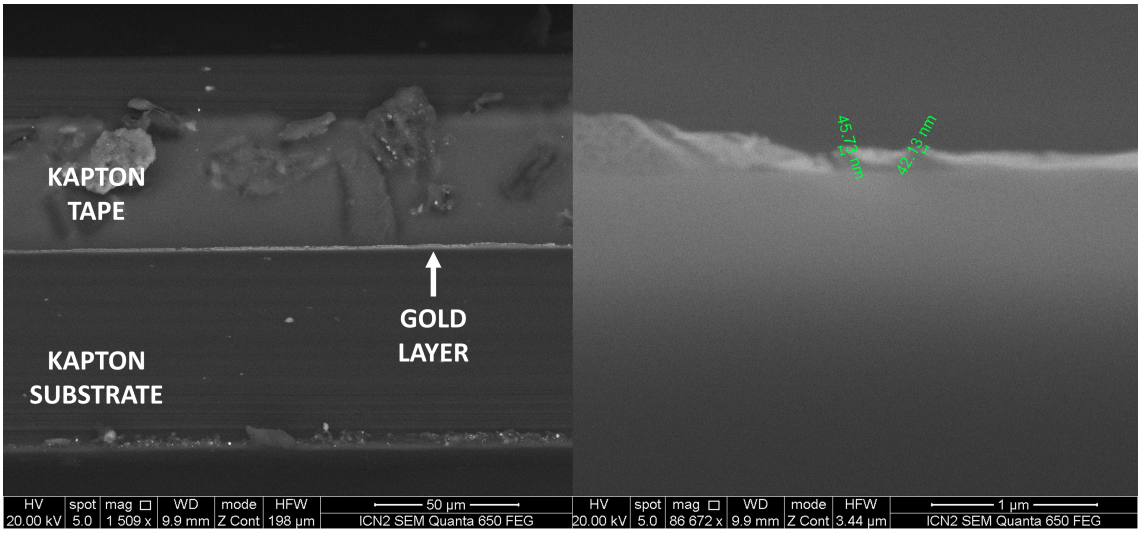


Figure 5.3: Scanning electron microscope images of nanoband electrodes made from Au sputtered onto Kapton and covered with Kapton tape, cut with surgical scissors.

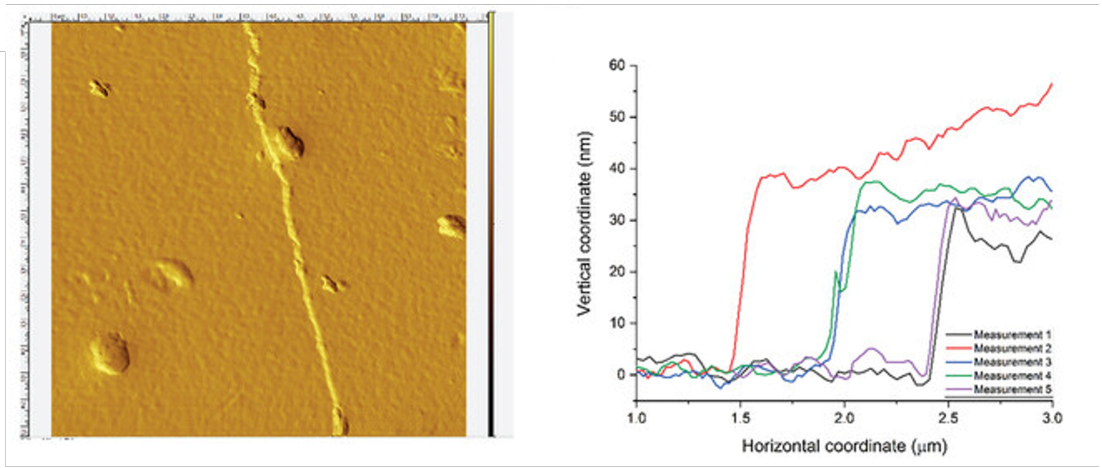


Figure 5.4: On the right: AFM image of the edge of one of the sputtered Au devices on Kapton (uncapped) with five corresponding step height measurements from left to right across the ridge. On the left it can be seen that the Au thickness is $\approx 30-40nm$ and the roughness of the Au surface is the same as that of the Kapton (single nanometres).

Typical CVs of macroelectrodes exhibit peaks attributed to current limitations by redox molecule mass transport to the electrode surface. In contrast, nanoelectrodes behave differently[143]; their small size establishes a hemispherical diffusion profile[144], resulting in observed waves rather than peaks in CVs[145–147]. The developed nanoband electrodes consistently demonstrate electrochemical responses characteristic of nanoscale electrodes (developed), with current ranges aligning with similar nanobands in similar buffers reported by other researchers[142].

The main advantage of nanoelectrodes over other conventional electrodes is their increased sensitivity. Therefore, it is useful to evaluate the sensitivity of the sputtered nanobands and compare them with conventional electrodes. We did this by diluting potassium ferricyanide and potassium ferrocyanide and measuring the concentration electrochemically using the sputtered nanobands (Figures 5.5 and 5.6), commercial screen-printed Au electrodes and standard macro-electrodes (Figure 5.7). While the commercial screen-printed electrodes and nanoband electrodes could be used as they arrived or immediately after cutting, the macro electrodes had to be cleaned before use. This was done using the standard combination of mechanical, chemical and electrochemical cleaning processes. This process is time consuming, taking 6 hours to complete, and requires trained personnel and harsh chemical treatments.

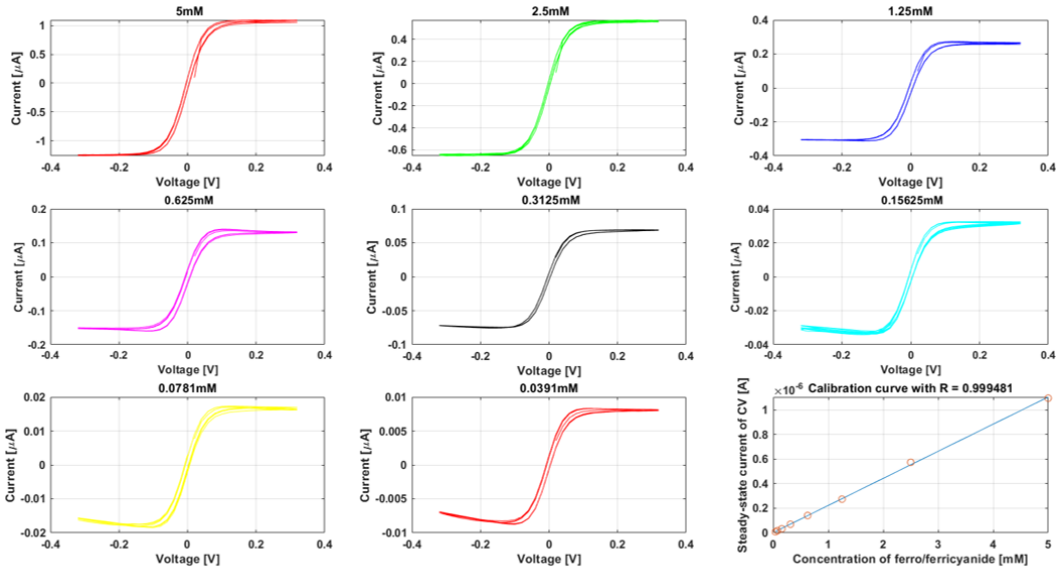


Figure 5.5: CycloVoltammetric (CV) measurements of Ferro/Ferricyanide at different concentrations from 5 mM to 39.06 μM. The calibration curve, with an R > 0.999, is shown at the bottom left.

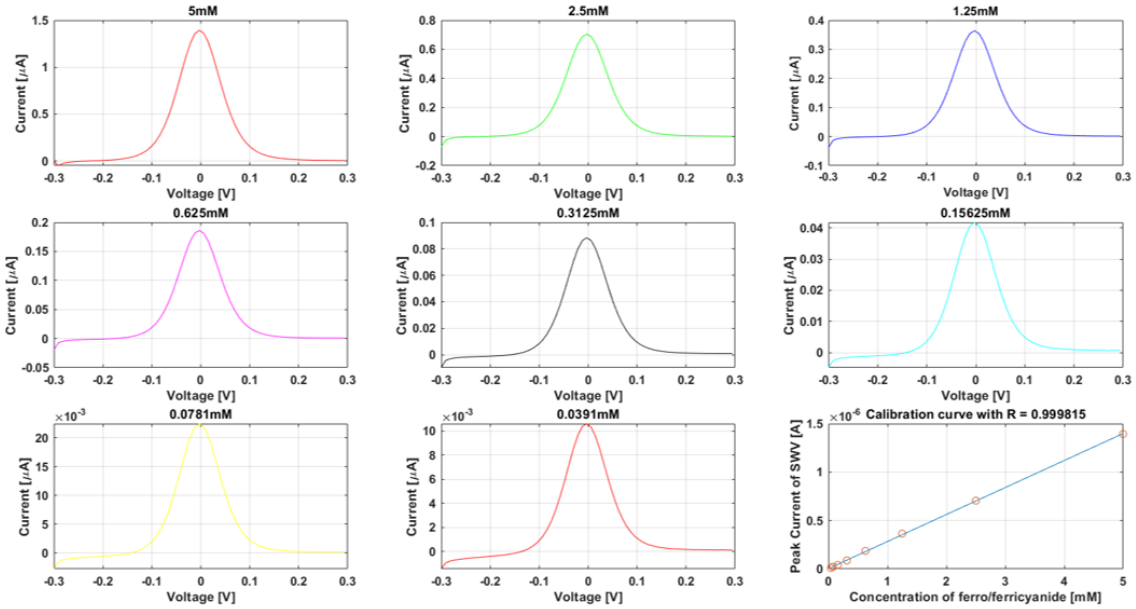
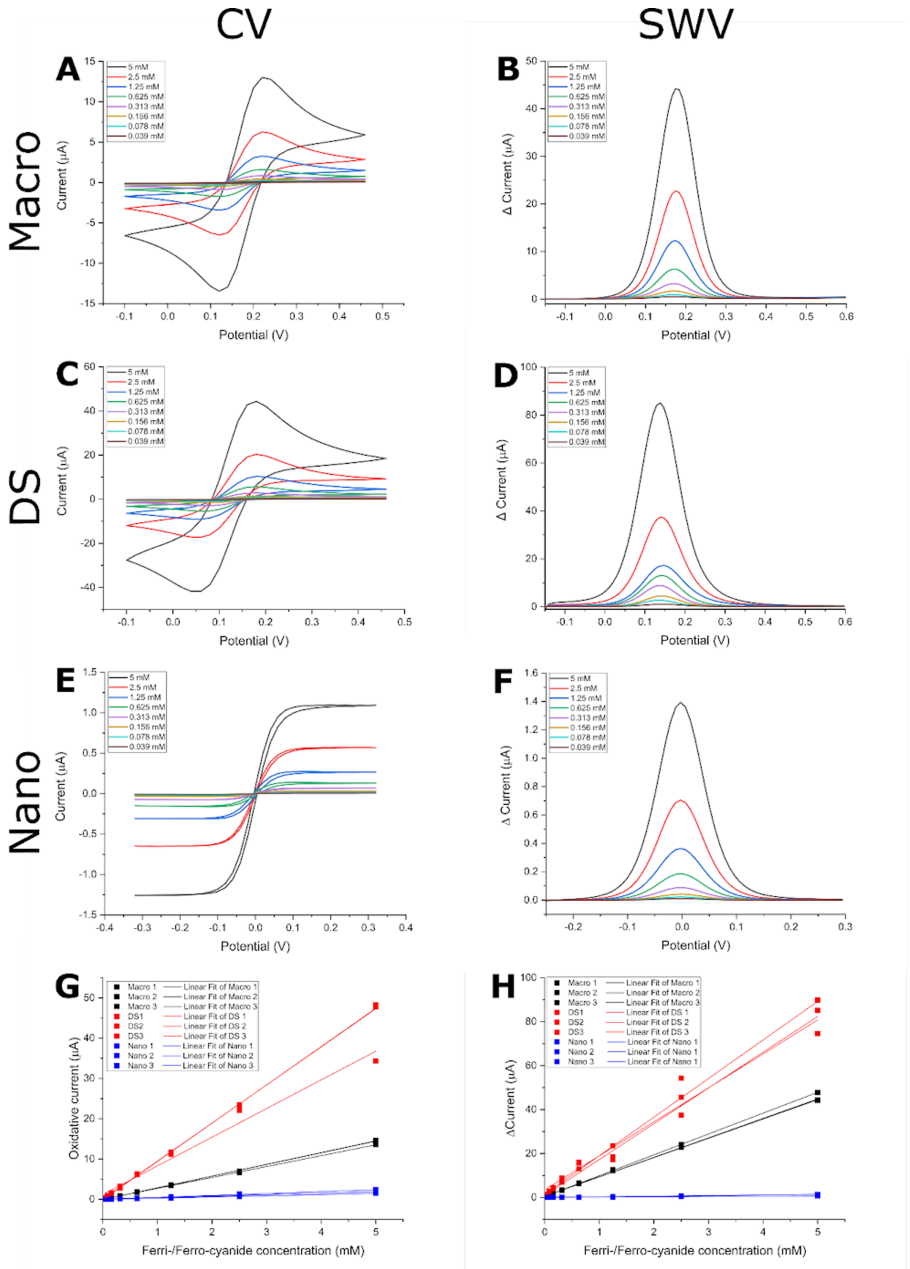


Figure 5.6: Squarewave voltammetry (SWV) measurements of Ferro/Ferricyanide at different concentrations from 5 mM to 39.06 μM. The calibration curve, with an R > 0.999, is shown at the bottom left.

From the calibration curves in Figure 5.7, we can compare the detection capabilities of these nanoband electrodes with the responses of the two different macro-electrodes. From the intercepts, which give the limits of detection (LOD) of the electrodes in this system, there are several trends. The first is that all electrode types have a LOD = 0 within error when looking at the CVs. However, in the SWV data this is only true for the nanoelectrodes. The average detection limit is lower for the nanobands than for the other electrode types, which is in line with previous reports on nanoelectrodes. Although the larger electrodes have higher sensitivities (gradients) than the nanoelectrodes in this concentration range, it is observed that in both SWV and CVs the nanoelectrodes have much higher levels of precision due to their improved signal-to-noise ratio. It is interesting to note that the CVs are generally better reproducible for these nanoband electrodes, comparable to the current state of the art.



		MACRO	DROPSENSE	NANO
cv	Intercept	-41 ± 118	369 ± 462	13 ± 42
	Gradient	2 843 ± 116	8 697 ± 1 354	376 ± 95
swv	Intercept	497 ± 84	1 953 ± 1 330	60 ± 75
	Gradient	9 047 ± 388	16 441 ± 1 060	172 ± 94

Figure 5.7: Comparative Cyclovoltammetry and SquareWaveVoltametry measurements of Macro Electrodes, ScreenPrinted Electrodes and Nanoband Electrodes. The average detection limit is lower for the nanobands than for the other electrode types, which is in line with previous reports on nanoelectrodes.

5.1.3 Different Electrode Designs - "LEGO-brick" concept

The methodology employed in the fabrication of electrodes offers a distinct advantage - the capacity for swift iteration of various electrode designs and configurations. The process allows for the creation of new plastic masks in a short span of time (less than 20 minutes), using cutting plotters or even manual crafting. This facilitates alterations in the pattern and dimensions of the metallic coatings to cater to diverse applications.

Moreover, the methodology provides the flexibility to amalgamate electrodes of varying designs and types, thereby enabling the creation of bespoke devices tailored to specific applications. The ease of fabricating an assortment of electrodes, characterized by different patterns, thicknesses, and materials, is another significant advantage. These individual components can be seamlessly integrated to devise new devices for a range of applications, including those requiring different numbers of electrodes, such as dual-electrode systems or multiplexed sensing applications.

Drawing a parallel to LEGO bricks, these components can be assembled in countless configurations, offering limitless design possibilities. To demonstrate the viability of this "LEGO-brick" concept, comprehensive three-electrode systems have been developed using several distinct methods. It is important to emphasize that this is merely a proof of concept, and the potential for design variations is infinite.

Illustrations, diagrams, and Scanning Electron Microscope (SEM) images of these diverse methods of device assembly are presented in Figure 5.8. Firstly, it is feasible to stack multiple capped devices atop one another using adhesives, as depicted in Figure 5.8A. In this method, the individual devices were capped with the acrylic spray. Multiple devices could be stacked on top of each other with the acrylic acting as an adhesive between them. In this system, each of the devices performed the function of a working, counter, or reference electrode. In these experiments, the acrylic was needed to be left for longer to dry (overnight) under ambient conditions. The connection pads of each device could be cut with scissors to allow easy connection after stacking. Secondly, devices can be constructed vertically by sputtering directly onto the capping layers, utilizing masks to segregate the different bond pads for the various layers, as shown in Figure 5.8B. this method, new electrodes were sputtered directly onto the capping layer of the underlying device. Three mask designs were used, one for each layer. The masks were designed to isolate the connections of each layer in the final device. The final layer, sputtered to be the counter electrode, was not capped, so that when dipped into a solution, the electrode area would be far greater than that of the working electrode. Thirdly, a mask can be designed such that the three electrodes exist within the same 2D plane, separated solely by the mask design, as illustrated in Figure 5.8C. A mask was made out of Kapton in which three electrodes could be patterned on a single device, running parallel to one another down the length of the device. The three electrodes were able to be used as a working electrode, pseudoreference electrode, and counter electrode.

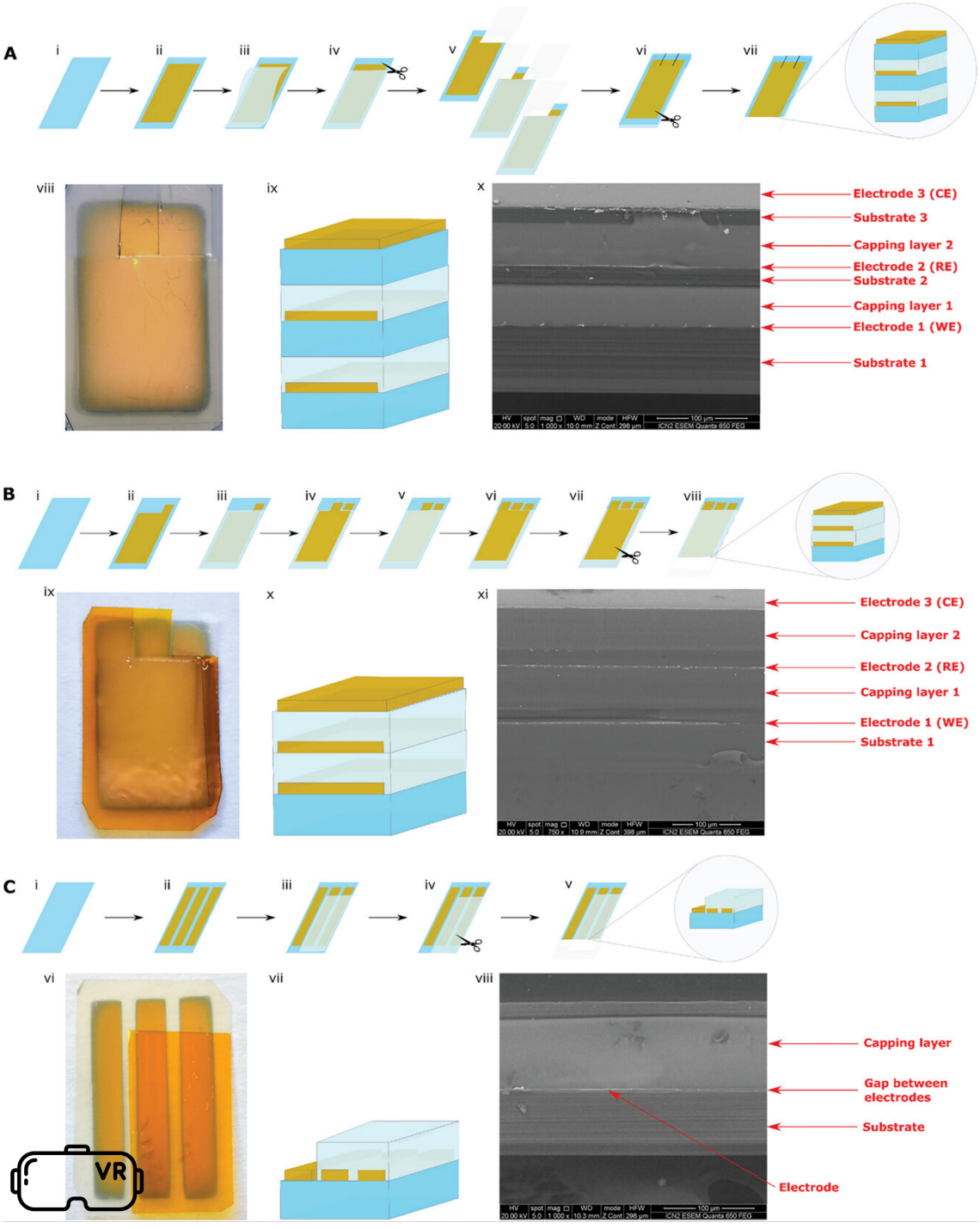


Figure 5.8: Schematics (not to scale), photographs and SEM images of the different LEGO brick designs fabricated and tested in this project. A) Bonding finished devices together. B) Sputtering directly onto the capping layers. C) 2D Devices.(https://youtu.be/8iuDemUqiwc)

The Cyclic Voltammetry (CV) of these devices, presented in Figure 5.9, reveals a shift in the half-wave potential (from +0.175 to +0 V) when transitioning from a Ag/AgCl reference electrode to a sputtered Au pseudoreference electrode, as anticipated. Apart from this, there is no discernible difference in the electrochemical signal obtained, thereby validating that fully functional three-electrode systems can be produced using this “Lego-brick” approach.

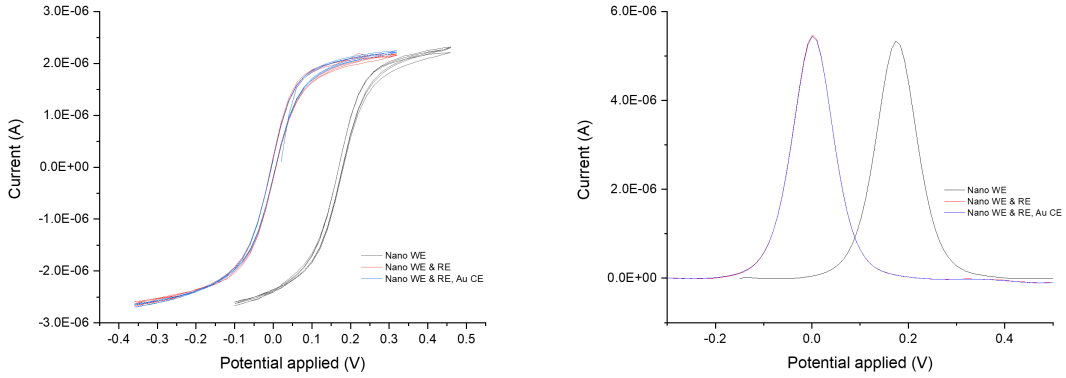


Figure 5.9: Electrochemical responses of the three electrode systems put together in the Lego brick design. (A) Overlayed cyclic voltammogramms and square wave voltammograms (SWV) of the completed three electrode device using the sputtered working nanoband electrode with an external Pt wire as a counter electrode (CE) and a comercial double junction Ag/AgCl reference electrode (RE), at a scan rate of $10mV/s$, in a solution of $5mM$ potassium ferricyanide and $5mM$ potassium ferrocyanide in $1xPBS$. In (B) the potential vs ΔI transients were recorded from $-0.15V to +0.6V$ vs the open circuit potential with a $9mV$ step, a modulation amplitude of $20mV$ and a frequency of $2.5Hz$.

5.1.4 DNA Detection

To assess the sensing performance of the electrodes, they were functionalised with an ssDNA probe to detect a DNA sequence specific for SARS-CoV-2. It is important to emphasise that this was a proof-of-concept experiment to establish the performance of the nanoband electrodes and to compare them with existing commercial electrodes. As such, it was considered appropriate to detect a synthetic complementary DNA sequence rather than RNA from real samples, and the authors wish to emphasise that no claim is made that an amplification-free SARS-CoV-2 sensor has been developed. The operation of the sensor is shown schematically in Figure 5.10.

First, the electrochemical response of a clean (bare) electrode was measured in a solution of $5\times10^{-3}MK[Fe(CN)_6]^{3-}$ and $5\times10^{-3}MK[Fe(CN)6]^{4-}$ in 1 × phosphate-buffered saline (PBS) containing $10\times10^{-3}MMgCl2$. The electrodes were then functionalised by the spontaneous formation of a mixed self-assembled monolayer from an aqueous solution containing 6-mercaptohexan-1-ol and a thiol-C6-modified ssDNA probe. This process takes at least 2 h on macroscopic electrodes, but was possible in less than 2 min on the nanoband electrodes. This is in agreement with previous publications and further demonstrates the nanoscale properties of these electrodes[148] When the electrodes were returned to the redox agent solution and the electrochemistry was measured again, there was a marked decrease in the limiting current, Figure 5.10. This is because charge transfer at the electrode is hindered by the steric blocking of the redox molecules by the SAM film, as well as the electrostatic repulsion of the anionic Fe species by the negatively charged phosphate backbone of the DNA.

The DNA probe was a thiol tagged primer approved by the Centre for Disease Control (CDC) for the detection of SARS-CoV-2. The sequences were ordered from Merck (Spain) and were as follows:

Probe 5´- ACCCCGCATTACGTTTGGTGGACC-(C6SH) - 3'

Target 5´- GGTCCACCAAACGTAATGCGGGGT - 3'

The electrodes were placed in an aqueous solution containing $30\times10^{-6}M$ 6-mercaptohexanol (MCH), $150\times10^{-6}M$ TCEP, and $1.5\times10^{-6}M$ of the probe DNA. The macroelectrodes were left in this solution for the self-assembled monolayer to form for 2 h, whereas the nanoelectrodes were left for 2 min, prior to rinsing with a stream of water to remove physisorbed thiols.

Before and after probe film formation, the electrodes were placed in a solution of 1x PBS with $10\times10^{-3}MMgCl_2$, $5\times10^{-3}M$ potassium hexacyanoferrate (III) and $5\times10^{-3}M$ potassium hexacyanoferrate (II). CVs were run between -0.1 and +0.45 V versus a Ag/AgCl reference electrode (macro) or Au pseudoreference electrode (nano) and Pt wire counter electrode, at a scan rate of $10mV/s$, for a total of four cycles. The square wave voltammetry was run in the same set up immediately after the CVs from -0.15 to +0.6 V versus the open circuit potential with a 9 mV step, a modulation amplitude of 20 mV, and a frequency of $2.5Hz$.

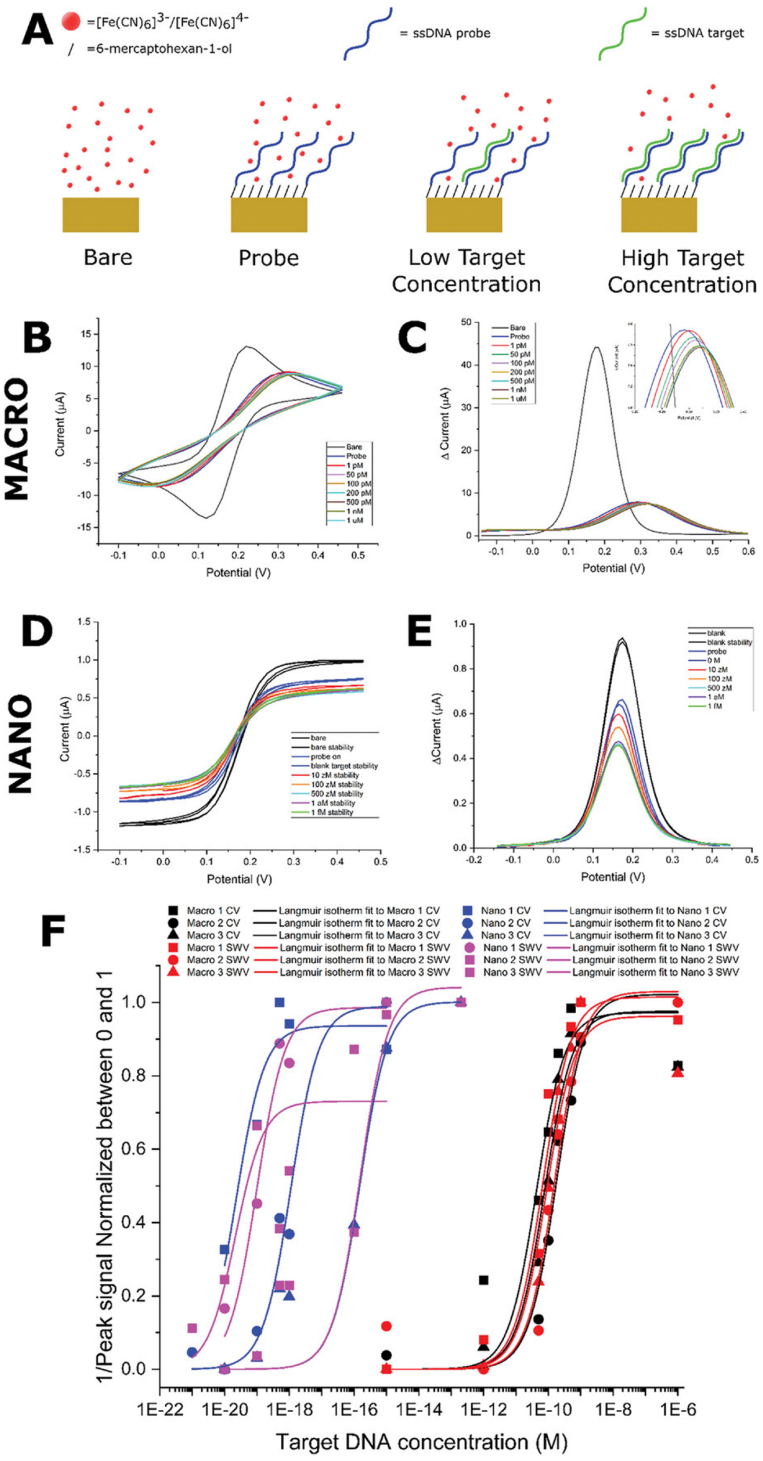


Figure 5.10: A) Schematic illustration of how the DNA sensing mechanism works. B) Overlayed CVs of the DNA sensing system response to different target DNA concentrations on a macroelectrode. Overlayed with Square Wave Voltammetry (SWV) data from the experiments, shown in (C). The results of the same experiment, with lower DNA target concentrations on nanoband electrodes are shown in (D) and (E). F) The calibration curves from the macro and nanoelectrode repeats with corresponding fits to the Langmuir isotherm.

After the probe film was formed the functionalized electrodes were placed in solutions containing increasing concentrations of DNA target, for 20 min each. Between target incubations, the electrodes were placed in the measurement solution, left for 20 min, and the electrochemical measurements were repeated. The DNA target concentrations tested were differed for the macro and nanoelectrodes. For the macroelectrodes, the target DNA concentrations tested were: $0M$, $1 \times 10^{-15}M$, $1 \times 10^{-12}M$, $500 \times 10^{-12}M$, $1 \times 110^{-9}M$, $500 \times 10^{-9}M$, and $1 \times 10^{-6}M$. For the nanoelectrodes, the target concentrations tested were $0M$, $10 \times 10^{-21}M$, $100 \times 10^{-21}M$, $500 \times 10^{-21}M$, $1 \times 10^{-18}M$, and $1 \times 10^{-15}M$.

A control experiment was performed to assess the stability of the SAM over the time scale of an assay, Figure 5.11, in which the functionalised nanobands were immersed in solutions of DNA-free water. In the main experiment, the functionalised electrodes were first placed in a solution of deionised water and then left in the measurement solution for 20 min to ensure that the probe monolayer was also stable. It was then placed sequentially in solutions containing increasing concentrations of target DNA before being rinsed with and measured in the measurement solution. Washing was important to remove any non-specifically bound DNA from the surface. As the target DNA sequence binds to the probe layer, it further impedes charge transfer at the electrode surface, causing a decrease in current that is proportional to the amount of target DNA bound to the surface.

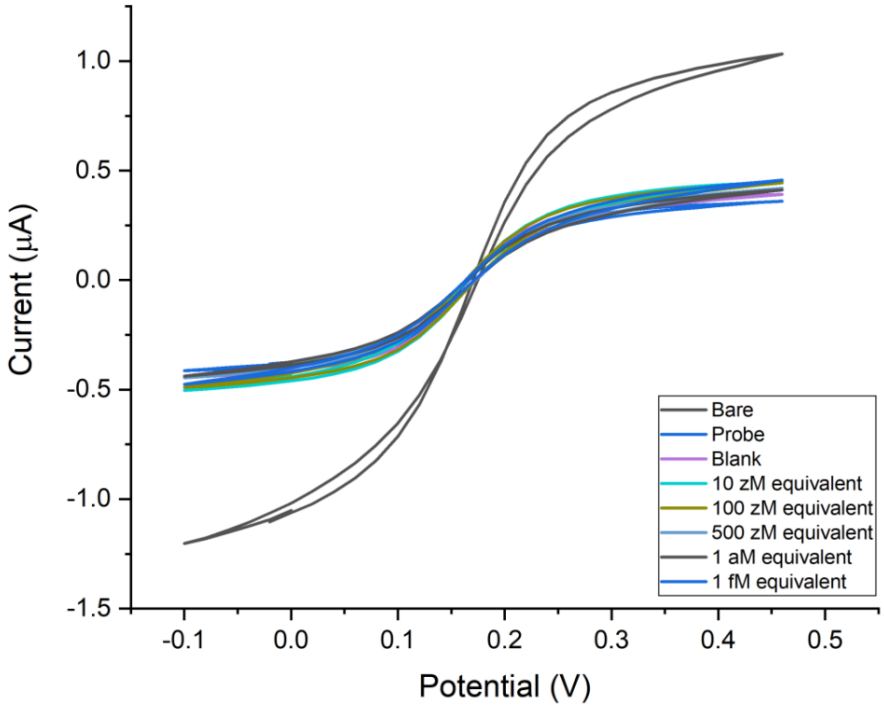


Figure 5.11: Cyclic voltammetry of a bare nanoband electrode, functionalized with the DNA probe sensing film, that was exposed to ultrapure DNA free water rather than different DNA target concentrations.

5.1.5 Nanoband Electrodes in combination with NFC

Taking advantage of the possibility of realising nanoband electrodes with the 2D concept, where all the electrodes are on a piece of Kapton, the possibility of realising a miniaturised device was evaluated. The NFC potentiostat SIC4341, described in detail in chapter two, was used for this purpose. The nanoband was attached to the PCB antenna using 3M anisotropic conductive tape. The result of the device is shown at the top of Figure 5.12. As a quick functional test of this device, measurements of $5 \times 10^{-3} MK[Fe(CN)_6]^{3-}$ and $5 \times 10^{-3} MK[Fe(CN)6]^{4-}$ in 1 × phosphate buffered saline (PBS) and half concentration were performed. Screenshots of the measurements obtained are shown at the bottom of Figure 5.12. It can be observed that the distinctive waveform of the nanoelectrodes has been achieved, and that the steady-state current of the second measurement is approximately half that of the first.

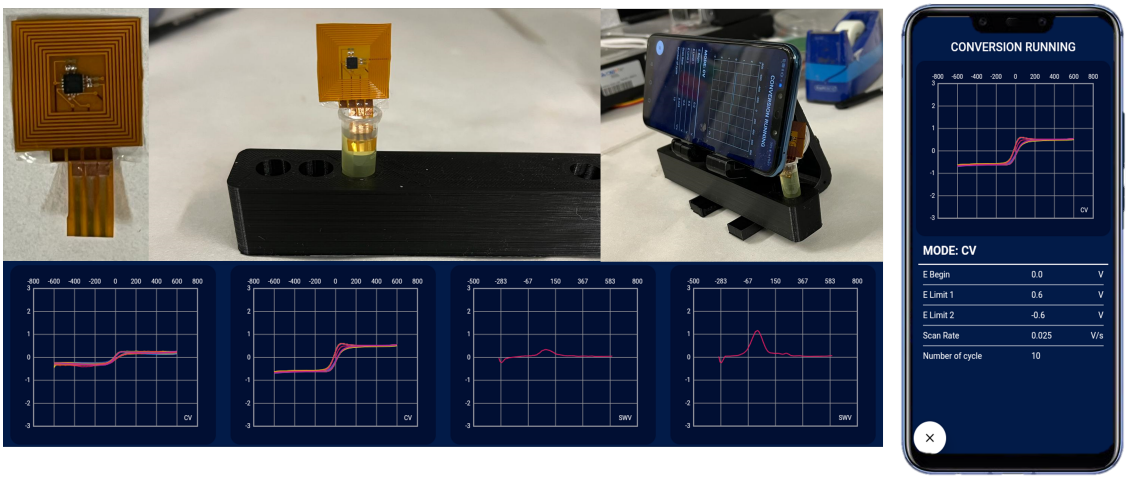


Figure 5.12: Top: Device obtained by combining the nanoband and the SIC4341 potentiostat with the PBC antenna. Bottom: Ferro/ferricyanide measurements at 5mM and 2.5mM.

5.2 Laser-induced Graphene Electrodes

The advent of graphene, a single layer of carbon atoms arranged in a two-dimensional honeycomb lattice, has revolutionised the field of materials science and opened up new avenues in various applications, including biosensors. Graphene's exceptional properties, such as high electrical conductivity, large surface area, excellent mechanical strength and unique optical properties, make it an ideal material for biosensor applications[149–152].

One of the most promising methods for producing graphene is laser-induced graphene (LIG) synthesis. In this technique, a laser is used to convert certain types of carbon precursors, such as polyimide sheets, into graphene. The LIG method offers several advantages over traditional graphene production methods. It allows graphene patterns to be written directly onto substrates, eliminating the need for post-processing steps such as lithography or etching[153]. In addition, the LIG method can produce porous graphene structures, which are particularly useful for biosensing applications due to their large surface area[16, 154].

In this section, we focus on the study of laser-induced graphene electrodes (LIGEs) and their application in biosensors in addition to the production methods, properties and performance. As a case study we will show the development of novel Prussian-blue (PB)-infused Catalytic Hetero-Interface Architecture (PB-CHIA) using poly(3,4-Ethylenedioxythiophene) (PEDOT) and gelatin for biosensing applications targeting non-invasive diabetes management through urine glucose analysis.

5.2.1 Fabrication and Characteristics

The fabrication of LIGEs involves a series of well defined steps, each contributing to the final properties of the electrodes. The process begins with the placement of a $40x110$ Kapton substrate on the laser machine. The working electrode surface ($\phi : 3mm$), neck ($1x2mm$ or $1x6mm$ or $1x12mm$), and counter electrode ($\phi : 1.5$ and $2.5mm$ with $1mm$ width) are then created on the Kapton in engrave mode. The laser settings for the working electrode surface are set to 30%-45%-60% power with a speed of 80%, while for the working electrode neck and counter electrode part, 30% power and 80% speed are used.

Following the laser engraving, the substrate undergoes a 2-minute plasma treatment to clean and activate the surface. Subsequently, the PCB printer is employed to draw the reference electrode using Ag/AgCl ink and the contacts using Ag ink, in order to facilitate connections with the NFC potentiostat, in accordance with the following drawing (Figure 5.13). After each ink application, the substrate is heated in an oven at $180 \circ C$ for 15 minutes to cure the ink.

Next, a line is drawn with dielectric ink, and the substrate undergoes another heat treatment ($180 \circ C$ for 15). The rectangular-shaped line is manually filled with varnish, and the substrate is left in the fume hood for one day to allow the varnish to dry. Three hours before the modification of the working electrode surface with Prussian-blue (PB)-infused Catalytic Hetero-Interface

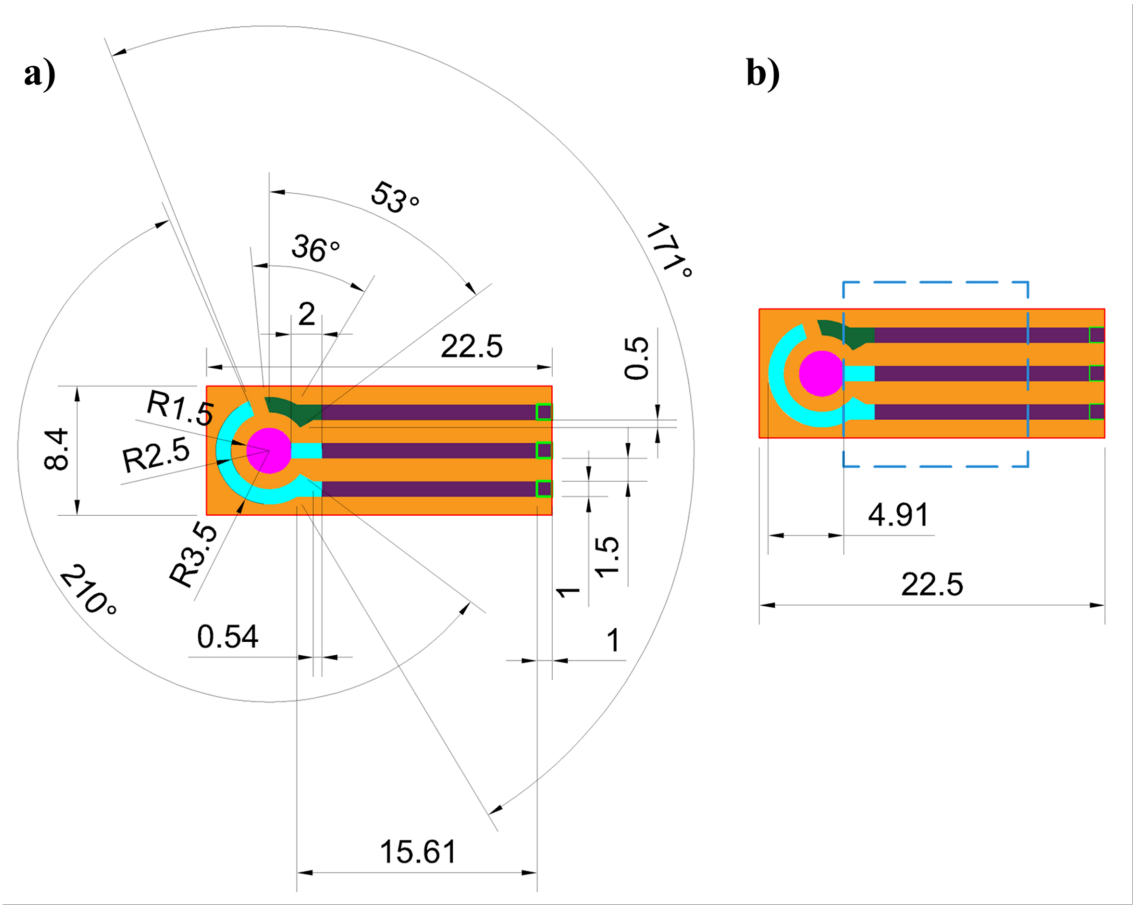


Figure 5.13: Dimensions of the three-electrode compartment on Polyimide substrate. a) Cutting edges (red), working electrode (pink), counter electrode and neck (cyan), Ag/AgCl ink (dark green), and Ag ink-made tracks (violet). b) Dashed blue line indicates the region to be covered with dielectric material. Dimensions expressed in [mm].

Architecture (PB-CHIA), a 6-minute plasma treatment is applied to the platform. The synthesis involves a water-processable interactive polymerization of PB and PEDOT, facilitated by gelatin, forming an intertwined structure. Gelatin acts as a polycationic soft template, ensuring homogeneous polymerization reactions by dispersing water-insoluble EDOT and initiating PB nucleation.

5.2.2 Characterization

Figs. 5.14 presents a comprehensive analysis of bare and PB-CHIA modified LIG-based working electrodes fabricated at different power levels and neck sizes. The SEM images (Figure 5.14a) and CV redox curves (Figs. 5.14b-5.14c) show distinct characteristics of these electrodes in PBS and ferric solutions. EIS plots (Figure 5.14d) and amperometric responses to H_2O_2 (Figure 5.14e) further elucidate their electrochemical behaviour.

A decrease in neck length from 12 to 2 mm results in a decrease in ΔE_{a-c} values and an

increase in ΔI_{a-c} values, indicating improved reaction kinetics. This is supported by the reduced equivalent series resistance (ESR) values and more pronounced capacitive CV redox curves observed in PBS.

Maintaining a constant neck length of 2 mm and reducing the power level of the working electrode surface results in a decrease in ΔI_{a-c} values and slight oscillations in ΔE_{a-c} values. This suggests that the neck length introduces an internal resistance to the electrochemical system, with further extension leading to increased system resistance. When modified with $(PEDOT:PB)G1:4$, the platforms exhibit distinct Prussian Blue E_{PB} and Prussian White E_{PW} peaks in PBS. Charge density values change proportionally with ΔI_{PB-PW} and inversely with ESR values, indicating a decrease in ΔI_{a-c} in ferric solution.

Our results show that an engraving power of 60% is optimal for working electrodes with the shortest neck $2-LIG_{\%60}$, resulting in a sensitivity to H_2O_2 of $433.330 \mu A\ mM^{-1}\ cm^{-2}$, exceeding that $2-LIG_{\%45}$ and $2-LIG_{\%30}$. The shortest neck platform produces faster responses and higher current levels than the longer neck working electrode. The use of $2-LIG_{\%60}$ as the working electrode substrate instead of commercial glassy carbon electrode has significantly improved the linear range and sensitivity of the electroanalytical performance of the PB-CHIA. This improvement is attributed to the nanofibrous fringes acting as nanoelectrodes, which enhance the charge transfer between the solid-liquid interface by increasing the film porosity and the contact area between the polymer composite and the working electrode surface (Figure 5.14g).

In summary, the length and degree of engraving of the working electrode neck have a significant effect on sensor performance. Shorter neck lengths and higher engraving levels result in improved reaction kinetics and higher sensitivity. These results highlight the potential of LIGEs in the development of efficient and sensitive biosensors.

5.2.3 Microfluidic cell with LIG-Electrodes and NFC

As is shown in Figure 5.15, the $2-LIG_{\%60}$-based biosensor was integrated into a fluidic cell and calibrated with glucose additions. The fluidic cell-based biosensor (LIG-FFC) operated in batch flow injection mode has a wider linear range, $10-400 \mu M$, compared to the GC electrode-based biosensor. The sensitivity was $29.88 \pm 4.98\ \mu A\ mM^{-1}\ cm^{-2}$, with a LOD of $4.52 \pm 2.24 \mu M$. The engraved electrode surface with nano-fringe multi-electrodes increased the total active area and electron transfer pathways, thereby improving the working range for glucose detection. Next, The LIG-FFC-based sensor quantified glucose levels in synthetic urine using batch injection mode and intermittent washing with blank PBS after each measurement to simulate real-life scenarios. For $20-100 \mu M$ glucose, the sensor exhibited recoveries ranging from 91.78% to 125.33% and 90.34% to 115.60%, respectively, with an relative standard deviation (RSD) in the range of $0.95-15.30\%$ and $0.84-9.33\%$. This suggests that the use of $1:20$ diluted urine with PBS allows the sensor to be used in batch mode throughout the day for glucose detection.

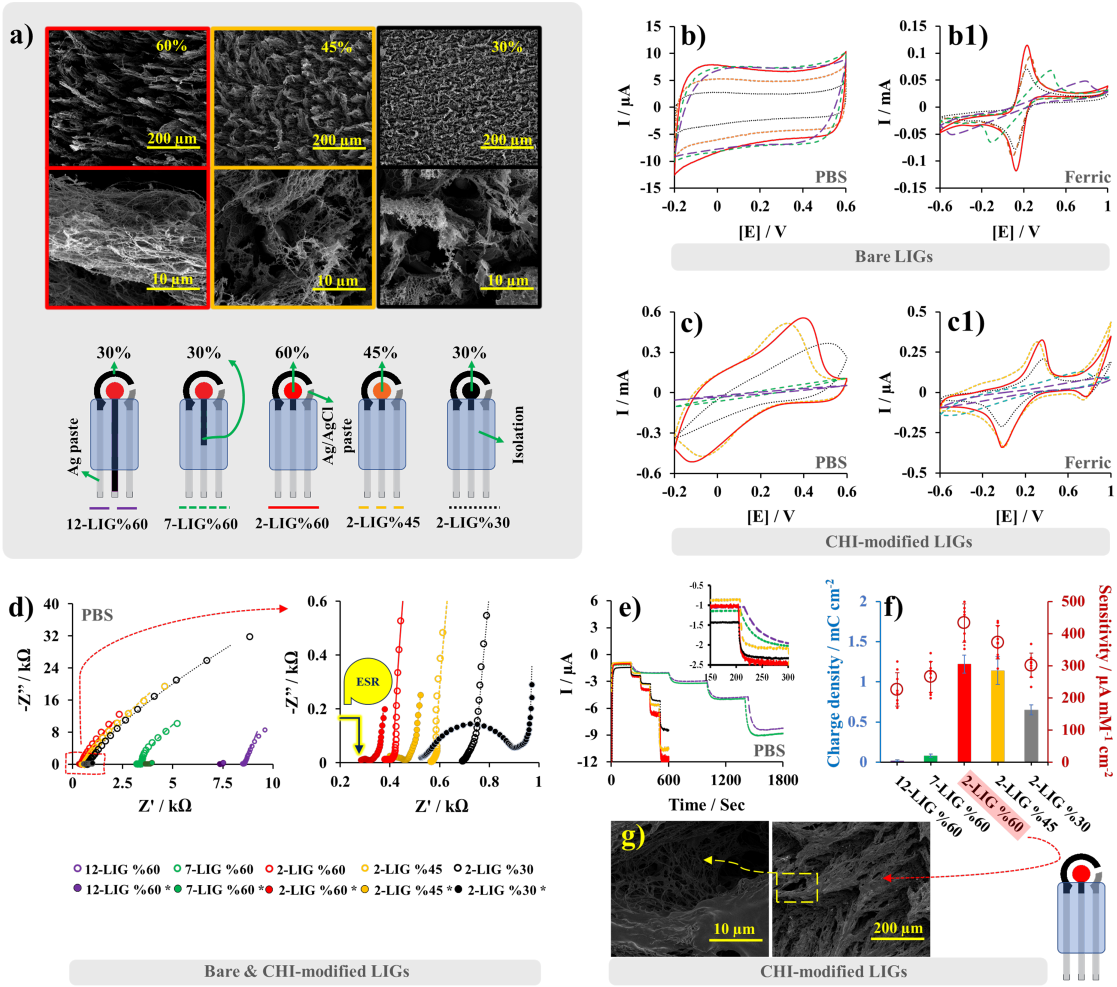


Figure 5.14: Optimal LIG-based three-electrode platform selection. a) Various bare LIG designs, b) their CV-redox signals in PBS and b1) in ferric solution, c) PB-CHIA-modified LIGs' CV-redox signals in PBS and c1) in ferric solution. d) EIS assays of bare and PB-CHIA-modified LIGs (LIG*) in PBS. e) Amperometric response of PB-CHIA-modified LIGs to H2O2 and f) corresponding charge density and sensitivity values. g) Surface morphology of $2-LIG_{\%60}$.

Having fabricated the fluidic cell and NFC potentiostat using automated techniques, we validated their electroanalytical performance. Integration with an NFC potentiostat enabled real-time smartphone glucose monitoring. The single-chip potentiostat, equipped with an integrated antenna for power supply and NFC transmission, supports various electrochemical techniques. The sensor responds linearly to glucose concentrations in the range $10-400\mu M$, with a calculated LOD of approximately $4.5\mu M$. When these values are adjusted for the dilution factor, the sensor consistently provides glucose readings in the $200-8x10^3\mu M$ range, which covers the medical normal of $0-0.25\ mg\ dL^{-1}$ ($0-1.4x103^3\mu M$) and higher glucose concentrations in urine. The glucose concentration in the sample was determined from the difference between the blank and reduction amperometric peak currents and the calibration curve.

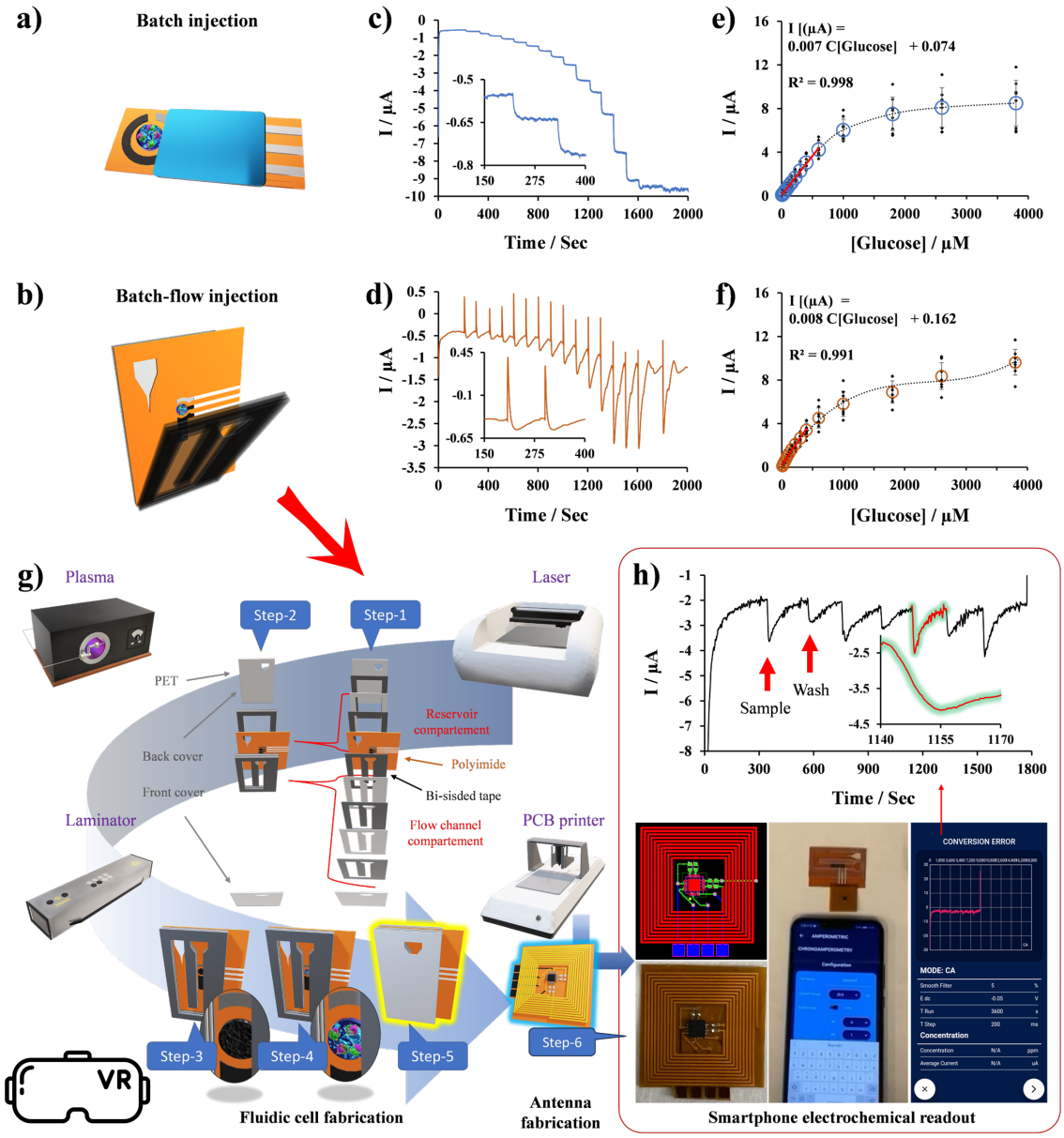


Figure 5.15: Quantification of LIG-F-based three-electrode platform and the fluidic cell. Prototype fabrication and validation. (a-b) LIG-F-based platform [LIG-F/(PEDOT:PB)G-GOx] and fluidic cell [LIG-FFC/(PEDOT:PB)G-GOx], (c-d) amperometric responses to successive glucose injections (Inset: magnified view of the first two injections, $10\mu M$ and $20\mu M$), and (e-f) corresponding calibration plots between $10\mu M$ and $4000\mu M$ glucose. g) Fabrication of fluidic cell and h) assembly of the NFC potentiostat read mode with a smartphone and its real-time glucose readout (inset curve showing amperometric signals of the four consecutive additions of the same sample containing glucose and intermittent rinsing with PBS) in synthetic urine-spiked samples.https://youtu.be/fIgEifUkSXE

The prototype, operating in batch-flow injection mode, accurately detected $200\mu M$ glucose in a $1:20$ diluted synthetic urine sample, demonstrating practicality, week-long stability and superior quantitative capabilities.

The potentiostat, embedded in a single chip, provides power and NFC transmission for electrochemical readouts, enabling fast glucose measurements. The fluidic cell holds $50\mu L$ of sample for each reading and can be re-used for up to a week with the recommended buffer solution.

Our proposed sensor system aligns electroanalytical performance with reported sensor electrodes and PoC devices, and stands out as a fully integrated, battery-free, wireless smartphone electrochemical readout for urine glucose self-monitoring. Following clinical validation, this cost-effective and environmentally friendly PoC solution has significant commercialisation potential, making it particularly suitable for SMUG approaches.

5.3 PCB-Electrodes

5.3.1 PCB: Introduction

PCB technology offers a viable alternative for sensor development[155–160]. This technology, which is a cost-effective method of creating electronic circuits, has become increasingly accessible due to the significant expansion of the electronics industry in recent years. PCB technologies allow the precise patterning of conductive electrodes that can serve as the basis for sensors. Despite the similarities between PCB technology and microfabrication processes, PCB offers a more affordable and widely available manufacturing solution[161–163].

This section explores the application of PCB technology in the creation of electrochemical sensors and compact sensing platforms. Albert Hanson and Thomas Edison were pioneers in the development of the first PCBs in the early 20th century, laying the foundation for a technology that would become an integral part of the electronics industry. The early designs, although rudimentary, laid the foundation for the evolution of PCBs[164]. From the 1900s to the 1940s, progress was slow, and PCBs were limited to single-sided use. The U.S. Army's use of PCBs for proximity fuses during World War II was a significant advancement in the field. This technology was made available to the public after the war.

In the 1950s, through-hole technology emerged as the preferred method for mounting electronic components onto PCBs, involving the insertion of component leads into drilled holes and soldering them from the underside of the board. The introduction of surface-mount technology (SMT) in the 1980s revolutionised PCB manufacturing, leading to a significant decrease in size, cost, and complexity. SMT eliminated the need for drilling holes, allowing for a higher component density and the possibility of placing components on both sides of the board. Surface Mount Technology (SMT) is the dominant manufacturing technology for PCBs, providing precise control over trace impedance and electromagnetic interference, making it ideal for high-speed electronics[165].

Although through-hole technology is still used for simpler boards and hand-soldering applications due to its larger size, the accessibility of computer-aided design (CAD) software has enabled anyone to design a PCB and have it manufactured, thus further democratizing the field. The historical perspective confidently underscores the potential of PCB technology in the development of electrochemical biosensors.

5.3.2 PCB: Fabrication

FR4 (Flame Retardant 4), the most commonly used substrate for PCBs, is a class of materials that comply with the requirements of the National Electrical Manufacturers Association Industrial Thermosetting Products (NEMA LI 1-1998). FR4 is a composite of woven fiberglass cloth and an epoxy resin binder that is flame-resistant. It has near-zero water absorption, an outstanding strength-to-weight ratio, and serves as an excellent insulator, regardless of ambient moisture

levels. No new content has been added. Bromine is typically used as the flame-resistant material in FR4. FR4 is the ideal substrate due to its ease of manufacture, cost-effectiveness, and excellent properties.

Polyimide laminates outperform FR4 in several aspects, such as temperature performance, electrical performance, survivability, and expansion resistance. Although the manufacturing cost of polyimides is higher than that of FR4, the superior performance justifies the investment. Teflon laminates offer the best electrical properties, surpassing both FR4 and polyimide-based substrates. However, their production is significantly more expensive and requires specialized equipment and a highly skilled workforce. Teflon laminates can be coated onto glass fabric or manufactured as an unsupported mesh, providing a level of versatility that surpasses both FR4 and polyimide[166].

The PCB fabrication process, which is detailed below, is well documented on the websites of PCB manufacturers such as PCBWay or Sierra Circuits [167, 168]. The multi-layer manufacturing process commences with the creation of a computer-aided design (CAD), which is sent to the selected manufacturer. The manufacturer verifies the compatibility of the CAD with their equipment. A photographic image of the CAD is printed on film, and the image is transferred to the board surface using photosensitive dry-film and ultraviolet light in a cleanroom. The photographic film is removed, and excess copper is etched from the board. The inner layers receive an oxide layer application and are then stacked with prepreg, which provides insulation between layers. Copper foil is added to the top and bottom of the newly created stack. The oxide layer, a chemical composition consisting of compounds such as sodium chlorite ($NaClO_2$), water, and sodium hydroxide, strengthens the laminate bond by increasing the roughness of clad copper. The internal layers are laminated by subjecting them to extreme pressure and high temperature. The pressure is gradually released, and the PCB cures while still at a high temperature. Holes are drilled to secure the stack, and excess copper is filed off. A chemical is used to fuse all the layers of the board together, and then the board is cleaned. After cleaning, a series of chemicals bathe the board, resulting in a layer of copper weighing 1 oz/ft^2 (305.152 g/m^2), which results in a thickness of 1.4mil (35μm), filling in the drill holes and settling on the top layer. The convention in the PCB industry is to use imperial units such as oz, mil, oz/ft^2 over metric units. In addition, oz is often used over oz/ft^2 to refer to copper weight spread evenly over 1 ft^2 (305.152 g/m^2) PCB area to determine the copper layer thickness. The board receives a photoresist application, but only on the outer layers. After the photoresist application, the outer layers are plated in the same way as the inner layers were, but a plating of tin is applied to protect the outer-layer copper from etching. Etching takes place on the outer layers, and excess copper is removed via a copper etchant, with the tin safeguarding the remaining copper. The panels are cleaned and prepared for a solder mask.

Following the cleaning process, ink epoxy and solder mask film are applied to the boards. These boards are then exposed to ultraviolet light, which delineates a specific area of the solder

mask for removal. The board is subsequently baked, allowing the solder mask to cure. The board is then plated with gold, silver, or hot air solder level (HASL), which facilitates the soldering of components to the pads and protects the copper. This plating process is known as electroless nickel immersion gold (ENIG). A layer of nickel is applied to the copper, serving as a diffusion barrier. A thin layer of gold follows the nickel layer, preventing nickel oxidation and maintaining a solid surface for soldering.

After the application of gold or silver plating, the board undergoes silk-screening, receiving essential information such as warning labels and company ID numbers. The board is then tested and cut to meet design specifications. The finishes applied to the board surface serve to protect exposed copper and provide solderable surfaces. Historically, HASL has been the most common finish in the industry due to its low cost and wide availability. The PCBs are immersed in a molten mixture of tin/lead, and excess solder is removed by blowing hot air across the board's surface.

However, the use of ENIG has been on the rise. In this process, a layer of nickel, which provides a barrier for the copper and serves as the solderable surface, is formed. Gold is then used to protect the nickel and provides the low contact resistance necessary for the thin gold deposits.

Electroless nickel electroless palladium immersion gold (ENEPIG), a relatively recent development, has seen increasing usage despite its high cost due to its reliance on palladium. ENEPIG is significantly more resistant to corrosion compared to ENIG and HASL, thereby extending the lifespan of the PCB. Across all measurable categories, ENEPIG outperforms HASL and ENIG, but it is also noticeably more expensive.

Another notable finish is the hard electrolytic gold finish, which consists of a layer of gold plated over a coat of nickel. Hard gold is highly durable and is used on boards that experience high wear. Hard electrolytic gold is similar to ENIG, but the hard gold layer is generally two to three times as thick ($0.005 - 0.010\ mil$ or $0.127 - 0.254\ \mu m$). For high-wear areas of the board that use hard gold as a protective layer, the gold can be as thick as 1 mil ($25.4\mu m$), making hard electrolytic gold plating a costly option.

5.3.3 PCB: Flexible

As the technology of PCBs has advanced, several key features have seen significant improvements. These include the number of conducting layers, minimum trace spacing, and minimum trace width. Some manufacturers are able to produce PCBs with up to 60 layers. The trace width and spacing are directly related to the weight of the copper plating the board. For instance, with only 0.5 oz (14.17 g) of copper on the inner layers, the trace width can be reduced to 3 mil ($76.2\mu m$). A 1 oz (28.35 g) copper deposit on the outer layers will yield the same 3 mil ($76.2\mu m$) trace width. The distance between traces is typically identical to the width for most manufacturers.

In many applications, there is a need for cyclic movement or stretching while maintaining an

electrical connection. Flexible PCBs (fPCBs) have evolved to meet this need and find applications in a variety of devices, from laptops and smartphones to engine management units and hard drives. For example, fPCBs are used in laptops to ensure the connection between the computer and monitor remains intact, given that a laptop may be folded thousands of times over its lifetime. Hard drives, which need to withstand high temperatures and transfer data quickly, also utilize fPCBs. Furthermore, fPCBs can be used as sensors in automobiles or for general purposes.

Flexible PCBs first emerged in the early 2000s, with polydimethylsiloxane (PDMS) being the most common substrate. However, the most popular substrate materials have since become polyimide film, polyester film, and polyethylene naphthalate (PEN). Polyimide film is favored due to its excellent thermal resistance capabilities and superior mechanical and electrical properties. Despite its susceptibility to high humidity absorption and tearing, some variants of polyimide film have improved these aspects. PEN, on the other hand, offers a more economical alternative with adequate performance for most applications, and its popularity is increasing each year.

For PEN the smallest boards can be as thin as 4 mil (101.6μm), while for polyimide film can be as thin as 1 mil (25.4μm). Trace width on a flexible PCB can be as low as 3 mil (76.2μm) and spacing also as low as 3 mil (76.2μm). The lowest weight of copper is 0.25 oz (7.09 g), but it can range up to 2.5 oz (70.9 g). Flex circuits can have multiple layers, with most manufacturers offering up to 16 layers.

5.3.4 PCB - Electrodes Fabrication

In the realm of PCB fabrication, copper is the predominant choice for creating traces and electrical contacts. However, its propensity for oxidation poses a significant limitation for its use in the development of electrochemical sensors. This hurdle can be surmounted by depositing a thin layer of inert metals like gold (Au) or platinum (Pt) onto the PCB pads.

Cyclic voltammetry analyses conducted on bare copper PCB-electrodes yield non-characteristic voltammograms due to copper's ease of oxidation. Conversely, the use of Au-plated PCB-electrodes leads to stable voltammograms with a broad potential window, making them suitable for electrochemical biosensing applications.

Various methods such as electroless plating, electrodeposition, and sputtering can be employed to deposit gold onto PCB-electrodes. PCB manufacturing services offer a range of surface finishes as part of their standard fabrication process, with Electroless Nickel Immersion Gold (ENIG) coating being the most popular. However, these coatings primarily aim to enhance the solderability and longevity of PCB boards, and may leave copper exposed at the pad edges. In contrast, electrodeposition of hard Au or Pt can lead to fully coated electrodes with increased surface roughness, thereby augmenting the electrode's effective surface area.

Taking all of the above into account, for this thesis we developed 2 types of PCB-electrodes, both flexible, made on polyimide, but varying the thickness of the polyimide and the thickness of the copper. One batch of electrodes was fabricated on 0.2mm thick polyimide with 1 oz (34.8μm)

copper and a 3 mil (76.2μm) ENIG finish. The other batch was fabricated on 0.1 mm thick polyimide with 0.5 oz copper (17.4μm) and a 3 mil (76.2μm) ENIG finish. The PCBs were designed using the Altium Designer Summer 09 tool (Figure 5.16) and sent for manufacturing to the Chinese company PCBWay.

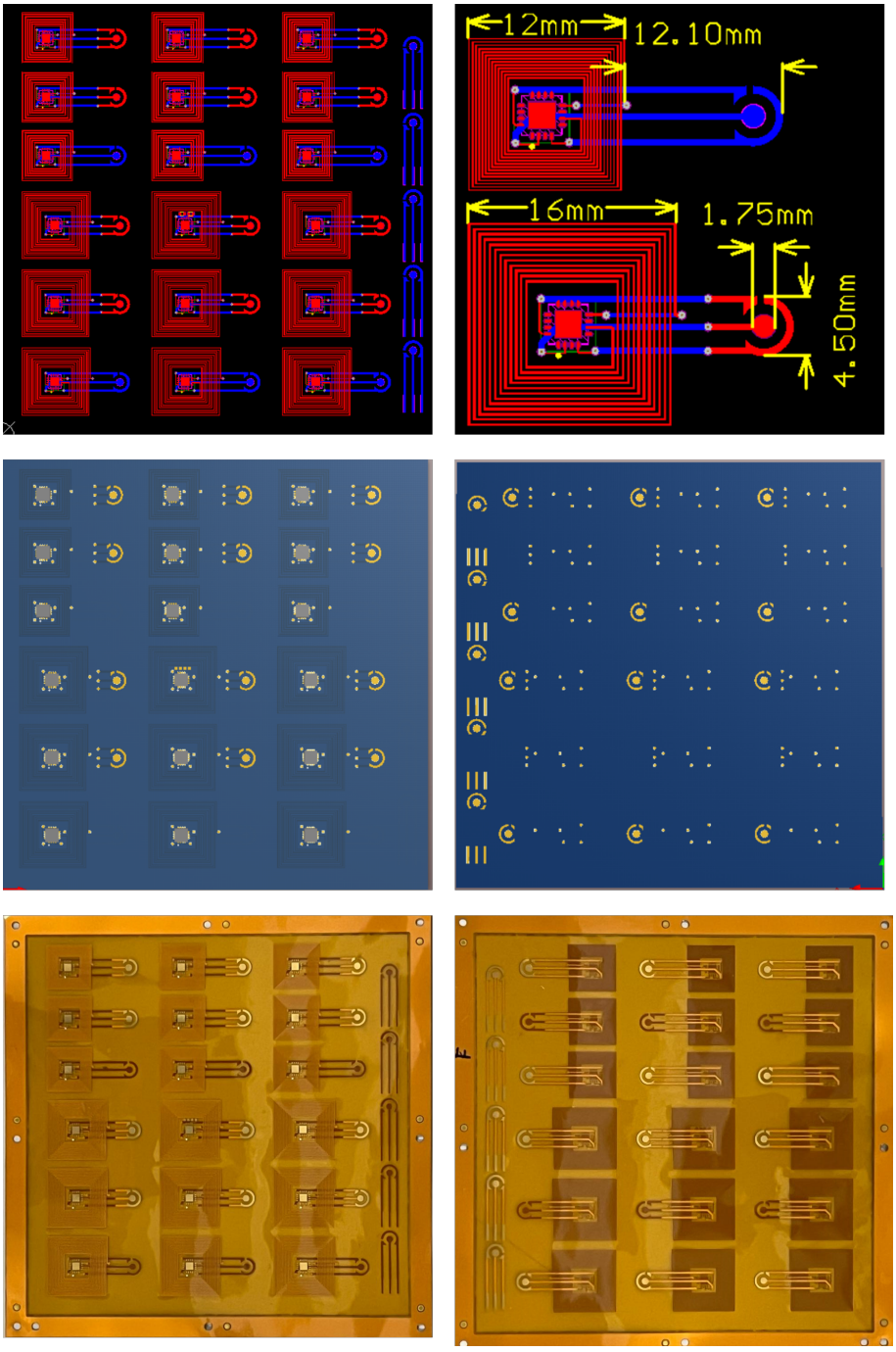


Figure 5.16: TOP: 2D view of the electrodes designed using Altium Designer Summer 09 and the dimensions of the most representative values of the design. Middle: 2D view of the electrodes designed in Altium Designer Summer 09 for both the top and bottom layers. Bottom: real images of the resulting flexible PBCs manufactured in polyamide. Note how the electrodes and pads are plated with gold.

5.3.5 Cleaning and Characterization

In electrochemical studies, gold electrodes are often chosen for their excellent conductivity, chemical stability and wide potential window. However, the surface of gold electrodes can be easily contaminated by organic and inorganic impurities, which can significantly affect the accuracy of electrochemical measurements. It is therefore essential to clean the electrode surface before use. A common cleaning method is electrochemical cleaning using cyclic voltammetry (CV) in a sulfuric acid solution. This oxidation-reduction process can effectively remove contaminants from the electrode surface.

The reason why sulfuric acid is often used for this process is that it is a strong acid that can effectively clean the electrode surface without damaging the gold. In addition, the CV process in sulfuric acid can produce well-defined peaks corresponding to the formation and reduction of gold oxide, which can be used to confirm the cleanliness of the electrode surface. However, this cleaning method is not recommended for PCB-electrodes. The PCB material can be damaged by strong acids such as sulfuric acid, leading to the degradation of the electrode and potentially the entire PCB[158]. In addition, the thin conductive coating on PCB-electrodes can be easily damaged or removed by the strong oxidation-reduction reactions that occur during the CV process.

It is therefore generally recommended that milder cleaning methods be used for PCB-electrodes, such as solvent rinsing or gentle physical cleaning. It's also important to handle PCB-electrodes carefully to avoid damaging the conductive coating. To illustrate the above concept, a pair of PCB-electrodes were subjected to a cleaning process using sulfuric acid. As described in the previous section, two variants of electrodes were prepared, differing in their copper thickness - one of $17.4\mu m$ and the other of $34.8\mu m$. The voltammograms obtained are shown in Figure 5.17.

A clear observation from the voltammograms is that the double thickness electrode shows a current increase by a factor of two. This observation is consistent with the theoretical understanding that the copper determines the series resistance of our electrode. When the thickness is doubled, the resistance is halved and, according to Ohm's law, the current is doubled. It is worth noting that the high value of the current, combined with the sulfuric acid, caused the gold to be stripped from both the counter electrode and the working electrode - the electrodes through which the current flows. This resulted in the complete destruction of these electrodes.

To further elucidate the effect of the cleaning process on the electrodes, a comparative analysis was carried out between a clean electrode that withstood the cleaning process and two uncleaned electrodes. The characterisation was performed using FerroFerricyanide at varying concentrations of $5mM$, $2.5mM$, and $1.25mM$. Cyclic voltammetry was performed at five different scan rates: 0.0025 V/s, 0.005 V/s, 0.075 V/s, 0.01 V/s and 0.0125 V/s. The results for each electrode are summarised in Tables 5.1, 5.2 and 5.3. The corresponding voltammograms are shown in Figure 5.18, Figure 5.19 and Figure 5.20.A noteworthy observation from the data is the linear relationship between the current peaks and the square root of the scan rate, which is a

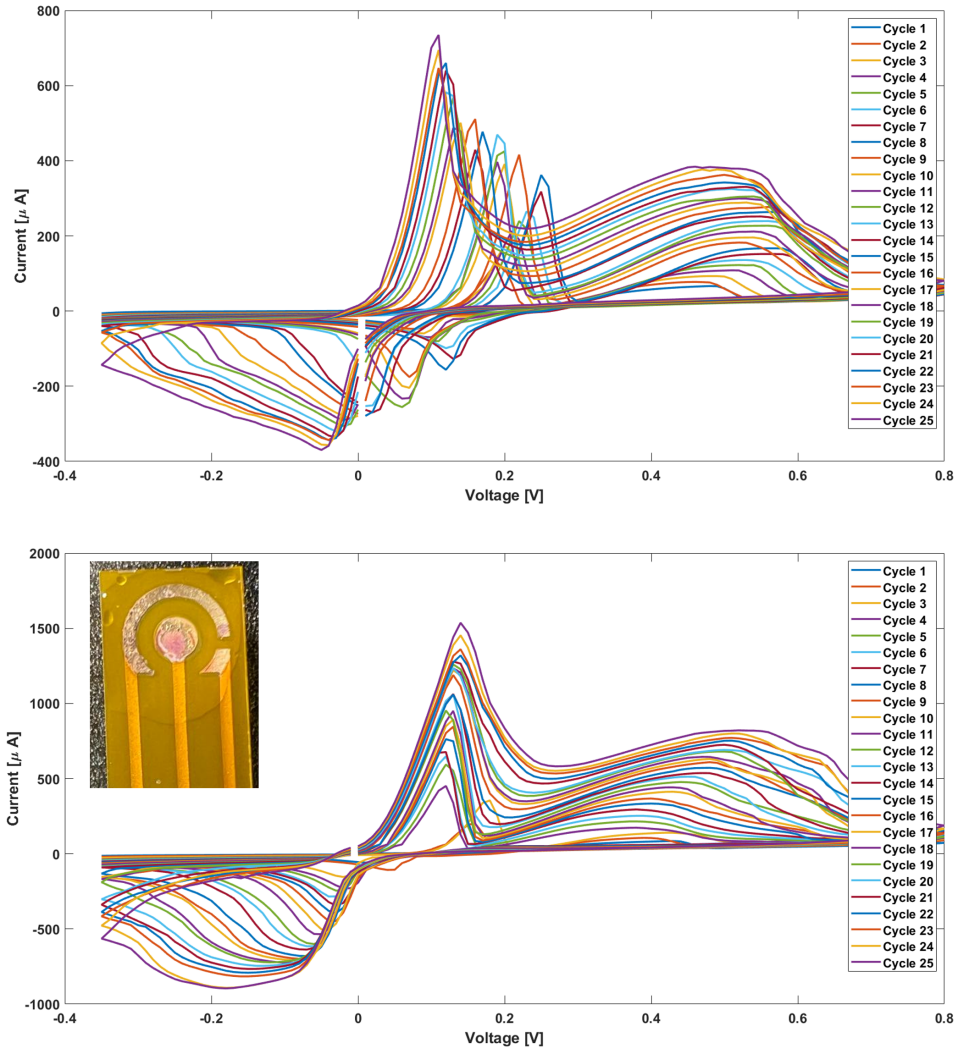


Figure 5.17: Cyclic voltammograms of PCB-electrodes subjected to a cleaning process using sulfuric acid. The voltammograms for the electrodes with copper thicknesses of 17.4μm (top) and 34.8μm (bottom) are shown.In both cases, it can be observed that despite 25 cycles, not only is stability not achieved, but also the current increases with each cycle, resulting in further damage to the electrode. The inset image clearly demonstrates that the working electrode has sustained damage, resulting in the detachment of the gold coating.

Conc.[mM]	Scan Rate	$\sqrt{ScanRate}$	$I_{op}[\mu A]$	$V_{op}[V]$	$I_{rp}[\mu A]$	$V_{rp}[V]$	Separation	E_0
5	0.025	0.158	22.250	0.350	-21.861	0.270	0.080	0.310
5	0.050	0.224	33.676	0.350	-31.377	0.260	0.090	0.305
5	0.075	0.274	40.762	0.350	-39.324	0.260	0.090	0.305
5	0.100	0.316	47.631	0.350	-45.137	0.260	0.090	0.305
5	0.125	0.354	54.095	0.350	-51.775	0.260	0.090	0.305
2.5	0.025	0.158	11.406	0.320	-9.177	0.240	0.080	0.280
2.5	0.050	0.224	17.076	0.330	-12.714	0.240	0.090	0.285
2.5	0.075	0.274	21.047	0.340	-16.299	0.250	0.090	0.295
2.5	0.100	0.316	21.785	0.360	-19.949	0.260	0.100	0.310
2.5	0.125	0.354	22.863	0.360	-22.421	0.260	0.100	0.310
1.25	0.025	0.158	2.358	0.420	-0.873	0.320	0.100	0.370
1.25	0.050	0.224	2.660	0.420	-1.566	0.310	0.110	0.365
1.25	0.075	0.274	2.871	0.430	-2.119	0.330	0.100	0.380
1.25	0.100	0.316	2.930	0.430	-2.424	0.320	0.110	0.375
1.25	0.125	0.354	3.224	0.430	-2.849	0.320	0.110	0.375

Table 5.1: This table presents the results of electrode measurements with a copper thickness of 17.4 μm, which demonstrated resistance to the cleaning process at varying concentrations of ferro-ferricyanide. This analysis focuses on the oxidation and reduction current peaks, which determine the reversibility of the process and the separation between peaks that determines the formal potential (E_0).

characteristic feature of diffusion-controlled processes. Additionally, a linear relationship was also observed between the current peaks and the concentration of FerroFerricyanide, indicating a direct proportionality between the current response and the concentration of the electroactive species.

We will begin by a detailed analysis of the tabulated data. The first table shows the electrode with a copper thickness of 17.4 µm, which has been cleaned. The average formal potential (E_0) observed is $0.325V$, with a standard deviation of $0.036V$. The peak separation averages at $95.3mV$, with a standard deviation of $9.90mV$. According to the literature, the ideal values for E_0 and peak separation versus the Standard Hydrogen Electrode (SHE) are $0.36V$ and $59mV$, respectively.

Upon initial inspection, it may appear that our cleaning process has successfully eliminated impurities, resulting in an electrode that is more 'ideal'. However, this electrode demonstrated the highest level of irreversibility, which is defined as the ratio of the oxidation current peak to the reduction current peak ($\frac{I_op}{I_rp}$). The average value was 1.19 with a standard deviation of 0.19, excluding the data for the concentration of $1.25mM$ and Scan Rate $0.025V/S$, where this ratio increased to 2.7. It should be noted that the voltammogram in Figure 5.18 appears slightly distorted, indicating potential inaccuracies in the baseline correction tracing. These irreversibilities may be due to material losses in the system. Additionally, the gold coating on our cleaned electrode has been affected and undergoes changes during electrochemical measurements.

Conc.[mM]	Scan Rate	$\sqrt{ScanRate}$	$I_{op}[\mu A]$	$V_{op}[V]$	$I_{rp}[\mu A]$	$V_{rp}[V]$	Separation	E_0
5.0	0.025	0.158	23.748	0.04	-22.985	-0.04	0.08	0.0
5.0	0.05	0.224	33.144	0.04	-32.302	-0.05	0.09	-0.005
5.0	0.075	0.274	40.375	0.05	-39.434	-0.05	0.1	0.0
5.0	0.1	0.316	46.853	0.05	-46.656	-0.05	0.1	0.0
5.0	0.125	0.354	52.807	0.05	-52.699	-0.05	0.1	0.0
2.5	0.025	0.158	11.531	0.04	-11.339	-0.05	0.09	-0.005
2.5	0.05	0.224	16.141	0.04	-15.926	-0.05	0.09	-0.005
2.5	0.075	0.274	19.55	0.04	-19.395	-0.05	0.09	-0.005
2.5	0.1	0.316	22.527	0.05	-22.45	-0.05	0.1	0.0
2.5	0.125	0.354	25.347	0.05	-25.554	-0.05	0.1	0.0
1.25	0.025	0.158	5.537	0.04	-5.553	-0.05	0.09	-0.005
1.25	0.05	0.224	7.668	0.05	-7.747	-0.05	0.1	0.0
1.25	0.075	0.274	9.256	0.05	-9.443	-0.05	0.1	0.0
1.25	0.1	0.316	10.592	0.05	-10.751	-0.05	0.1	0.0
1.25	0.125	0.354	11.77	0.05	-12.081	-0.05	0.1	0.0

Table 5.2: This table presents the results of electrode measurements with a copper thickness of 17.4 μm, without the cleaning process at varying concentrations of ferro-ferricyanide. This analysis focuses on the oxidation and reduction current peaks, which determine the reversibility of the process and the separation between peaks that determines the formal potential (E_0).

Conc.[mM]	Scan Rate	$\sqrt{ScanRate}$	$I_{op}[\mu A]$	$V_{op}[V]$	$I_{rp}[\mu A]$	$V_{rp}[V]$	Separation	E_0
5.0	0.025	0.158	22.643	0.05	-22.414	-0.05	0.1	0.0
5.0	0.05	0.224	31.881	0.05	-31.709	-0.05	0.1	0.0
5.0	0.075	0.274	38.961	0.05	-38.808	-0.05	0.1	0.0
5.0	0.1	0.316	45.084	0.05	-44.944	-0.05	0.1	0.0
5.0	0.125	0.354	50.542	0.05	-50.578	-0.05	0.1	0.0
2.5	0.025	0.158	11.623	0.04	-11.539	-0.05	0.09	-0.005
2.5	0.05	0.224	15.994	0.05	-15.747	-0.05	0.1	0.0
2.5	0.075	0.274	19.273	0.05	-19.329	-0.05	0.1	0.0
2.5	0.1	0.316	22.12	0.05	-22.272	-0.05	0.1	0.0
2.5	0.125	0.354	24.64	0.05	-24.88	-0.05	0.1	0.0
1.25	0.025	0.158	5.182	0.05	-5.134	-0.05	0.1	0.0
1.25	0.05	0.224	6.896	0.06	-7.005	-0.06	0.12	0.0
1.25	0.075	0.274	8.08	0.06	-8.262	-0.06	0.12	0.0
1.25	0.1	0.316	9.074	0.07	-9.334	-0.06	0.13	0.005
1.25	0.125	0.354	9.963	0.07	-10.265	-0.06	0.13	0.005

Table 5.3: This table presents the results of electrode measurements with a copper thickness of 34.8 μm, without the cleaning process at varying concentrations of ferro-ferricyanide. This analysis focuses on the oxidation and reduction current peaks, which determine the reversibility of the process and the separation between peaks that determines the formal potential (E_0).

Electrode 2 has the same thickness as Electrode 1 but has not undergone cleaning. In this case, the E_0 value is far from ideal, averaging at $-0.0016V$ with a standard deviation of $0.0024V$. This is not a problem in itself, as it is defined by the type of reference being used. For PCB-electrodes, a pseudo-reference made of gold-coated copper is used. The peak separation is the most important parameter. For the uncleaned electrode, the average separation value is $95.3mV$, same as the cleaned electrode, but with a smaller standard deviation of $4.93mV$. Additionally, the electrode without electrochemical cleaning in sulfuric acid shows better reversibility, with a cathodic to anodic peak current ratio of 1.005 and a standard deviation of 0.017, which is significantly better than that of the cleaned electrode.

Finally, the values for Electrode 3 can be analysed from the last table. This electrode was not chemically cleaned and is distinguished by its double copper thickness. Its E_0 is very stable, with an average value of $0.003V$ and a standard deviation of $0.002V$. Similarly, its reversibility tends towards an ideal value, with an average of 0.9978 and a deviation of 0.014, indicating a deviation of less than 0.22% from the ideal value. The currents obtained from the three electrodes are very similar in absolute values, indicating that the IR resistance of the electrode is defined by the resistance of the porous gold coating. We observed that the thicker electrode presented double the current during cleaning, but this was not the case in the initial cycles. The cleaning process with sulfuric acid removes the superficial gold, defining the resistance based on the exposed copper.

To continue the electrochemical analysis of our electrodes, the Randles-Ševčík equation was used. The Randles–Ševčík equation is a mathematical model that describes the relationship between the peak current and the scan rate in cyclic voltammetry, which is a common electrochemical technique. The equation is given by:

$$i_p = 2.69 \times 10^5 n^{3/2} A D^{1/2} \nu^{1/2} c \tag{5.1}$$

, Where, i_p is the peak current, n is the number of electrons involved in the redox reaction, A is the electrode area, D is the diffusion coefficient of the analyte, ν is the scan rate, and c is the concentration of the analyte. The Randles–Ševčík equation allows us to extract valuable information about the electrode and the analyte. For instance, by measuring the peak current at various scan rates, we can estimate the diffusion coefficient of the analyte. Similarly, if we know the diffusion coefficient, we can estimate the electrode area.

However, it's important to note that the Randles–Ševčík equation assumes that the process is diffusion-controlled and that the electrode is planar and infinitely large. Therefore, care must be taken when applying this equation to real-world systems, as these assumptions may not always hold. The graphical representation of the equation under consideration can be observed in the three plots on the right of Figure 5.18, Figure 5.19 and Figure 5.20. The slope of each line represents the product of $2.69x10^5 n^{3/2} A D^{1/2} c$. We can group the terms $2.69x10^5 n^{3/2} c$ as a constant, so each slope will be a function of the electrochemical area (A) and the square root of the diffusion coefficient (D). According to the literature, the diffusion coefficient for Ferro/Ferricyanide is approximately $6.4Ö10^{-6} cm^2/s$.

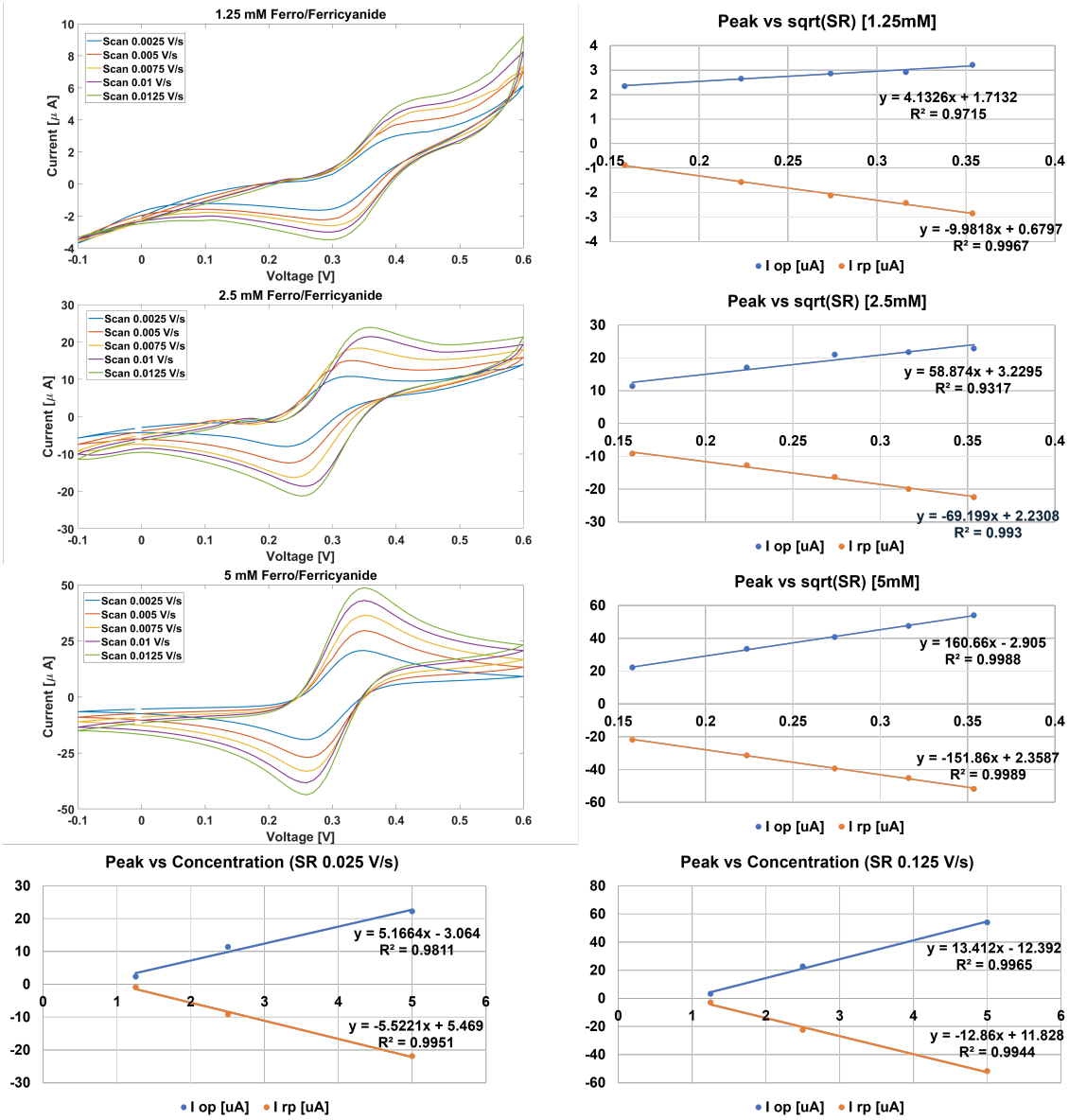


Figure 5.18: Cyclic voltammograms of the electrode, with a copper thickness of 17.4μm, that withstood the cleaning process at different concentrations of Ferro-FerriCyanide (5 mM,2.5 mM and 1.25 mM) and at different ScanRates (2.5 mV/s, 5 mV/s, 7.5 mV/s, 10 mV/s and 12.5 mV/s). The graphs on the left show the linearity obtained between the peak currents and the square root of the ScanRate. While the graphs on the bottom show the linearity with respect to Ferro-FerriCyanide concentration.

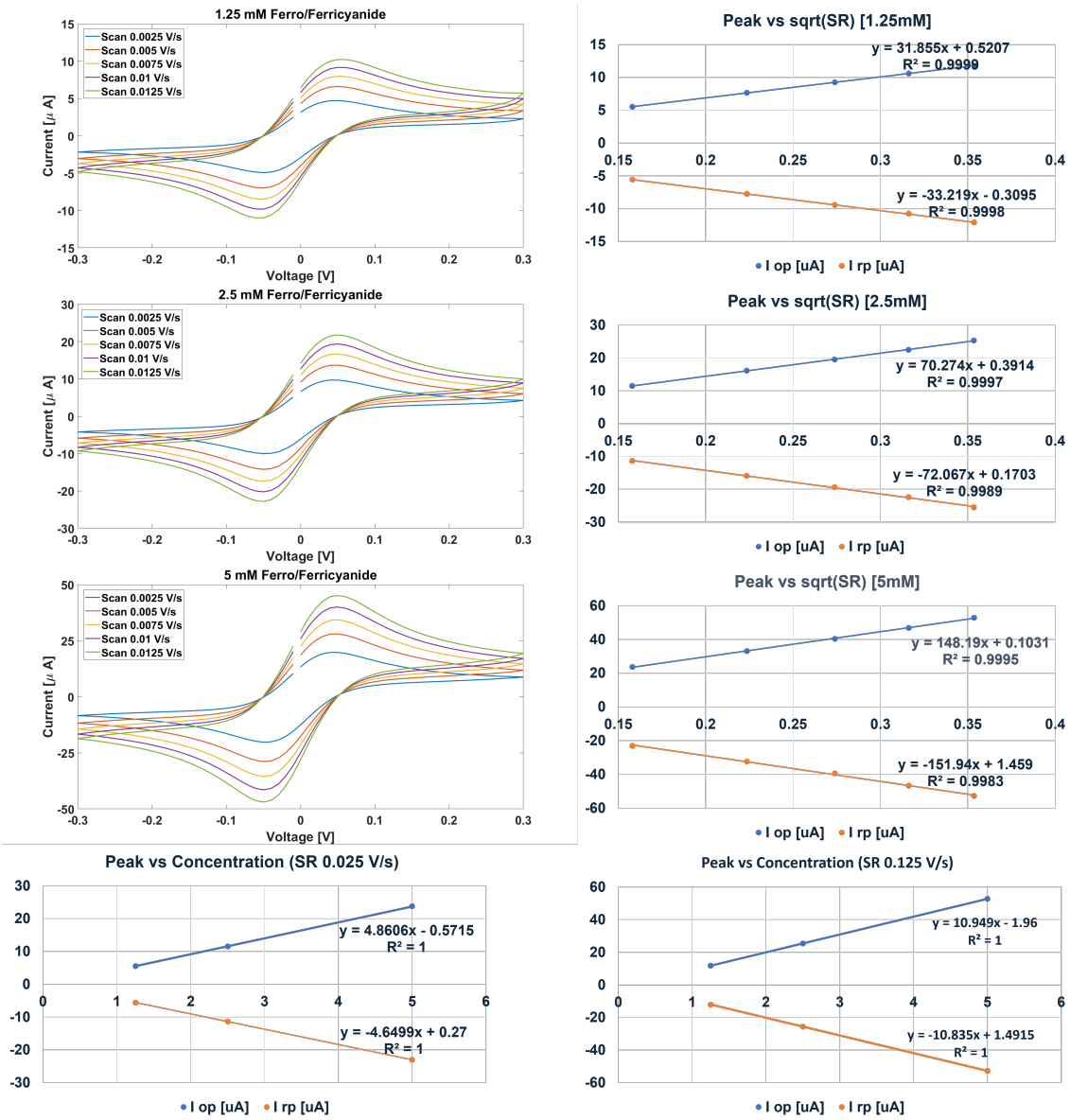


Figure 5.19: Cyclic voltammograms of the electrode, with a copper thickness of 17.4μm, without the cleaning process at different concentrations of Ferro-FerriCyanide (5 mM,2.5 mM and 1.25 mM) and at different ScanRates (2.5 mV/s, 5 mV/s, 7.5 mV/s, 10 mV/s and 12.5 mV/s). The graphs on the left show the linearity obtained between the peak currents and the square root of the ScanRate. While the graphs on the bottom show the linearity with respect to Ferro-FerriCyanide concentration.

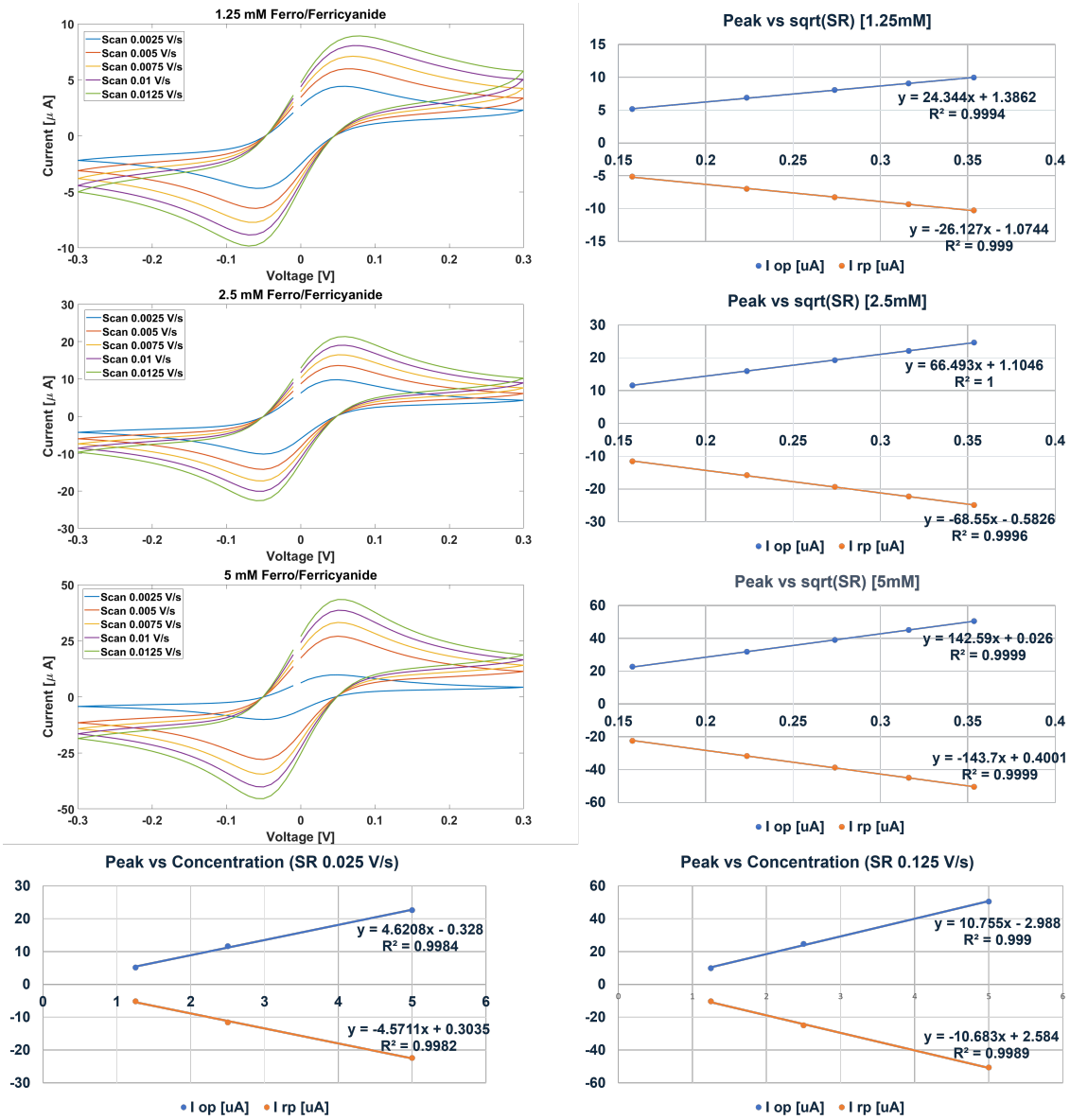


Figure 5.20: Cyclic voltammograms of the electrode, with a copper thickness of 34.8μm, without the cleaning process at different concentrations of Ferro-FerriCyanide (5 mM,2.5 mM and 1.25 mM) and at different ScanRates (2.5 mV/s, 5 mV/s, 7.5 mV/s, 10 mV/s and 12.5 mV/s). The graphs on the left show the linearity obtained between the peak currents and the square root of the ScanRate. While the graphs on the bottom show the linearity with respect to Ferro-FerriCyanide concentration.

Although it is not possible to have absolute values for the diffusion coefficient and the electrochemical area, some relationships can be established. At the same concentration, the diffusion coefficient can be expected to be similar, so we can compare the slopes for different concentrations. For the concentration of $5mM$ the slopes are very similar. Looking only at the negative slopes, we have a value of -151.86, -151.94 and -143.7, corresponding to electrodes 1, 2 and 3 respectively. Dividing by the concentration of $5mM$, the absolute values are 30.372, 30.388 and 28.74. These values are the product of $A \times D^{1/2}$. Assuming that the diffusion coefficient is constant, we can say that the electrochemical area of electrodes 1 and 2 is basically the same and slightly smaller for electrode 3.

Performing a similar analysis with the concentration of $2.5mM$, we have 27.68, 28.83, 27.42. Firstly, we can conclude that the product $A \times D^{1/2}$ is now smaller, since the diffusion coefficient is smaller, since "D" depends on the concentration. It can also be seen that in practice there is no change in the electrochemical area between the clean and unclean electrodes. It can therefore be concluded that electrochemical cleaning with sulphuric acid not only destroys the electrode when the current is triggered during cycling, but also does not offer any significant electrochemical advantage.

Finally, from the graphs at the bottom of each figure, we can observe the linearity of the electrodes as a function of the concentration of the redox species. The slope of the line represents the sensitivity of the electrode. In this particular case, the clean electrode has an advantage, a higher sensitivity of the order of 10% compared to the unclean electrodes for the scan rate of $0.025V/S$ and almost 20% for the scan rate of $0.125V/S$.

In conclusion, working with PCB-electrodes can indeed be a challenge, but their versatility invites further exploration of their potential. In Chapter 6, we will look at a case study of these electrodes, specifically for PoC devices. In such applications, where the electrodes are disposable, PCB-electrodes prove to be an excellent low-cost alternative. Their affordability does not compromise their performance, making them a promising choice in the development of low-cost and efficient electrochemical devices.

5.4 Conclusions of the chapter

This chapter examines the development and application of three innovative types of electrochemical electrodes: nanoband electrodes, laser-induced graphene electrodes (LIGEs), and PCB-electrodes. Each of these electrodes offers unique advantages and faces specific challenges in their fabrication and use.

Nanoband electrodes leverage the advantages of nanoscale dimensions to provide heightened sensitivity and rapid functionalisation, which are crucial for detecting low concentrations of analytes. The development process, which makes use of affordable materials and commonplace laboratory equipment, positions these electrodes as a viable option for widespread adoption, despite the historical challenges related to their fabrication costs and methods.Additionally, the fact that they have a very high sensitivity can result in a problem by quickly saturating the sensor.

Laser-induced graphene (LIG) electrodes, produced by irradiating a polymer precursor with a laser, present a versatile and scalable method for creating porous graphene structures. This technique allows for precise patterning and customization, making LIG electrodes cost-effective and environmentally friendly. They can be produced on various substrates, including those for flexible electronics. However, the quality and properties of LIG depend on the precursor material, and achieving consistent uniformity can be challenging. Additionally, surface defects introduced during the laser process may impact performance in specific applications. Despite these drawbacks, LIG electrodes hold significant promise for widespread use.

PCB-Electrodes offer a practical approach by integrating traditional PCB manufacturing techniques with electrode fabrication. This method benefits from the existing infrastructure of PCB production, making it cost-effective and scalable. Nevertheless, the performance of PCB-Electrodes may be constrained by the intrinsic characteristics of the materials employed in PCB fabrication processes. Particularly since those electrodes are made of gold-coated copper and not pure gold, not only can the gold be removed with some ease at high potentials but naturally the copper diffuses through the gold generating copper oxide peaks in the voltagrams.

Electrode Type	Manufacture Process	Advantages	Disadvantages	Applications
Nanoband Electrodes	Fabricated using sputtering techniques on flexible substrates like polyimide, PET, and PEN. This method is cost-effective and involves depositing nanometer-thin metallic films using commonplace laboratory equipment.	Heightened sensitivity due to nanoscale dimensions; rapid functionalization; cost-effective fabrication using affordable materials.	High sensitivity can lead to quick saturation of the sensor; historical challenges in fabrication costs and methods.	Highly sensitive diagnostics, particularly in detecting low concentrations of biomarkers; PoC sensors for early disease diagnosis.
Laser-Induced Graphene Electrodes	Produced by irradiating a polymer precursor (e.g., polyimide) with a laser, converting it into a porous graphene structure. This involves photothermal and photochemical reactions to restructure carbon bonds.	Cost-effective and scalable; precise patterning and customization; environmentally friendly; versatile for various substrates and applications.	Potential issues with reproducibility and consistency; performance may be affected by the specific conditions of the laser irradiation process.	Flexible electronics, biosensors, environmental monitoring, and other applications requiring customized graphene structures.
PCB-electrodes	Manufactured using traditional PCB manufacturing techniques, integrating gold-coated copper electrodes. This process leverages existing PCB infrastructure for scalability.	Cost-effective and scalable due to existing PCB infrastructure; practical integration with traditional PCB manufacturing.	Performance limitations due to the use of gold-coated copper instead of pure gold; potential for gold removal at high potentials and copper diffusion leading to copper oxide peaks.	General electrochemical applications, practical for integrating with existing electronic systems; potentially useful in cost-sensitive diagnostic tools.

Table 5.4: Comparative table of Nanoband Electrodes, Laser-Induced Graphene Electrodes , and PCB-electrodes.

CHAPTER 6

ELECTROPHORETIC DEVICE FOR PORTABLE DIAGNOSTICS

Electrophoresis is a highly effective laboratory separation technique. It separates charged macromolecules in an electric field based on their differential mobility, which is determined by their charge, shape, and mass. This chapter provides a comprehensive introduction to the technique's fundamentals and the development of a full electrophoretic system with an electrochemical readout that employs paper as a support.

Electrophoresis is a highly relevant technique in diagnostics, with the ability to characterise a patient's hemoglobin types and evaluate the presence of anemias and hemoglobinopathies through electrophoresis of a blood sample. Additionally, electrophoresis is a valuable tool in paternity tests for separating DNA fragments and diagnosing hereditary diseases.

The applications of electrophoresis have far exceeded their original limits, demonstrating its versatility and importance in the field of diagnostics. Electrophoresis served as the basis for sequencing genetic information, allowing complete genomes to be sequenced. This chapter covers the theoretical and practical aspects of the technique.

6.1 Fundamentals of electrophoresis

Electrophoresis is a separation technique based on the phenomenon of differential migration of electrically charged particles under the influence of an electric field[169, 170]. This section examines the fundamentals of electrophoresis and analyses the variables that affect the distance a substance migrates in an electrophoretic run. An electric charge immersed in an electric field experiences a force of attraction or repulsion $|\vec{F}_e|$, as described by Coulomb's law: $|\vec{F}_e| = k\frac{q_1 q_2}{d^2}$. The charge in the medium will move towards the pole of opposite charge as a result of the electric attraction force: positively charged molecules will move towards the cathode (negative pole) and negatively charged molecules will move towards the anode (positive pole) (Figure 6.1.a).

In a medium where the electric field is homogeneous, the magnitude of the electric force acting on the charge depends both on the intensity of the electric field and on the value of the charge being studied($|\vec{F}_e| = q.|\vec{E}|$).

Initially, as a result of the electric force, the charged particle experiences an initial acceleration and consequently begins to move. Newton's second law describes the relationship between acceleration and force: $\sum \vec{F} = m.\vec{a}$. where:$\vec{F}$ is the force applied, m is the mass of the object, and $\vec{a}$ is the acceleration of the object (Figure 6.1.b).

This law states that the acceleration of an object is directly proportional to the net force acting on it and inversely proportional to its mass. Thus, the same force will result in less acceleration if the mass of the object is larger. Conversely, a smaller mass will result in greater acceleration for the same applied force. This principle is fundamental in understanding the motion of charged particles in an electric field.

When the particle is immersed in a fluid (in the case of electrophoresis, this medium corresponds to the running buffer), a frictional force acts on it, as the fluid in which the particle moves opposes its movement. The frictional force is proportional to the speed of the particle, has the same direction as the electric force but in the opposite sense. This means that as the particle moves faster, the frictional force increases, opposing the motion and eventually reaching a balance with the electric force. This balance of forces is what determines the final velocity of the particle in the electrophoretic process ($|\vec{F}_r| = k.|\vec{v}|$).

The frictional coefficient, denoted as k, encompasses variables such as the viscosity of the medium, and the size and shape of the particle. Therefore, the frictional force depends on these three variables, in addition to the velocity of the particle. Considering a spherical particle moving under conditions where Stokes' Law is applicable, the expression for the frictional force can be written as: $|\vec{F}_r| = 6\pi\eta r v$. where:$\eta$ is the viscosity of the medium at the working temperature, r is the radius, and v is the velocity of the particle.

As soon as the molecule begins to move in the buffer due to the electric force $|\vec{F}_e|$, the opposing frictional force $|\vec{F}_r|$ appears. The net force acting on the particle will then be the resultant of the electric force and the frictional force, and is equal to the difference between the two. This resultant force will determine its migration in the running medium.

In fact, the frictional force is not constant, as it increases with the velocity of the particle, resulting in a progressive decrease in acceleration. There comes a point when the frictional force is equal to the electrical force (Figure 6.1.c). Since both forces have the same module but opposite directions, the resulting force on the particle will be zero. Consequently, from this moment on, the particle will not experience any acceleration and will move at a constant speed. This speed is the maximum it will reach in the fluid under a uniform electric field. As this situation is reached within a few seconds, it can be assumed that the velocity is constant throughout the displacement (Figure 6.1.d).

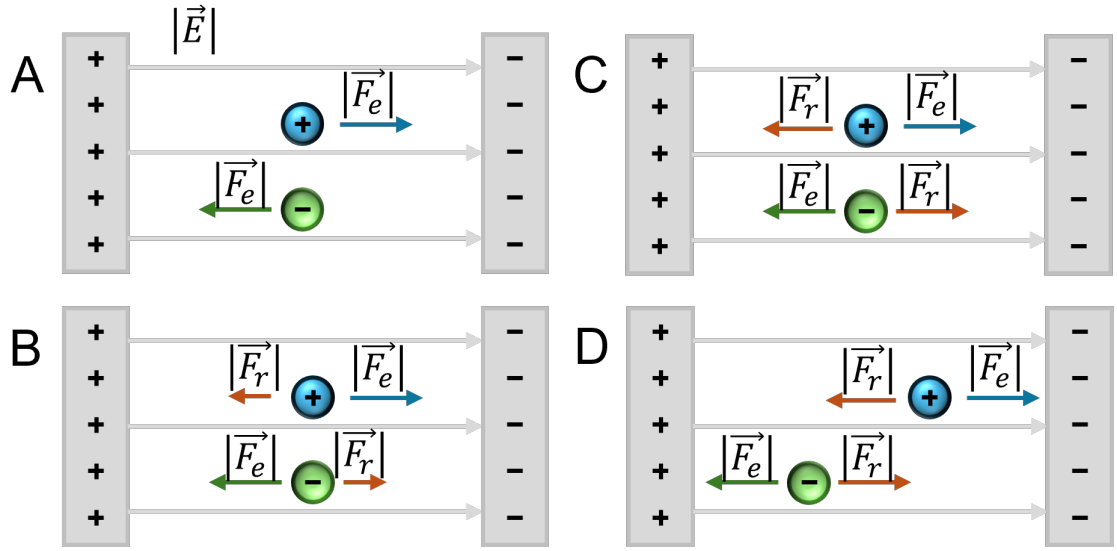


Figure 6.1: Charges in a uniform electric field. $|\vec{E}|$: electric field vector; : $|\vec{F_e}|$: electric force vector; $|\vec{F_r}|$: frictional force vector; + : positive pole or anode; - : negative pole or cathode. A - Charges experience an electric force directed towards the opposite pole of the charge. B - When the charged particles begin to move, they experience a frictional force in the opposite direction. The arrows indicate the direction and sense of the vectors, and the lengths of the force vectors are proportional to their respective moduli. C- An equilibrium is quickly reached where the moduli of the forces are equal, $|\vec{F_e}| = |\vec{F_r}|$. At this point, the acceleration is zero and the displacement velocity is constant. D- The particles continue to move at a constant velocity towards the opposite poles.

The migration of a particle in a medium subjected to an electric field depends on the velocity it acquires in it. Let's consider, then, what inherent variables of the system affect this velocity. In the initial stages of movement, the sum of forces acting on the particle is zero, indicating a state of equilibrium where the electric force ($|\vec{F_e}|$) equals the frictional force ($|\vec{F_r}|$). This can be expressed as ($q.|\vec{E}| = k.|\vec{v}|$), and therefore$|\vec{v}| = \frac{q.|\vec{E}|}{k}$. From this equation, it's evident that the velocity of an electrically charged particle in an electric field is influenced by the particle's properties (charge, size, shape), the viscosity of the medium, and the intensity of the applied electric field. It's also important to note that particle movement is affected by natural diffusion and working temperature. Additionally, the pH and ionic strength of the medium can alter the particle's velocity by changing its net charge or causing charge shielding, respectively.

As illustrated in Figure 6.2, ionic strength, a measure of the concentration of ions in a solution, plays an important role in electrophoresis. It reflects the activity of electrolytes based on their charge and concentration. When a charged particle is in a solution, it's surrounded by electrolytes of opposite charge due to electrostatic attraction. This charge field, which depends on the number and type of charges dissolved, i.e. the ionic strength, can affect the migration of the particle. In electrophoresis, the presence of electrolytes around the charged particle tends to counterbalance the migration of the particle, as counterions tend to move in the opposite direction. Therefore, the

velocity of a particle in a medium with many electrolytes will be lower than in an environment with fewer total charges. This can be seen as a shielding effect of the net charge of the particle by the surrounding counterions.

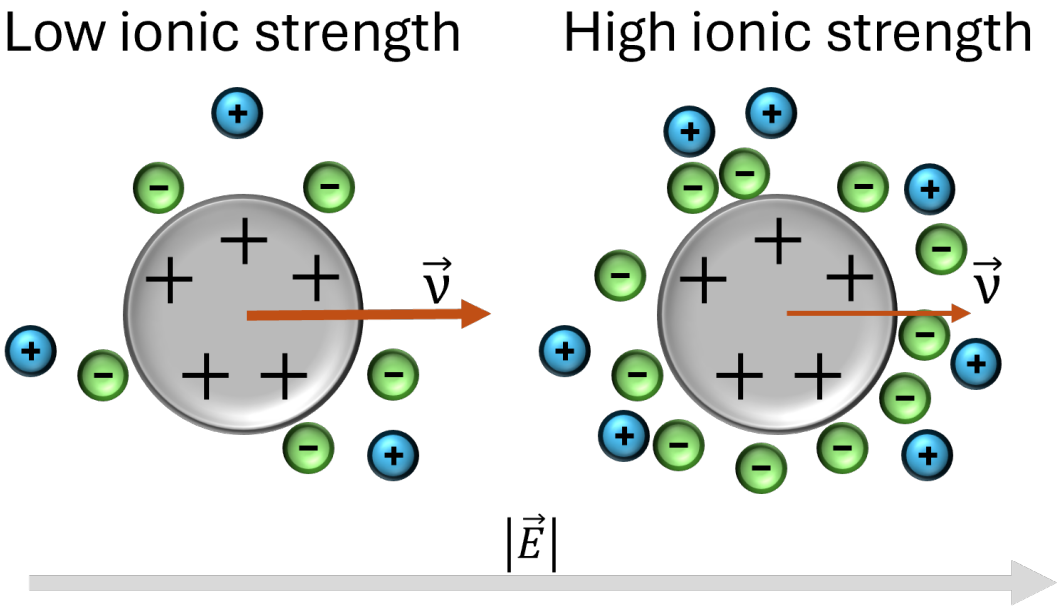


Figure 6.2: Effect of ionic strength on the migration of a charged particle in a solution, under the influence of an electric field $|\vec{E}|$, is significant. A higher ionic strength results in a lower migration speed due to the particle's need to counteract the movement of its counterions in the opposite direction. Conversely, when the charge concentration is lower, the particle can move more freely through the medium. The diagram shows the velocity vector $|\vec{v}|$ in each case, with the length of the vector being proportional to its modulus. The direction and sense of the electric field vector $|\vec{E}|$ are indicated by the lower arrow.

The pH of the medium influences the charge acquired by acidic and basic groups present in molecules. Biological molecules often have weak acid or base groups that partially ionise in solution, coexisting in equilibrium with different species. The degree of ionisation of these functional groups is related to the pH of the medium, since the species H_3O^+ and OH^- are part of the equilibrium situation. Therefore, depending on the pH conditions, any weak acid or base group present in the molecule will be ionised to a greater or lesser extent.

Temperature can also affect the speed at which the particle moves in three different ways. Firstly, the viscosity of the buffer, a physical constant, depends on the temperature and therefore the coefficient of friction will vary. Secondly, the intrinsic kinetic energy of the molecules, which determines the phenomenon of diffusion, is directly related to temperature. Finally, under certain temperature conditions, solvent evaporation from the buffer can change its ionic strength. Under the same operating conditions (same running buffer - ionic strength, pH and viscosity; same electric field; same temperature), particles of different charge, size and/or shape will migrate at

different speeds and therefore travel different distances in the same time. This is the physical phenomenon that underlies the separation technique known as electrophoresis. As can be seen from the expression:$|\vec{v}| = \frac{q.|\vec{E}|}{k}$, the speed of the particles also depends on the electric field applied. Therefore, in order to compare different substances, it would be useful to become independent of the electric field. To do this, we will use the concept of electrophoretic mobility instead of particle velocity.

6.1.1 Electrophoretic mobility

Electrophoretic mobility, a key concept in the field of electrophoresis, is defined as the velocity attained by a charged molecule per unit of applied electric field,$\mu = \frac{\vec{v}}{\vec{E}}$. This parameter provides a standardised measure of the behaviour of a particle under an electric field, allowing comparisons between different substances under identical conditions, regardless of the specific electric field applied. This concept is crucial to the analysis and interpretation of electrophoretic experiments, providing insight into the characteristics and behaviour of charged particles in an electric field. It is a fundamental parameter in the design and optimisation of electrophoretic processes.

Using the definitions provided in the previous section, it is possible to define 'mobility' as follows: $\mu = \frac{\vec{v}}{\vec{E}} = \frac{q}{k}$. The equation clearly indicates that electrophoretic mobility is contingent upon the particle's charge and the friction coefficient. The latter is influenced by the particle's shape and size, as well as the viscosity of the medium. As for the charge, it is an intrinsic property of the molecule but can be modulated by the ionic strength and pH of the buffer used in the electrophoretic run. The equation $|\vec{v}| = \frac{q.|\vec{E}|}{k}$ clearly demonstrates that the velocity acquired depends on the intensity of the applied electric field. It is important to note that velocity and electric field are interrelated variables in the analyzed equations. If the electric field is increased, the velocity will increase, provided that the mobility (μ) of the substance in the system under study remains constant. This unequivocally shows that mobility does not depend on the applied electric field.

Mobility is a physical constant for a substance under constant medium pH, ionic strength, viscosity, and temperature. It can be used as an identification criterion under given conditions and is closely related to the selected working conditions. This understanding is important for the effective design and interpretation of electrophoretic experiments.

Electrophoretic mobility is influenced by the previously mentioned parameters (characteristics of the particle and the medium in which it is immersed) but can also be analyzed in relation to the experimental variables that are controlled during the run in the electrophoretic equipment.Figure 6.3 depicts an electrophoretic run conducted on a paper support.

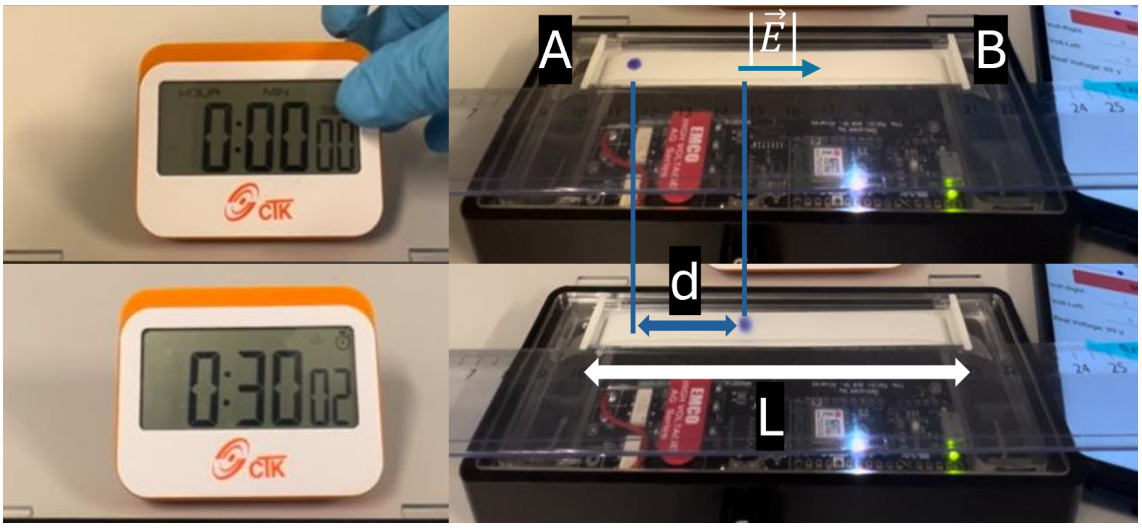


Figure 6.3: Example of an electrophoretic run of a substance. A strip of paper - support - is shown, where a potential difference was established between the points A and B (ΔV_{AB}), $|\vec{E}|$: Vector electric field; L: length of the support; d: distance run by the sample.

At the end of the run, it is observed that the chemical species under study have moved a distance, d, in a time, t, on an electrophoretic support of length L, between whose ends (A and B) a potential difference, ΔV_{AB}, was applied. We have seen that the electrophoretic mobility is the proportionality constant that relates the velocity of a particle to the applied electric field: $\mu = \frac{\vec{v}}{\vec{E}}$, given that $\vec{v} = \frac{dx}{dt} = \frac{d}{t}$, where: d = the distance travelled by the particle and t = the run time, and that in a homogeneous field: $|\vec{E}| = \frac{dV}{dx}$ where: dV = potential difference and dx = differential distance between the poles generating the field. As in the case of electrophoresis, the electric field can be considered homogeneous along the length of the support (L): $|\vec{E}| = \frac{\Delta V}{L}$ where ΔV is the voltage supplied by the power source.

The electrophoretic mobility of a substance can be determined with confidence using the following expression: $\mu = \frac{d.L}{\Delta V.t}$. This formula allows for the accurate determination of μ under specific working conditions. The potential difference is directly proportional to the circulating current in the strip, as per Ohm's Law, and can be mathematically expressed as $\mu = \frac{d.L}{R.i.t}$. It is important to note that electrophoretic mobility is a fundamental characteristic of a substance in a particular medium and is independent of any experimental conditions. This has been demonstrated through various experiments, where changes in experimental conditions resulted in changes in the distance run by the sample, but the mobility remained constant. By varying the length L of the running support while keeping ΔV_{AB} and running time constant, the distance travelled by the particle will vary. This is because the substance experiences a change in velocity due to the variation of the intensity of the electric field applied to the ends of the strip. It is important to note that μ will remain constant in all cases. Therefore, the choice of experimental conditions can be made by analyzing this equation: $d = \frac{\mu\ \Delta V\ t}{L}$. Electrophoresis can be used for analytical or preparative purposes depending on the objective pursued: the identification

of substances or their separation when it is part of a mixture. Likewise, depending on the experimental design, it can be used to determine molecular weights, quantify substances, etc. In all cases, it is necessary to apply the correct conditions to obtain a good resolution of the components to be analyzed and/or separated. Resolution is called the ability of a system to distinguish as different the distances traveled by two different substances under the same running conditions. In electrophoretic runs, among other things, the choice of voltage, suitable supports and the running time are the experimental parameters that must be considered to obtain a good resolution.

6.1.2 Isoelectric point

The isoelectric point, or pI, is the pH at which a molecule carries no net electrical charge. In other words, it's the pH at which the electrophoretic mobility (μ) equals zero. To determine this point, electrophoretic runs are performed on the substance under study using buffer solutions of equal ionic strength and viscosity, but with different pH values. In each case, the electrophoretic mobility is calculated and plotted as a function of pH.

Given the direct relationship between the distance traveled and the electrophoretic mobility, a graph can also be constructed showing distance as a function of the pH of the running buffer. This can be used to determine electrophoretic mobility. However, care must be taken to keep all other conditions constant when performing runs at different pH levels. This ensures that the proportionality between electrophoretic mobility and the distance traveled is maintained. In essence, the isoelectric point is a critical parameter in electrophoresis, and its determination requires careful experimental design and control of various factors, including pH, ionic strength, and viscosity.

6.1.3 Electroendosmotic flow

The support medium plays a pivotal role in providing resistance to the free diffusion of the sample, thereby facilitating the separation of the sample's components based on the principles governing this technique. In certain media, such as paper, depending on the running conditions, a phenomenon known as electroendosmosis or the electroendosmotic effect may occur. These media contain chemical groups that can exhibit acidic or basic properties. Under specific pH conditions, these groups may become ionised, acquiring a charge. This results in a polarization effect on the charges of the buffer in contact with the support medium.

For instance, in the case of paper, carboxyl groups at pH levels close to or above their pKa will be ionized (forming carboxylates), thus presenting a net negative charge. The positive counterions that neutralize these charges are free to move with the buffer, causing the buffer in direct contact with the support to exhibit a net positive charge due to the solution's polarization.

As shown in Figure 6.4, when a potential difference is applied to the system, the positive ions move towards the cathode, dragging their solvation sphere along with them. Consequently,

there is a net flow of the solution that carries all the molecules towards the cathode. As a result, any substance present on the support medium will migrate towards the cathode regardless of its charge. The electroendosmotic effect is dependent on the pH, as it results from the ionization of

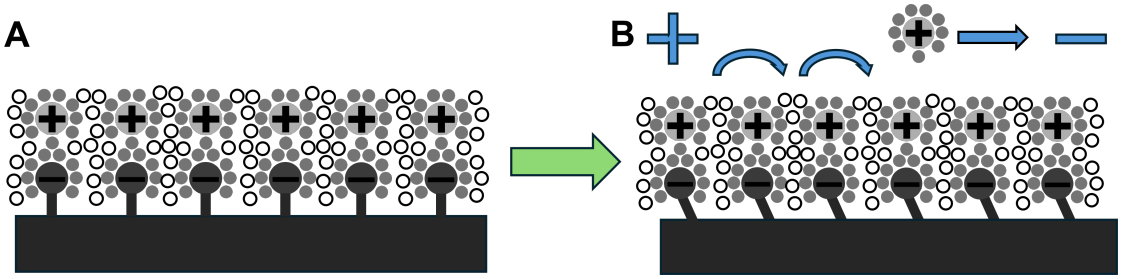


Figure 6.4: Electroendosmotic Effect. In part A), the polarization of the solution is illustrated when the support medium is ionized. Positively charged ions, or cations, gather around the negatively charged anions that are fixed to the paper. B) When a potential difference is applied, the cations will migrate towards the cathode, bringing their hydration sphere along with them. The anions, being fixed to the paper, do not migrate.

the support's functional groups, as previously mentioned. In paper, this effect becomes significant under pH conditions greater than 4

The necessity of considering this effect hinges on the specific objective of the electrophoresis.

- In the case of attempting to separate two compounds, the electroendosmotic effect may be deemed to have no impact on the separation.
- In the event that the objective is to identify a substance based on the distance travelled, to determine the isoelectric point or the electrophoretic mobility of a substance, it will be necessary to correct for this phenomenon.

Conversely, there are techniques that are based on this effect, such as counter-immunoelectrophoresis. In this method, the electroendosmotic effect allows two substances seeded in different positions to meet in the middle. This occurs because one of the substances runs in one direction, while the other is dragged in the opposite direction by the electroendosmotic effect.

The pole to which the solvation spheres migrate as a consequence of the electroendosmotic effect is contingent upon the functional groups present on the support. In the case of paper, the solvation spheres migrate towards the cathode. However, the system can be developed in such a way that with another support, the migration is towards the anode.

6.2 Electrophoresis device for Point Of Care applications

LFAs have emerged as a popular choice for PoC testing due to their simplicity, rapidity, and cost-effectiveness. These assays are designed to be user-friendly, requiring minimal training to operate, and can deliver results within minutes. This makes them ideal for use in resource-limited settings, where access to sophisticated laboratory equipment and trained personnel may be limited.

However, LFAs have limitations, especially when dealing with blood samples. Blood is a complex biological fluid containing various cells, proteins, and other components that can interfere with the assay's performance. High levels of red and white blood cells can cause non-specific binding and lead to false-positive results. Similarly, the presence of serum proteins can affect the assay's sensitivity and specificity.

In addition, LFAs usually depend on the passive diffusion of analytes, which can restrict their sensitivity and speed. This is especially problematic when detecting low-abundance targets in blood, as the target must diffuse through a complex matrix to reach the detection zone.

To address these challenges, recent studies have investigated the incorporation of an electrophoretic source with LFAs. The integration of an electrophoretic source with LFAs has been reported in recent studies to enhance the sensitivity and speed of the assay, actively driving the migration of charged analytes. This approach shows promising results, particularly in improving the detection of low-abundance targets in blood, as the active migration of analytes can overcome the limitations of passive diffusion. Moreover, the use of an electrophoretic source can also reduce the interference caused by blood components, thereby improving the assay's specificity.

In the following sections of this chapter we will see the step-by-step development of an innovative device, an electrophoresis source that can be powered by a mobile phone, controlled via Bluetooth, and integrates the PCB electrodes with NFC technology to provide an electrochemical readout during the electrophoresis process.

6.3 Electronic design of the Power Supply

The electronic development of this project is based on a DC-DC converter, which are electronic devices that transform direct current (DC) from one voltage level to another. There are two primary types of DC-DC converters: step down (buck) converters and step up (boost) converters (Figure 6.5).

Step down converters, or buck converters, reduce the input voltage to a lower output voltage. They are commonly employed in power supply units for electronic devices that require a lower, stable voltage, such as the conversion of a 12V car battery to 5V for USB charging. The buck converter functions by utilising a series of inductors, capacitors, and switches (typically transistors) to effectively reduce the voltage. When the switch is in the 'on' position, the inductor

stores energy; when the switch is in the 'off' position, the energy is transferred to the output load, thereby producing a voltage that is in accordance with the desired lower voltage.

The boost converter functions in a manner analogous to the buck converter, albeit with the configuration altered to facilitate an increase in voltage. When the switch is in an active state, energy is stored in the inductor; when the switch is in a passive state, the energy is transferred to the load through a diode, resulting in an elevated output voltage. Inductors and capacitors serve to store and release energy, thereby facilitating the smooth transition of pulses resulting from switching actions, thus ensuring the generation of a stable DC output. Control circuitry is responsible for maintaining the desired output voltage, with the duty cycle of the switching signal being adjusted based on feedback from the output voltage. This kind of converter has a high voltage output that depends on the input voltage, as shown in Figure 6.6, taken from the Manufacturer's data-sheet.

DC-DC converters typically employ switching regulators, which are markedly more efficient than their linear regulator counterparts. The fundamental operation entails the rapid activation and deactivation of a semiconductor switch to regulate energy transfer. Inductors and capacitors serve to store and release energy, thereby facilitating the smooth transition of pulses resulting from the switching action, thus ensuring the generation of a stable DC output. The control circuitry maintains the desired output voltage by adjusting the duty cycle of the switching signal based on feedback from the output voltage (Control Pin Figure 6.5).

These converters are highly efficient, often achieving efficiencies above 90%. This efficiency is really important in battery-operated devices, where conserving energy is essential for extending battery life. The main advantages of DC-DC converters include high efficiency, flexibility in providing various output voltages from a single input source, and compactness, making them suitable for portable and space-constrained applications. Other authors have used similar

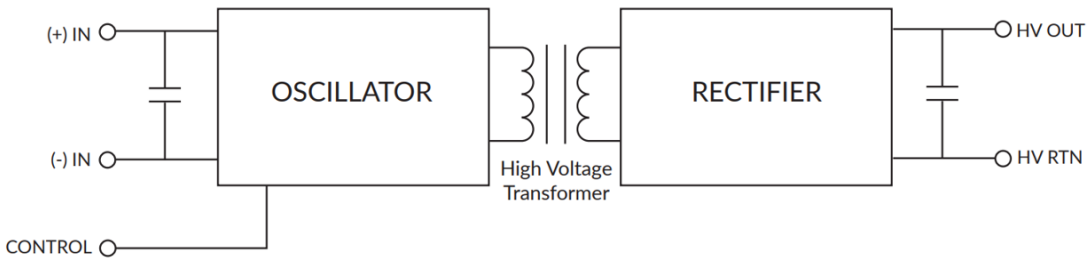


Figure 6.5: Block diagram of the DC-DC converter. The pin assignment can be observed. Diagram taken from the manufacturer's data-sheet.

converters to create electrophoretic sources for PoC applications. However, these implementations often lack control over the output voltage. Throughout our development, we will emphasize the importance of incorporating a feedback loop to maintain a constant output. A feedback loop will allow us to adjust the input based on the output, ensuring that the output voltage remains stable

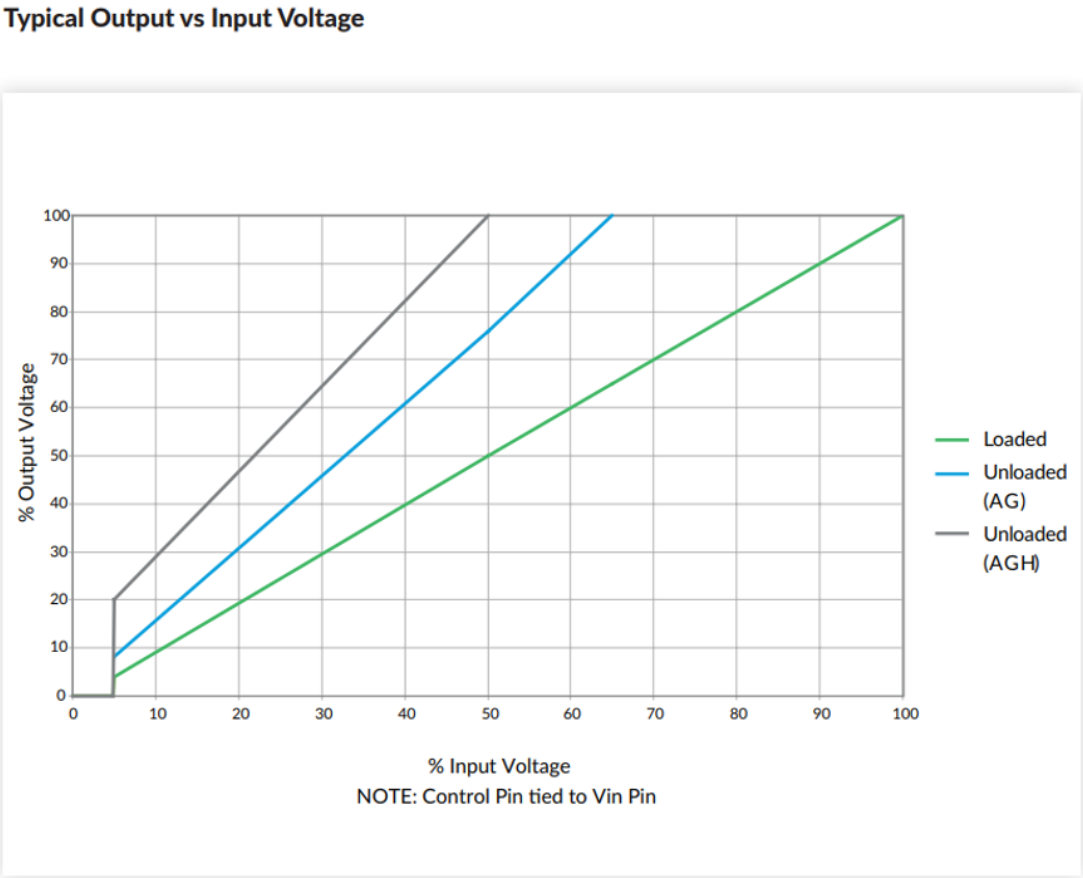


Figure 6.6: Output voltage as input voltage under the condition that the control pin is short-circuited to the input pin. It can be seen that the output voltage also depends on the load. Graph taken from the manufacturer's data-sheet.

even if load fluctuates. This is key point for electrophoretic applications, where a stable voltage is necessary for consistent and reliable results, as discussed in the previous sections.

Incorporating a feedback loop into the DC-DC converter design will require careful consideration of the system's dynamics and stability. We will need to select appropriate components for the feedback loop, and design the control logic to provide the desired response characteristics. This involves a combination of theoretical analysis and practical testing to ensure that the feedback loop performs as expected.

By taking these steps, we can enhance the performance of the DC-DC converter and make it more suitable for use in electrophoretic PoC applications. This will contribute to the development of more reliable and effective diagnostic tools, helping to improve patient care and outcomes.

6.3.1 First version of the device

The device's initial design was intended to operate with either a mobile phone or a $9V$ battery. Therefore, the $A03P-12$ DC-DC converter was selected. As we will see later, the letter 'A' indicates the series, this series is 1W power, '03' indicates that the maximum output voltage is $300V$,the letter 'P' indicates that it will only generate positive voltages with respect to ground, and '12' is the maximum input voltage. As shown in Figure 6.6, the converter can achieve the maximum output voltage, and even higher, without applying the maximum input voltage when it is underloaded.

The schematic in Figure 6.7 shows the connection of the converter. At the output of the converter, three resistors are present, forming a resistive divider. This is necessary to sense the output voltage, as most electronic circuits only support logic levels of $3.3V$ or $5V$. The equation $V_o = \frac{R_2}{R_2+R_1} * V_i$ is used to calculate the output voltage of the divider. In our case, $R1$ is composed of two series resistors: $R1$ and $R1p$. The reason for this choice was the availability of components during the manufacturing of the first version of the PCB. The selected values for $R1$, $R1P$, and $R2$ were 1 $M\Omega$, 1 $M\Omega$, and 22 $k\Omega$, respectively. This way, $V_o = \frac{22k\Omega}{2.022k\Omega} * V_i$, and the divider is 0.01088. Therefore, when the output is $300V$, we sense $3.26V$, which is perfectly compatible with the Arduino inputs. If the sensing pin were directly connected to the Arduino input, the input impedance of the Arduino's analog pin would be in parallel with $R2$. Therefore, it is necessary to implement an operational amplifier in buffer or follower mode. Operational amplifiers ideally have an infinite input impedance. However, in practice, the input impedance is typically in the order of $M\Omega$. When this impedance is placed in parallel with the 22 $k\Omega$ of $R2$, the resulting

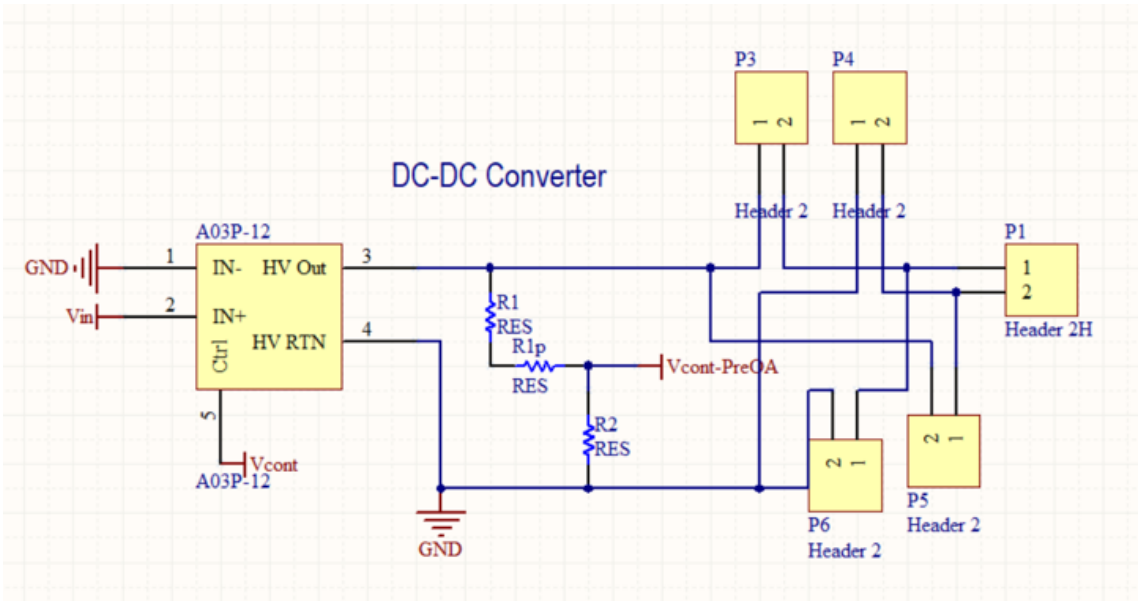


Figure 6.7: Wiring diagram for the $A03P-12$ DC-DC converter. It shows the resistive divider made up of $R1$, $R1p$, and $R2$, as well as the headers used to change the output polarity.

impedance remains at $22k\Omega$. Therefore, the operational amplifier does not draw current from our system. On the right of Figure 6.7, we can observe two pairs of two-pin headers(P3-P6). By connecting a pair of headers, we can manually select the direction of the current that will come out of P1.

As stated previously, it is essential to measure the output voltage in order to implement a feedback loop. The Arduino microcontroller receives the measured voltage value and adjusts the input voltage to the DC-DC converter accordingly, ensuring a constant output.

This feedback mechanism is essential for maintaining the stability and reliability of the system. The microcontroller continuously monitors the output voltage and adjusts the input voltage accordingly to compensate for any fluctuations or disturbances, ensuring that the output voltage remains stable.

The schematic in Figure 6.8 shows a Digital Analog Converter (DAC) MCP4725. The component choice is based on the voltages that the Arduino microcontroller can handle. It is not possible to obtain 9V from the Arduino's analog port. Instead, we send a digital signal through I2C communication to the converter. This signal produces an output voltage proportional to the signal that ranges from 0V to the power supply voltage of the DAC. In our case, the voltage is 9V if we use the battery or 5V if we use the mobile. Also, in Figure 6.8, a Bluetooth module is shown for Arduino communication with a mobile device. An ad hoc application, developed by us, allows the user to select the desired voltage. Additionally, a 2x16 LCD display is included to visualize the output voltage.

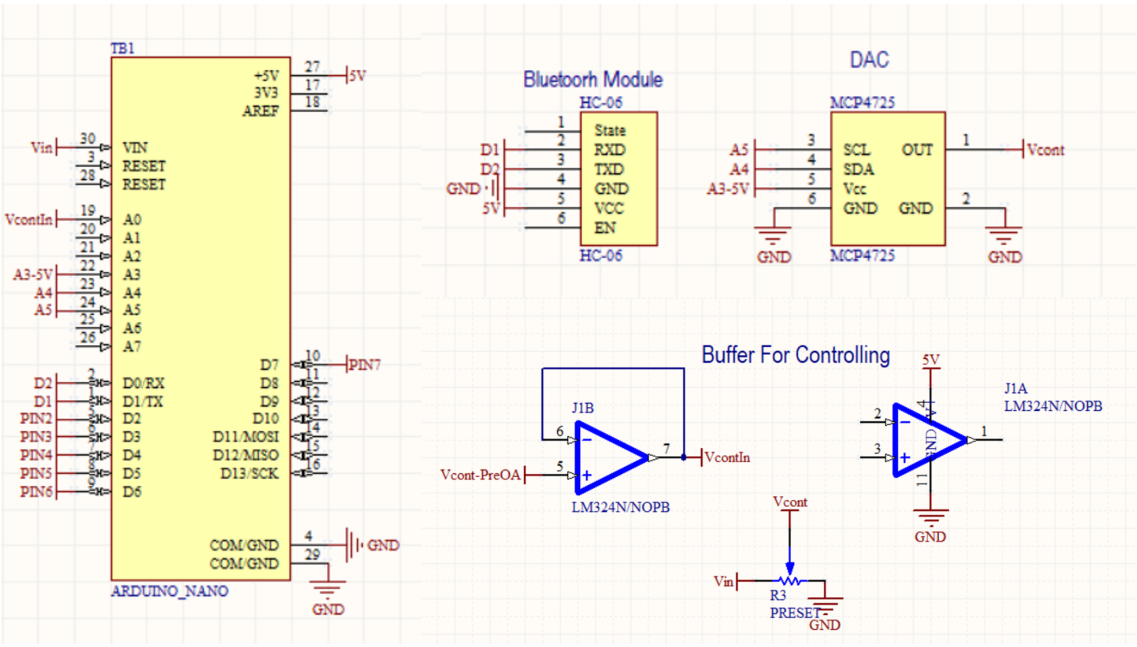


Figure 6.8: Schematic of some of the main components of Version 1 of the electrophoretic source. It shows the Arduino Nano; the Bluetooth Module HC-06, the DAC MCP4725 and the buffer formed by the LM324N op amps.

Figure 6.9 provides an overview of the complete schematic, including the previously described components, a 2-pin terminal block for powering the device with either $5V$ or $9V$, a 16-pin header for connecting the $2X16$ LCD, and a potentiometer to control the backlight of the display.

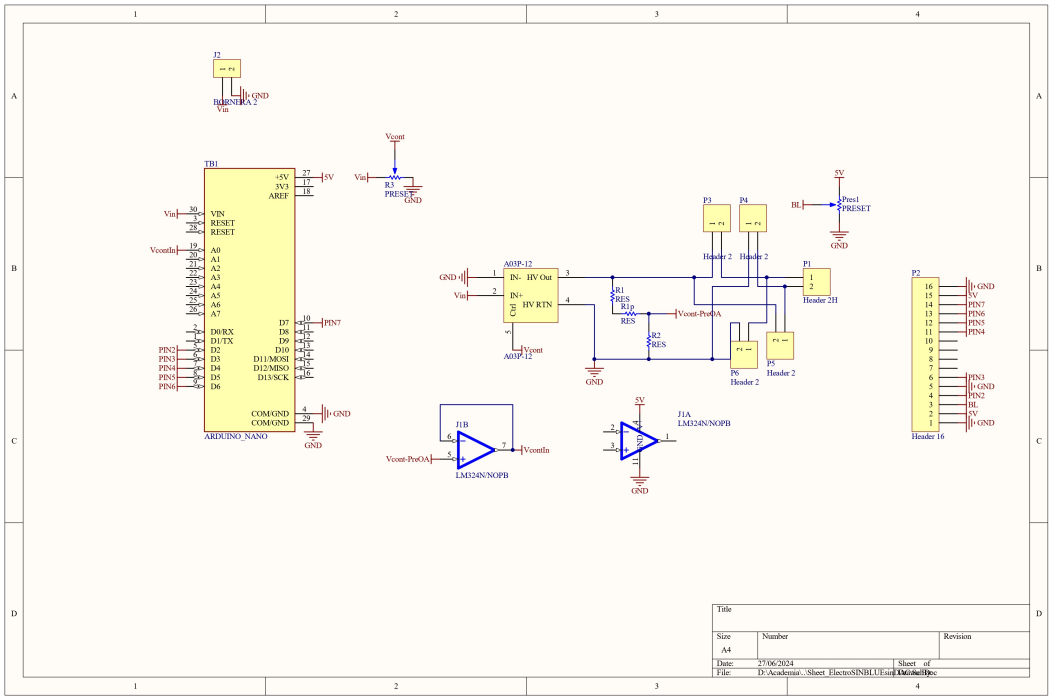


Figure 6.9: Complete overview of Version 1 of the Electrophoretic Power Supply (EPS) schematic.

After selecting all the components, they were tested using a protoboard. Subsequently, the PCB design was carried out in Altium Designer Summer 09. Figure 6.10 shows the $2D$ view of the component routing and the $3D$ view of the printed circuit.

Altium Designer is a powerful tool for designing and simulating PCBs, offering a wide range of features to facilitate the design process. The $2D$ view presents a detailed layout of the components and their connections, while the $3D$ view provides a realistic representation of the final printed circuit. The design process involves the careful placement and routing of components to ensure optimal performance and reliability. Special attention is given to the layout of critical components, such as the DC-DC converter, to minimize interference and signal degradation.

Once the design is finalized, it can be exported for manufacturing. However, for this first version, the decision was made to print the PCB with silver paste for the tracks using the Voltera V-One PCB printer, which was introduced in Chapter 3 of this thesis. This approach allows for rapid prototyping and testing, enabling adjustments to be made quickly and efficiently before the final manufacturing process. The use of silver paste ensures good electrical conductivity for the tracks, which is essential for the performance of the system.

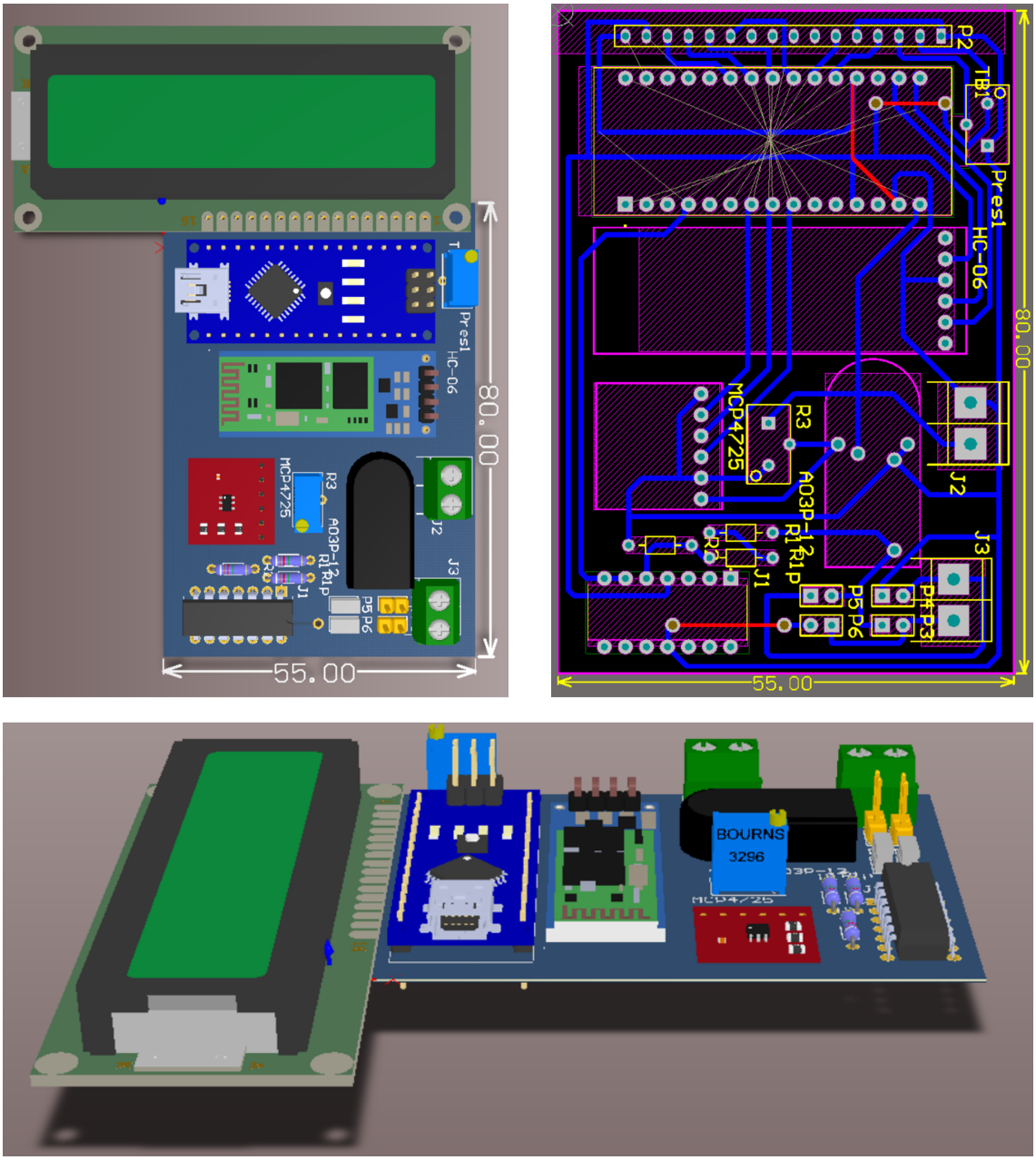


Figure 6.10: 2D and 3D views of the PCB design for the first version of the device, created using Altium Designer Summer 09. The 2D view details the layout of the components and their connections, while the 3D view offers a realistic depiction of the final printed circuit. Dimensions expressed in [mm].

Figure 6.11 displays the device produced using the Voltera V-one printer and after the components have been mounted on the board. The voltage reported by the display is compared with that measured by a multimeter at the output of the electrophoretic source.



Figure 6.11: Left: final device, which was fabricated using the Voltera V-one printer, with all components mounted on the board. Right: The voltage displayed on the device is compared with the voltage measured by a multimeter at the output of the electrophoretic source, providing a comparative analysis of the device's performance and accuracy.

The first version of the device was used to understand the system's dynamic behavior, advantages, and disadvantages. The advantages included the correct operation of the control loop to maintain a constant output voltage and the proper communication between the different components. The key points for improvement in this version were:

- to eliminate the LCD display since the voltage value could be viewed on the mobile app.
- To better utilize the entire dynamic range, it is recommended to use a DC-DC converter with a maximum input voltage of $5V$.
- For a more compact PCB, it is better to use an Arduino microcontroller that includes the Bluetooth module.
- replace most components with their SMD (surface-mount device) version.
- Finally, the output jumpers should be replaced with two solid-state reels to enable automatic selection of the current direction through the APP.

6.3.2 Second version of the device

Following the aforementioned guidelines, we designed and manufactured the second version of the EPS. For this version, we selected the $AGH03P-5$ DC-DC converter. Unlike the $1W$ power converter in the 'A' series, the AGH series offers $1.5W$. As previously mentioned, the component is a single source with a maximum output voltage of $300V$ and a maximum input voltage of $5V$.

Figure 6.12 shows the schematic of the DC-DC converter, including its resistive divider made up of $R5$ and $R6$, which were custom purchased with values of $1G\Omega$ and $100M\Omega$ to create a divider of 0.099. This allows for sensing of approximately $3V$ when the output is $300V$, which is compatible with the Arduino technology. On the right side of the figure, the 2-pin headers have been replaced by 2-channel solid-state relays (AC31S) with optocoupled transistors. When one of them is activated, the current flows in one direction. When it is deactivated and the other is activated, the current flows in the opposite direction. The selected microcontroller for this new version is the Arduino Nano 33 BLE. The device includes a Bluetooth Low Energy module, which is vital for portable device development as it prevents excessive energy consumption during device communication. Only few pins were required from the microcontroller, specifically $D2$ and $D3$ to control the solid state relays, pin $A7$ as an analog input for the source's output voltage, and pins $A4$ and $A5$ for I2C communication with the external DAC. As noted, pin $A7$ includes a reverse Zener diode to protect against potential overvoltages. It is important to keep in mind that our DC-DC converter may generate voltages higher than the maximum when it is underloaded, such as when the paper is dry and the source experiences an open circuit (Figure 6.6).

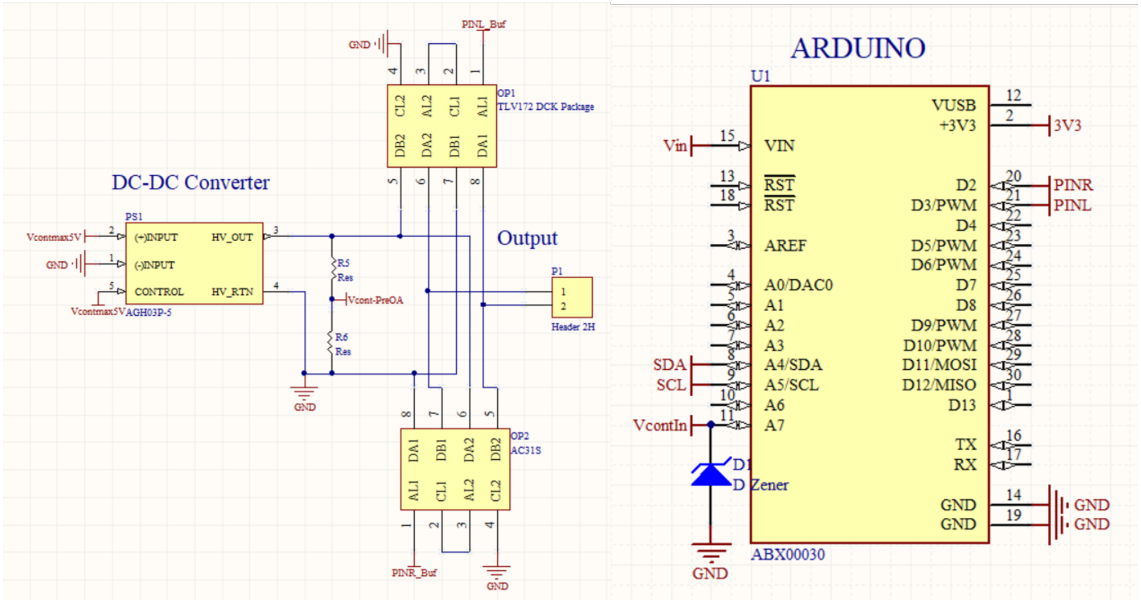


Figure 6.12: Left: Wiring diagram for the $AGH03P-5$ DC-DC converter. It shows the resistive divider made up of $R5$ and $R6$, as well as the solid-state relays used to change the output polarity. Right: Schematic of the Arduino Nano 33 BLE and pinout used.

It would be advantageous to remove the external DAC, as the Arduino already incorporates one, thereby reducing the number of components required and enhancing the overall system compactness. However, this was not possible due to two reasons. Firstly, the pins of the Arduino Nano can only deliver up to $3.3V$, limiting the performance of our source. Secondly, the internal DAC of the Arduino has a lower resolution than the DAC $MCP4725$.

On the right schematic of Figure 6.13, an arrangement with two N-channel MOSFET transistors can be observed, creating a Level Shifter circuit. The Level Shifter configuration is used to convert logic signals of different voltage levels. To be able to use the full input range of the converter (0 to 5 V), the DAC must be connected to 5 V to deliver the maximum voltage when requested. However, since the Arduino handles $3.3V$ logic signals, without the Level Shifter, the DAC will not interpret a logical 1 (a $3.3V$ signal) as such. The previous version of the board explained the use of Buffers. In this version, four op amps are implemented in a follower configuration. One is for the output voltage, as explained above. Two are used to interface the Arduino with the solid-state relays, and the other is used to interface the DAC with the DC-DC converter. The DAC can generate $5V$ but is limited in the current it can deliver, i.e. it cannot generate 1.5 W of power. For this purpose, we selected $AD8534$ integrated circuits. These circuits consist of 4 op-amps, although only one would be sufficient in principle.

However, due to the power requirements, we had to split the buffers into two integrated circuits. Another important aspect of this amplifier is that it is a rail-to-rail input/output single-supply amplifier. This means that it does not require a separate power supply, and if the power supply voltage is 5V, for example, the output voltage is almost 5V as well. There are no significant voltage drops inside the integrated circuit.

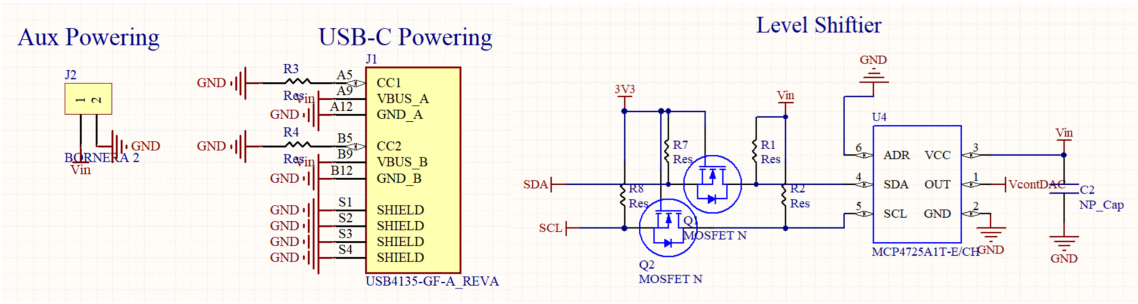


Figure 6.13: Left: Connection diagram of the USC-C port, with the charging resistors necessary to activate the USB OTG or host mode. Right: wiring diagram for the MCP4725 DAC, which is connected to an Arduino microcontroller through a level shifter to ensure compatibility between the two devices.

In addition, in the schematic on the left of Figure 6.13, the incorporation of a USB-C port is observed. The $CC1$ and $CC2$ pins of the USB port are intentionally connected to two resistors. This connection activates the USB OTG or host mode when a smartphone is connected, providing $5V$. Without these resistors, measuring the voltage between GND and VBUS would result in voltages less than $1V$.

Figure 6.14 presents an overview of the complete schematic of the second version of the EPS.

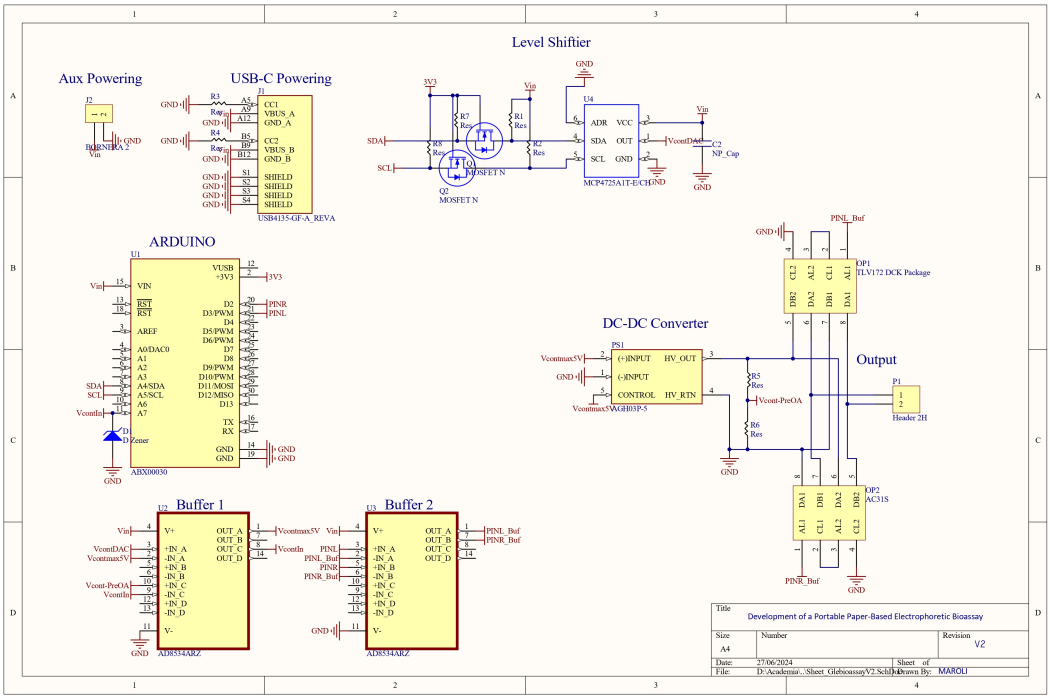


Figure 6.14: Complete overview of Version 2 of the Electrophoretic Power Supply schematic.

The PCB was designed using Altium Designer Summer 09. Figure 6.15 illustrates the routing of components in a $2D$ view and the final printed circuit in a $3D$ view. The $2D$ view presents a complete layout of the components and their interconnections, while the $3D$ view provides a realistic depiction of the final printed circuit. In the lower image of the $2D$ view, it is important to note that the entire PCB is covered in red. This red area represents a copper polygon, which is a contiguous area of copper on a PCB layer. Copper polygons are significant features in PCB design and are used for a variety of purposes, including heat dissipation, grounding, and power distribution. In this design, the copper polygon is connected to the ground plane, which plays a key role in the PCB's performance. It provides a return path for current from different components, reducing the loop area and inductance. Furthermore, the ground plane serves as a shield against electromagnetic interference (EMI), preventing the propagation of electromagnetic waves within the PCB. This reduces the circuit's susceptibility to external interference. The copper polygon is interconnected to GND to minimize interference and enhance the overall performance and reliability of the PCB.

Therefore, the red bend in the $2D$ view is not just an aesthetic choice, but a strategic design decision aimed at enhancing the functionality and efficiency of this PCB. It is evidence of the meticulous planning and careful consideration that goes into every aspect of PCB design.

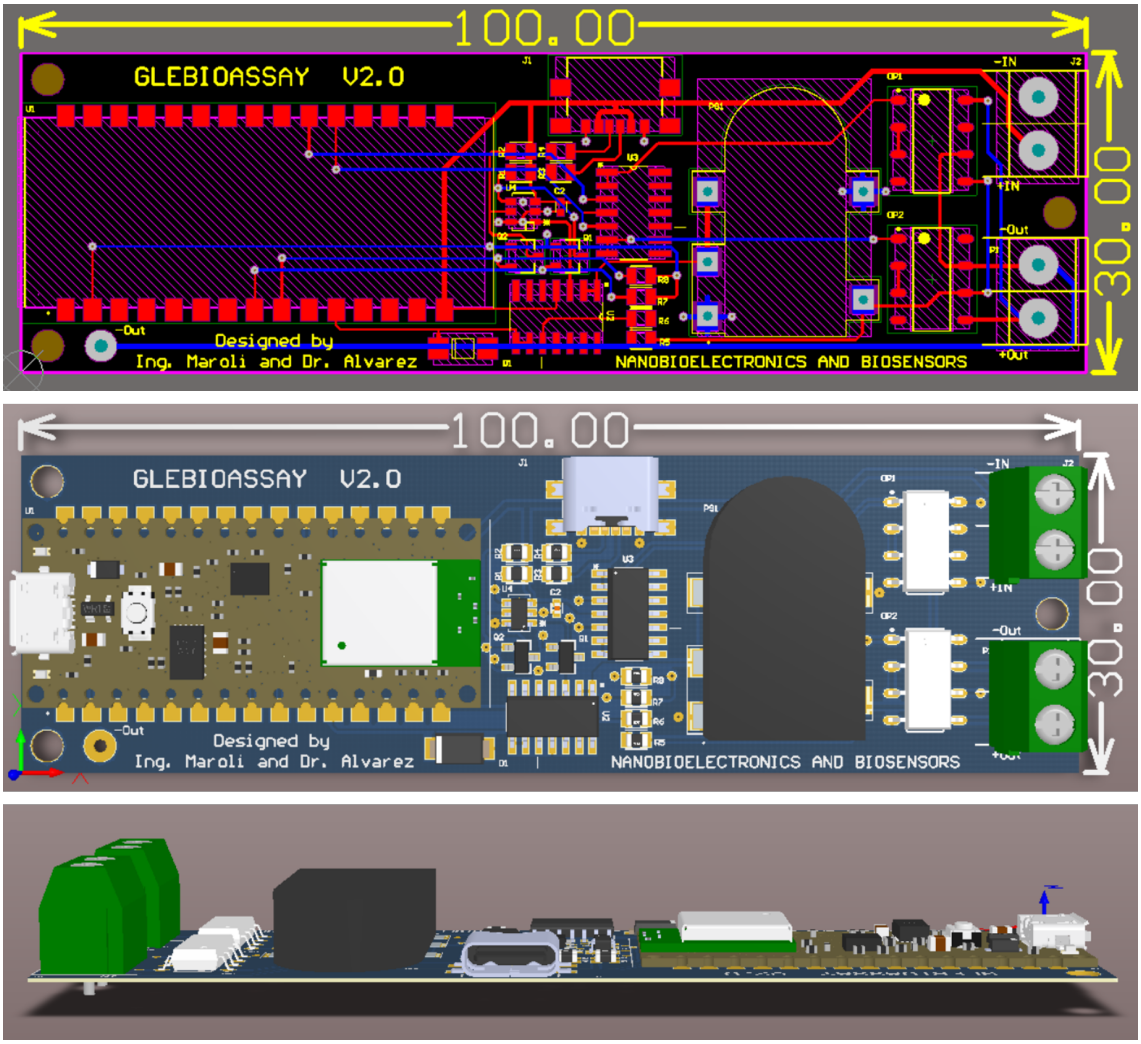


Figure 6.15: 2D and 3D views of the PCB design for the second version of the device, created using Altium Designer Summer 09. The 2D view details the layout of the components and their connections, while the 3D view offers a realistic depiction of the final printed circuit. Dimensions expressed in [mm].

As with the initial version, after finalizing the design, it was prototyped using the Voltera V-One, as illustrated in the top of Figure 6.16. After confirming its proper functionality, the PCB was outsourced to PCB-Way, a China-based service. The board was constructed from FR-4: TG150 material, with a thickness of $1.6mm$. It featured a black solder mask and a 1 Oz copper finish.

To provide context, 1 Oz of copper refers to the thickness of the copper layer on the board. In the section on PCB electrodes, we have explained how this translates to the actual thickness on a board. This PCB version was created as part of a prototyping service. Since none of the dimensions exceeded 100mm, the cost of producing 10 boards was remarkably economical, amounting to only 5 dollars. This cost-effectiveness makes it a viable option for prototyping and small-scale production.

Figure 6.16 shows the image of the PCB obtained before and after the assembly of all its components.

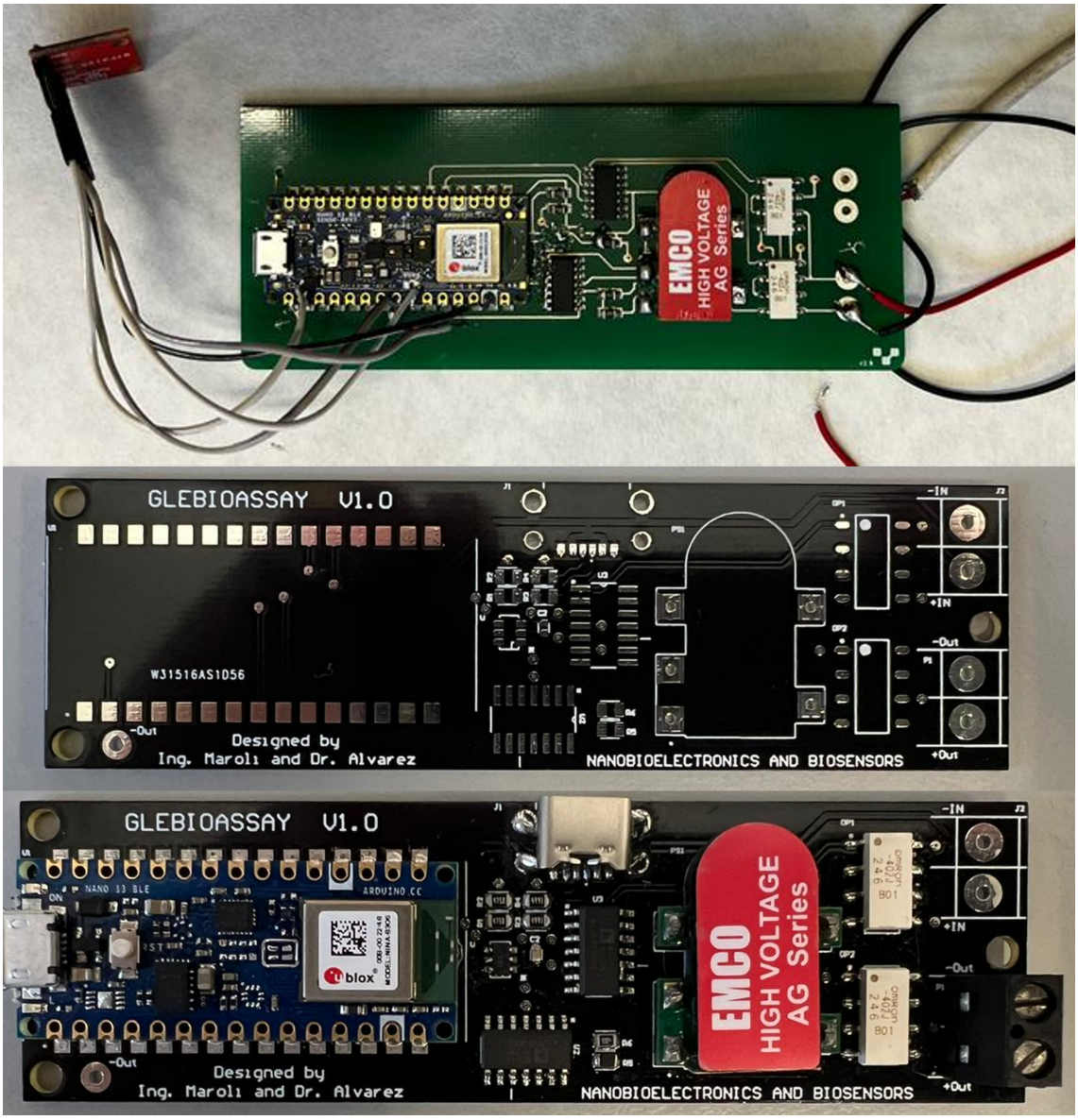


Figure 6.16: The images depict the PCB prototype created with the Voltera V-One (top), the PCB manufactured by PCB-Way, and the final EPS after all components have been assembled (bottom).

The Table 6.1 summarises the fabrication costs for each EPS. From this table, we can draw two important conclusions. Firstly, the device has a manufacturing cost that is significantly lower than what is offered on the market. Additionally, the DC-DC converter accounts for 71.4% of the total value of the electronic circuit. Purchasing more than 100 of these components can reduce its value by over 10%.

Bill of Materials for Electrophoretic Power Supply				
Component Name	Brief description	Quantity	Unit Price	SubTotal
Arduino Nano 33 BLE	Microcontroller	1	27.38€	27.38€
AGH03P-5	DC-DC Converter	1	126.37€	126.37€
USB-C Port	Connector	1	0.71€	0.71€
Molex 39889 – 0042	Fixed Terminal Blocks 5.08MM	2	1.05€	2.1€
AD8534ARZ	Op Amps QUAD CMOS RAIL-TO-RAIL	2	1.78€	3.56€
BS170FTA	MOSFET N-Chnl	2	0.63€	1.26€
MCP4725A3T	Digital-to-Analog Converter	1	1.27€	1.27€
G3VM-402J	Solid state relays	2	4.41€	8.82€
HVCB0805 FDC100M	Thick Film Resistor $100M\Omega$	1	3.95€	3.95€
Resistors	S0805 Resistors -Different Values	7	0.009€	0.063€
PCB	Printed Circuit Board	1	0.46€	0.46€
Total Price	175.94€			

Table 6.1: Table of component costs for the Electrophoretic Power Supply circuit.

6.4 Development and Implementation of Arduino Code

To achieve operational efficiency for the Arduino microcontroller, it is crucial to develop a robust and reliable codebase. This codebase was created using the Arduino Integrated Development Environment (IDE), which significantly streamlines the development process. The IDE offers a user-friendly interface, a wide range of built-in functions, and numerous libraries that simplify microcontroller programming.

Figure 6.17 presents a visual representation of the code's flow, showing the interaction between various functions and states. This flowchart acts as a guide for comprehending the detailed explanations and discussions that follow. Referring to this figure can aid in understanding the code and how it controls the electrophoretic source.

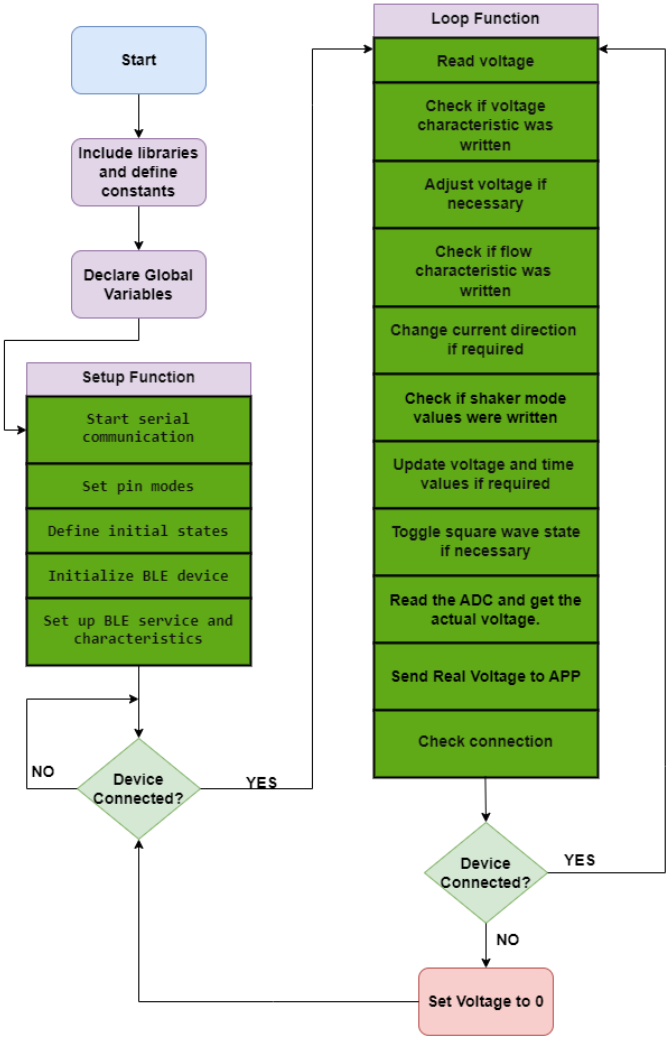


Figure 6.17: Flowchart of the code running inside the Arduino. It shows the different stages of initialisation and the section that runs in loop while the device is connected..

As shown in the flow diagram, one of the initial steps is to incorporate the necessary libraries. In the code the following libraries were used:

- ***ArduinoBLE.h*** provides the necessary functions for using the Bluetooth Low Energy (BLE) capabilities of the Arduino Nano 33 BLE. It enables wireless communication between the Arduino and the mobile app to control the electrophoretic source.

- ***Wire.h*** is used for communication between the Arduino and the DAC via the I2C protocol. The combination of the Adafruit_MCP23017.h and Adafruit_MCP4725.h libraries, along with the Arduino IDE, simplifies the process of sending and receiving data over I2C.

- ***Adafruit_MCP4725.h*** is specifically designed for the MCP4725 digital-to-analog converter (DAC) and provides functions for setting the output voltage of the DAC, which is used to control the voltage of the electrophoretic source.

To understand this flow chart clearly, we can to examine its composition. In the realm of Bluetooth Low Energy, a service refers to a set of data and associated behaviors that enable a specific function or feature of a device. Conversely, a characteristic denotes a data value that is exchanged between the device and the client, which in this case is the mobile app. Each characteristic is identified by a UUID and can have properties such as read, write, and notify to determine how its value can be accessed.

The *loop()* function is the core of the Arduino program, running continuously after the *setup()* function has finished. Within the code, the *loop()* function verifies the availability of a central device and establishes a connection. While the device is connected, it reads the voltage and adjusts it based on the requested voltage. It also checks if the voltage characteristic was written and changes the direction of the current if the flow characteristic was written.

Additionally, if the "shaker mode" values are written, it updates the voltage and time values and toggles the square wave state. The code includes a mechanism for voltage adjustment. If the voltage read is higher than the requested voltage, it is decreased until it matches the requested voltage. Similarly, if the voltage read is lower than the requested voltage, it is increased until it matches the requested voltage. These adjustments are made within the while loops inside the if (diff > 0.001) block. In order to know the error between requested and actual voltage, the difference is calculated objectively as the absolute difference between the two, divided by the actual voltage. This calculation is represented by the $'diff'$ variable in the code. To read the actual voltage, we use the $'analogRead(A7)'$ function, which reads the voltage at the A7 pin of the Arduino. Scale this value to the actual voltage using the formula $'analogRead(A7)/1023.0 * 3.3'$.

Finally, we send the actual voltage to the app. The app receives the actual voltage through the $CaracteristicaRealVolt.\ writeValueLE(Voltage_Read)$ function. This function writes the current voltage value to the *CaracteristicaRealVolt* characteristic, which can be read by the app. The full script is located in Appendix 8 of this thesis.

6.5 Smartphone Application Development

6.5.1 MIT App Inventor

To enable smartphone control of the electrophoretic source, we developed a mobile application (APP) using MIT App Inventor, a user-friendly development environment. This open-source, web-based platform was chosen over programming languages like JAVA for its ease of use. The App Inventor is a platform that enables users to create custom, fully functional mobile applications for Android devices without any prior programming experience. Its intuitive, visual programming environment allows users to drag-and-drop visual objects to create an application that can run on Android devices.

The platform comprises two main parts: the Designer and the Blocks Editor.

The Designer is the primary interface through which the user can modify the visual appearance and overall feel of the application. This visual interface is akin to a flowchart, where various components such as buttons, images, labels, and other elements define the user interface of the app. Each component can have properties specified, such as its color, size, and initial state.

The Blocks Editor is where the behavior of the app is defined. It uses a graphical interface that allows to create application logic by fitting together 'blocks' of code like pieces of a puzzle. These blocks represent various programming constructs, such as variables, loops, and conditionals. This approach abstracts the coding syntax, allowing to focus on the app's logic.

App Inventor also provides access to a wide range of functionality, including GPS location data, accelerometer data, and phone functions, which can be incorporated into the app. Once the app is complete, App Inventor generates an APK file that can be installed on Android devices. The app can also be published on the Google Play Store to share it with others.

6.5.2 User Interface

In order to control the electrophoretic source from the mobile, an ad hoc APP has been developed, using the integrated development environment (IDE) "APP inventor", presented in the previous section. The start-up screen of the APP can be seen in Figure 6.18.

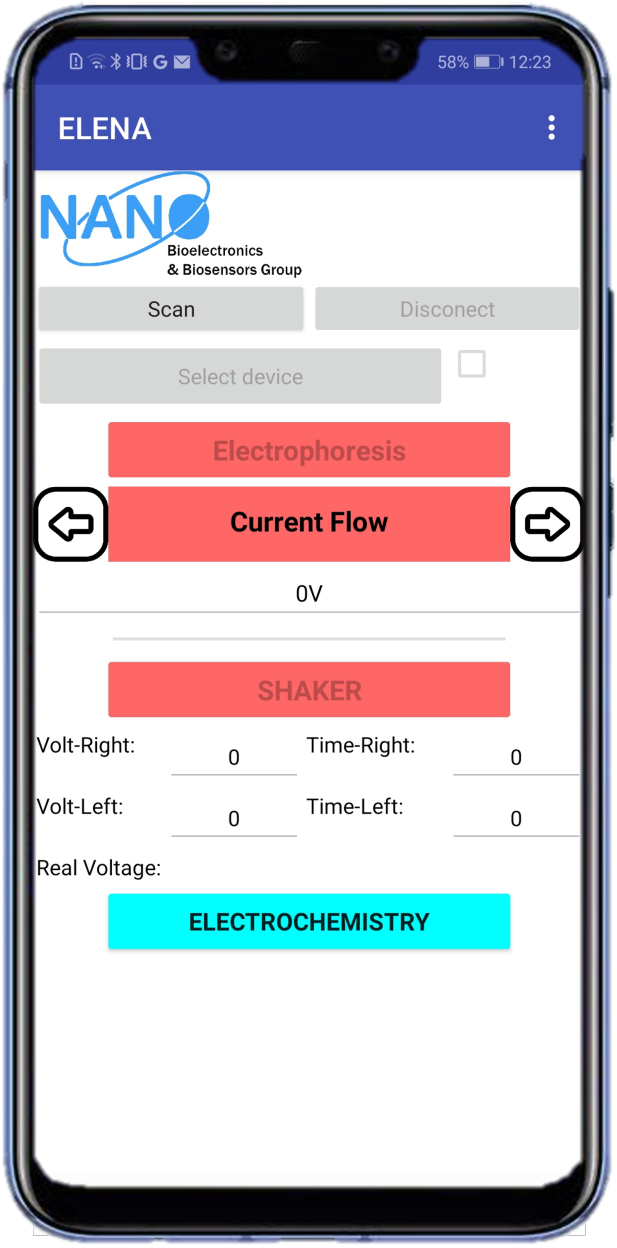


Figure 6.18: Screenshot of the App developed to control the electrophoretic Power Supply. At the top, the device can be connected and disconnected. In the middle is the manual control of the source and at the bottom the Shaker mode and the redirection to the Electrochemistry App.

The application's functionality is described in the following sequence:

- Device Scanning - Upon launching the application, the user initiates a scan for nearby Bluetooth devices by pressing the 'Scan' button. The application then displays a list of detected devices.
- Device Connection - The user selects a device from the list with the aim of connecting to the Arduino that controls the Electrophoretic Power Supply. Upon successful connection, the application activates its control buttons and initiates a timer to periodically monitor the hardware connection status.
- Electrophoresis control: Pressing the 'Electrophoresis' button activates a slider that allows the user to select a voltage value from 0 to 300V. In addition, two arrow buttons are provided for the user to select the current direction. Any changes made by the user to the slider value or current direction are sent to the hardware via Bluetooth.
- Shaker mode: Pressing the 'Shaker' button disables the voltage slider and activates four text boxes, two for voltage and two for time. This mode is used to generate a square wave voltage. The information entered in these boxes is sent to the hardware via Bluetooth. If a value changes, the updated information is sent again. Pressing the 'Shaker' button again will disable these text boxes and send a zero to the hardware, ensuring no output voltage from the electrophoretic source.
- Connection monitoring: A control timer periodically checks that the unit remains connected. If so, the timer is reset. If not, a message is displayed indicating that the unit has been disconnected.
- Disconnect: When the user presses the 'Disconnect' button, a zero is sent, Bluetooth communication is terminated, all buttons are disabled and a message indicating 'The device has been disconnected' is displayed.
- Chemister Redirection: At the bottom of the application, there is a button labelled 'ELECTROCHEMISTRY'. When this button is pressed, the application will redirect to another application called 'Chemister'.

This application offers a user-friendly interface for controlling the electrophoretic source. It provides adjustable voltage, allows for current direction selection, and includes a shaker mode for generating a square wave voltage. The system also includes robust connection monitoring and easy disconnection, enhancing user experience and system reliability. Additionally, a redirection button to the 'Chemister' application adds further functionality. To comprehend the functioning of the application, refer to Figure 6.19 for a flow chart. The programming blocks used for the application can be found in Appendix 8.

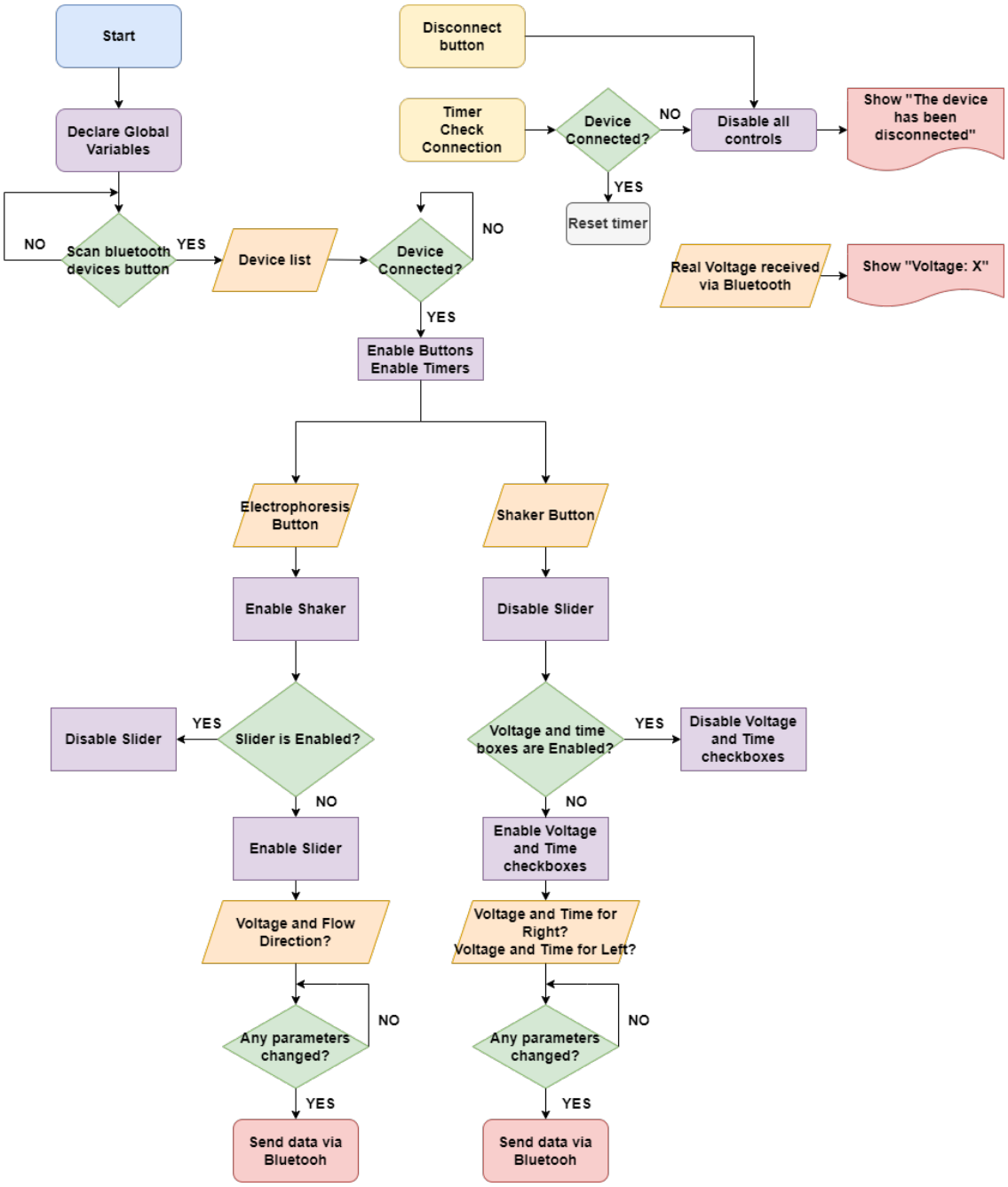


Figure 6.19: Flowchart of the Smartphone App developed with MIT App Inventor.

6.6 Housing Development

Hardware and software development are essential components of the device, yet they represent merely one part of the entire system. The design process involves creating a housing unit that accommodates the PCB, provides space for the buffers containing solutions, and houses the substrate (nitrocellulose) in which the electrophoresis runs. The paper strip is placed between the buffers, which are electrically connected using platinum wires.

The design of these housing units was accomplished using the 2017 version of Solidworks software. This powerful tool for creating $3D$ models provides a wide range of features that simplify the design process. The initial design utilized plastic Eppendorf tubes, which were connected to the source through two platinum wires of $0.025mm$ diameter. These wires were coiled around a steel wire that was electrically connected to the PCB. While this design demonstrated the hardware's operational principles, it had limitations. For example, the strip did not remain completely flat, which is very important for the device's proper functioning, as is shown in Figure 6.20.



Figure 6.20: On the left, the housing with plastic Eppendorf where the nitrocellulose strip was not flat. On the right, one of the first proposed solutions where a lateral flow cassette was used to keep the strip flat.

To address this issue, we considered using a Lateral Flow cassette. We made two perforations at the ends of the cassette and introduced an absorption pad, which is more malleable than nitrocellulose, as is shown in Figure 6.20. The absorption pads were then inserted into the Eppendorf tubes. This design change helped to keep the strip flat.

In the third iteration of the device, we substituted the commercial plastic Eppendorf tubes with custom-made stainless steel ones Figure 6.21. These metallic reservoirs could be directly connected to the source without the need for auxiliary cables.



Figure 6.21: Next improvement of the housing where the plastic eppendors were replaced by stainless steel eppendors to connect the director to the source. The top of the housing was modified to fit the side flow case.

However, the low buffer volume did not allow for maintaining a constant pH of the solution. As shown in Figure 6.22, the Bromophenol Blue indicator changes colour from blue (alkaline pH) to yellow (pH below 3.5) after a certain running time.

This change is caused by the migration of buffer ions, with anions migrating to the positive pole and cations to the negative pole. This depletion of the buffer generates highly acidic zones at one end and highly alkaline pH at the other end. An attempt was made to back-mix the buffer using the shaker mode, however, it was not homogenised. Instead, two distinct zones of alkaline and acidic pH were generated, as illustrated in Figure 6.22c.

To address this limitation, we have developed larger reservoirs that incorporate 0.5 mm diameter platinum wires. These wires are soldered to a magnet, which magnetically connects to another magnet connected by a cable to the PCB. These new reservoirs can hold more than 10 ml of buffer, which is expected to maintain a constant pH.

Furthermore, we have replaced the Lateral Flow cassette with a piece that has a slot where the nitrocellulose is placed directly. The device's new version underwent an iterative design process that involved 3D printing and machining (Figure 6.23). This process included multiple versions and improvements, highlighting the significance of prototyping and testing in developing a robust and reliable device.

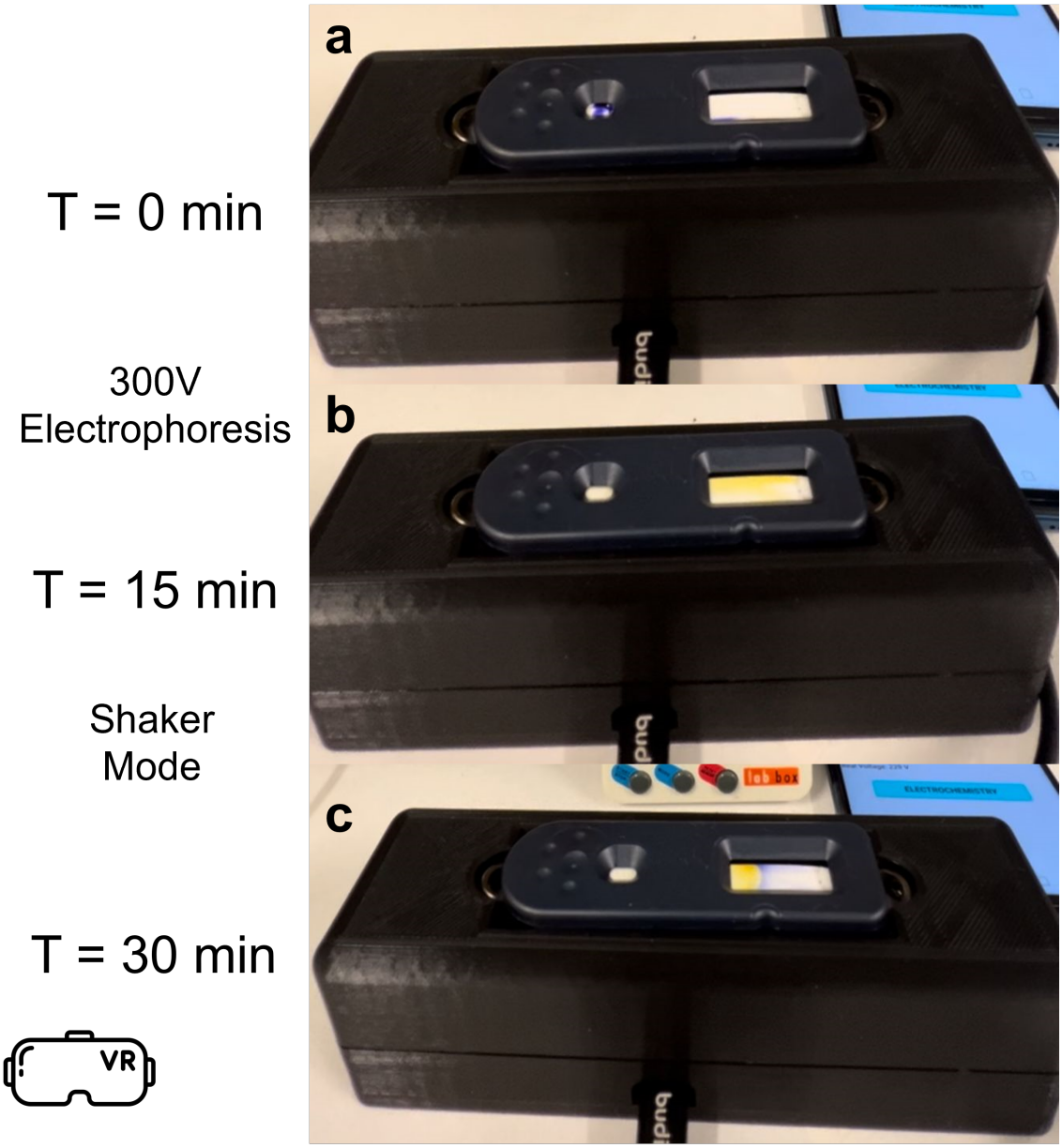


Figure 6.22: a) Bromophenol Blue drop on the sample holder before starting the electrophoresis. b) After 15 minutes the drop reaches the detection window (in this case there is no recognition element) and the colour of the drop has changed to yellow due to the pH change. c) Shaker mode is implemented and 2 zones of acidic and alkaline pH are well defined.https://youtu.be/aDAqDQ2kfI4



Figure 6.23: The Final Electrophoretic device. On the right the 3D printed device in PLA. The buffer reservoirs were coated with varnish to make them waterproof. On the left, the machined device. The reservoirs are made of methacrylate and a platinum wire goes through the reservoirs and contacts the source with magnets. The nitrocellulose support was 3D printed with resin.

6.7 Characterization

To evaluate the performance of the electrophoretic source, systematic runs using 1 mM Bromophenol Blue were conducted. The experiments employed two different buffer solutions, Borate Buffer (pH = 8.4) and Phosphate Buffer(pH = 7), at concentrations of 10 mM and 100 mM. Furthermore, the assays were performed across a range of voltages: 99 V, 150 V, 201 V, 249 V, and 300 V.

Firstly, electrophoretic runs were conducted using 1mM Bromophenol Blue in a 10mM Borate Buffer. A 1μl droplet was deposited onto the nitrocellulose, and the distance it travelled was observed over a period of 30 minutes.

This procedure was repeated for five different voltage settings: 99 V, 150 V, 201 V, 249 V, and 300 V. The graph in Figure 6.24 illustrates that, in all cases, the relationship between distance and run time was linear. By analysing the slope of the lines, we determined the mobility of bromophenol blue in this specific buffer. This was achieved by utilising the equation from the section 6.1.1, where $\mu = \frac{d.L}{\Delta V.t}$, we calculate the following mobilities, $\mu_{99} = 1.30\ \frac{\mu m.cm}{V.s}$, $\mu_{150} = 1.15\ \frac{\mu m.cm}{V.s}$, $\mu_{201} = 1.05\ \frac{\mu m.cm}{V.s}$, $\mu_{249} = 1.09\ \frac{\mu m.cm}{V.s}$, $\mu_{300} = 1.04\ \frac{\mu m.cm}{V.s}$. Obtaining an average mobility of $\mu = 1.13 \pm 0.11\ \frac{\mu m.cm}{V.s}$. Although very close values would be expected, observations indicate that for low voltages, the mobility value is slightly elevated, up to 25% higher. This phenomenon may be attributed to a number of factors. For instance, at higher voltages, a greater current flows, which, due to the Joule effect, partially dries the nitrocellulose strip, thereby increasing its resistance.

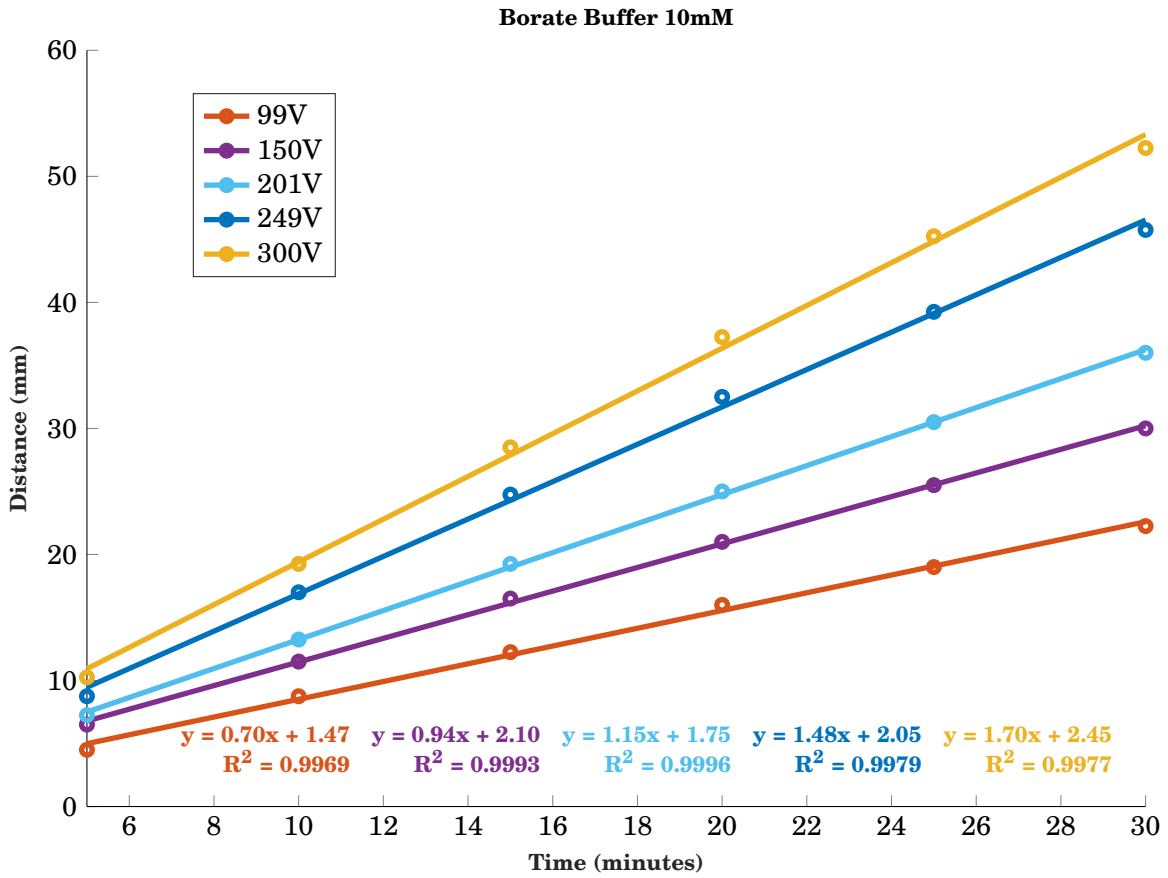


Figure 6.24: Electrophoretic runs of 1 μl of 1 mM Bromophenol Blue in 10 mM Borate Buffer at five different voltages. The displacement distance vs. time has been plotted. It can be seen that for all cases the response is linear.

Subsequently, the concentration of the borate buffer was changed from 10 mM to 100 mM. The results are presented in Figure 6.25. Initially, it can be observed that the response is not linear for voltages exceeding 150 V. This is due to the inherent limitations of our EPS. As previously outlined in this chapter, the DC-DC converter has a power rating of 1.5 W. This implies that the maximum current that can be applied at 300 V is 5 mA. In contrast to the observations made in the 10 mM borate buffer, the electrical resistance of the nitrocellulose strip and the buffer in this instance is significantly lower. Furthermore, as the sample traverses the strip, it leaves residual matter behind, creating low-impedance pathways.

Consequently, at a certain point the resistance drops too low and due to the power limitation of the device, the applied potential drops, consequently the electric field strength decreases. This ultimately leads to a stagnation of the sample, which is reflected in an asymptotic response. In order to analyse the mobility, it is possible to consider the results obtained for 99 V and 150 V, given that for the 100 mM buffer concentration the other results are not linear. The results of the aforementioned tests yielded $\mu_{99} = 1.17\ \frac{\mu m.cm}{V.s}$ and $\mu_{150} = 0.91\ \frac{\mu m.cm}{V.s}$. As can be observed

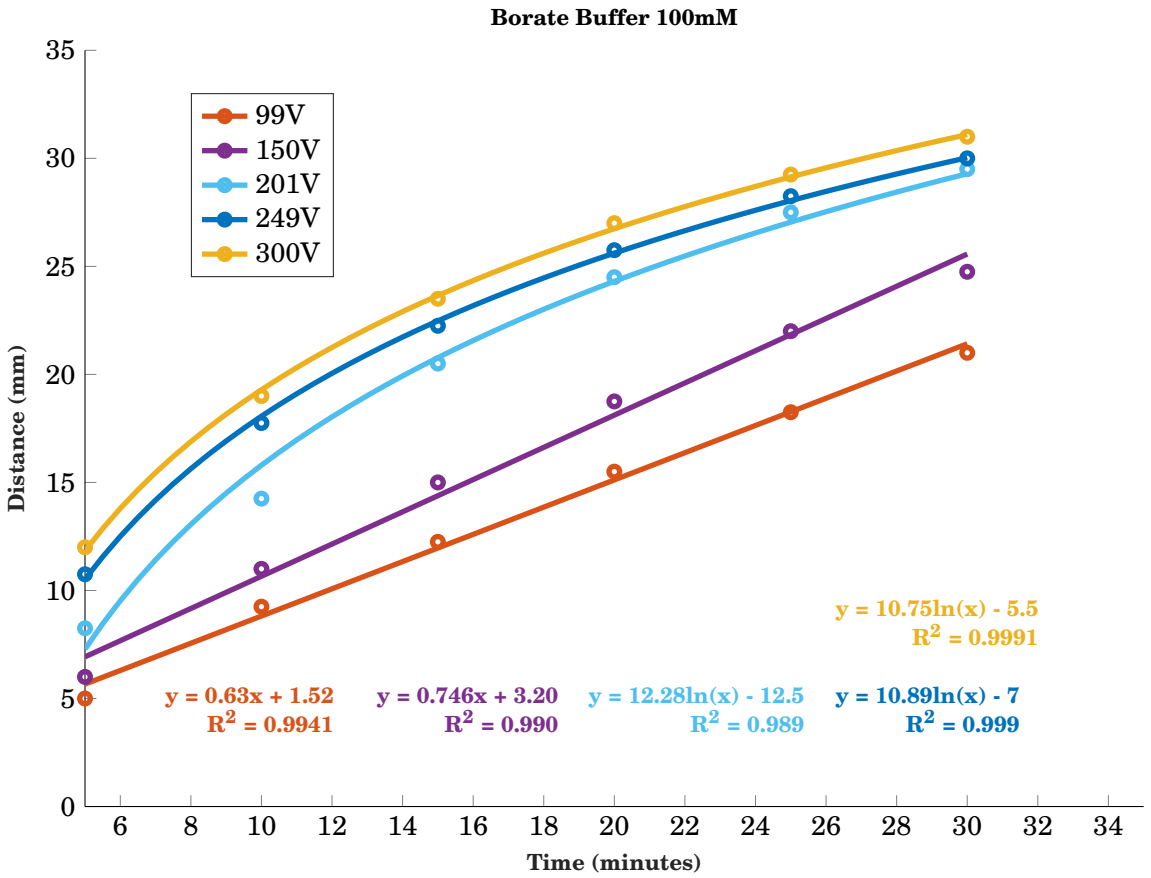


Figure 6.25: Electrophoretic runs of 1 μl of 1 mM Bromophenol Blue in 100 mM Borate Buffer at five different voltages. The displacement distance vs. time has been plotted. It can be seen that only for voltages of 99 V and 150 V the response is linear, while for higher voltages it becomes logarithmic.

in both cases, the mobility is lower than when the concentration of the buffer is lower. This phenomenon can be attributed to the influence of ionic strength, which was previously discussed in the introductory section of this chapter (Figure 6.2).

In addition to the borate buffer, another buffer used to study the behaviour of the EPS was the phosphate buffer with a pH of 7. Figure 6.26 illustrates the results obtained when the concentration of the buffer was 10 mM. Once more, the response is linear for this concentration. However, in contrast to the borate buffer, a significantly lower slope than expected was observed during the 300 V test, indicating a notable reduction in mobility. In light of this discrepancy, the test was repeated on three separate occasions, yielding comparable outcomes each time and straight lines consistently below the 249 V result. The mobilities obtained were as follows: $\mu_{99} = 1.28\ \frac{\mu m.cm}{V.s}$, $\mu_{150} = 1.26\ \frac{\mu m.cm}{V.s}$, $\mu_{201} = 1.04\ \frac{\mu m.cm}{V.s}$, $\mu_{249} = 0.96\ \frac{\mu m.cm}{V.s}$, $\mu_{300} = 0.71\ \frac{\mu m.cm}{V.s}$.Obtaining an average mobility of $\mu = 1.05 \pm 0.23\ \frac{\mu m.cm}{V.s}$.

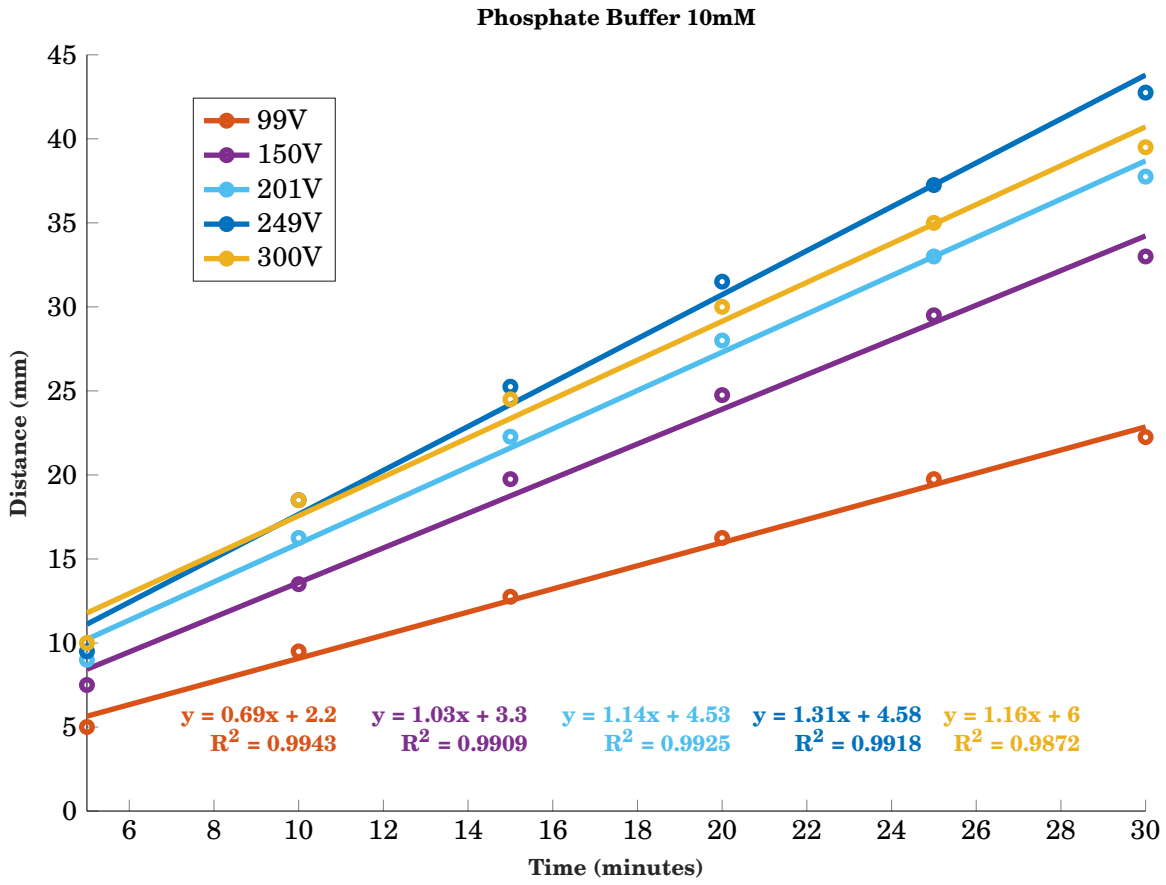


Figure 6.26: Electrophoretic runs of 1 μl of 1 mM Bromophenol Blue in 10 mM Phophate Buffer at five different voltages. The displacement distance vs. time has been plotted. It can be seen that for all cases the response is linear. However for 300 V slope is lower than expected

However, if the mobility obtained for 300 V is disregarded due to its anomalous nature, the average mobility for the other four is $\mu = 1.13 \pm 0.16 \ \frac{\mu m.cm}{V.s}$. This value is the same as that of the borate buffer at 10 mM. Furthermore, a similar behaviour is observed, whereby the mobilities for 99 V and 150 V are found to be very similar to each other and approximately 25% higher than the others.

As with the borate buffer, a higher concentration of phosphate buffer results in a decrease in electrical resistance due to an increase in ions on the nitrocellulose strip. Consequently, in electrophoretic tests, only the first two cases yield a linear response. However, for voltages exceeding 150 V, the response becomes logarithmic. The mobilities obtained for the first two cases were $\mu_{99} = 1.28 \ \frac{\mu m.cm}{V.s}$ and $\mu_{150} = 0.88 \ \frac{\mu m.cm}{V.s}$. A comparison of these mobilities with those obtained for the 10 mM concentration demonstrates the effect of ionic strength as expected.

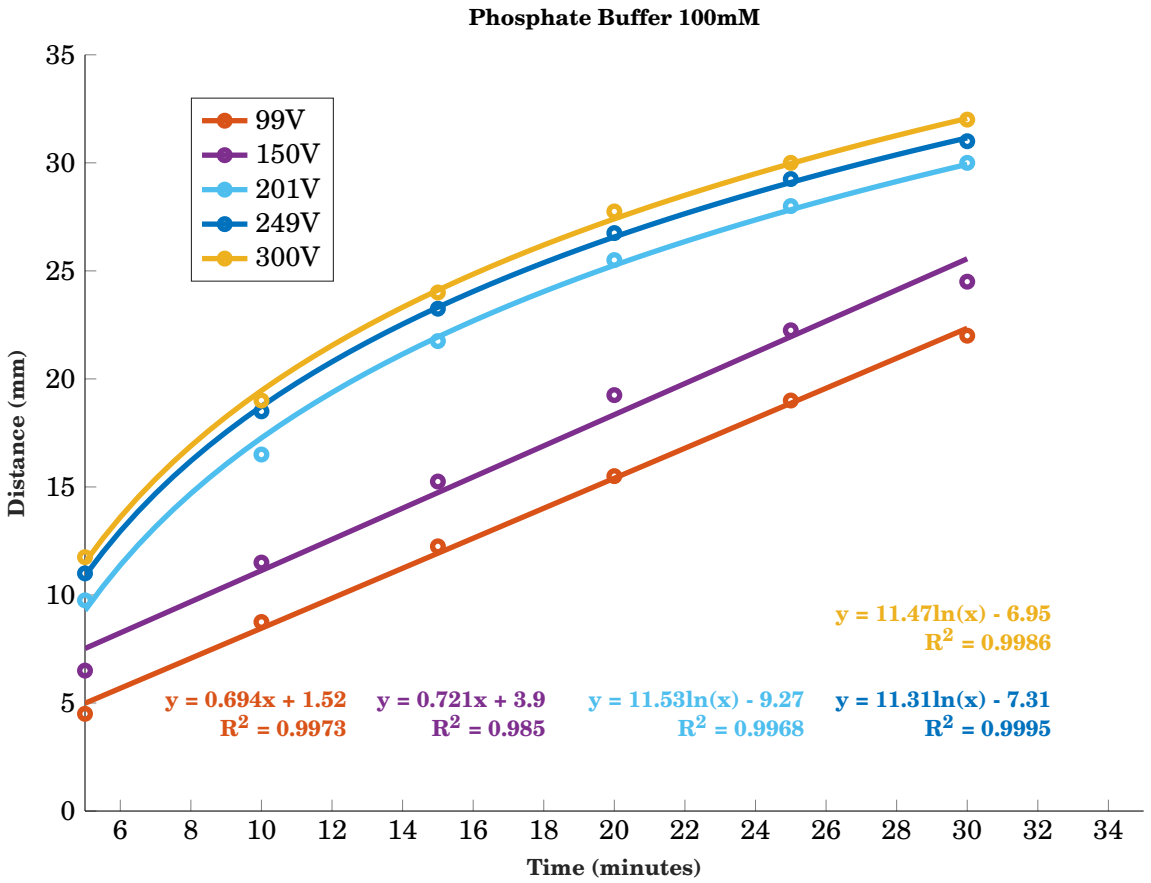


Figure 6.27: Electrophoretic runs of 1 μl of 1 mM Bromophenol Blue in 100 mM Phosphate Buffer at five different voltages. The displacement distance vs. time has been plotted. It can be seen that only for voltages of 99 V and 150 V the response is linear, while for higher voltages it becomes logarithmic.

A comparison of the mobilities obtained for the two buffer concentrations reveals that, for the 99 V voltage, the mobility is identical, whereas for the 150 V case, there is a clear ionic strength effect, resulting in a significant reduction in the mobility of Bromophenol Blue. Following the assessment of the device's performance with a single compound, we proceeded with the separation of three compounds. For this purpose, we employed the a tipical DNA loading dye, typically used in electrophoretic separations, the TriTrack, which, in addition to bromophenol blue, contains xylene cyanol FF and orange G. In light of the outcomes observed in previous experiments, an initial separation test was conducted at 201 V using 10 mM Borate Buffer, with 1 μl of TriTrack as the stock solution (6x).

Figure 6.24, which corresponds to the Bromophenol Blue assay in 10 mM Borate Buffer, indicates that after 15 minutes, the compound had moved by 19 mm, and after 30 minutes, by 36 mm. In agreement with these results, in Figure 6.28, it can be seen that the dye in the center, Bromophenol Blue, reaches displacements similar to those expected, albeit with a slight

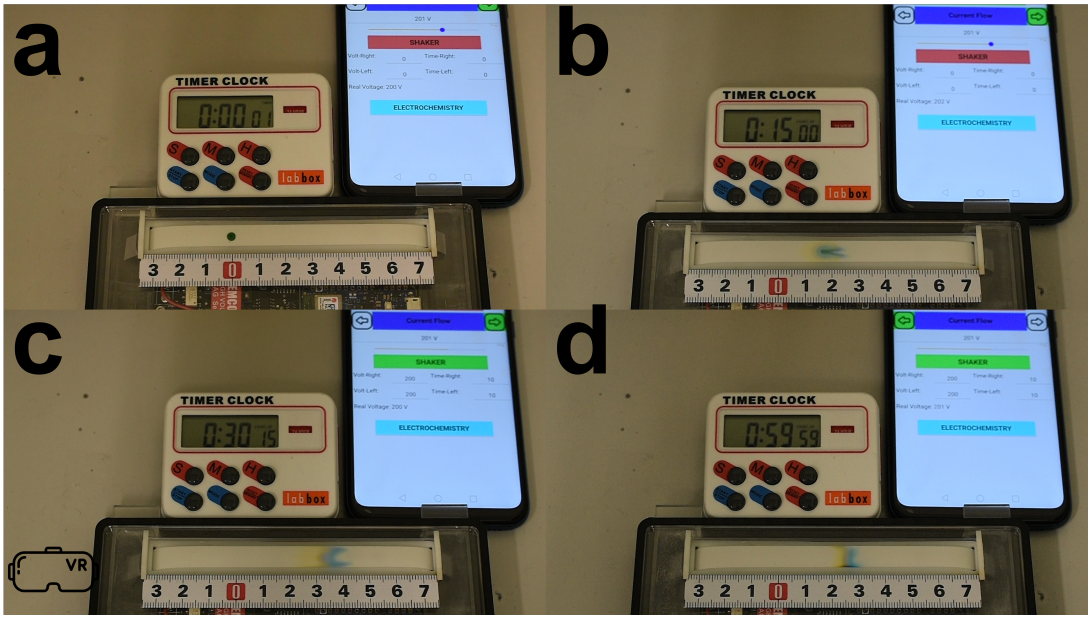


Figure 6.28: a) A droplet of TriTrack 6X is placed on the nitrocellulose at 0 on the scale. b) After 15 minutes the sample reaches 2 cm displacement and begins to separate. c) After 30 minutes, the sample is separated, but dispersed. d) Shaker mode is implemented by applying 200 V to each side for 10 seconds. The separation is better defined after 30 minutes.https://youtu.be/D0MFp07oTIg

reduction due to interactions with other dyes. Conversely, due to the high concentration of TriTrack, it is challenging to achieve a complete separation. At this juncture, the shaker mode of the device becomes pertinent, enabling the attainment of a well-defined separation. This involves the concentration of each of the dyes in three distinct stripes. As a counterpart, the sample tends to migrate towards the centre of the device, as a consequence of the electric fields.

To improve the separation of the TriTrack, its concentration was reduced 6-fold to 1X. The conditions of the previous experiment were repeated, resulting in a much more appreciable separation, while the mobility of Bromophenol Blue was the same as that observed in the individual assay. This is a crucial point, as a compound's mobility is a fundamental parameter in electrophoretic identification. In these two experiments, we have demonstrated the significance of accurately determining the concentration of the dye load, as erroneous conclusions may be drawn due to interferences if this is not done correctly.

To conclude the characterization of the EPS, another buffer, $TRIS \cdot HCl$(pH = 4), which is widely used in classical electrophoresis, was utilized. The concentration employed was 100 mM, and a voltage of 201 V was applied. As shown in Figure 6.30 and the associated video, the sample does not exhibit displacement with a laminar flow front or a flat front, as observed in previous tests. Instead, in this case, the TriTrack migrates towards the edges, leaving a depleted area in the center (Figure 6.30a). This behaviour has been observed in other experiments, particularly

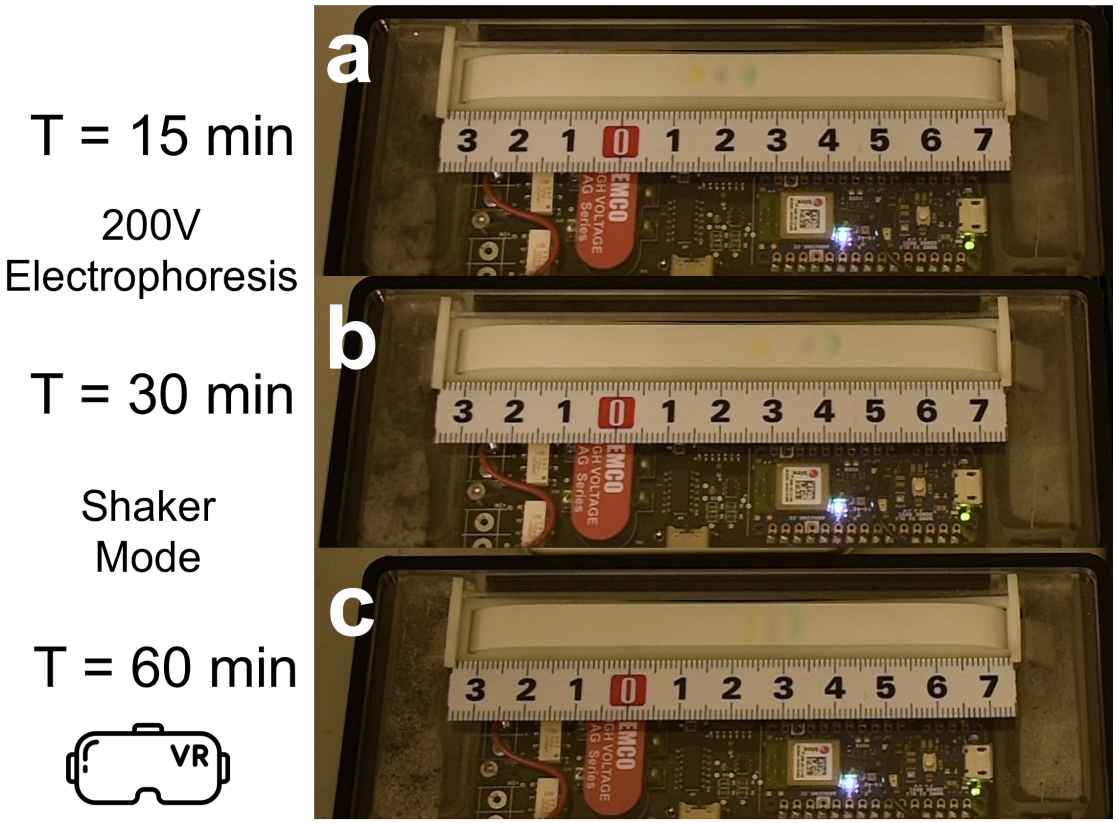


Figure 6.29: Separation of TriTrack 1X, in Borate Buffer 10 mM applying 200 V. a) After 15 minutes the dyes are already separated. b) After 30 minutes the separated dyes begin to diffuse in the nitro. c) 30 minutes of shaking is applied to reconcentrate the dyes with the drawback that the dyes tend to move towards the centre of the strip.https://youtu.be/9l1v-xUeFCc

when Eppendorfs were used as buffer reservoirs. The underlying issue is a pH change caused by the migration of cations from the buffer to the negative pole, the cathode, indicating that the buffer is not fulfilling its intended function. Despite this, separation can still be achieved, although the Bromophenol Blue changes from blue to yellow, leading to confusion with Orange G. In order to atemp to homogenize the pH, the Shaker mode was employed, applying 200 V on each side for 5 seconds over 30 minutes. This resulted in well-defined dye lines; however, the pH remained acidic near the cathode (left side of the source) and basic near the anode (right side of the source) (Figure 6.30d).



Figure 6.30: Separation of TriTrack 6X, in $TRIS \cdot HCl$ Buffer 100 mM applying 200 V. a) After 15 minutes, a channel was observed in the centre of the dye, which corresponded to the migration of the cations towards the negative pole, the cathode. b) After 30 minutes, the flow front is partially homogenised, and two colours are visible, due to the turning of the bromophenol blue from blue to yellow. c) Shaker mode is applied for 30 minutes at 200 V for 5 seconds per side. d) It is shown how the anode is left with a basic solution while the cathode is left with an acidic solution.https://youtu.be/KVHKFqHjOX8

6.8 Electrochemical Readout

Performing electrochemical measurements simultaneously with an electrophoretic run is inherently complex and requires careful planning and execution. Without proper precautions, an improper connection can result in ground loops, potentially causing significant damage to the potentiostat. To successfully integrate these two processes, such as conducting chronoamperometry while the sample undergoes electrophoretic displacement, galvanic isolation between the EPS and the potentiostat is essential. Here, the NFC potentiostat, introduced in Chapter 3, becomes particularly relevant.

This potentiostat operates by harvesting energy through its antenna from a mobile device, creating a natural galvanic isolation. This setup ensures that the ground reference of the potentiostat is isolated from the ground of the EPS. The mobile device powers the EPS via the USB cable, therefore it shares the same ground, however the potentiostat remains isolated due to its wireless power transfer. Consequently, the voltage applied between the Working Electrode and the Reference Electrode in the potentiostat is entirely independent of the EPS, avoiding potential interference and ensuring accurate electrochemical measurements. This galvanic isolation is

critical for maintaining the integrity of the electrochemical data while the electrophoretic process is ongoing.

To ascertain the efficacy of this approach, the initial step involved the separation of dopamine from ascorbic acid, while chronoamperometry was employed.

It is important to highlight that in an electrophoresis experiment aimed at separating ascorbic acid from dopamine, the order in which these compounds reach the detector is significant. Ascorbic acid typically precedes dopamine due to several factors. Firstly, under the typical electrophoresis conditions, ascorbic acid carries a negative charge, making it highly mobile towards the anode. This rapid migration is facilitated by its small molecular size and high charge-to-mass ratio compared to dopamine. Conversely, dopamine may exist in a neutral or less negatively charged state at neutral pH, resulting in slower movement through the separation medium. At neutral to alkaline pH levels, ascorbic acid exists predominantly in its anionic form, further enhancing its mobility towards the anode. Dopamine, depending on its protonation state, may exhibit less pronounced movement under these conditions.

It is therefore reasonable to conclude that ascorbic acid will arrive at the detector before dopamine in an electrophoretic separation experiment, given the charge, size, and electrophoretic mobility of the molecules. In this assay, lab-made screen printed electrodes connected to the NFC potentiostat were used. The electrode was simply rested on the nitrocellulose ensuring proper contact with the nitrocellulose. The result of the chronoamperometry, which is in line with the expected. is shown in Figure 6.31.

As shown in Figure 6.31, it is not practical to work with the SPE and the antenna printed with silver ink in addition to the small FR4 PCB to interface the chip. Therefore, to create a compact device, the electrode PCBs introduced in the previous chapter were integrated into the system. Both the electrode and the antenna were fabricated on a single flexible Kapton PCB.

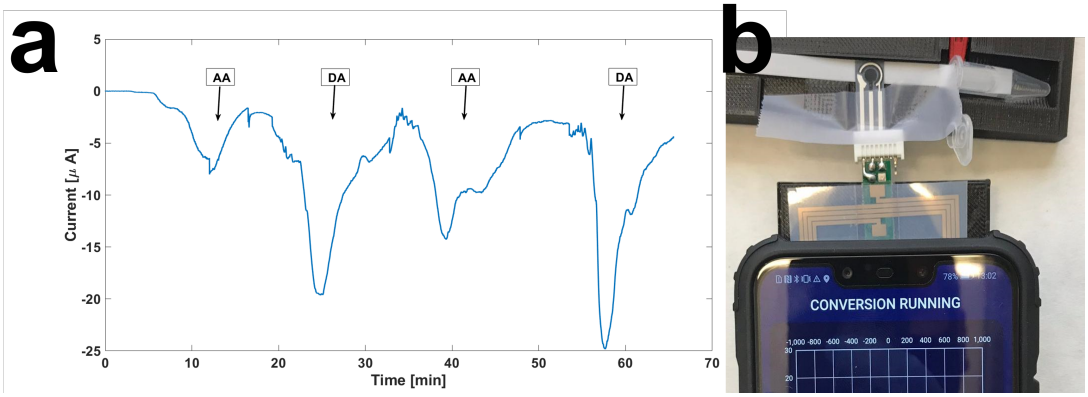


Figure 6.31: a) Chronoamperometry of the separation of Ascorbic Acid and Dopamine. The mixture was added twice to the system, so that two peaks of each component appear. b) The setup used was that of screen-printed electrodes, with the antenna printed with silver ink.

In particular, for the EPS, an even smaller antenna was designed to fit into the nitrocellulose holder, 12 mm side, 13 turns, 150 μm trace width and 100 μm trace spacing. Figure 6.32 illustrates the PCB electrode, the antenna, and its positioning on the nitrocellulose holder. Additionally, a chronoamperometry test was conducted to assess the electrode's performance in detecting ascorbic acid.

It is evident that this platform possesses considerable potential. The capacity to perform electrochemical readings during electrophoresis is a highly advantageous feature, as, for example, it eliminates the necessity for the use of dyes, which have been demonstrated to influence the mobility of molecules. Furthermore, these electrodes and others can be functionalised to perform a specific biorecognition assay. The potential applications of this technology are numerous. This chapter was focused on the development of the tool, demonstrating its capabilities and limitations.

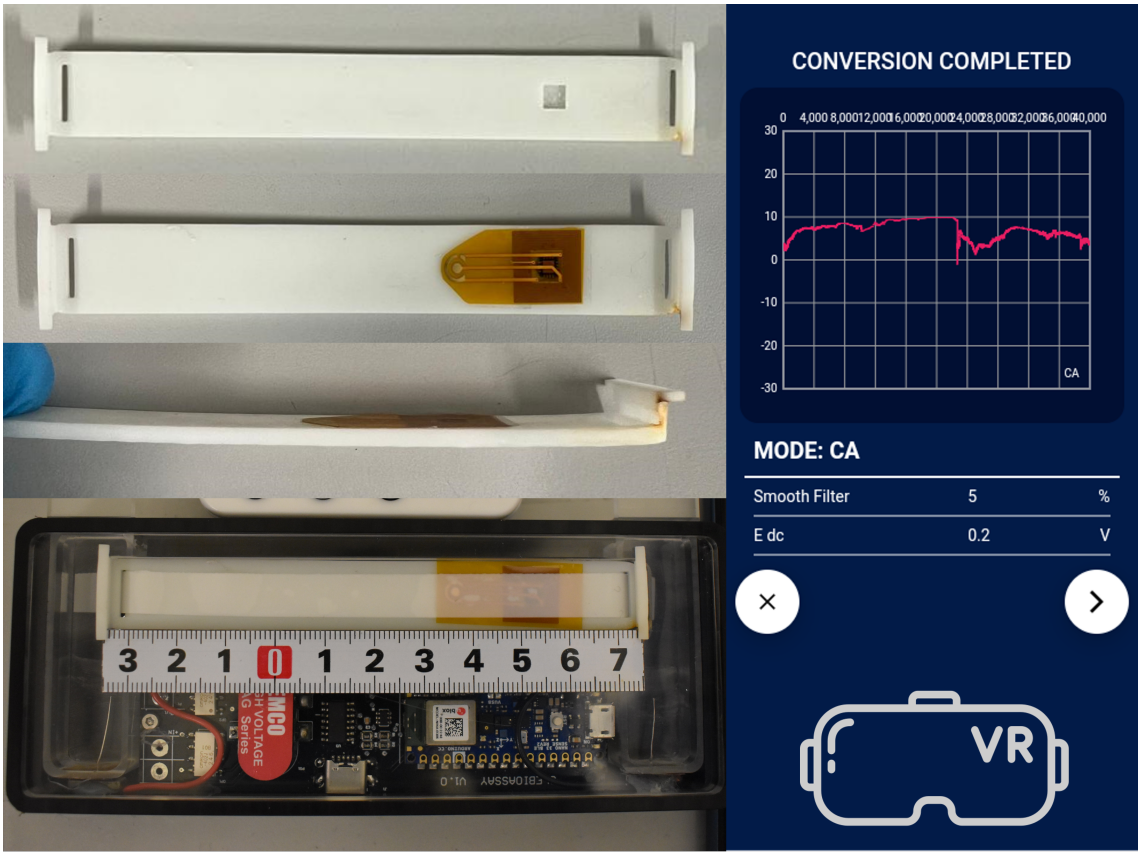


Figure 6.32: On the left, the nitrocellulose support with the PCB electrode and antenna system is shown. At the bottom, with the nitrocellulose already wet, it can be seen how it is added to the electrode. On the right, a screenshot of the chronoamperometry performed for the detection of ascorbic acid is displayed.

6.9 Conclusions of the chapter

In this chapter, we have shown the development of a portable electrophoretic device, which has great potential to become a PoC device that integrates electrophoresis and electrochemical detection in a compact and easy-to-use platform. This chapter detailed the iterative design process and technical refinements that led to a functional and efficient device capable of supporting real-time diagnostic applications.

1. **Successful Integration of Electrophoresis and Electrochemical Sensing:**

   The chapter demonstrated how the device integrates both electrophoresis and electrochemical sensing within a portable form factor. The synergy between electrophoretic separation and subsequent electrochemical detection promises high specificity and sensitivity in analyzing complex biological samples. This dual-functionality is pivotal for rapid diagnostics, allowing for the detection of various biomarkers and analytes with minimal sample preparation. Further testing is still required for proper demonstration.

2. **Enhanced Design and Prototyping:**

   Multiple iterations of the device were undertaken, from initial conceptual designs to fully functional prototypes. Key advancements included:

   - **Electronic Design:** The integration of a versatile power supply with DC-DC converters and microcontrollers enabled precise control over the electrophoretic process. This ensured stable and accurate voltage application, critical for consistent electrophoretic runs.
   - **Software Development:** The development of Arduino code and a smartphone application facilitated user interaction and device control. The smartphone app, developed using MIT App Inventor, provided a seamless interface for device operation, data acquisition, and real-time monitoring.
   - **Housing and Portability:** The evolution of the device housing, from basic 3D-printed pieces to refined machined components, enhanced the durability, functionality, and portability of the system. Improvements in the housing design also contributed to the stability and reproducibility of electrophoretic runs.

3. **Validation of Electrophoretic and Electrochemical Performance:**

   Comprehensive characterization and validation of the device's performance were conducted through various tests and experimental runs:

   - **Electrophoretic Runs:** The device's ability to perform consistent and reliable electrophoretic separations was demonstrated through experiments with Bromophenol

Blue in different buffer systems. Linear and logarithmic displacement responses under varying voltages validated the device's adaptability to different requirements.

- **Electrochemical Readout:** The integration of screen-printed electrodes and antenna-based energy harvesting enabled effective chronoamperometric detection of analytes like ascorbic acid and dopamine. This was validated by clear, reproducible signals corresponding to the electrophoretic separation of these analytes.

4. **Innovations in Energy Harvesting and Galvanic Isolation:**

   The chapter highlighted the innovation of utilizing NFC for energy harvesting, which provided a key advantage in terms of galvanic isolation. This isolation ensures that the electrochemical measurements remain unaffected by the electrophoretic power supply, enhancing the accuracy and reliability of the diagnostic results.

5. **Potential for Broader Applications:**

   The successful development and validation of this electrophoretic device open avenues for broader applications in medical diagnostics, environmental monitoring, and biochemical research. The portability and integration capabilities make it suitable for various POC settings, including remote and resource-limited environments.

CHAPTER 7

CONCLUSION AND FUTURE DIRECTIONS

Key Findings of the Thesis and Future Research Directions

Development of Pocketable Sensor Interfaces

The research successfully developed compact, portable sensor capable of wireless communication. These sensors, utilizing the SIC4340 and SIC4341 chips, demonstrated their applicability in various sensor systems, including wearables for humidity and temperature sensing, and surface myography for muscle contraction measurements.

These commercial chips have great potential, however in the future it would be desirable to be able to design our own chip, understanding the limitations of these ICs, and in the light of new CMOS technologies, I believe that we can develop a chip with better performance, even incorporating the processing of information in situ.

Printed Sensors for Wearables

A technique for printing sensors on fragile substrates, such as mussel-inspired free-standing membranes, was developed using a Voltera V-one printer. In contrast to ink-based printers, this device can dispens pastes of different materials.

There are several future challenges in this field. First of all, it is necessary to improve the mechanical strength of the brittle substrate used in our paper. Also, it is necessary to find a way to miniaturise the device, due to the conductivity of the silver pastes it is necessary to make antennas of 35cm, when for wearables it would be advisable to have something below 5cm, similar to the kapton antenna used in the electrophoretic device.

Development and Application of Electrochemical Electrodes

The thesis explored three types of innovative electrochemical electrodes: nanoband electrodes, laser-induced graphene electrodes (LIGEs), and PCB electrodes. Each type demonstrated unique advantages in sensitivity, cost-effectiveness, and scalability:

- **Nanoband Electrodes**: Provided heightened sensitivity and rapid functionalization, crucial for detecting low concentrations of analytes, despite challenges related to fabrication costs.
- **LIGEs**: Presented a scalable method for creating porous graphene structures through laser irradiation, allowing precise patterning and customization suitable for flexible electronics and biosensors.
- **PCB Electrodes**: Offered a low-cost alternative for PoC devices without compromising performance, proving beneficial for disposable applications.

All these electrodes are tools in themselves. Their applicability is very wide. Although most of them have been in development for years, getting electrodes that are truly reproducible is complex. Despite the problems seen with PCB-electrodes, I believe they can be an excellent alternative for single-use devices.

Electrophoretic Sources

The thesis delved into the development and characterization of an electrophoretic power supply for biosensing applications. These sources provided a reliable means to generate and control electrophoretic motion within microfluidic devices, potentially enhancing the sensitivity and specificity of biosensors. This work contributed to the broader field of electrophoretic manipulation and its integration into lab-on-a-chip systems.

This is the most ambitious project for the future, the development of the device has been shown in the present thesis, but due to time constraints a biosensor as such was not developed. Further testing of this source in combination with electrochemical readout is planned for the future. Especially taking advantage of the Shaker mode to concentrate the sample on the working electrode and to improve incubation times.

These findings collectively underscore the advancements made in the field of biosensors, particularly in the development of portable, cost-effective, and high-performance sensor systems. The innovations in sensor interfaces, printed sensors, electrochemical electrodes, and electrophoretic sources in combination with the NFC technology offer significant contributions to wearable technology and PoC diagnostics, paving the way for future research and practical applications.

BIBLIOGRAPHY

[1] Bankmycell. 2024. “How Many Smartphones Are In The World? (2024)”.

[2] Steve Moss. 2021. “From “brick” to smartphone: the evolution of the mobile phone”. 10.1557/s43577-021-00067-7.

[3] ABS. 2022. “IBM Simon, the first smartphone of the history”.

[4] Science Museum Group. 2001. “World First Camera Phone the Kyocera VP-210”.

[5] Zhaoxin Geng et al. 2017. “Recent progress in optical biosensors based on smartphone platforms”. 10.3390/s17112449.

[6] Chet Haase. 2022. “Androids: The team that built the android operating system”.

[7] Rossana E. Madrid et al. 2022. “Smartphone-Based Biosensor Devices for Healthcare: Technologies, Trends, and Adoption by End-Users”. 10.3390/bioengineering9030101.

[8] M Mosa, I Yoo, and L Sheets. 2012. “A systematic review of healthcare applications for smartphones. BMC Med.Inf. Decision Making”. doi:10.1186/1472-6947-12-67.

[9] Robin Singh Chandel et al. 2021. “Smart watches: A review of evolution in bio-medical sector”. 10.1016/j.matpr.2021.07.460.

[10] Selin Olenik, Hong Seok Lee, and Firat Güder. 2021. “The future of near-field communication-based wireless sensing”. 10.1038/s41578-021-00299-8.

[11] Daniel Quesada-González and Arben Merkoçi. 2017. “Mobile phone-based biosensing: An emerging “diagnostic and communication” technology”. 10.1016/j.bios.2016.10.062.

[12] Xidi Sun et al. 2022. “Wearable Near-Field Communication Sensors for Healthcare: Materials, Fabrication and Application”. 10.3390/mi13050784.

[13] The Huy Bui et al. 2023. “Smartphone-Based Portable Bio-Chemical Sensors: Exploring Recent Advancements”. 10.3390/chemosensors11090468.

[14] Lingyan Kong et al. 2024. “Wireless Technologies in Flexible and Wearable Sensing: From Materials Design, System Integration to Applications”. 10.1002/adma.202400333.

[15] Aiguo Wu and Waheed S. Khan. 2020. “Nanobiosensors: From design to applications”. 10.1002/9783527345137.

[16] Duygu Beduk et al. 2023. “Smart Multiplex Point-of-Care Platform for Simultaneous Drug Monitoring”. 10.1021/acsami.3c06461.

[17] Thanh Binh Nguyen, Viet Thang Tran, and Wan Young Chung. 2019. “Pressure Measurement-Based Method for Battery-Free Food Monitoring Powered by NFC Energy Harvesting”. 10.1038/s41598-019-53775-1.

[18] Stephen P. Lee et al. 2018. “Highly flexible, wearable, and disposable cardiac biosensors for remote and ambulatory monitoring”. 10.1038/s41746-017-0009-x.

[19] Tutku Beduk et al. 2022. “Smartphone-Based Multiplexed Biosensing Tools for Health Monitoring”. 10.3390/bios12080583.

[20] Chen Chen and Junsheng Wang. 2020. “Optical biosensors: An exhaustive and comprehensive review”. 10.1039/c9an01998g.

[21] Diming Zhang and Qingjun Liu. 2016. “Biosensors and bioelectronics on smartphone for portable biochemical detection”. 10.1016/j.bios.2015.08.037.

[22] George S. Luka et al. 2021. “Portable on-chip colorimetric biosensing platform integrated with a smartphone for label/PCR-free detection of Cryptosporidium RNA”. 10.1038/s41598-021-02580-w.

[23] Curtis T. Rueden et al. 2017. “ImageJ2: ImageJ for the next generation of scientific image data”. 10.1186/s12859-017-1934-z.

[24] Johannes Schindelin et al. 2015. “The ImageJ ecosystem: An open platform for biomedical image analysis”. 10.1002/mrd.22489.

[25] Liming Hu et al. 2022. “Selection and characterisation of bioreceptors to develop nanoparticle-based lateral-flow immunoassays in the context of the SARS-CoV-2 outbreak”. 10.1039/d2lc00486k.

[26] Ana Rubio-Monterde, Daniel Quesada-González, and Arben Merkoçi. 2023. “Toward Integrated Molecular Lateral Flow Diagnostic Tests Using Advanced Micro- and Nanotechnology”. 10.1021/acs.analchem.2c04529.

[27] Amadeo Sena-Torralba et al. 2022. “Toward Next Generation Lateral Flow Assays: Integration of Nanomaterials”. 10.1021/acs.chemrev.1c01012.

[28] David N. Breslauer et al. 2009. “Mobile phone based clinical microscopy for global health applications”. 10.1371/journal.pone.0006320.

[29] Isa Navruz et al. 2013. “Smart-phone based computational microscopy using multi-frame contact imaging on a fiber-optic array”. 10.1039/c3lc50589h.

[30] Manoj Kumar Kanakasabapathy et al. 2017. “Rapid, label-free CD4 testing using a smartphone compatible device”. 10.1039/c7lc00273d.

[31] Hongying Zhu et al. 2011. “Cost-effective and compact wide-field fluorescent imaging on a cell-phone”. 10.1039/c0lc00358a.

[32] Xin Meng et al. 2017. “Smartphone based hand-held quantitative phase microscope using the transport of intensity equation method”. 10.1039/c6lc01321j.

[33] Derek Tseng et al. 2010. “Lensfree microscopy on a cellphone”. 10.1039/c003477k.

[34] Seung Ah Lee and Changhuei Yang. 2014. “A smartphone-based chip-scale microscope using ambient illumination”. 10.1039/c4lc00523f.

[35] Liyun Guan et al. 2014. “Barcode-like paper sensor for smartphone diagnostics: An application of blood typing”. 10.1021/ac503300y.

[36] José Francisco Bergua et al. 2021. “Lateral flow device for water fecal pollution assessment: From troubleshooting of its microfluidics using bioluminescence to colorimetric monitoring of genericEscherichia coli”. 10.1039/d1lc00090j.

[37] Weronika Schary et al. 2022. “Open-Source, Adaptable, All-in-One Smartphone-Based System for Quantitative Analysis of Point-of-Care Diagnostics”. /doi.org/10.3390/diagnostics12030589.

[38] Nadine Urban et al. 2021. “OptoAssay – Light-controlled Dynamic Bioassay Using Optogenetic Switches”. https://doi.org/10.1101/2021.11.06.467572.

[39] Monika Colombo et al. 2023. “Real-time, smartphone-based processing of lateral flow assays for early failure detection and rapid testing workflows”. 10.1039/d2sd00197g.

[40] Emine Guler et al. 2017. “Mobile Phone Sensing of Cocaine in a Lateral Flow Assay Combined with a Biomimetic Material”. 10.1021/acs.analchem.7b03017.

[41] Wenbin Hao et al. 2022. “Smartphone-Based Photothermal Lateral Flow Immunoassay Using Rhenium Diselenide Nanosheet”. 10.1021/acsami.2c22616.

[42] Ahyeon Koh et al. 2017. “A soft, wearable microfluidic device for the capture, storage, and colorimetric sensing of sweat Ahyeon”. 10.1126/scitranslmed.aaf2593.

[43] Li Ju Wang et al. 2017. “A multichannel smartphone optical biosensor for high-throughput point-of-care diagnostics”. 10.1016/j.bios.2016.09.021.

[44] Frank N. Crespilho. 2023. “Covid-19 Metabolomics and Diagnosis: Volume 2”. 10.1007/978-3-031-27922-5.

[45] Jie Wu et al. 2023. “Device integration of electrochemical biosensors”. 10.1038/s44222-023-00032-w.

[46] Alexander C. Sun and Drew A. Hall. 2019. “Point-of-Care Smartphone-based Electrochemical Biosensing”. 10.1002/elan.201800474.

[47] Jinhong Guo. 2017. “guo-2017-smartphone-powered-electrochemical-dongle-for-point-of-care-monitoring-of-blood-β-ketone.pdf”. 10.1021/acs.analchem.7b02531.

[48] Terrance Frederick Fernandez et al. 2021. “Hardware-software interfacing in smartphone centered biosensing”. 10.1016/B978-0-12-823727-4.00017-1.

[49] Giulio Rosati et al. 2022. “A plug, print & play inkjet printing and impedance-based biosensing technology operating through a smartphone for clinical diagnostics”. 10.1016/j.bios.2021.1137

[50] H. Ceren Ates et al. 2022. “End-to-end design of wearable sensors”. 10.1038/s41578-022-00460-x.

[51] Alar Ainla et al. 2018. “Open-Source Potentiostat for Wireless Electrochemical Detection with Smartphones”. 10.1021/acs.analchem.8b00850.

[52] Sayan Sarkar and Manisha Bhattacharya. 2020. “SStat: Wi-Fi and Bluetooth integrated Multimodal Do-It-Yourself Electrochemical Potentiostat”. 10.1109/IECON43393.2020.9254701.

[53] Antonio Lazaro et al. 2023. “Recent Advances in Batteryless NFC Sensors for Chemical Sensing and Biosensing”. 10.3390/bios13080775.

[54] Luis Antonio Panes-Ruiz et al. 2018. “Toward Highly Sensitive and Energy Efficient Ammonia Gas Detection with Modified Single-Walled Carbon Nanotubes at Room Temperature”. 10.1021/acssensors.7b00358.

[55] Sakda Jampasa et al. 2022. “Resistance-Based Lateral Flow Immunosensor with a NFC-Enabled Smartphone for Rapid Diagnosis of Leptospirosis in Clinical Samples”. 10.1021/acs.analchem.2c02409.

[56] Cui Ye et al. 2024. “A wearable aptamer nanobiosensor for non-invasive female hormone monitoring”. 10.1038/s41565-023-01513-0.

[57] Jiaobing Tu et al. 2023. “A wireless patch for the monitoring of C-reactive protein in sweat”. 10.1038/s41551-023-01059-5.

[58] Robert P. Hirten et al. 2024. “Longitudinal assessment of sweat-based TNF-alpha in inflammatory bowel disease using a wearable device”. 10.1038/s41598-024-53522-1.

[59] Minqiang Wang et al. 2022. “A wearable electrochemical biosensor for the monitoring of metabolites and nutrients”. 10.1038/s41551-022-00916-z.

[60] Yansong Gai et al. 2022. “Small Methods - 2022 - Gai - A Self-Powered Wearable Sensor for Continuous Wireless Sweat Monitoring (1).pdf”. 10.1002/smtd.202200653.

[61] Tuo Xie et al. 2019. “A Wi-Fi-based wireless indoor position sensing system with multipath interference mitigation”. 10.3390/s19183983.

[62] Ezgi Tan, İbrahim Mizan Kahyaoglu, and Selcan Karakus. 2022. “A sensitive and smartphone colorimetric assay for the detection of hydrogen peroxide based on antibacterial and antifungal matcha extract silver nanoparticles enriched with polyphenol”. 10.1007/s00289-021-03857-w.

[63] Guoqing Zhang. 2020. “A wearable device for health management detection of multiple physiological parameters based on ZigBee wireless networks”. 10.1016/j.measurement.2020.108168.

[64] Abbas Dehghani et al. 2023. “Recent Advances and Challenges in Internet of Things (IoT)-Based Smartphone Biosensors for COVID-19 and Zika Viruses Detection: A Review”. 10.1109/JSEN.2023.3314656.

[65] Fan Wu et al. 2021. “Edge-Based Hybrid System Implementation for Long-Range Safety and Healthcare IoT Applications”. 10.1109/JIOT.2021.3050445.

[66] Marco Cattani, Carlo Alberto Boano, and Kay Römer. 2017. “An experimental evaluation of the reliability of lora long-range low-power wireless communication”. 10.3390/jsan6020007.

[67] Panagiotis Gkotsiopoulos, Dimitrios Zorbas, and Christos Douligeris. 2021. “Performance determinants in LoRa networks: A literature review”. 10.1109/COMST.2021.3090409.

[68] Nutcha Larpant et al. 2019. “Sensing by wireless reading Ag/AgCl redox conversion on RFID tag: universal, battery-less biosensor design”. 10.1038/s41598-019-49245-3.

[69] Petar Kassal et al. 2015. “Smart bandage with wireless connectivity for uric acid biosensing as an indicator of wound status”. 10.1016/j.elecom.2015.03.018.

[70] Yuanjing Lin, Mallika Bariya, and Ali Javey. 2021. “Wearable Biosensors for Body Computing”. 10.1002/adfm.202008087.

[71] Le Cai et al. 2021. “Osseosurface electronics—thin, wireless, battery-free and multimodal musculoskeletal biointerfaces”. 10.1038/s41467-021-27003-2.

[72] Simiao Niu et al. 2019. “A wireless body area sensor network based on stretchable passive tags”. 10.1038/s41928-019-0286-2.

[73] Michele Borgese et al. 2017. “An Inkjet Printed Chipless RFID Sensor for Wireless Humidity Monitoring”. 10.1109/JSEN.2017.2712190.

[74] Giada Marchi et al. 2023. “Tailoring the Performance of a Nafion 117 Humidity Chipless RFID Sensor: The Choice of the Substrate”. 10.3390/s23031430.

[75] Florian Requena et al. 2022. “Combined Temperature and Humidity Chipless RFID Sensor”. 10.1109/JSEN.2022.3189845.

[76] N. Javed, M. A. Azam, and Y. Amin. 2021. “Chipless RFID Multisensor for Temperature Sensing and Crack Monitoring in an IoT Environment”. 10.1109/LSENS.2021.3083218.

[77] Soo Hong Min et al. 2020. “Stretchable chipless RFID multi-strain sensors using direct printing of aerosolised nanocomposite”. 10.1016/j.sna.2020.112224.

[78] Kevin Mc Gee, Prince Anandarajah, and Collins David. 2021. “Strain sensor”. https://doi.org/10.3390/s2118622

[79] Minjae Ku et al. 2020. “Smart, soft contact lens for wireless immunosensing of cortisol”. 10.1126/sciadv.abb2891.

[80] Baptiste Garnier et al. 2023. “Textile dual-band NFC-A4WP (13.56–6.78 MHz) combiner for wireless energy and data transmission for connected clothing”. 10.1038/s41598-023-31832-0.

[81] Saikat Banerjee and Gymama Slaughter. 2022. “Flexible battery-less wireless glucose monitoring system”. 10.1038/s41598-022-16714-1.

[82] Yong Suk Oh et al. 2021. “Battery-free, wireless soft sensors for continuous multi-site measurements of pressure and temperature from patients at risk for pressure injuries”. 10.1038/s41467-021-25324-w.

[83] Dengfeng Li et al. 2024. “Battery-free, wireless, and electricity-driven soft swimmer for water quality and virus monitoring”. 10.1126/sciadv.adk6301.

[84] Mohammad Zulqarnain et al. 2020. “A flexible ECG patch compatible with NFC RF communication”. 10.1038/s41528-020-0077-x.

[85] Do Hee Keum et al. 2020. “Wireless smart contact lens for diabetic diagnosis and therapy”. 10.1126/sciadv.aba3252.

[86] Zhenghan Shi et al. 2022. “Wearable battery-free theranostic dental patch for wireless intraoral sensing and drug delivery”. 10.1038/s41528-022-00185-5.

[87] Gabriel Maroli et al. 2024. “Wearable, battery-free, wireless multiplexed printed sensors for heat stroke prevention with mussel-inspired bio-adhesive membranes”. https://doi.org/10.1016/j.bios.

[88] Antonio Lazaro et al. 2019. “Battery-Less Smart Diaper Based on NFC Technology”. 10.1109/JSEN.2019.2933289.

[89] Karnpimon Krorakai et al. 2021. “Smartphone-based nfc potentiostat for wireless electrochemical sensing”. 10.3390/app11010392.

[90] P. Escobedo et al. 2022. “Smart facemask for wireless CO2 monitoring”. 10.1038/s41467-021-27733-3.

[91] Rongzhou Lin et al. 2020. “Wireless battery-free body sensor networks using near-field-enabled clothing”. 10.1038/s41467-020-14311-2.

[92] Gang Xu et al. 2019. “Battery-Free and Wireless Epidermal Electrochemical System with All-Printed Stretchable Electrode Array for Multiplexed In Situ Sweat Analysis”. 10.1002/admt.201800658.

[93] Pablo Escobedo et al. 2021. “Flexible Strain and Temperature Sensing NFC Tag for Smart Food Packaging Applications”. 10.1109/JSEN.2021.3100876.

[94] Longqing Zhang et al. 2018. “Fresh-Water Fish Quality Traceability System Based on NFC Technology”.

[95] Ramakant Kumar et al. 2021. “Smart Sensing for Agriculture: Applications, Advancements, and Challenges”. 10.1109/MCE.2021.3049623.

[96] Caroline Peres et al. 2021. “Development of a low-power underwater nfc-enabled sensor device for seaweed monitoring”. 10.3390/s21144649.

[97] Jeonghyun Kim et al. 2017. “Miniaturized Battery-Free Wireless Systems for Wearable Pulse Oximetry”. 10.1002/adfm.201604373.

[98] Tauseef Hussain et al. 2023. “Wearable Sensors for Respiration Monitoring: A Review”. 10.3390/s23177518.

[99] Frederic Flament et al. 2021. “Skin moisture assessment using Hydration Sensor Patches coupled with smartphones via Near Field Communication (NFC). A pilot study with the first generation of patches that allow self-recordings of skin hydration”. 10.1111/srt.13049.

[100] Marti Boada et al. 2019. “Battery-Less NFC Sensor for pH Monitoring”. 10.1109/ACCESS.2019.2904109.

[101] Luke J. Currano et al. 2018. “Wearable Sensor System for Detection of Lactate in Sweat”. 10.1038/s41598-018-33565-x.

[102] Chen Cheng et al. 2021. “Battery-free, wireless, and flexible electrochemical patch for in situ analysis of sweat cortisol via near field communication”. 10.1016/j.bios.2020.112782.

[103] George Cheng. 2023. “A Continuous Oral-fluid Monitoring of Glucose (O.M.G.) Device with Near-field & Bluetooth Communication Capability”. 10.47611/jsrhs.v12i3.4805.

[104] H. Ceren Ates et al. 2021. “Wearable devices for the detection of COVID-19”. 10.1038/s41928-020-00533-1.

[105] P. Irving, R. Cecil, and M. Z. Yates. 2021. “MYSTAT: A compact potentiostat/galvanostat for general electrochemistry measurements”. 10.1016/j.ohx.2020.e00163.

[106] Qiuyue Yang et al. 2022. “Wearable and fully printed microfluidic nanosensor for sweat rate, conductivity, and copper detection with healthcare applications”. https://doi.org/10.1016/j.bios.2022.11400

[107] Isa Anshori et al. 2022. “ESPotensio: A Low-Cost and Portable Potentiostat with Multi-Channel and Multi-Analysis Electrochemical Measurements”. 10.1109/ACCESS.2022.3213725.

[108] Shawn Chia Hung Lee and Peter J. Burke. 2022. “NanoStat: An open source, fully wireless potentiostat”. 10.1016/j.electacta.2022.140481.

[109] Xuan Cai et al. 2020. “Smartphone-coupled Electrochemical Analysis of Cellular Superoxide Anions Based on Mnx(PO4)y Monolayer Modified Porous Carbon”. 10.1002/elan.201900623.

[110] Daniel M. Jenkins et al. 2019. “ABE-Stat, a Fully Open-Source and Versatile Wireless Potentiostat Project Including Electrochemical Impedance Spectroscopy”. 10.1149/2.0061909jes.

[111] Pablo Escobedo et al. 2019. “General-purpose passive wireless point–of–care platform based on smartphone”. 10.1016/j.bios.2019.111360.

[112] Laura Gonzalez-Macia et al. 2023. “Facilitating Electrochemical Lateral Flow Assay using NFC-Enabled Potentiostat and Nitrocellulose-based Metal Electrodes”. 10.1101/2023.03.0.

[113] Petar Kassal, Ivana Murković Steinberg, and Matthew D. Steinberg. 2013. “Wireless smart tag with potentiometric input for ultra low-power chemical sensing”. 10.1016/j.snb.2013.04.049.

[114] Matthew D. Steinberg et al. 2015. “A wireless potentiostat for mobile chemical sensing and biosensing”. 10.1016/j.talanta.2015.05.028.

[115] Tatjana Fedtschenko et al. 2019. “A new configurable wireless sensor system for biomedical applications with ISO 18000-3 interface in 0.35 µm CMOS”. 10.3390/s19194110.

[116] Inge Siegl et al. 2018. “NFC Powered cyclic voltammetry with dynamic output voltage range exploitation”. 10.1109/ICSensT.2018.8603604.

[117] SiliconCraft. 2021. “Silicon Craft Technology Public Company Limited”.

[118] Lukas Rauter et al. 2023. “Sustainable Multifunctional Biface Sensor Tag”. 10.1002/adsr.202200027.

[119] I. Ortego et al. 2012. “Inkjet printed planar coil antenna analysis for NFC technology applications”. 10.1155/2012/486565.

[120] Snezana Jenei, Bart K.J.C. Nauwelaers, and Stefaan Decoutere. 2002. “Physics-based closed-form inductance expression for compact modeling of integrated spiral inductors”. 10.1109/4.974547.

[121] Philip Pieters et al. 2001. “Accurate Modeling of High- Q Spiral Inductors in Thin-Film Multilayer Technology for Wireless Telecommunication Applications”. 10.1109/22.915431.

[122] Salvio Suárez-García et al. 2017. “Copolymerization of a catechol and a diamine as a versatile polydopamine-like platform for surface functionalization: The case of a hydrophobic coating”. 10.3390/biomimetics2040022.

[123] Noemí Contreras-Pereda et al. 2024. “Melanin-inspired conductive thin films for multimodal-sensing wearable on-skin electronics”. 10.1016/j.mtchem.2023.101855.

[124] Antonio Lazaro, Ramon Villarino, and David Girbau. 2018. “A survey of NFC sensors based on energy harvesting for IoT applications”. 10.3390/s18113746.

[125] H. Ceren Ates and Can Dincer. 2023. “Wearable breath analysis”. 10.1038/s44222-022-00011-7.

[126] Annalisa Scroccarello et al. 2023. “One-Step Laser Nanostructuration of Reduced Graphene Oxide Films Embedding Metal Nanoparticles for Sensing Applications”. 10.1021/acssensors.2c01782.

[127] Abdulhadee Yakoh et al. 2018. “Screen-Printed Electroluminescent Lamp Modified with Graphene Oxide as a Sensing Device”. 10.1021/acsami.8b04883.

[128] Allen j. Bard and Larry R Faulkner. 1980. “Electrochemical Methods: Fundamentals and Applications”.

[129] Noémie Elgrishi et al. 2018. “A Practical Beginner’s Guide to Cyclic Voltammetry”. 10.1021/acs.jchemed.7b00361.

[130] Edmund J.F. Dickinson and Richard G. Compton. 2011. “Influence of the diffuse double layer on steady-state voltammetry”. 10.1016/j.jelechem.2011.08.002.

[131] Morena Silvestrini, Ljiljana Fruk, and Paolo Ugo. 2013. “Functionalized ensembles of nanoelectrodes as affinity biosensors for DNA hybridization detection”. 10.1016/j.bios.2012.07.041.

[132] Helena Louise Woodvine and Dr A R Mount. 2011. “Development and Characterisation of Microelectrode and Nanoelectrode Systems”. https://era.ed.ac.uk/handle/1842/9570.

[133] Grace Henihan et al. 2016. “Label- and amplification-free electrochemical detection of bacterial ribosomal RNA”. 10.1016/j.bios.2016.03.037.

[134] D. K. Corrigan et al. 2013. “Development of a PCR-free electrochemical point of care test for clinical detection of methicillin resistant Staphylococcus aureus (MRSA)”. 10.1039/c3an01319g.

[135] Kiyoshi Kuribayashi et al. 1983. “Preparation of low resistance contact electrode in screen printed CdS/CdTe solar cell”. 10.1143/JJAP.22.1828.

[136] Daniel Mandler and Shlomit Kraus-Ophir. 2011. “Self-assembled monolayers (SAMs) for electrochemical sensing”. 10.1007/s10008-011-1493-6.

[137] Nobutoshi Komuro et al. 2013. “Inkjet printed (bio)chemical sensing devices”. 10.1007/s00216-013-7013-z.

[138] Jonathan G. Terry et al. 2013. “Nanoscale electrode arrays produced with microscale lithographic techniques for use in biomedical sensing applications”. 10.1049/iet-nbt.2013.0049.

[139] Matthias Schwartzkopf et al. 2015. “Real-Time Monitoring of Morphology and Optical Properties during Sputter Deposition for Tailoring Metal-Polymer Interfaces”. 10.1021/acsami.5b02901.

[140] Matthias Schwartzkopf et al. 2017. “Role of Sputter Deposition Rate in Tailoring Nanogranular Gold Structures on Polymer Surfaces”. 10.1021/acsami.6b15172.

[141] Courtney S. Smith et al. 2011. “Electrochemical investigation of nano-electrodes for biomedical sensing applications in the brain”. 10.1117/12.880567.

[142] Rael B. Morris, David J. Franta, and Henry S. White. 1987. “Electrochemistry at Pt band electrodes of width approaching molecular dimensions. Breakdown of transport equations at very small electrodes”. 10.1021/j100297a019.

[143] Damien W.M. Arrigan. 2004. “Nanoelectrodes, nanoelectrode arrays and their applications”. 10.1039/b415395m.

[144] Helena L. Woodvine et al. 2010. “The development and characterisation of square microfabricated electrode systems”. 10.1039/b924342a.

[145] Kamonwad Ngamchuea et al. 2014. “Planar diffusion to macro disc electrodes—what electrode size is required for the Cottrell and Randles-Sevcik equations to apply quantitatively?” 10.1007/s10008-014-2664-z.

[146] Edmund J F Dickinson and Richard G Compton. 2009. “Diffuse Double Layer at Nanoelectrodes”. https://doi.org/10.1021/jp906404h.

[147] Ilka Schmueser et al. 2013. “A systematic study of the influence of nanoelectrode dimensions on electrode performance and the implications for electroanalysis and sensing”. 10.1039/c3fd00038a.

[148] Andrew Piper, Damion K. Corrigan, and Andrew R. Mount. 2022. “An electrochemical comparison of thiolated self-assembled monolayer (SAM) formation and stability in solution on macro- and nanoelectrodes”. 10.1002/elsa.202100077.

[149] Xiaowen Yu et al. 2017. “Graphene-based smart materials”. 10.1038/natrevmats.2017.46.

[150] Zengguang Cheng et al. 2010. “Suspended graphene sensors with improved signal and reduced noise”. 10.1021/nl100633g.

[151] Janire Peña-Bahamonde et al. 2018. “Recent advances in graphene-based biosensor technology with applications in life sciences”. 10.1186/s12951-018-0400-z.

[152] Xiu Liang et al. 2021. “Carbon-based SERS biosensor: from substrate design to sensing and bioapplication”. 10.1038/s41427-020-00278-5.

[153] Shirin Movaghgharnezhad and Pilgyu Kang. 2024. “Laser-induced graphene: synthesis advances, structural tailoring, enhanced properties, and sensing applications”. 10.1039/d3tc04677j.

[154] Yiran Yang et al. 2020. “A laser-engraved wearable sensor for sensitive detection of uric acid and tyrosine in sweat”. 10.1038/s41587-019-0321-x.

[155] P. Salvo et al. 2014. “Fabrication and functionalization of PCB gold electrodes suitable for DNA-based electrochemical sensing”. 10.3233/BME-140982.

[156] Gorachand Dutta, Anna Regoutz, and Despina Moschou. 2018. “Commercially Fabricated Printed Circuit Board Sensing Electrodes for Biomarker Electrochemical Detection: The Importance of Electrode Surface Characteristics in Sensor Performance”. 10.3390/proceedings2130741.

[157] Daniel Evans et al. 2018. “A novel microfluidic point-of-care biosensor system on printed circuit board for cytokine detection”. 10.3390/s18114011.

[158] M. S. Kumar et al. 2021. “Electrochemical sensing of SARS-CoV-2 amplicons with PCB electrodes”. 10.1016/j.snb.2021.130169.

[159] Ruchira Nandeshwar et al. 2022. “Molecular Imprinting With Polyaniline on ENIG Finish PCB Electrodes for Electrochemical Detection of Melamine”. 10.1109/JSEN.2021.3137515.

[160] Ruchira Nandeshwar and Siddharth Tallur. 2024. “Electrochemical detection of myeloperoxidase (MPO) in blood plasma with surface-modified electroless nickel immersion gold (ENIG) printed circuit board (PCB) electrodes”. 10.1016/j.bios.2023.115891.

[161] Joseph LaDou. 2006. “Printed circuit board industry”. 10.1016/j.ijheh.2006.02.001.

[162] Hamed Shamkhalichenar, Collin J. Bueche, and Jin Woo Choi. 2020. “Printed Circuit Board (PCB) Technology for Electrochemical Sensors and Sensing Platforms”. 10.3390/bios10110159.

[163] Despina Moschou and Angeliki Tserepi. 2017. “The lab-on-PCB approach: tackling the μTAS commercial upscaling bottleneck”. 10.1039/c7lc00121e.

[164] 911EDA.inc. 2024. “History of Printed Circuit Boards: Beginning to Now”.

[165] R.P. Prasad. 1997. “Introduction to Surface Mount Technology Chapter”.

[166] ALCANTA. 2024. “FR4 PCB MATERIAL: PROPERTIES AND ADVANTAGES EXPLAINED”.

[167] PCBWay. 2024. “PCBWay PCB Prototype the Easy Way”.

[168] Sierra Circuits Proto Express. 2024. “Best-in-Class PCB Fabrication, Assembly, Components”.

[169] Hai Yen Ta et al. 2021. “Twenty years of amino acid determination using capillary electrophoresis: A review”. 10.1016/j.aca.2021.338233.

[170] László Hajba et al. 2023. “Capillary Gel Electrophoresis of Proteins: Historical overview and recent advances”. 10.1016/j.trac.2023.117024.

Appendix A - Matlab Code for Inductance Design

Matlab Code for Inductance Design

June 28, 2024

```
close all
clc
clear

%% Constants
mu0  =  4*pi*1e-7;      % Magnetic permeability  [T.m.A^-1]
eps0 =  8.85e-12;    %[F/m]
eps_PET = 3.1; %PET Dielectric Constant
Cchip = 50e-12; %Chip Capacitance [F]

%% Design parameters

w    =   1500e-6;        % Track Width [m]
s    =   250e-6;         % Gap between tracks [m]
t    =   1.8e-6;         % Track thickness [m]
n    =   5;              % Number of turns of the inductor [a.u.]
din = 43000e-6;          % Inner diameter of the inductor [m]
h_sust = 125e-6;         % Substrate thickness PET


%% Jenei model for square inductances

Ni   =   floor(n);   % Integer part of the number of turns [a.u.]
len = (4*n+1)*din + (4*Ni+1)*Ni*(w+s); % Total inductor length [m]
dp   =   (w + s)*(3*n - 2*Ni -1)*(Ni +1)/(3*(2*n - Ni -1));  % Average
    distance proposed by Jenei [m]
A    =   w.*t;            % Cross-section of the track [m2]
l_seg_Avg = len/(4*n); % Average length of an inductor segment [m]

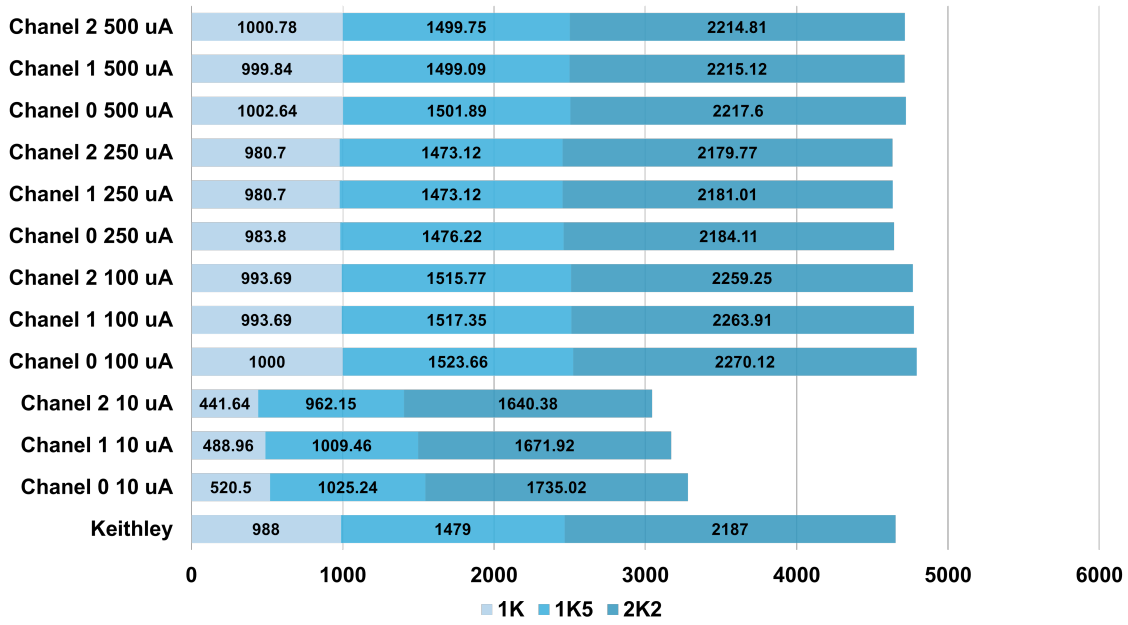
L    = (mu0/(2*pi))*len*(log(len./(n*(w+t))) - 0.2 - 0.47*n + (n-1)*...
    (log(sqrt(1+(len/(4*n*dp))^2)+len/(4*n*dp)) - ...
    sqrt(1+(len/(4*n*dp))^-2)+((4*n*dp)/len))); % Total inductance [H]
```

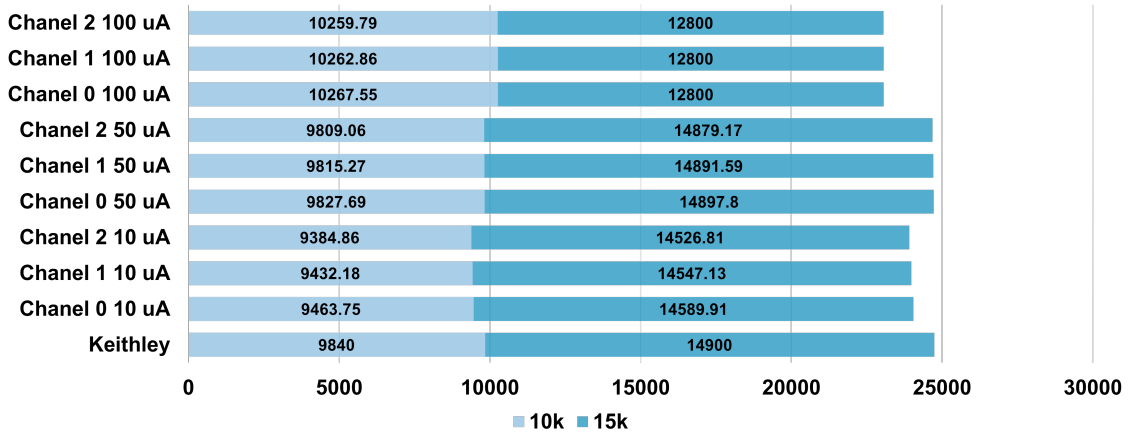
```
32
33 %% DC resistance
34 ro = 1.09e-7; %Ink resistivity [ohm*m]
35 R_DC = ro*len/(w*t);
36
37 %% Resistance as a function of frequency
38 f = [1e3 1e4 1e5 1e6 1e7 1e8];
39 delt = 1./sqrt(pi.*f*mu0*(1/ro));
40     for i=1:1:length(delt)
41 teff(i) = delt(i)*(1-exp(-t/delt(i)));
42 R_RF(i) = ro*len/(w*teff(i));
43     end
44 figure
45 plot(f,R_RF)
46 xlabel('Frequency ')
47 ylabel('Resistance [ohm]')
48 title('Resistance vs Frequency')
49 %% Paracitic capacitance Cp
50 xa = s/2;           % Is the coordinate for the integral, spacing/2.
51
52 xb = xa+w;
53
54 k  = sqrt(1-(xa./xb).^2); % Value for the elliptic integral according
    to Pieters
55
56 kp = sqrt(1-k.^2);       % k prime for the elliptic integral
57
58 k1 = sqrt(1-((sinh(pi.*xa./(2.*h_sust))).^2./(sinh(pi.*xb./(2.*h_sust))
    )));   %Elliptical Integral for the substrate
59
60 kp1 = sqrt(1-k1.^2);
61
62 % Calculation of the effective epsilon of coplanar traces on kapton
    according to Pieters
63
64 eps_eff = 1 + 0.5.*(eps_PET - 1).*ellipke(k).*ellipke(kp1)./(ellipke(kp
    ).*ellipke(k1));
65
66 C0  = eps0.*ellipke(k)./ellipke(kp);
67
68 Cxl     = C0.*eps_eff;     %[F/m] Capacitance per unit length of
    coplanar traces, Cxl:capacitance per length
69
```

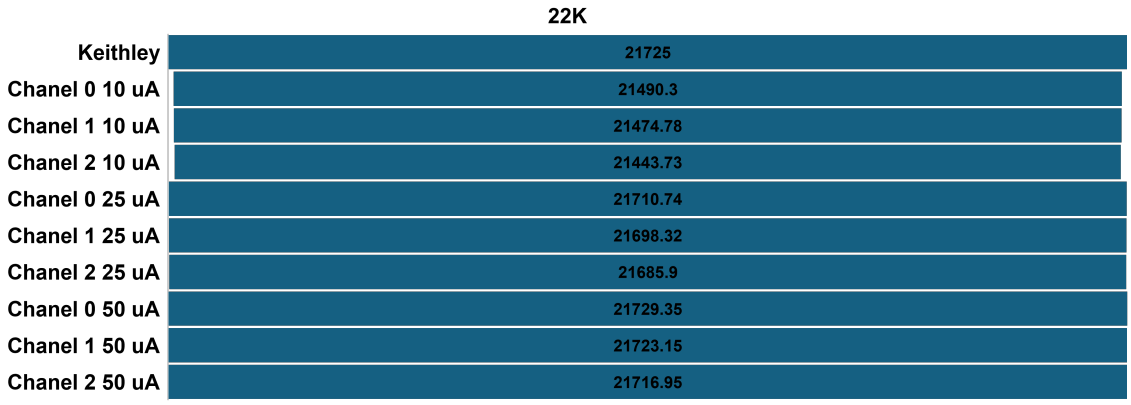
```
70 Pc = len/2; %being half of the total sum of all circular perimeters on
       the center line of the spiral turns
71 Cp = Cxl.*Pc; % [F] capacidad debido a las trazas en el eje X
72
73 Ctot = Cp + Cchip; %Total capacity, taking into account paracite and
       chip capacitance.
74
75 Cs = 2.3e-12; %The Cs capacitance is calculated in the same way as
       above, it is not included so as not to make the code too long.
76
77 %% Modelo Compacto
78 L_lumped = circuit('left');
79 add(L_lumped,[1 4], inductor(L))
80 add(L_lumped,[4 2], resistor(R_DC))
81 add(L_lumped,[1 2], capacitor(Ctot))
82 add(L_lumped,[1 3], capacitor(Cs))
83 add(L_lumped,[2 3], capacitor(Cs))
84 disp(L_lumped)
85 setports(L_lumped,[1 3])
86 figure
87 freq = logspace(1,7.5,2000);
88 S_L_lumped = sparameters(L_lumped,freq);
89 rfplot(S_L_lumped,1,1);
```

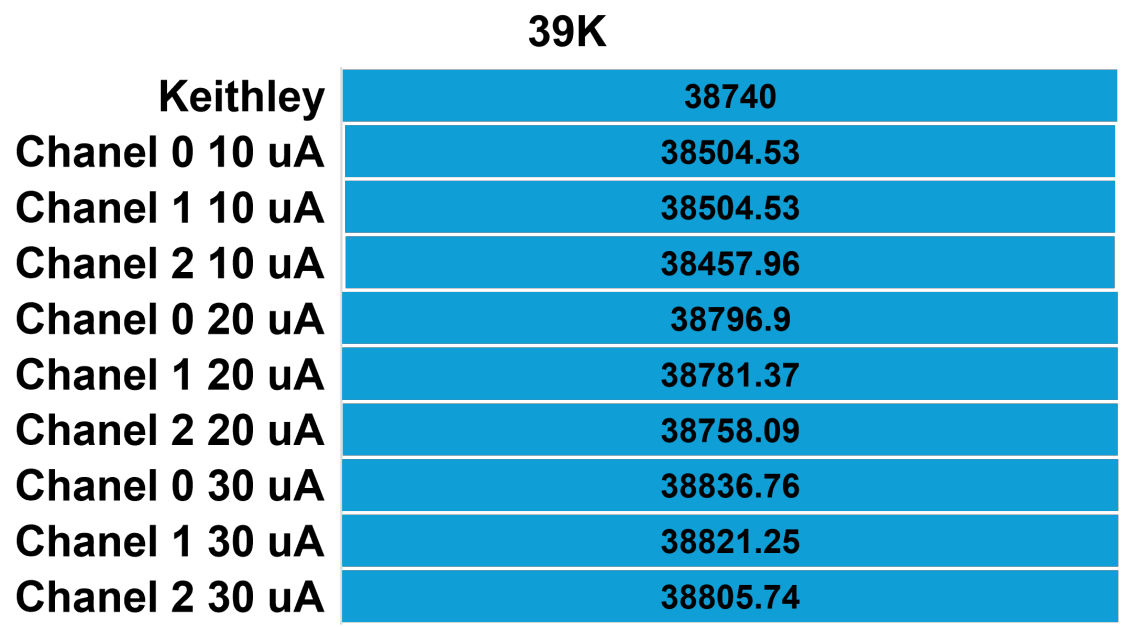
Listing 1: Código MATLAB para el cálculo de inductancia

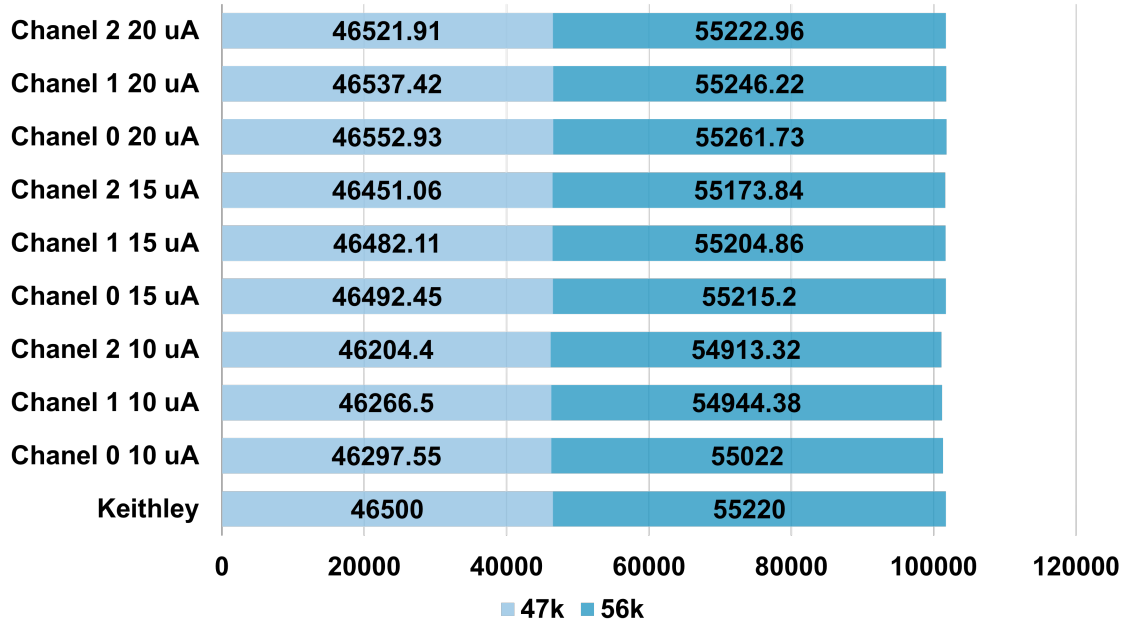
Comparison of a wide range of resistors measured with the NFC system and the Keithley DMM6500 Digital Multimeter.

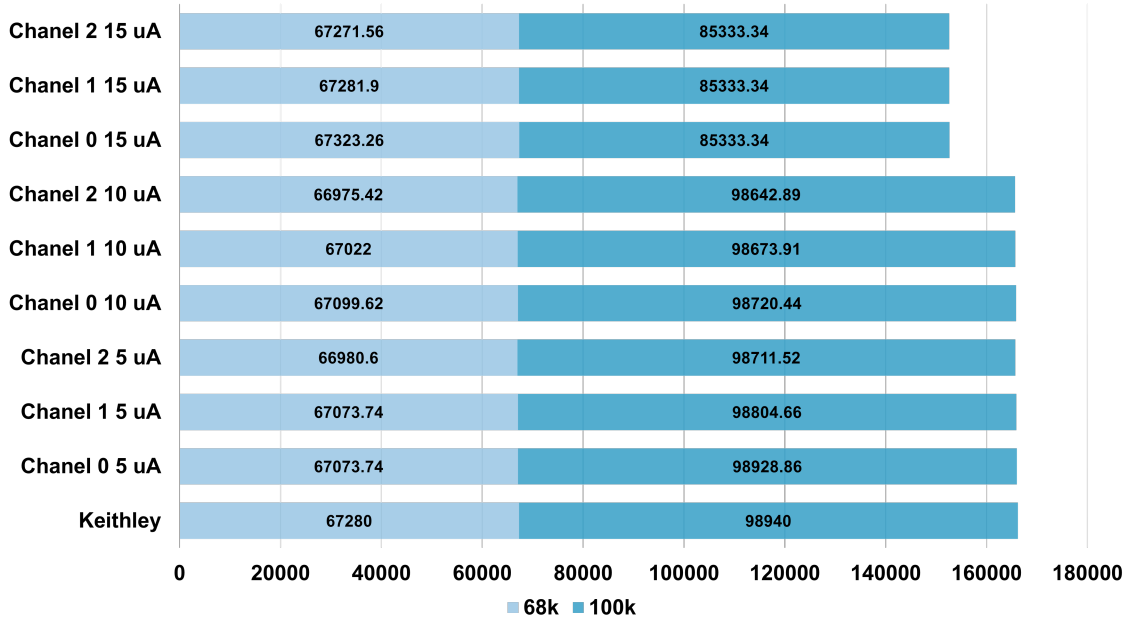


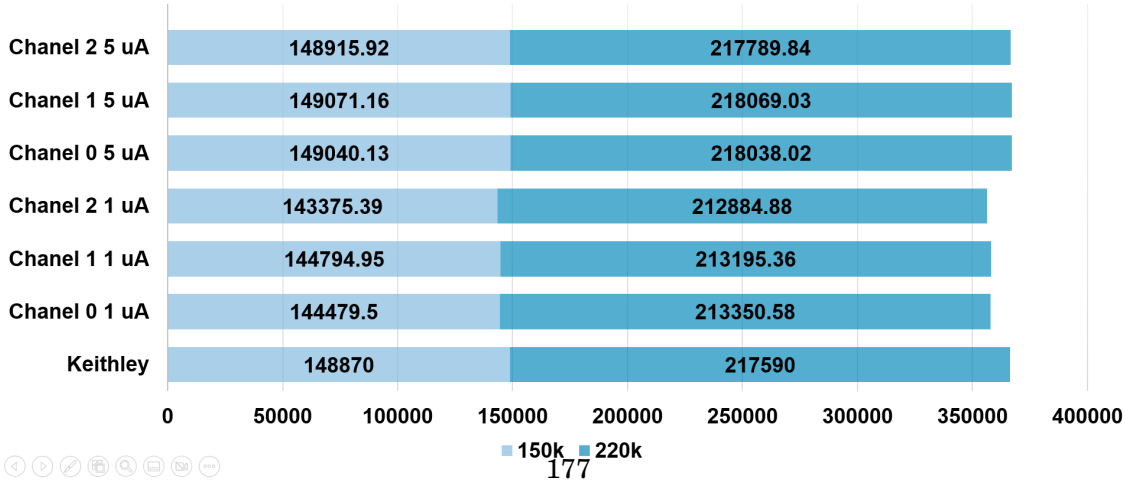

Chanel 2 100 uA
Chanel 1 100 uA
Chanel 0 100 uA
Chanel 2 50 uA
Chanel 1 50 uA
Chanel 0 50 uA
Chanel 2 10 uA
Chanel 1 10 uA
Chanel 0 10 uA
Keithley
10259.79
10262.86
10267.55
9809.06
9815.27
9827.69
9384.86
9432.18
9463.75
9840
12800
12800
12800
14879.17
14891.59
14897.8
14526.81
14547.13
14589.91
14900
0
5000
10000
15000
20000
25000
30000
10k
15k


22K
Keithley
Chanel 0 10 uA
Chanel 1 10 uA
Chanel 2 10 uA
Chanel 0 25 uA
Chanel 1 25 uA
Chanel 2 25 uA
Chanel 0 50 uA
Chanel 1 50 uA
Chanel 2 50 uA
21725
21490.3
21474.78
21443.73
21710.74
21698.32
21685.9
21729.35
21723.15
21716.95

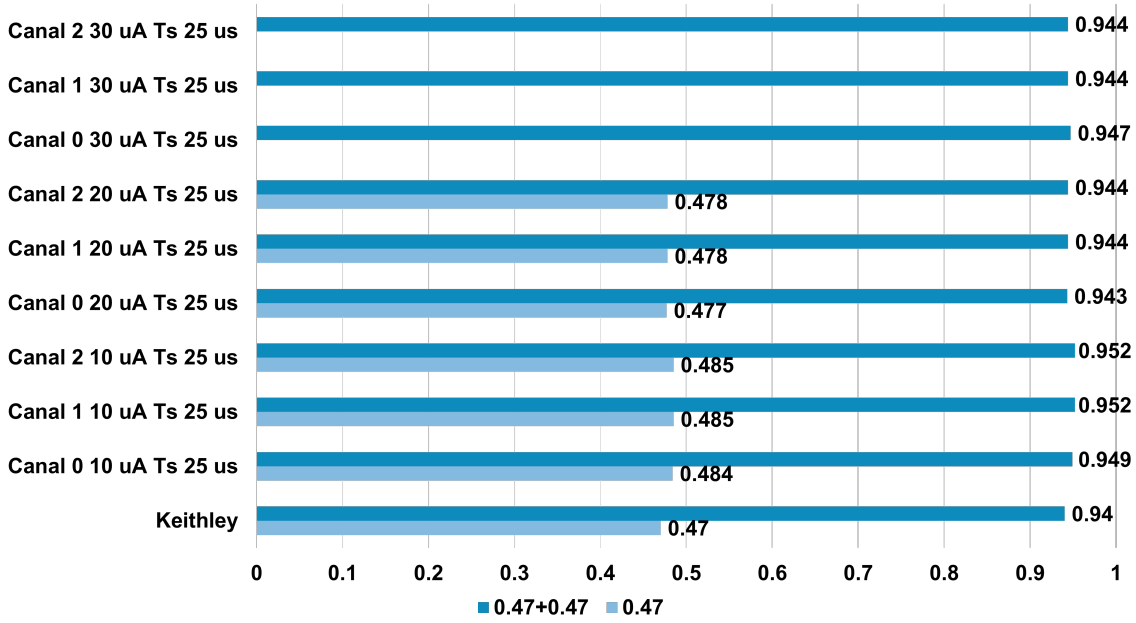

39K
Keithley
Chanel 0 10 uA
Chanel 1 10 uA
Chanel 2 10 uA
Chanel 0 20 uA
Chanel 1 20 uA
Chanel 2 20 uA
Chanel 0 30 uA
Chanel 1 30 uA
Chanel 2 30 uA
38740
38504.53
38504.53
38457.96
38796.9
38781.37
38758.09
38836.76
38821.25
38805.74

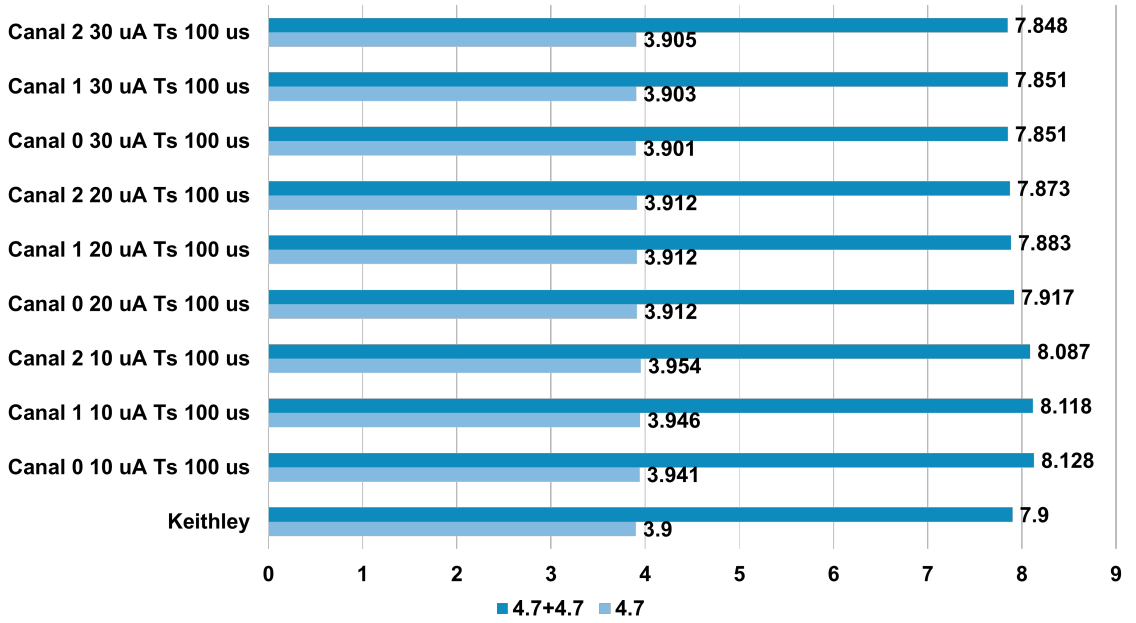

Chanel 2 20 uA
46521.91
55222.96
Chanel 1 20 uA
46537.42
55246.22
Chanel 0 20 uA
46552.93
55261.73
Chanel 2 15 uA
46451.06
55173.84
Chanel 1 15 uA
46482.11
55204.86
Chanel 0 15 uA
46492.45
55215.2
Chanel 2 10 uA
46204.4
54913.32
Chanel 1 10 uA
46266.5
54944.38
Chanel 0 10 uA
46297.55
55022
Keithley
46500
55220
0
20000
40000
60000
80000
100000
120000
47k
56k

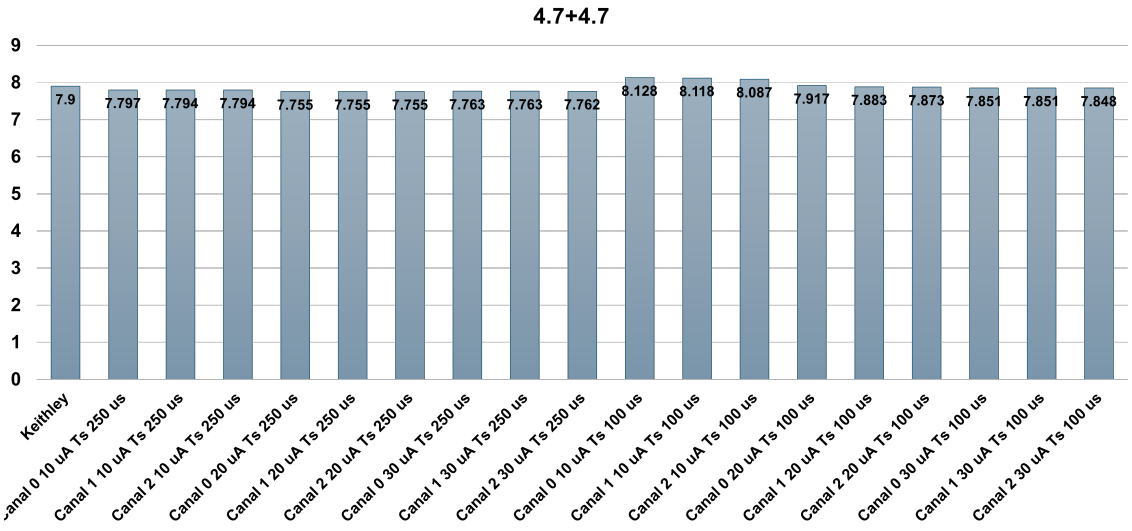

Chanel 2 15 uA
67271.56
85333.34
Chanel 1 15 uA
67281.9
85333.34
Chanel 0 15 uA
67323.26
85333.34
Chanel 2 10 uA
66975.42
98642.89
Chanel 1 10 uA
67022
98673.91
Chanel 0 10 uA
67099.62
98720.44
Chanel 2 5 uA
66980.6
98711.52
Chanel 1 5 uA
67073.74
98804.66
Chanel 0 5 uA
67073.74
98928.86
Keithley
67280
98940
0
20000
40000
60000
80000
100000
120000
140000
160000
180000
68k
100k

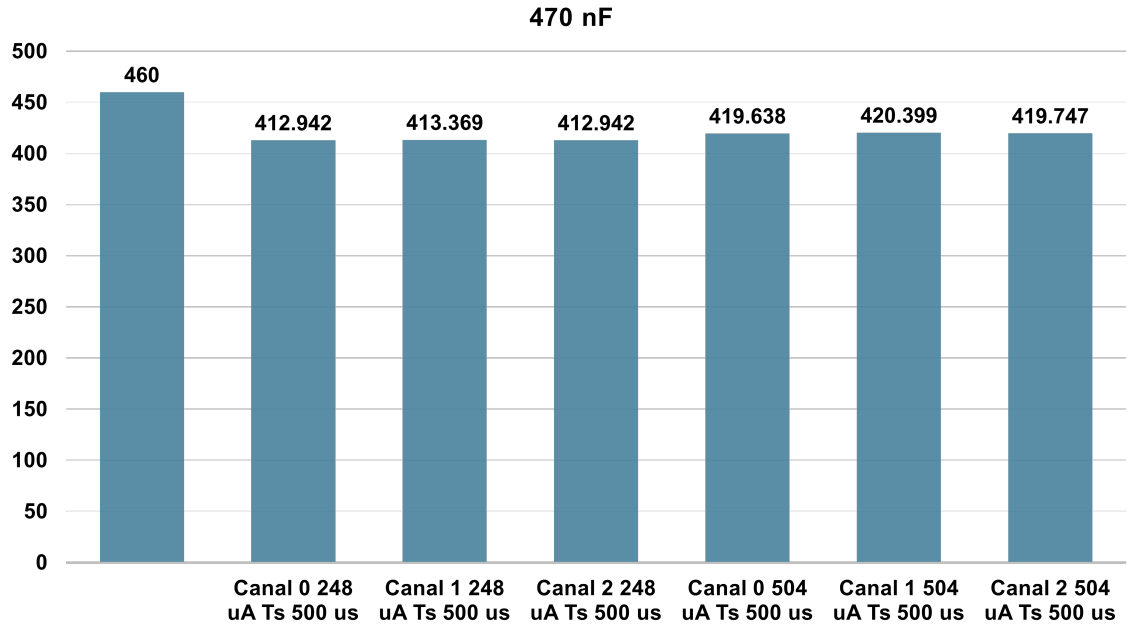

Chanel 2 5 uA
148915.92
217789.84
Chanel 1 5 uA
149071.16
218069.03
Chanel 0 5 uA
149040.13
218038.02
Chanel 2 1 uA
143375.39
212884.88
Chanel 1 1 uA
144794.95
213195.36
Chanel 0 1 uA
144479.5
213350.58
Keithley
148870
217590
0
50000
100000
150000
200000
250000
300000
350000
400000
150k
220k

Comparison of a wide range of capacitors measured with the NFC system and the Keithley DMM6500 Digital Multimeter






4.7+4.7
9
8
7
6
5
4
3
2
1
0
7.9
7.797
7.794
7.794
7.755
7.755
7.755
7.763
7.763
7.762
8.128
8.118
8.087
7.917
7.883
7.873
7.851
7.851
7.848
Keithley
Canal 0 10 uA Ts 250 us
Canal 1 10 uA Ts 250 us
Canal 2 10 uA Ts 250 us
Canal 0 20 uA Ts 250 us
Canal 1 20 uA Ts 250 us
Canal 2 20 uA Ts 250 us
Canal 0 30 uA Ts 250 us
Canal 1 30 uA Ts 250 us
Canal 2 30 uA Ts 250 us
Canal 0 10 uA Ts 100 us
Canal 1 10 uA Ts 100 us
Canal 2 10 uA Ts 100 us
Canal 0 20 uA Ts 100 us
Canal 1 20 uA Ts 100 us
Canal 2 20 uA Ts 100 us
Canal 0 30 uA Ts 100 us
Canal 1 30 uA Ts 100 us
Canal 2 30 uA Ts 100 us


470 nF
500
450
400
350
300
250
200
150
100
50
0
460
412.942
413.369
412.942
419.638
420.399
419.747
Canal 0 248 uA Ts 500 us
Canal 1 248 uA Ts 500 us
Canal 2 248 uA Ts 500 us
Canal 0 504 uA Ts 500 us
Canal 1 504 uA Ts 500 us
Canal 2 504 uA Ts 500 us

APPENDIX C - ELECTROPHORESIS CODES

Contained within this appendix is the comprehensive codebase instrumental to the development of the Electrophoretic Power Supply. The software is bifurcated into two integral components:

- The primary component is the code scripted in the Arduino Integrated Development Environment (IDE). This code is specifically designed to operate within the Arduino Nano 33 BLE microcontroller, serving as the control center for the electrophoretic source.
- The secondary component comprises the block-based code developed in the MIT App Inventor, a visual programming environment. This code facilitates the user interface of the mobile application, enabling user interaction and control over the electrophoretic source.

Arduino Code

This is the Arduino code used to control the Electrophoretic Power Supply
Version 2.0
21/08/23
By: Gabriel Maroli

```
#include <ArduinoBLE.h> //Library enables Bluetooth Low Energy (BLE) communication for Arduino devices enables Bluetooth Low Energy (BLE) communication for Arduino devices
#include <Wire.h> // Library enables I2C communication
#include <Adafruit_MCP4725.h> // Library facilitates control of the MCP4725 digital-to-analog converter (DAC)

#define PIN_LEFT D3 // Pin that will control the solid state relay so that the current flows to the Left.
#define PIN_RIGHT D2 // Pin that will control the solid state relay so that the current flows to the Right.
#define Volt_Read_Port A7 // Analogue pin where actual output voltage is read

#define SERVICE_UUID "0000FFE0-0000-1000-8000-00805F9B34FB" // Unique identifier for the Bluetooth Low Energy (BLE) service
#define VOLTAGE_CHARACTERISTIC_UUID "0000FFE2-0000-1000-8000-00805F9B34FB" // Unique identifier characteristic to receive the required Voltage
#define FLOW_CHARACTERISTIC_UUID "0000FFE3-0000-1000-8000-00805F9B34FB" // Unique identifier characteristic to receive the flow direction
#define RealVolt_CHARACTERISTIC_UUID "0000FFE4-0000-1000-8000-00805F9B34FB" // Unique identifier characteristic to send the real Voltage
#define VR_CHARACTERISTIC_UUID "0000FFE5-0000-1000-8000-00805F9B34FB" // Unique identifier characteristic to receive the required Voltage Right in Shaker Mode
#define tR_CHARACTERISTIC_UUID "0000FFE6-0000-1000-8000-00805F9B34FB"// Unique identifier characteristic to receive the required Time Right in Shaker Mode
#define VL_CHARACTERISTIC_UUID "0000FFE7-0000-1000-8000-00805F9B34FB" // Unique identifier characteristic to receive the required Voltage Left in Shaker Mode
#define tL_CHARACTERISTIC_UUID "0000FFE8-0000-1000-8000-00805F9B34FB" // Unique identifier characteristic to receive the required Time Left in Shaker Mode


BLEService ServicioElectro(SERVICE_UUID); //Creates a Bluetooth Low Energy (BLE) service with the specified UUID
BLEUnsignedShortCharacteristic CaracteristicaVoltage(VOLTAGE_CHARACTERISTIC_UUID, BLERead | BLEWrite | BLENotify);
BLEUnsignedCharCharacteristic CaracteristicaFlow(FLOW_CHARACTERISTIC_UUID, BLERead | BLEWrite | BLENotify);
```

```
BLEFloatCharacteristic CaracteristicaRealVolt(RealVolt_CHARACTERISTIC_UUID,
BLERead | BLEWrite | BLENotify);
BLEUnsignedCharCharacteristic CaracteristicaVR(VR_CHARACTERISTIC_UUID,
BLERead | BLEWrite | BLENotify);
BLEUnsignedCharCharacteristic CaracteristicatR(tR_CHARACTERISTIC_UUID,
BLERead | BLEWrite | BLENotify);
BLEUnsignedCharCharacteristic CaracteristicaVL(VL_CHARACTERISTIC_UUID,
BLERead | BLEWrite | BLENotify);
BLEUnsignedCharCharacteristic CaracteristicatL(tL_CHARACTERISTIC_UUID,
BLERead | BLEWrite | BLENotify);
//Creates a BLE characteristic with the specified UUID. It can be read, written, and
notify a central device of changes.
Adafruit_MCP4725 dac; // Declares an instance of the Adafruit_MCP4725
int counter = 0; // Declares a variable named counter
float Voltage_Read = 0; //Voltage read at port Volt_Read_Port
float Voltage_Requested = 0; // User Requested Voltage
float Voltage_RequestedR = 0; // User Requested Voltage Right Shaker
float Voltage_RequestedL = 0; // User Requested Voltage Left Shaker
unsigned long Time_RequestedR = 0; // User Requested Time Right Shaker
unsigned long Time_RequestedL = 0; // User Requested Time Left Shaker
bool squareWaveState = false; // This variable is used to keep track of the state of
the square wave in shaker mode in your code
unsigned long previousMillis = 0; // Used to store the time that has passed since
the Arduino board began running
unsigned long currentMillis = 0; // Used to store the current time (in milliseconds
since the Arduino board began running the current program)
unsigned long currentPeriod = 0; // Used to calculate the difference between the
current time and the time that has passed

void setup() {
 Serial.begin(9600); // Initializes the serial port at a baud rate of 9600  for serial
communication
 pinMode(PIN_RIGHT, OUTPUT); // Sets the digital pin as an output pin
 pinMode(PIN_LEFT, OUTPUT); // Sets the digital pin as an output pin
 pinMode(Volt_Read_Port, INPUT); // Sets the analogue pin as an input pin
 digitalWrite(PIN_RIGHT, LOW); // Sets the digital output of the pin to LOW (OFF)
 digitalWrite(PIN_LEFT, LOW);// Sets the digital output of the pin to LOW (OFF)

 if (!BLE.begin()) { // Initialize the Bluetooth Low Energy (BLE) module If the
initialization fails, BLE.begin() returns false, and the condition !BLE.begin()
becomes true
   while (1); // If the initialisation fails, I will stay in this while
 }
 BLE.setLocalName("ELENA - POC Next Generation"); // Sets the local name of
the BLE device that will be broadcasted to other BLE devices during the discovery
process
```

```
  BLE.setAdvertisedService(ServicioElectro); // Sets the service that the BLE device
advertises to other BLE devices
  ServicioElectro.addCharacteristic(CaracteristicaVoltage); // Adds the
characteristic to the ServicioElectro service
  ServicioElectro.addCharacteristic(CaracteristicaFlow); // Adds the characteristic
to the ServicioElectro service
  ServicioElectro.addCharacteristic(CaracteristicaRealVolt); // Adds the
characteristic to the ServicioElectro service
  ServicioElectro.addCharacteristic(CaracteristicaVR); // Adds the characteristic to
the ServicioElectro service
  ServicioElectro.addCharacteristic(CaracteristicatR); // Adds the characteristic to
the ServicioElectro service
  ServicioElectro.addCharacteristic(CaracteristicaVL); // Adds the characteristic to
the ServicioElectro service
  ServicioElectro.addCharacteristic(CaracteristicatL); // Adds the characteristic to
the ServicioElectro service
  BLE.addService(ServicioElectro); // Adds the ServicioElectro service to the BLE
device. This makes the service available for other BLE devices to discover and
connect to
  BLE.advertise(); // Starts advertising the BLE device. This makes the device
discoverable and connectable by other BLE devices
    Wire.begin(); // Initializes the I2C communication interface. This allows the
Arduino to communicate with I2C devices like the MCP4725 DAC
  dac.begin(0x66); // Initializes the MCP4725 DAC with the I2C address 0x66
  dac.setVoltage(counter, false);  // Sets the output voltage of the MCP4725 DAC to
the value of counter = 0.
}

void loop() { //This is a core function that runs continuously after the setup()
function finishes. It's where the main logic of your program goes
  BLEDevice central = BLE.central(); // Creates an instance of the BLEDevice class
named central.
                          // This instance represents the central device that is currently
connected to your Arduino, or null if no central device is connected
  if (central) { // Checks if a central device is currently connected to your Arduino. If
a central device is connected, the code inside the if statement will execute
    Serial.print("Connected to central: "); // For Debugging -  Sends the string
"Connected to central: " to the serial port
    Serial.println(central.address()); // For Debugging - Sends the address of the
connected central device to the serial port

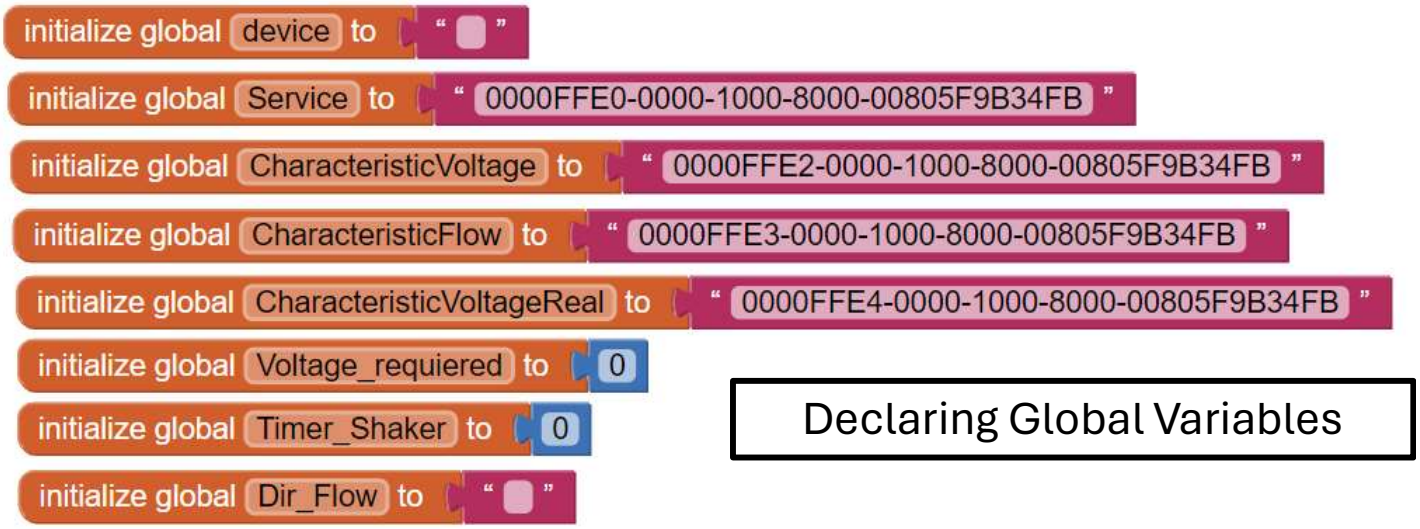
    while (central.connected()) { // Creates a loop that continues as long as the
central device remains connected to the Arduino
      Voltage_Read = (float)analogRead(Volt_Read_Port)/1023*3.3*100; // Reads the
voltage from the Volt_Read_Port analog input, scales it from the 10-bit ADC range
(0-1023)
```

```
                                        // to the voltage range (0-3.3V), and then
multiplies it by 100 because of the resistive divider
    CaracteristicaRealVolt.writeValueLE(Voltage_Read); // Writes the value of
Voltage_Read to the CaracteristicaRealVolt characteristic
                                    // This allows to send the current voltage reading to
APP
    if (CaracteristicaVoltage.written()) { //Checks if the CaracteristicaVoltage
characteristic has been written to by the central device
      Voltage_Requested = CaracteristicaVoltage.value()/100.0; // Reads the value
of the CaracteristicaVoltage and divides it by 100
                                        // This value is then stored in the
Voltage_Requested variable
      }
      Voltage_Read = (float)analogRead(A7)/1023 * 3.3;// // Reads the voltage from
the Volt_Read_Port analog input
      float diff = abs(Voltage_Requested - Voltage_Read) / Voltage_Read; //
Calculates the relative difference between the requested voltage and the actual
voltage read
      if (diff > 0.001) { // If the difference is greater than 0.001, adjust the voltage
       if (Voltage_Read > Voltage_Requested && counter > 5) { // Checks if the actual
voltage read is greater than the requested voltage and if the counter is greater than
5
        while (Voltage_Read > Voltage_Requested) { // Loop that continues as long
as the actual voltage read  is greater than the requested voltage
        dac.setVoltage(counter, false); // Sets the output voltage of the MCP4725
DAC to the value of counter
        counter--; // Used to gradually decrease the voltage until it matches the
requested voltage
        Voltage_Read = analogRead(A7) / 1023.0 * 3.3; // Reads the voltage from the
A7 analog input, scales it from the 10-bit ADC range (0-1023) to the voltage range
(0-3.3V)
         if (counter == 6){Serial.println("Minimum voltage");} // For Debugging - If
counter == 6 sends the string “Minimum voltage” to the serial port
        }
       } else {
        while (Voltage_Read < Voltage_Requested && counter < 4095) { //  Loop that
continues as long as the actual voltage read  is lower than the requested voltage
        dac.setVoltage(counter, false); // Sets the output voltage of the MCP4725
DAC to the value of counter
        counter++; // Used to gradually increse the voltage until it matches the
requested voltage
        Voltage_Read = analogRead(A7) / 1023.0 * 3.3; // Reads the voltage from the
A7 analog input, scales it from the 10-bit ADC range (0-1023) to the voltage range
(0-3.3V)
        if (counter == 4094){Serial.println("Maximum voltage");} // For Debugging - If
counter == 4094 sends the string “Maxium voltage” to the serial port
        }
```

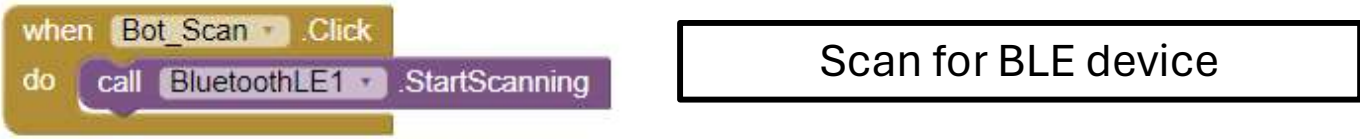
```
181         }
182       }
183         if (CaracteristicaFlow.written()) { // checks if the CaracteristicaFlow
184   characteristic has been written to by the central device
185         if (CaracteristicaFlow.value() == 'L') {  // checks if the new Value is "L" means
186   Left Flow
187         digitalWrite(PIN_RIGHT, LOW); // Turns OFF the pin that controls the solid
188   state relay for the flow in the Right direction
189         digitalWrite(PIN_LEFT, HIGH); // Turns ON the pin that controls the solid state
190   relay for the flow in the left direction
191       } else if (CaracteristicaFlow.value() == 'R') { // If not, checks if the new Value is
192   "R" means Left Flow
193         digitalWrite(PIN_LEFT, LOW); // Turns OFF the pin that controls the solid state
194   relay for the flow in the Left direction
195         digitalWrite(PIN_RIGHT, HIGH); // Turns ON the pin that controls the solid
196   state relay for the flow in the Right direction
197       }
198       else if (CaracteristicaFlow.value() == 'N') { // If not, checks if the new Value is
199   "N" means None Flow
200         dac.setVoltage(0, false); // Sets the output voltage of the MCP4725 DAC to 0
201         Voltage_Requested = 0; // Sets the variable Voltage_Requested to 0
202         delay(3000); // Wait 3 seconds
203         digitalWrite(PIN_LEFT, LOW); // Turns OFF the pin that controls the solid state
204   relay for the flow in the Left direction.
205         digitalWrite(PIN_RIGHT, LOW); // Turns OFF the pin that controls the solid
206   state relay for the flow in the Right direction
207       }
208     }
209     if (CaracteristicaVR.written() || CaracteristicatR.written() ||
210   CaracteristicaVL.written() || CaracteristicatL.written()) {
211       // If any of the characteristics of the shaker mode change
212       Voltage_RequestedR = CaracteristicaVR.value()/100.0; // Reads the value of
213   the Caracteristic, with the Right Voltage
214       Voltage_RequestedL = CaracteristicaVL.value()/100.0; // Reads the value of
215   the Caracteristic, with the Left Voltage
216       Time_RequestedR = CaracteristicatR.value()*1000; // Reads the value of the
217   Caracteristic, with the Right Time
218       Time_RequestedL = CaracteristicatL.value()*1000; // Reads the value of the
219   Caracteristic, with the Left time
220       Voltage_Requested = Voltage_RequestedR; // Sets the Voltage_Requested
221   variable to the value of Voltage_RequestedR
222       currentPeriod = Time_RequestedR; // Sets the currentPeriod variable to the
223   value of Time_RequestedR
224       digitalWrite(PIN_LEFT, LOW); // Turns OFF the pin that controls the solid state
225   relay for the flow in the Left direction.
226       digitalWrite(PIN_RIGHT, HIGH); // Turns ON the pin that controls the solid state
227   relay for the flow in the Right direction
```

```
228         }
229       currentMillis = millis(); // Assigns the current time in milliseconds since the
230     Arduino board started running the current program to the currentMillis variable
231       if (currentMillis - previousMillis >= currentPeriod) { // checks if the difference
232     between the current time and the last recorded time is greater than or equal to the
233     currentPeriod
234         previousMillis = currentMillis; // Assigns the current time to the variable
235     previousMillis
236         squareWaveState = !squareWaveState; //  Toggles the value of the
237     squareWaveState variable.
238         }
239       if (squareWaveState) { // If True it is considered flow to the right
240         currentPeriod = Time_RequestedR; // Sets the currentPeriod variable to the
241     value of Time_RequestedR
242         Voltage_Requested = Voltage_RequestedR; // Sets the Voltage_Requested
243     variable to the value of Voltage_RequestedR
244         digitalWrite(PIN_LEFT, LOW); // Turns OFF the pin that controls the solid state
245     relay for the flow in the Left direction
246         digitalWrite(PIN_RIGHT, HIGH); // Turns ON the pin that controls the solid state
247     relay for the flow in the Right direction
248       }
249       else { // If False it is considered flow to the Left
250       currentPeriod = Time_RequestedL; // Sets the currentPeriod variable to the
251     value of Time_RequestedL
252       Voltage_Requested = Voltage_RequestedL; // Sets the Voltage_Requested
253     variable to the value of Voltage_RequestedL
254       digitalWrite(PIN_RIGHT, LOW); // Turns OFF the pin that controls the solid state
255     relay for the flow in the Right direction
256       digitalWrite(PIN_LEFT, HIGH); // Turns ON the pin that controls the solid state
257     relay for the flow in the Left direction
258     }
259     delay(100); // Wait 100 ms before check the BLE characterics again
260     }
261     Serial.print("Disconnected from central: "); // For Debugging -  Sends the string
262     "Disconnected from central: " to the serial port
263     Serial.println(central.address());// For Debugging - Sends the address of the
264     connected central device to the serial port
265
266    }
267   }
```

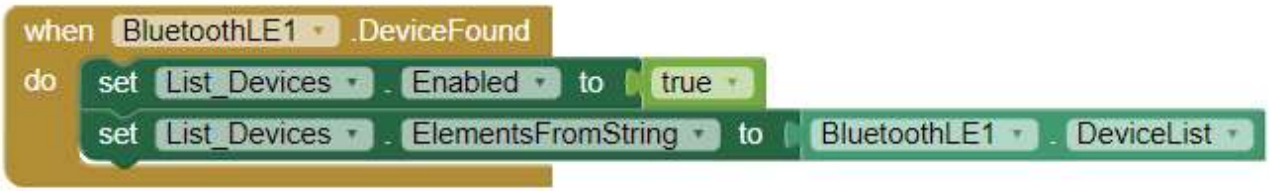
Smartphone APP Code



Declaring Global Variables

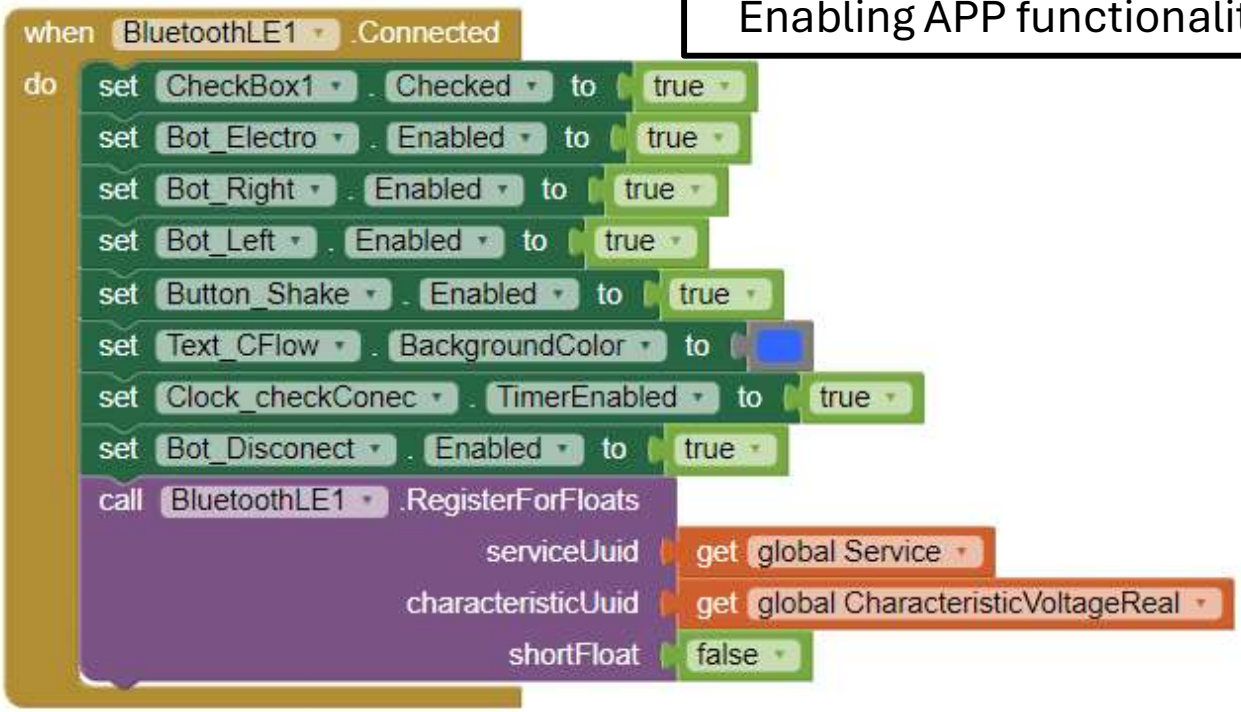


Scan for BLE device

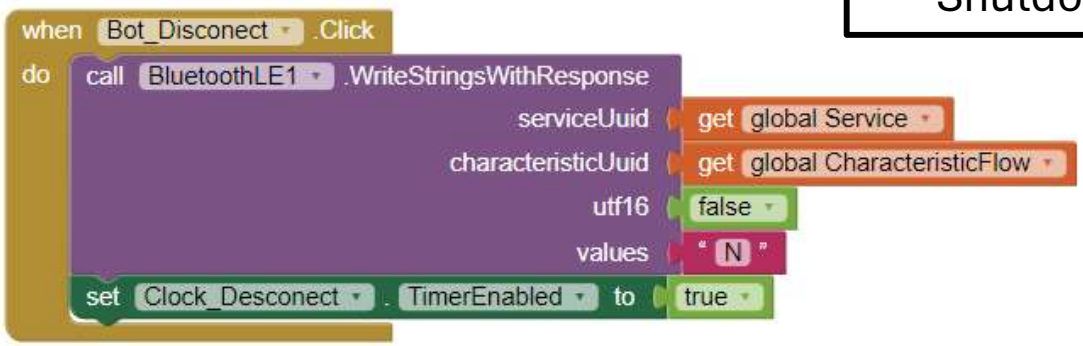


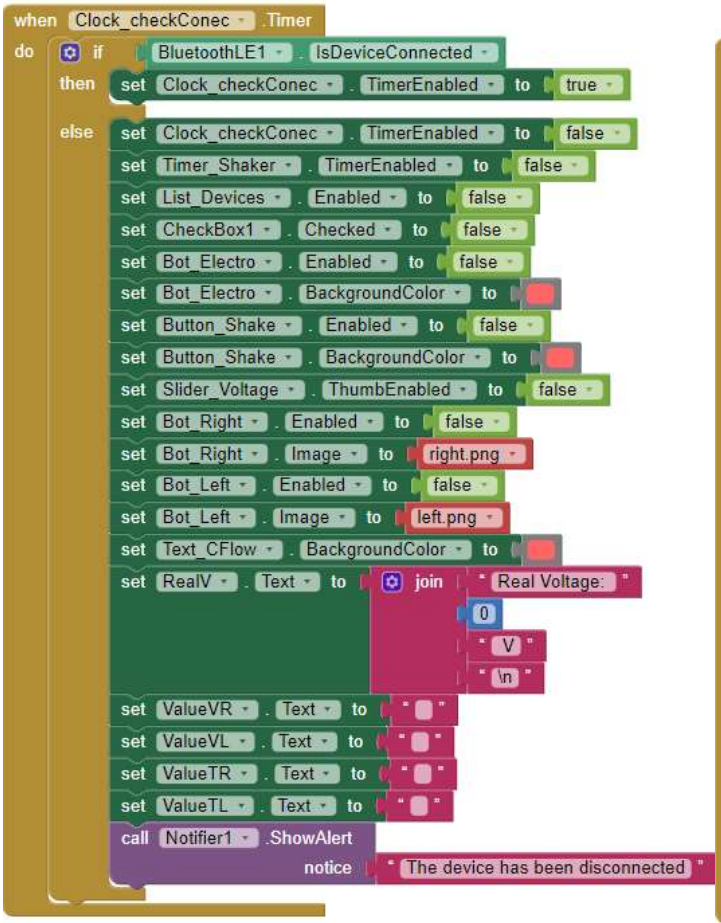


Enabling APP functionalities



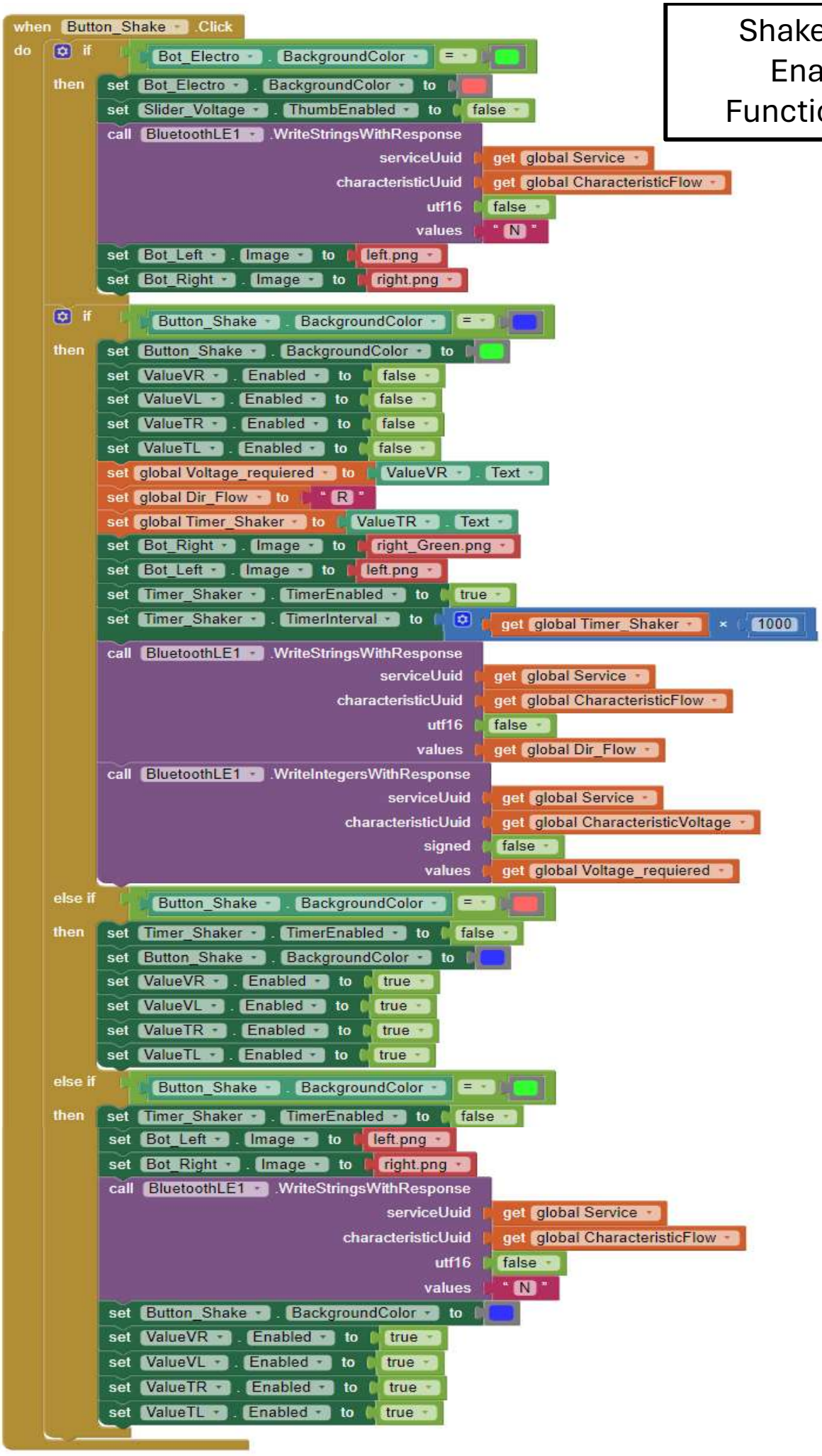
Shutdown protocol



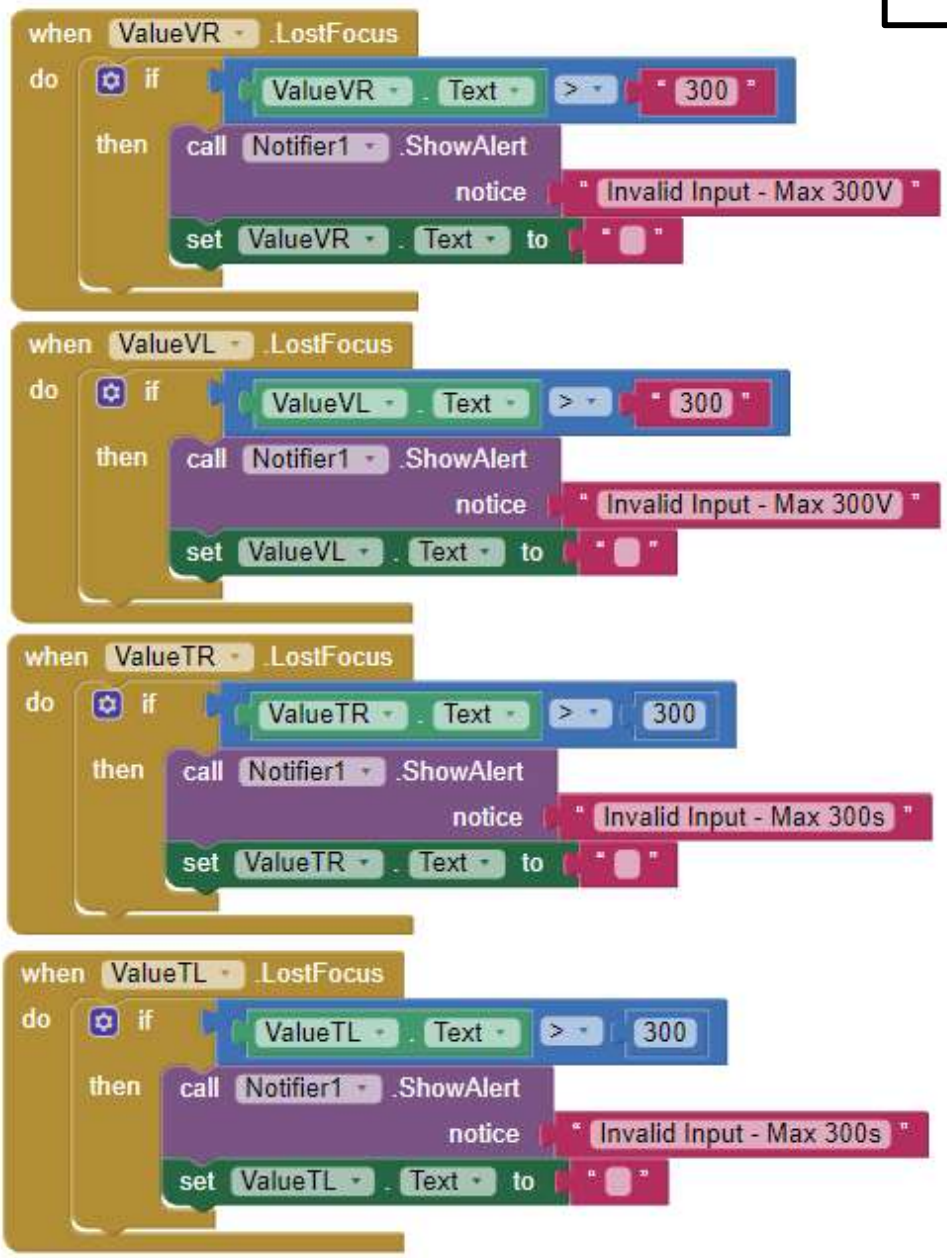




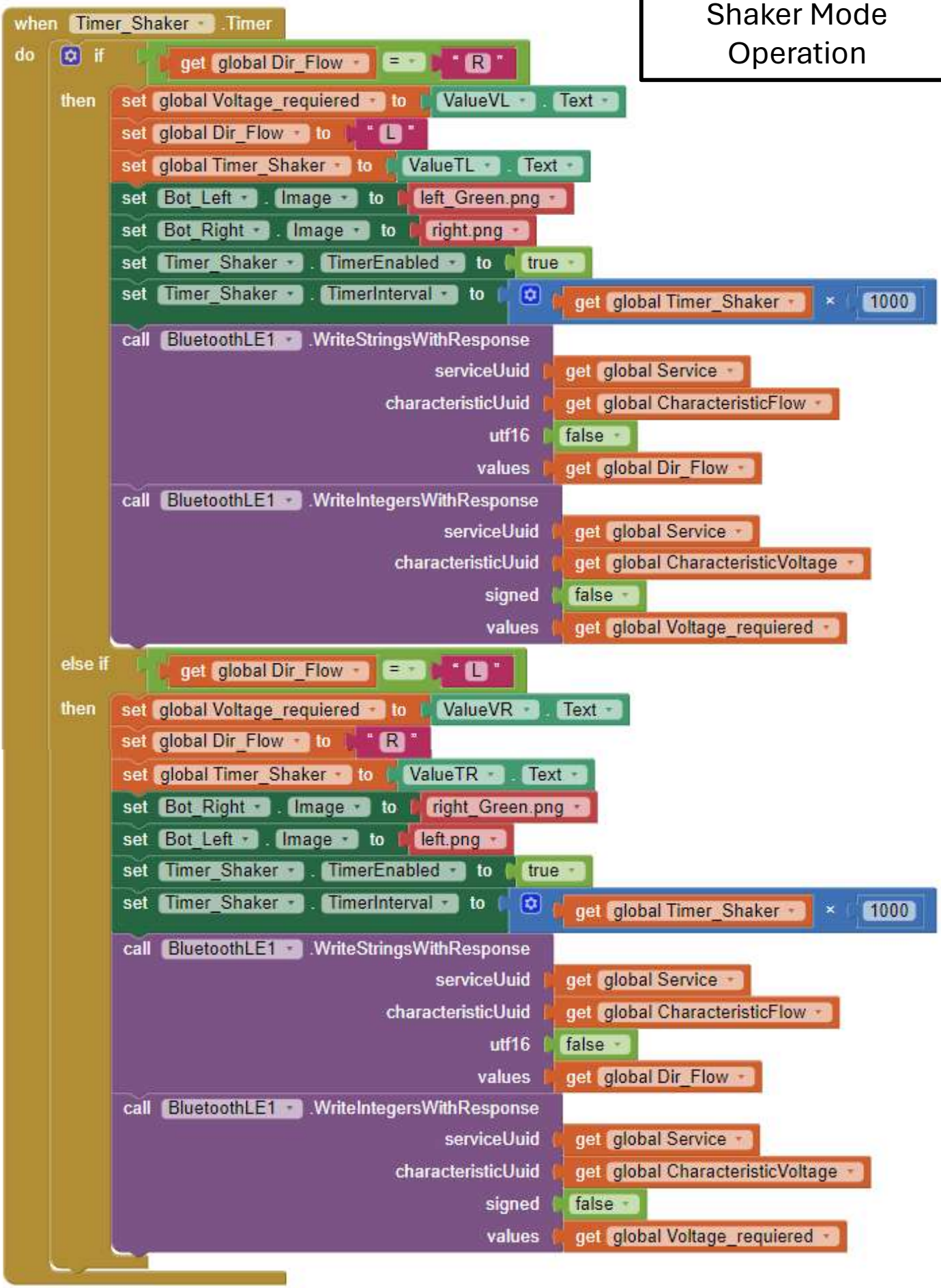
Shaker Mode Enabling Functionalities



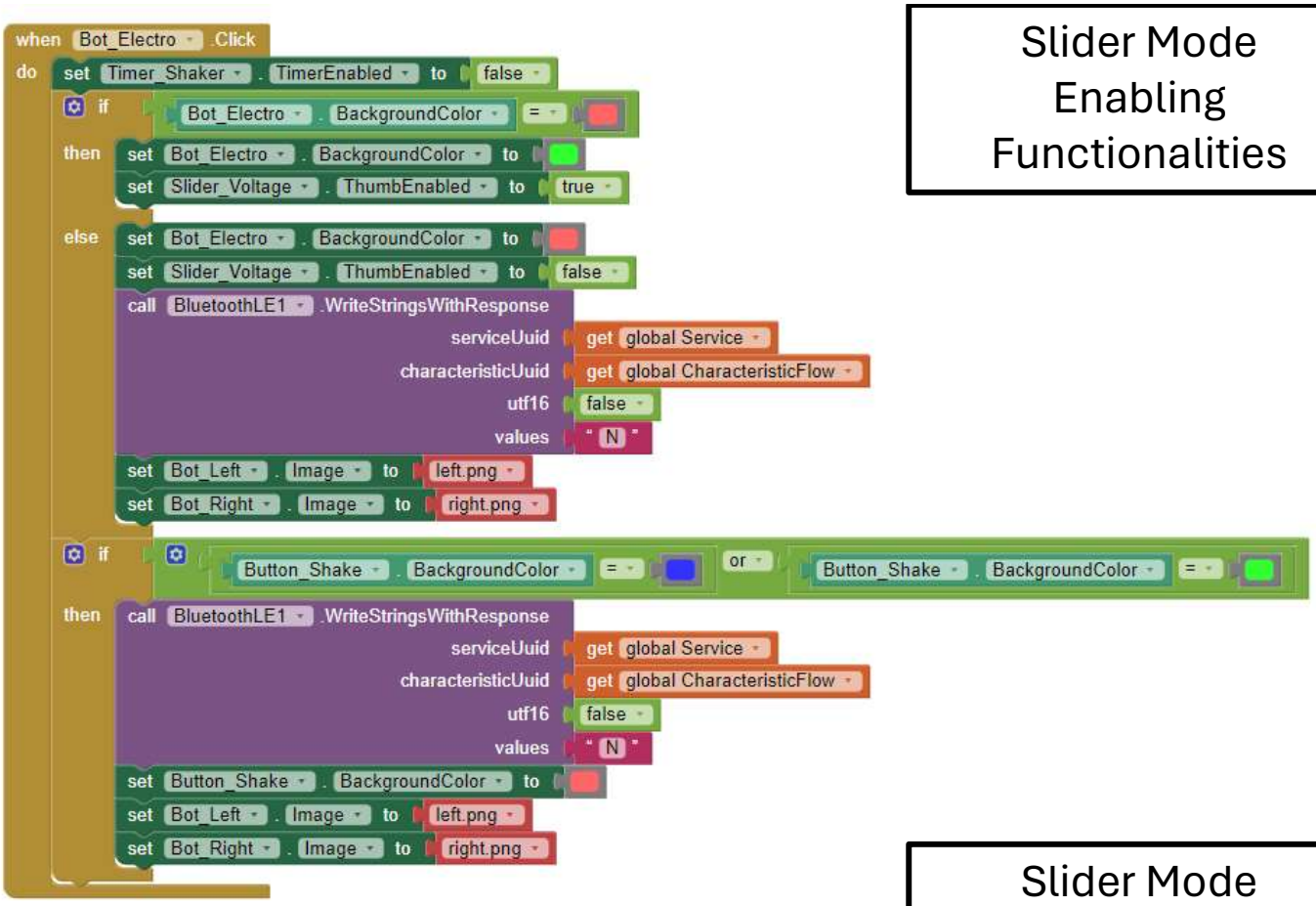
Shaker Mode Entries Validation



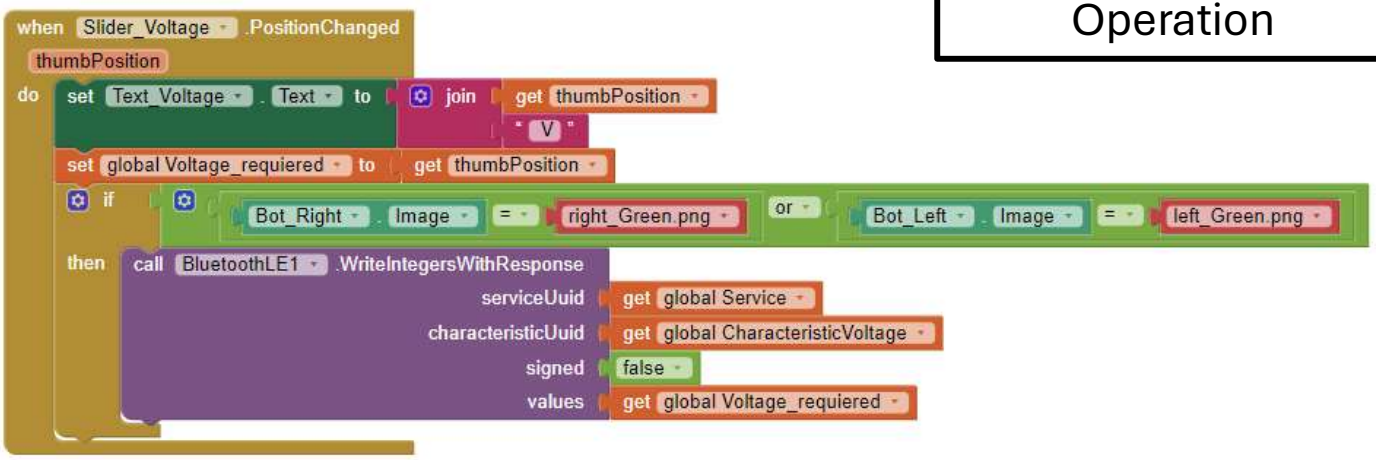
Shaker Mode Operation



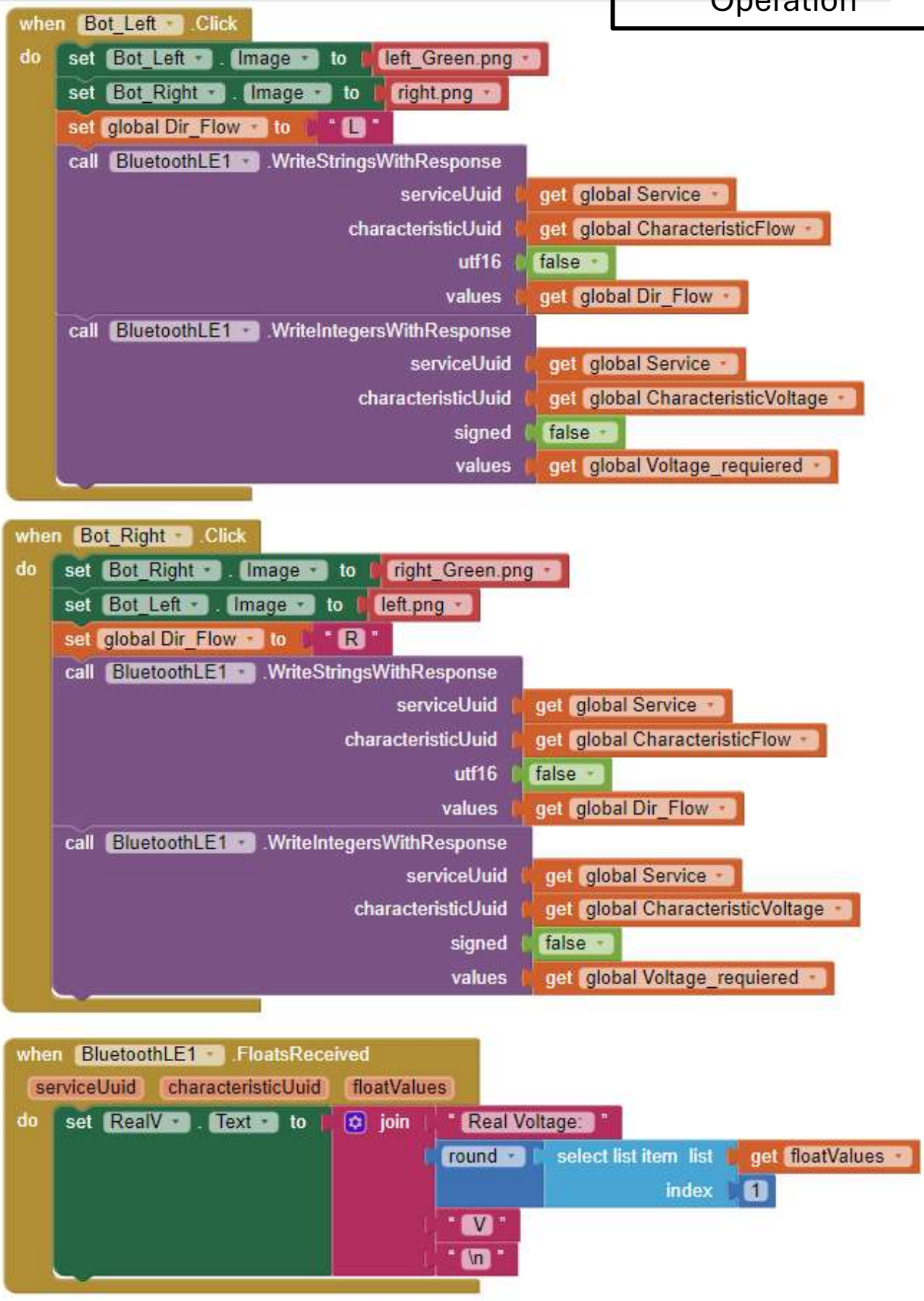
Slider Mode Enabling Functionalities



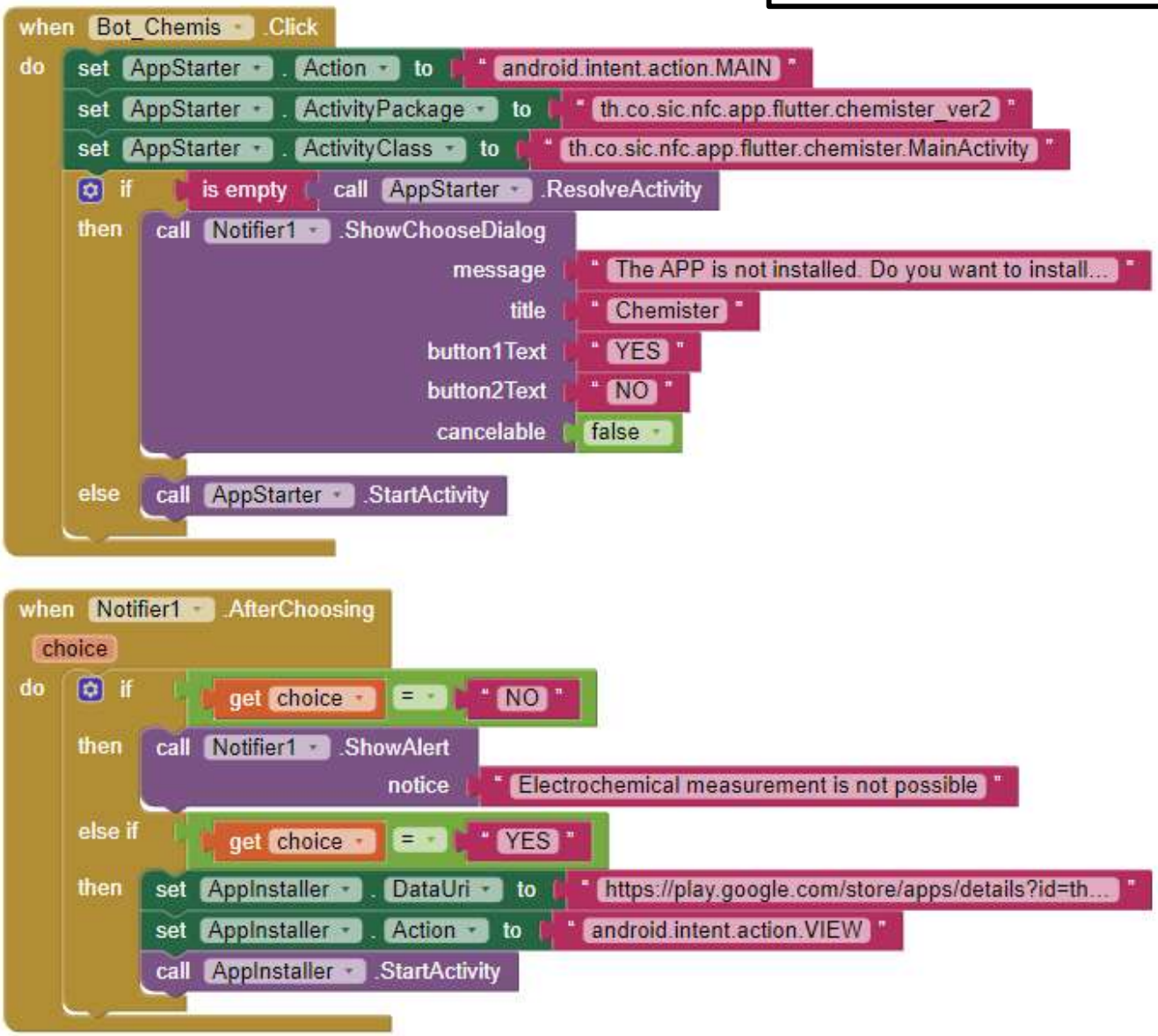
Slider Mode Operation



Slider Mode Operation



Chemister App Interface



Appendix D - Conferences & Congresses

NFC technology for data transmission in wearables. Can graphene be the technological solution for flexible antennas?

Gabriel Maroli[1,2]
Giulio Rosati[1]
Arben Merkoçi[1,3]

[1]Nanobioelectronics & Biosensors Group, Institut Català de Nanociència i Nanotecnologia (ICN2), Campus UAB, Bellaterra, 08193 Barcelona, Spain
[2]National Technological University (UTN-FRBA), Buenos Aires, Argentina
[3]Catalan Institution for Research and Advanced Studies (ICREA), 08010 Barcelona, Spain

Arben.merkoci@icn2.cat

Printed electronics have opened a plethora of new opportunities in the world of wearables and point of care devices. These devices present two major challenges, how to transmit the data to the user and how to power the device. In this context, NFC technology can be the solution, not only transmitting the results to the user's smartphone but also powering our wearable device.

One of the main issues of the implementation of this technology on printed flexible devices is that antennas printed with silver nanoparticles-based ink (the most widespread commercial ink for inkjet printing) typically have a high electrical resistance. Consequently, these antennas have high losses and, in consequence, it is necessary to place the smartphone very close to the device.

In the case of environmental sensors, it is often necessary to obtain the information through a glass or acrylic wall; therefore, it is required to have a larger reading distance. Therefore, with the aim to face this issue, there are two possibilities: designing antennas with wider tracks (limiting the miniaturization of the device), or exploring new nanomaterials with higher electrical conductivity, giving the possibility to transmit at a greater distance.

In this work, we will evaluate and compare silver nanoparticles printed antennas with flexible antennas obtained from high conductivity sheets of graphene with a very simple and fast fabrication method.

References

[1] Olenik, S., Lee, H.S. & Güder, F. The future of near-field communication-based wireless sensing. Nat Rev Mater 6, 286–288 (2021). https://doi.org/10.1038/s41578-021-00299-8
[2] Zulqarnain, M., Stanzione, S., Rathinavel, G. et al. A flexible ECG patch compatible with NFC RF communication. npj Flex Electron 4, 13 (2020). https://doi.org/10.1038/s41528-020-0077-x
[3] G. Maroli, A. Fontana, S. M. Pazos, F. Palumbo and P. Julián, "A Geometric Modeling Approach for Flexible, Printed Square Planar Inductors under Stretch," 2021 Argentine Conference on Electronics (CAE), 2021, pp. 61-66, doi:10.1109/CAE51562.2021.9397568.

Acknowledgements

Gabriel Maroli acknowledge the Fundación Carolina for the Doctoral Scholarship granted under the program “Doctorado 2020”

Challenges of printing on brittle and delicate substrates and membranes

Gabriel Maroli[1,2]
Giulio Rosati[1], Salvio Suárez-García[1], Massimo Urban[1], Patricia Batista Deroco[1,3], Daniel Ruiz-Molina[1] and Arben Merkoçi[1,4]
[1]*Catalan Institute of Nanoscience and Nanotechnology (ICN2), CSIC and BIST, Campus UAB, Bellaterra, 08193 Barcelona, Spain*
[2]*National Technological University (UTN-FRBA), Buenos Aires, Argentina*
[3]*Institute of Chemistry, University of Campinas (UNICAMP), Campinas, Sao Paulo, Brazil*
[4]*Catalan Institution for Research and Advanced Studies (ICREA), 08010 Barcelona, Spain*
Arben.merkoci@icn2.cat

Printed sensors, both on flexible substrates and directly on the skin, have been shown to have great potential for developing wearables and point-of-care devices. For this reason, integrating sensors by printing methods into already developed mussel-inspired membranes as artificial skin for tissue regeneration is of great interest not only for sensing on the skin, but also for treating wounds.

However, printing on delicate materials such as artificial skin presents many challenges, especially when a common desktop printer is used. To print on these materials, they must be dry, making them fragile and brittle. Due to this, some of the inside components of the desktop printer, like the rollers and wheels for dragging the paper can easily damage and eventually break them apart.

This work presents the comparison, advantages, and disadvantages of printing on the mussel-inspired membrane using a Dimatix (Fujifilms DMP 2800 series) research grade printer and an Epson XP-15000 desktop printer. As a case study, the resistivity obtained from the inks has been compared and its possible application for the construction of RF antennas as well as for a temperature sensor on the skin.

References

[1] MacNeil, S. Nature 2007, 445, 874-880.
[2] Rahmati, M. et al. Mater. Today Adv. 2020, 5, 100051.
[3] Ruiz-Molina, D. et al. Angew. Chem. 2019, 58, 696-714
[4] Ershad, F. et al, Nat. Commun. 2020, 11, 3823.

Figures

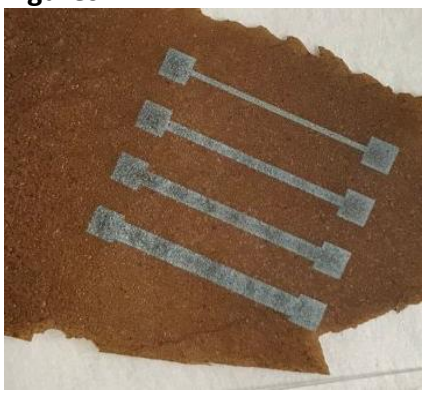


Figure 1: Silver tracks printed whit Epson printer on the mussel-inspired free-standing membrane

Acknowledgements

The ICN2 is funded by the CERCA program/Generalitat de Catalunya and supported by the Severo Ochoa "Centers of Excellence" program, grant SEV-2017-0706 funded by MCIN/AEI/10.13039/501100011033. This work was supported by grant RTI2018-098027-B-C21 funded by MCIN/AEI/10.13039/501100011033 and by ERDF – "A way of making Europe". Also, it has been financed by the Severo Ochoa Seed Funding for Emerging Topics 2021 Program. GM acknowledge the Fundación Carolina for the Doctoral Scholarship granted under the program "Doctorado 2020". PBD is particularly grateful to the São Paulo Research Foundation (FAPESP) for the award of a post-doctoral scholarship (Grant no. 2021/14732-0).

Challenges of printing on Mussel-Inspired free-standing films as Artificial biosensing Skin

Gabriel Maroli[1,2],
Giulio Rosati[1], Salvio Suárez-García[1],
Massimo Urban[1], Patricia Batista Deroco[1,3],
Daniel Ruiz-Molina[1] and Arben Merkoçi[1,4]

[1]Catalan Institute of Nanoscience and Nanotechnology (ICN2), CSIC and BIST, Campus UAB, Bellaterra, 08193 Barcelona, Spain
[2]National Technological University (UTN-FRBA), Buenos Aires, Argentina
[3]Institute of Chemistry, University of Campinas (UNICAMP), Campinas, Sao Paulo, Brazil
[4]Catalan Institution for Research and Advanced Studies (ICREA), 08010 Barcelona, Spain

Arben.merkoci@icn2.cat

Printed sensors, both on flexible substrates and directly on the skin, have been shown to have great potential for developing wearables and point-of-care devices. For this reason, integrating sensors by printing methods into already developed mussel-inspired membranes as artificial skin for tissue regeneration is of great interest not only for sensing on the skin, but also for treating wounds.

However, printing on delicate materials such as artificial skin presents many challenges, especially when a common desktop printer is used. To print on these materials, they must be dry, making them fragile and brittle. Due to this, some of the inside components of the desktop printer, like the rollers and wheels for dragging the paper can easily damage and eventually break them apart. For tailoring some of these issues, can be may be beneficial to use more dedicated and advanced equipment, like research grade inkjet printers.

This work presents the comparison, advantages, and disadvantages of printing on mussel-inspired membranes using a Dimatix (Fujifilms DMP 280) research grade printer and an EPSON xp 15000 desktop printer. As a case study, the resistivity obtained from the inks has been compared and its possible application for the construction of RF antennas as well as for a temperature sensor on the skin.

References

[1] MacNeil, S. Nature 2007, 445, 874-880.
[2] Rahmati, M. et al. Mater. Today Adv. 2020, 5, 100051.
[3] Ruiz-Molina, D. et al. Angew. Chem. 2019, 58, 696-714.
[4] Ershad, F. et al, Nat. Commun. 2020, 11, 3823.

Figures

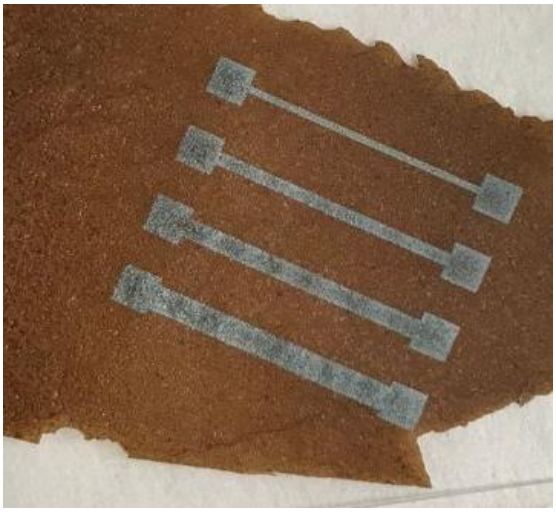


Figure 1. Silver tracks printed whit Epson printer on the mussel-inspired free-standing membrane

Building Your Device and App: A Guide for Pocketable Biosensors

Gabriel Maroli1,2
Ruslan Álvarez-Diduk1, Andy Jesus Bruno1, Arben Merkoci1,3
1- Catalan Institute of Nanoscience and Nanotechnology (ICN2), CSIC and BIST, Campus UAB, Bellaterra, 08193 Barcelona, Spain
2- Instituto de Investigaciones en Ingeniería Eléctrica Alfredo Desages (IIIE),Universidad Nacional del Sur – CONICET
3- Catalan Institution for Research and Advanced Studies (ICREA), 08010 Barcelona, Spain
gabriel.maroli@icn2.cat ; ruslan.alvarez@icn2.cat; arben.merkoci@icn2.cat

Biosensors, comprised of the bioreceptor, transducer, and signal output components, have traditionally leaned towards using laboratory potentiostats for electrochemical applications, with limited exploration of portable alternatives. However, in today's landscape, individuals with basic electronics and programming knowledge can craft portable potentiostats, develop custom smartphone apps, and engineer compact devices. This school delves into the fabrication of pocketable devices. As a practical case study, we will showcase the development of an electrophoretic power supply tailored for paper-based sensors with wireless electrochemical readout—a project executed by our research group. We will highlight key points to consider during the design, how to control it in a wireless way through Bluetooth. Additionally, the design of antennas specifically tailored for NFC (Near Field Communication) potentiostats, considering factors like series resistance and geometry will be presented. Finally, in order to have a user-friendly pocketable device, we will provide an introductory overview of creating mobile applications using a block-based approach, without the need for advanced programming skills.

Enhancing Resistive Humidity Sensors with rGO Resistors for Thermal Compensation

---

Gabriel Maroli[1,2], Robert Kobrin[1,3], Ruslan Álvarez-Diduk[1], Arben Merkoci[1,4]

1- Catalan Institute of Nanoscience and Nanotechnology (ICN2), CSIC and BIST, Campus UAB, Bellaterra, 08193 Barcelona, Spain

2- Instituto de Investigaciones en Ingeniería Eléctrica Alfredo Desages (IIIE), Universidad Nacional del Sur – CONICET

3- Joint Department of Biomedical Engineering, NC State & UNC Chapel Hill

4- Catalan Institution for Research and Advanced Studies (ICREA), 08010 Barcelona, Spain

gabriel.maroli@icn2.cat; ruslan.alvarez@icn2.cat; arben.merkoci@icn2.cat

---

Environmental measurements often require monitoring ambient humidity, with sensors commonly employing capacitive or resistive technologies. While capacitive sensors are commonly used, implementing resistance measurement at the circuit level offers distinct advantages, including greater sensitivity and ease of quantification. However, resistive sensors introduce a significant challenge: their resistance values not only vary with humidity but also fluctuate with temperature. In the case of silver printed sensors, this variation in resistance is due to the positive thermal coefficient of the material. In contrast, carbon-based materials, including reduced graphene oxide (rGO), exhibit a negative thermal coefficient. In most scenarios, temperature-induced resistance variations are negligible. Yet, in extreme environments like deserts, characterized by wide temperature fluctuations, or during measurements in volcanic areas, thermal effects can become substantial. Consequently, it becomes imperative to apply correction or compensation techniques. In this study, we explore the application of rGO resistors in series circuits to counteract the thermal changes observed in silver tracks. Through this innovative approach, we aim to develop humidity sensors that remain temperature-independent, ensuring their accuracy and reliability in environmental monitoring applications.

Development of a Portable Paper-Based Electrophoretic Bioassay with Simultaneous Electrochemical Readout

G. Maroli[1]; E. Calucho Palma[1]; A. Bruno; R. Álvarez Diduk*[1] and Arben Merkoçi*[1,3]

[1]Catalan Institute of Nanoscience and Nanotechnology (ICN2), CSIC and BIST, Campus UAB, Bellaterra, 08193 Barcelona, Spain

[3]Catalan Institution for Research and Advanced Studies (ICREA), 08010 Barcelona, Spain

Gabriel.Maroli@icn2.cat - Ruslan.alvarez@icn2.cat - Arben.merkoci@icn2.cat

Introduction

Biosensors, especially lateral flow assays (LFAs), have become increasingly popular in point-of-care (PoC) diagnosis due to their versatility and affordability. However, their sensitivity and quantification capabilities are limited by their principle of operation, which can result in inaccurate or inconclusive results, especially when complex samples such as blood, serum, and plasma are involved. To address these challenges, our team has developed a new approach for the next generation of paper-based biosensors that combine LFA automation, electrophoresis separation, and electrochemical readout sensitivity

In our recent work, we have successfully patterned conductive reduced graphene oxide electrodes on a nitrocellulose substrate, which, when coupled with electrophoretic separation up to 300 V, allows for electrochemical detection and eliminates unwanted interferences. Furthermore, our device is powered by a smartphone and takes advantage of near-field communication technology as an electrochemical reader, making it a viable PoC device that overcomes the limitations of traditional LFAs while remaining cost-effective.

Our approach, despite adding more complexity to the system, offers improved sensitivity and accuracy over traditional LFAs, making it a promising tool for diagnosing various diseases at the PoC. Our work builds upon the latest research in the field, including Parolo et al.'s (2020) comprehensive review of biosensors and their applications in diagnosis [1], recent advancements in LFA automation [2], and electrochemical readout sensitivity [4], as well as the successful implementation of electrophoresis separation in nitrocellulose substrates [3]. Additionally, our device benefits from the expertise and methods described in Giacomelli et al.'s (2020) study on the patterning of reduced graphene oxide electrodes [5].

NFC System and App

Turn on your NFC and TAP ME !





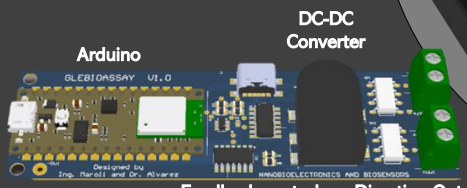
Check our group and also download the Chemister App to see the possibilities you have with this system.

We developed an App capable of controlling the electrophoretic source, its voltage and the direction of the current as well as performing the electrochemical measurement

Don't have NFC? Use QR!



Electrophoretic System



We developed a hardware that converts the 5V of the cell phone up to 300V, a feedback system controls that the voltage is constant, an arduino has been used to be able to communicate the hardware via Bluetooth with the mobile. A system of gates was placed at the output of the system in order to control the direction of the current.



Results

As a test, an electrophoresis of 2 uL Bromophenol blue was performed, in borate buffer 10mM. After 20 minutes the sample was moved from side to side on the 9 cm nitrocellulose strip.



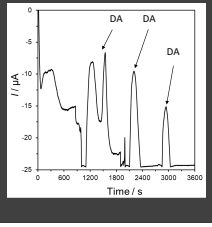


Use the Artivive App to see the system working

Electrochemistry



This system allows us to perform electrochemical measurements during electrophoresis because since the reading is done through the NFC antenna, a galvanic isolation is generated between the source and the electrochemical reading, avoiding noise problems and ground leakage currents.



Conclusions

-We have developed a portable electrophoretic system, which only requires a mobile phone for its operation.
-With the use of a power bank it is possible to operate this source from a distance.
-We have developed an electrochemical reading system using NFC technology
-The system allows electrochemical measurements to be made during electrophoresis, thus improving the accuracy of the measurements.

References

[1] Parolo, C., et al. "Biosensors and biosensing technologies for diagnostics applications." Nature Protocols, vol. 15, no. 12, 2020, pp. 3788-3816.
[2] Chem. Rev. 2022, 122, 18, 14881–14910.
[3] Anal. Chem. 2021, 93, 6, 3112–3121.
[4] ACS Sens. 2021, 6, 11, 4067–4075
[5] Giacomelli, Caterina, et al. 2D Materials, vol. 7, no. 2, 2020, p. 024006

Nanosensors network to monitor wounds healing by naturally adhesive bioinspired membranes by battery-free wireless smartphone readout.

Gabriel Maroli[1]+, Giulio Rosati[1]+*, Salvio Suarez[1]+*, Daniel Ruiz[1], Arben Merkoçi[1]*

[1]*Catalan Institute of Nanoscience and Nanotechnology, BIST, and CSIC, Edifici ICN2 Campus UAB, 08193 Bellaterra, Barcelona, Spain*

* giulio.rosati@icn2.cat; salvio.suarez@icn2.cat; arben.merkoci@icn2.cat

Abstract - Wounds and chronic wounds are an ever-increasing issue considering the effects of diseases such as diabetes and of accidents like burns. The early detection of infections is of vital importance for the patients. Currently, no easy solution is present in the clinical practice to face this issue. We propose a naturally adhesive bioinspired membrane obtained with a low-cost and high-throughput green method using derivative mussels' adhesion molecules to be applied to the wounds tightly fitting them and protecting from infection. Furthermore, we inkjet print nanofunctional inks and antennas on these membranes to be able to monitor the wound progression over time with a battery-free and wireless smartphone-based readout. In our poster, we will show the concept of the membrane fabrication, its modification thanks to inkjet printing, and the smartphone-based readout of temperature, humidity and pressure sensors.

Step 1

Scan the QR and download your ARTIVIVE App

SCAN ME

Step 2

Point your camera to the picture and follow our augmented reality instructions or go to Step 3.

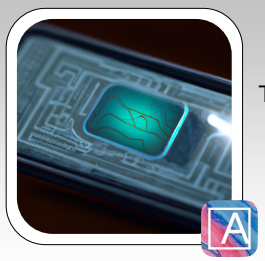
Step 3

Download the NFC app lying your smartphone over the NFC logo to perform measurements with our printed sensors

Step 4

Enjoy our e-poster testing the sensors by yourself (touch and breathe) while keeping your smartphone over the NFC logo!

Demo zone



Temperature sensor

Pressure sensor

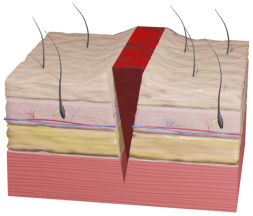
Humidity sensor

NFC

Smartphone

Temperature and humidity sensors have been fabricated by inkjet printing of silver nanoparticles on commercially available porous substrates. The pressure sensor have been purchased.

Wounds and chronic wounds



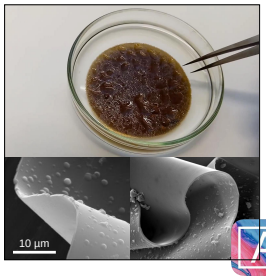
Wounds, particularly chronic wounds, present a **significant healthcare challenge**. Chronic wounds not only affect the physical well-being of individuals but also have a **considerable socioeconomic impact**. Patients with chronic wounds often experience **reduced quality of life**.

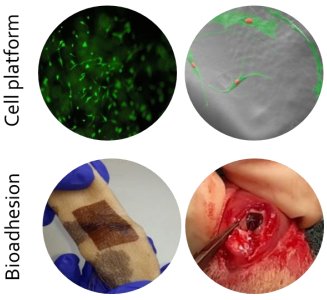
One **promising avenue of research** involves **bioactive scaffolds** that promote cellular migration, proliferation, and tissue remodeling. These materials **may contain growth factors, stem cells, or other biomolecules to enhance wound healing.** Additionally, tissue engineering techniques have paved the way for the development of **skin substitutes**, including dermal equivalents, which can be used **to replace damaged tissue** and **stimulate wound closure.**



Membranes

Bioinspired solution. Our platform consists on a **membrane that can act as a ready-to-use patch** usable **for tissue regeneration**. This novel technology has been **validated in preclinical studies** for cartilage regeneration and wound healing.





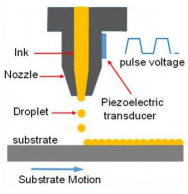
Our membranes already demonstrated **high biocompatibility, bioadhesion** and **promising results for hosting and transferring cells** to damaged tissue. The **next step** is to **endow the membranes with sensing capabilities to monitor the healing process**.

Inkjet-printed (bio)sensors

Among other fabrication methods, **inkjet printing** offers **resolution in the micrometric range**, **Drop-on-Demand** ink dispension, **ultra-low concept-to-prototype time** and a **wide range of** nanofunctional (conductive, dielectric, semiconducting) **inks**.

This allows to use it to fabricate scalable (bio)sensing devices [1-3].

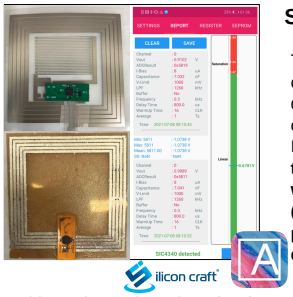




Silver nanoparticles (AgNPs) based inks are commercially **available, cheap and stable** for more than 6 months. **Special coated substrates** allow their **rapid drying and (chemical) sintering** at **room temperature**. Therefore, **conductive structures can be fabricated with even consumer printers** just drawing them and printing.

[1] G Rosati, et al. Biosensors and Bioelectronics, Volume 196, 2022, 113737.
[2] Q Yang et al. Biosensors and Bioelectronics, Volume 202, 2022, 114005.
[3] G Rosati et al. Scientific Reports Volume 11, 2021, 1-12

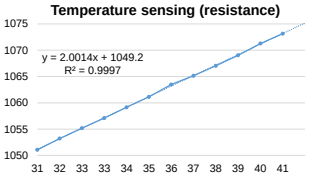
Smartphone-based wearables



There are **several technologies** which can be used **for wearable (bio)sensing**, depending on the distance needed to operate the (bio)sensors.
In **case of short distances NFC technology** allows for **battery-free and wireless communication** with **printed (bio)sensors** through simple and small **printed antennas and smartphone-detection.**

In this work we show that **simple temperature and humidity sensors can be inkjet-printed (top left corner in the figure)** even **on naturally adhesive membranes (bottom left corner in the figure)** and **used with a smartphone and a printed NFC antenna.**

Test it in our DEMO ZONE!



Conclusions & acknowledgments

In this work we have setup a network of simple inkjet-printed (bio)sensors with just a AgNP nanofunctional commercial ink on a commercial coated substrate and an antenna for NFC powering and communication of the collected data (wireless and battery-free). The developed (bio)sensors will be transferred to our naturally adhesive membranes and tested for the sensing of temperature humidity and strain in wounds, in order to monitor the healing process.

This project has received funding from the European Union's Horizon 2020 research and innovation programme under grant agreement No 101008701 (Project EMERGE). Views and opinions expressed are however those of the author(s) only and do not necessarily reflect those of the European Union. The European Union cannot be held responsible for them. This research was supported by grant PID2021-27983OB-C21 funded by MCIN/AEI/10.13039/501100011033 and by ERDF A way of making Europe. Also, it has been financed by the ICN2 Severo Ochoa Seed Funding for Emerging Topics 2021 Program. The ICN2 is funded by the CERCA programme/Generalitat de Catalunya. Grant SEV-2017-0706 funded by MCIN/AEI/ 10.13039/501100011033. The ICN2 is supported by the Severo Ochoa Centres of Excellence programme, Grant CEX2021-001214-S, funded by MCIN/AEI/10.13039.501100011033.

Appendix E - Published Papers

Check for updates

RESEARCH ARTICLE

NANO · MICRO small
www.small-journal.com

The Cleanroom-Free, Cheap, and Rapid Fabrication of Nanoelectrodes with Low zM Limits of Detection

Gabriel Maroli, Vernalyn Abarintos, Andrew Piper, and Arben Merkoçi**

Nanoscale electrodes have been a topic of intense research for many decades. Their enhanced sensitivities, born out of an improved signal-to-noise ratio as electrode dimensions decrease, make them ideal for the development of low-concentration analyte sensors. However, to date, nanoelectrode fabrication has typically required expensive equipment and exhaustive, time-consuming fabrication methods that have rendered them unsuitable for widespread use and commercialization. Herein, a method of nanoband electrode fabrication using low cost materials and equipment commonly found in research laboratories around the world is reported. The materials' cost to produce each nanoband is less than €0.01 and fabrication of a batch takes less than 1 h. The devices can be made of flexible plastics and their designs can be quickly and easily iterated. Facile methods of combining these nanobands into powerful devices, such as complete three-electrode systems, are also displayed. As a proof of concept, the electrodes are functionalized for the detection of a DNA sequence specific to SARS-CoV-2 and found to display single molecule sensitivity.

1. Introduction

For many years now, electrochemists have been limited by the choice of available electrodes. Traditional gold, silver, and carbon electrodes are routinely used around the world and can be purchased for a few hundred euros each. However, these electrodes require polishing by hand in alumina slurries, chemical cleaning in harsh, environmentally unfriendly solvents (such as piranha solution), sonication, and electrochemical cycling in strong acids (e.g., H_2SO_4), in order to clean them before use.[1–3] This is all done to try and get the electrodes as clean, flat, and reproducible as possible. The oldest alternative to these electrodes is the dropping mercury electrode,[4] where mercury is dropped through a small capillary to constantly create a fresh electrode surface of a defined area at which measurements can be taken. Due to safety concerns over working with mercury, these are rarely used nowadays.

More modern alternatives include inkjet and screen-printed electrodes.[5–8] In such electrodes, nano-/microparticle inks are patterned onto a substrate. To prevent aggregation, the nanoparticles need to be stabilized in solution by adding bulky organic ligands to make them stable colloids. The presence of these ligands can impede subsequent electrode performance and their removal post-printing is difficult given their size and covalent attachment to the nanoparticles. The printed electrodes are incredibly rough and irreproducible, which contributes to irreproducibility in the intended applications. In most cases, the devices are not conductive immediately after printing and need to be "sintered," a process by which the conductive particles morph to increase the contact area between them.[9,44] Printed electrodes can be purchased commercially for several euros per electrode, with the exact price depending on the electrode type.

Alternatively, electrodes can be made in clean rooms. These facilities are expensive to build and their maintenance and running costs are prohibitively expensive for many research and commercial applications. Inside the clean room, conductive materials can be deposited on substrates in a highly controlled fashion with sub-nanometer resolution using chemical or physical vapor deposition, atomic layer deposition (ALD), or electron beam evaporation (E-beam).[10,11] ALD is a surface-controlled and self-limiting method for depositing thin films from gaseous precursors. This self-limiting growth mechanism allows sub-nanometer-level control of film thickness with an excellent conformity.[12] With E-beam, an electron beam is focused onto a target metal under high vacuum, vaporizing the metal in a high vacuum chamber where it can be deposited in a uniform thin film on a chosen substrate.[13,14] The cost of these tools is in the range of hundreds of thousands of euros. Electrodes made by this method offer the best electrode purity and smoothness. Likewise, by fabricating in a cleanroom, photolithographic processes can be used to make a variety of electrode designs and architectures with incredibly high resolution.

G. Maroli, V. Abarintos, A. Piper, A. Merkoçi
Catalan Institute of Nanoscience and Nanotechnology (ICN2)
UAB Campus
Bellaterra, Barcelona 08193, Spain
E-mail: andrew.piper@icn2.cat; arben.merkoci@icn2.cat
G. Maroli
UIDI-CONICET Universidad Tecnológica Nacional
Buenos Aires C1041AAJ, Argentina

The ORCID identification number(s) for the author(s) of this article can be found under https://doi.org/10.1002/smll.202302136

© 2023 The Authors. Small published by Wiley-VCH GmbH. This is an open access article under the terms of the Creative Commons Attribution License, which permits use, distribution and reproduction in any medium, provided the original work is properly cited.

DOI: 10.1002/smll.202302136

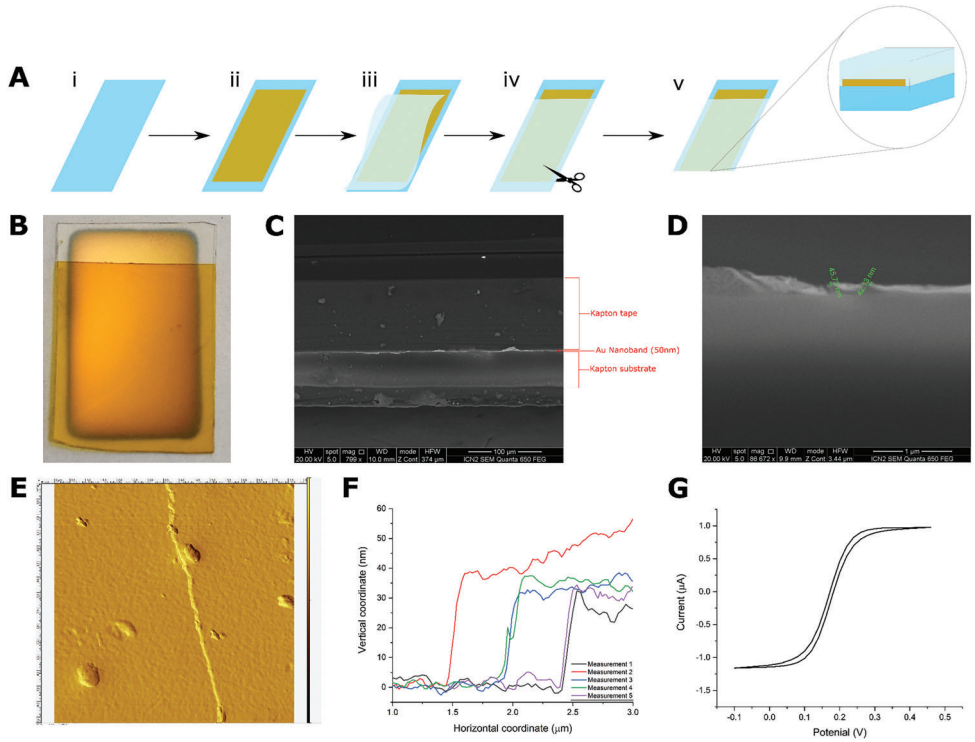


Figure 1. A) Schematic representation of the nanoband electrode fabrication showing i) the cleaned prepared substrate ii) after sputtering a nanometer thin layer of conductive electrode material through a mask iii) application of a capping layer iv) cutting to relieve a nanometer high edge electrode v) the completed device with a cross-section schematic (not to scale). B) Photograph of a device at step (iv), in this photograph the device was made with a PET substrate and Kapton tape capping layer. C,D) Scanning electron micrograph images of nanoband electrodes made with Au sputtered onto Kapton and capped with Kapton tape, cut with surgical grade scissors E) is an AFM image of the edge of one of the sputtered Au devices on Kapton (uncapped) with five corresponding step height measurements from left to right across the ridge in (F) showing that the Au thickness is ≈30–40 nm and the roughness of the Au surface is the same as the Kapton (single nanometers). G) CV of nanoband electrode, in 5×10^{-3} M potassium ferricyanide, 5×10^{-3} M potassium ferrocyanide, 100×10^{-3} M KNO_3 recorded at a scan rate of 10 mV s^{-1} versus a Ag/AgCl reference electrode and Pt wire counter electrode.

A nanoelectrode is defined as any electrode that has at least one of its dimensions on the nanoscale.[15,16] Nanoelectrodes have many advantages over conventional, macroscopic electrodes. Chief among which is their superior sensitivity.[17–20] This improvement in sensitivity as the electrodes get smaller can be attributed to three factors: The first comes from their enhanced mass transport, which allows them to measure a steady-state current; second, they have smaller double layers, which means that a greater proportion of the current is Faradaic; and finally, they have relatively smaller iR drops than larger electrodes.[17,20,21] Recent studies have also shown that nanoscale electrodes can be functionalized through the spontaneous formation of thiolate self-assembled monolayers (SAMs), the most common method of electrode functionalization, in a matter of seconds; rather than the hours taken to functionalize macroscale electrodes.[3] This means that sensor development and fabrication can be rapidly sped up if done on nanoscale electrodes. At the time of writing, nanoelectrodes are typically either made using complementary metal–oxide semiconductor fabrication techniques,[13,22] finely controlled chemical growth,[23] made in the form of nanowires[24,25] or grown on nanoscale templates.[26] These methods are either expensive or unsuitable for large-scale electrode manufacturing.

Here, we report a cleanroom-free method of nanoelectrode fabrication using sputter coaters. With this method, we are able to deposit metallic thin films with sub-nanometer resolution, outside of a cleanroom, using cheap equipment found in most research laboratories onto any substrate. These thin films are sandwiched between the substrate and a capping layer before being cut to relieve a nanoband electrode, see **Figure 1**. These electrodes are extremely cheap, with raw materials costing less than €0.10 per device, and can be cut multiple times in a matter of seconds to relieve brand new, pristine electrodes that require no cleaning prior to use. By cutting each device multiple times, the cost of each electrode can be reduced to below €0.01. We show that these electrodes possess the characteristic electrochemical properties of nanoelectrodes, including better signal-to-noise ratios and faster functionalization times than larger electrodes. As a proof of principle, we show the superior performance of these electrodes in the detection of DNA with the same sequence tested for in the quantitative reverse transcription polymerase chain reaction (PCR) diagnosis of SARS-CoV-2; where they exhibited superior sensitivities and limits of detection to conventional electrodes.

These electrodes are cheap, easy to fabricate, can be made in any lab in the world with commonplace, affordable equipment,

© 2023 The Authors. Small published by Wiley-VCH GmbH

16136829, 2023, 51, Downloaded from https://onlinelibrary.wiley.com/doi/10.1002/smll.202302136 by Spanish Cochrane National Provision (Ministerio de Sanidad), Wiley Online Library on [15/01/2024]. See the Terms and Conditions (https://onlinelibrary.wiley.com/terms-and-conditions) on Wiley Online Library for rules of use; OA articles are governed by the applicable Creative Commons License

are more sensitive than the commonly used electrodes, and can be functionalized to make sensors in minutes. They therefore have the potential to revolutionize any research that uses electrodes. They are superior in every way to electrodes made by other methods and have the potential to replace existing electrodes immediately, with little to no upfront capital costs. The faster functionalization times and lack of required cleaning means that assay development can be rapidly sped up on these electrodes. Finally, it is intended that the electrodes will allow more sensitive point of care sensors to be developed, allowing the diagnosis and prognosis of diseases with biomarkers too low in concentration for conventional sensors to detect, the earlier diagnosis of diseases (when the concentration of biomarkers is lower), and perhaps even the amplification-free detection of nucleic acid biomarkers.

2. Results and Discussion

2.1. Electrode Fabrication and Characterization

The nanoelectrodes in this project were fabricated by sputtering gold, using a conventional sputter coater, through a mask (stencil) onto various flexible plastic substrates. The substrates tested were polyimide (Kapton), polyethylene terephthalate (PET), and polyethylene naphthalate (PEN). These substrates were chosen because they are cheap, widely available, flexible, and easy to cut. The ability to form these electrodes on any vacuum stable substrate, without any optimization of the fabrication, is a major advantage of this work over alternative methods. The masks used in this project as stencils were made of aluminium or any of the aforementioned plastics, theoretically they can be made out of any material that does not interfere with the sputtering. The stencils are required to have sufficient weight to sit flush on the substrate and keep it in place during the evacuation of the sputter chamber. This is important to make electrodes reproducibly, as any lifting or deformation of the mask can change the sputtered electrode dimensions. The ability to rapidly design, cut, and use masks with different layouts allows a fast iterative approach for electrode design. This is not possible using photolithography where new masks take much longer to design and fabricate. In this study, a simple design motif of 1.2 cm wide and 2.4 cm long rectangles was used, Figure 1A,B and Figures S1 and S2 in the Supporting Information.

The rate of Au deposition by sputtering is well reported in the literature, and our measurements of the electrode thickness as a function of time and deposition current were found to be in agreement with other publications.[27,28] This method allows for the controlled deposition of nanometer thin metallic films with sub-nanometer precision; using cheap equipment that is routinely found in most laboratories around the world, since sputter coaters are used in scanning electron microscope (SEM) sample preparation. In this work, we sputtered metallic layers 50–100 nm thick. The rationale behind this was to make the devices thick enough to ensure a good connection through a crocodile clip on the bond pad, to ensure a homogenous coverage of the substrate and to have the same thicknesses as similar cleanroom-fabricated nanoelectrodes present in the literature.[3,17,18,27–29]

The deposited metal (in this case Au) was initially tested with a four-point probe to assess its conductivity. The mask allowed us to make five devices on each substrate, see Figure S2 in the Supporting Information, the sheet resistances of the sputtered metal films on different substrate have been provided in Table S1 in the Supporting Information, as well as that of E-beamed Au on Kapton, for reference. All the measured values are the same order of magnitude ($m\Omega\ sq^{-1}$) with the E-beamed Au having a sheet resistance about half that of the sputtered Au. There is no significant difference between the resistances of the gold sputtered onto any of the different substrates, this is pleasing as it evidences that the substrate does not affect the electrochemical performance of the devices.

In order to create nanoelectrodes, the sputtered metal needed to be "capped" and cut. Several capping methods were tested, including: covering with Kapton tape, spray coating with acrylic, and laminating with an office laminator. All were found to work, Figures S3–S6 in the Supporting Information, and may be suited to different applications. The requirements for a good capping layer are that it strongly adheres to both the electrode material and the substrate, is chemically inert in the media in which it will be tested, forms a good physical and dielectric barrier, and does not damage the underlying electrode. It should also be easy to cut with the intended cutting method. In this project, we favored using the Kapton tape because it was quicker to make devices with this than the other methods which need to be left to dry (acrylic) or heated (lamination).

Once the devices are capped, they must be cut to relieve nanoband electrodes. The cutting was performed with scissors, scalpels, or a paper guillotine, see Figure S4 in the Supporting Information, all were capable of producing nanoband electrodes. In order to make functioning electrodes, the blades in each of the cutting methods need to be as sharp and clean as possible (e.g., it is necessary to use surgical grade or microscopy scissors rather than office scissors). If the blade was blunt, it would cause a deformation of the layers, Figure S7 in the Supporting Information. Finally, the capping layers do not all set hard and should be cut face down to drag the adhesive away from the electrode, so as not to cover it.

Cyclic voltammograms (CVs) of each substrate type, with each capping layer and cutting method have been included in Figure S6 in the Supporting Information. It is clear from the wave-like shapes of the CVs and the low capacitances of the electrodes that they are all nanoelectrodes. From Figure S6 in the Supporting Information, the most reproducible cutting method was the precision cutter, followed by the scissors and finally the scalpel. This trend can be explained by the methods that allow for the most human error causing the most irreproducibility. When cutting with the scalpel, the angle, pressure, and straightness of the cut are more irreproducible than with the other cutting methods.

Regarding the capping layers, the acrylic is the most reproducible owing to the fact that it sets the hardest. The softer setting adhesives of the tape and melt layer of the laminate are prone to being smeared on the electrodes during cutting. This is why it is important to cut the electrodes in a fashion that drags the adhesive away from the electrode. Although some damage is still possible, which is why the precision cutter gave not only the most reproducible cuts, see Figure S6 in the Supporting Information, but also consistently yielded electrodes with a higher area; as there is less adhesive on the electrodes. Examples of the adhesive smearing can be seen in Figure S8 and the video in the Supporting

© 2023 The Authors. Small published by Wiley-VCH GmbH

16136829, 2023, 51, Downloaded from https://onlinelibrary.wiley.com/doi/10.1002/smll.202302136 by Spanish Cochrane National Provision (Ministerio de Sanidad), Wiley Online Library on [15/01/2024]. See the Terms and Conditions (https://onlinelibrary.wiley.com/terms-and-conditions) on Wiley Online Library for rules of use; OA articles are governed by the applicable Creative Commons License

Information. In all experiments, the substrates tested had no discernible impact on the final electrode quality.

The time taken to make a single batch of electrodes, including sputtering, capping, and cutting was less than 1 h. Once the devices are made, fresh electrodes can be made by cutting in a matter of seconds. This is a crucial advancement over other cleanroom-free nanoelectrode fabrication methods such as those reported by the White group,[30] in which substrates are sputter coated through a mask and then encapsulated in resin which takes 24 h to dry, before being mechanically polished for hours to create pristine flat electrodes. A video showing the entire fabrication process has been made to accompany this publication. The equipment used is commonly found in most laboratories around the world but the up-front capital costs are also very low if they do need to be purchased. Table S2 in the Supporting Information summarizes these capital costs and the cost of consumables used for electrode fabrication. If the upfront equipment costs are excluded, then the materials' cost per electrode is below €0.01, on the condition that the devices are cut a minimum of ten times each, to yield at least ten electrodes per device. This makes these electrodes cheap and therefore inherently disposable, it is cheaper to cut and create a new electrode rather than trying to clean and re-use them. The ability to cut one device several times to make multiple electrodes is a novel advantage of these devices. The devices can take up to an hour to make but cutting and making a fresh nanoelectrode takes seconds.

To confirm that the fabricated electrodes are truly nano in nature, the bands were imaged by SEM, Figure 1C,D, the height of the uncapped sputtered metal edges was measured by atomic force microscopy (AFM), Figure 1E,F, and the nanoscale electrochemical responses of the bands were evaluated. The SEM images clearly show a nanoscale conductive band between the substrate and capping layer. Using the SEM software (xT microscope Control), the height of this band could be estimated and was found to be between 40 and 45 nm, which was slightly below the 50 nm targeted sputtering thickness of these devices. This slight variation is attributed to experimental errors in the sputtering since the AFM measurements of uncapped Au layers sputtered onto Kapton also had a step height of about 40 nm.

Typical CVs of macroelectrodes have peaks that form as the current becomes limited by the mass transport of the redox molecule to the electrode surface. The response of nanoelectrodes is different,[24,31] because the electrodes are so small, a hemispherical diffusion profile is rapidly established.[15,32] Therefore, waves rather than peaks are observed in the CVs of nanoscale electrodes.[33–35] The nanoband electrodes developed in this project exhibit electrochemical responses typical of nanoscale electrodes, Figure 1G. Likewise, the current ranges observed are in good agreement with nanobands of similar dimensions in similar buffers reported by other groups.[30] Another interesting electrochemical feature of the nanoelectrodes is the extremely low capacitances that they display, in this system the only capacitance present is the double layer capacitance (C_{dl}). The magnitude of the C_{dl} is given by the Helmholtz equation, Equation (1)[31]

$$C = \frac{\varepsilon_0 \varepsilon_r A}{H} \quad (1)$$

where C is the capacitance in Farads, ϵ_0 is the dielectric permittivity of a vacuum, ϵ_r is the dielectric permittivity of the measurement solution, A is the area of the electrode, and H is the separation distance between the plates in the model. In aqueous systems, H can be taken as the inner Helmholtz plane (the diameter of a water molecule in pure water).[31] It is possible to approximate the electrochemical surface area of the nanoband electrodes using Equation (1), since the C_{dl} follows the electrode surface very accurately and the other values can all be taken from the literature for pure water ($\epsilon_0 = 8.854 \times 10^{-12}$ F m^{-1}; $\epsilon_r = 78.3$; $H = 2.75$ Å).[31] In these experiments, 75 nm thick electrodes were sputtered, with a geometric electrode surface area of 9×10^{-4} mm^2. We calculated the area of our electrode, from its voltammetric capacitance, Figure S9 in the Supporting Information, to be $13.5 \times 10^{-4} \pm 0.6 \times 10^{-4}$ mm^2, within experimental error the same as the geometric area. These data further evidence the nanoscale nature of the electrodes. Likewise, the standard deviation was obtained from three electrodes cut on a single device, showing the reproducibility of the cutting method and the uniformity of the sputtered Au over the entire device. The slightly larger electrochemical surface area than geometric surface area is attributed to surface roughness and heterogeneity.[36] It is satisfying that our so-called "roughness factor" is 1.5, which is better than reported for other electrode types in the literature.[37] In this system, we postulate that as the capping layer adhesive is setting, it may move (during handling), dragging the Au layer out of the device, much like the filling in a sandwich when it is pressed. This theory is based on the SEM data, Figure 1D, where films appear to protrude from the device. This is further supported by the findings that the signals from the hardest setting capping layers (acrylic) gave the most reproducible electrodes. Also, anecdotally, the electrode reproducibility could be improved by leaving any of the capping layer types for extended periods of time (days/weeks depending on the capping material), to allow them to set harder.

To further characterize the electrochemical response of the nanobands, they were analyzed by electrochemical impedance spectroscopy. The Nyquist plot from these experiments has been provided in Figure S12 in the Supporting Information, within an inset showing the equivalent circuit to which it has been fit. This is the established equivalent circuit for nanoelectrodes.[3,15,35] The fitted values of the fit, reported in Table S5 in the Supporting Information, include an R_{ct} of 29 980 Ω ± 3.5% (error from the fitting). This was used to determine an electron transfer rate of 8.03 cm s^{-1}, the derivation of which is included in Figure S13 in the Supporting Information, which is in agreement with other nanoelectrodes in the literature.[32,35,38]

2.2. Different Electrode Designs

One of the advantages of making electrodes using this methodology is the ability to rapidly iterate different electrode designs and configurations. New plastic masks can be made quickly (in under 20 min) and easily using cutting plotters (or by hand) to change the pattern and size of the metallic coatings to suit different applications. Likewise, it is very easy to combine electrodes of different designs and types to create customized devices for different applications. It is easy to fabricate a library of electrodes of different patterns and thicknesses, sputtered from different materials.

© 2023 The Authors. Small published by Wiley-VCH GmbH

16136829, 2023, 51, Downloaded from https://onlinelibrary.wiley.com/doi/10.1002/smll.202302136 by Spanish Cochrane National Provision (Ministerio de Sanidad), Wiley Online Library on [15/01/2024]. See the Terms and Conditions (https://onlinelibrary.wiley.com/terms-and-conditions) on Wiley Online Library for rules of use; OA articles are governed by the applicable Creative Commons License

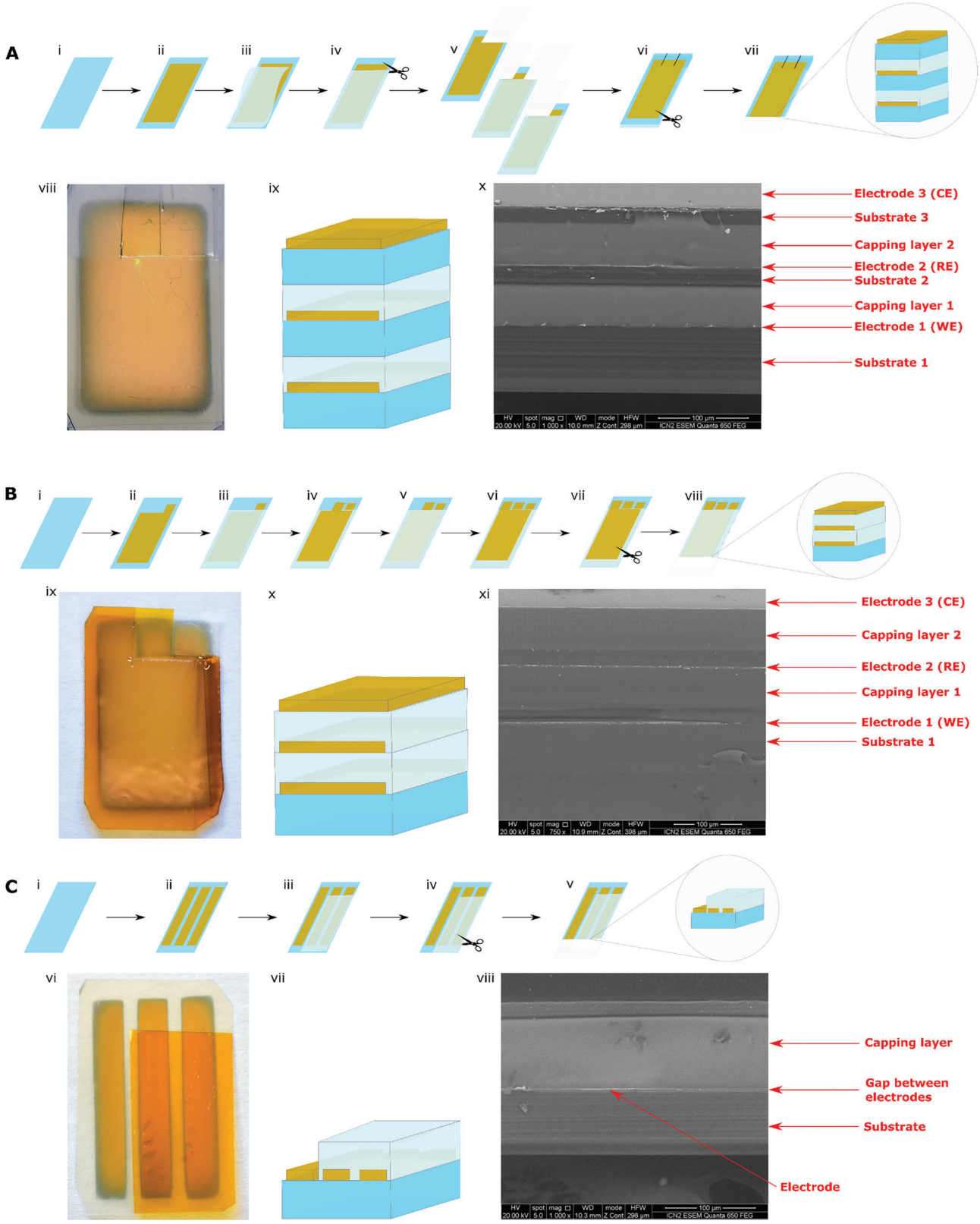


Figure 2. Schematics (not to scale), photographs, and SEM images of the different LEGO brick designs fabricated and tested in this project. A) Sticking completed devices on top of each other: i) a cleaned substrate, ii) is sputter coated with a nanometer thin film of Au, iii) before being capped, and iv) the bond pads cut so that each will open to the environment in the final 3D device, v) multiple separate devices are stacked and stuck to each other, vi,viii) before the three nanobands are exposed by cutting. viii) A photograph of one such completed device, ix) as well as a schematic and x) SEM of the

© 2023 The Authors. Small published by Wiley-VCH GmbH

16136829, 2023, 51, Downloaded from https://onlinelibrary.wiley.com/doi/10.1002/smll.202302136 by Spanish Cochrane National Provision (Ministerio de Sanidad), Wiley Online Library on [15/01/2024]. See the Terms and Conditions (https://onlinelibrary.wiley.com/terms-and-conditions) on Wiley Online Library for rules of use; OA articles are governed by the applicable Creative Commons License

These individual components can then be easily combined to develop new devices for different applications, including those with different numbers of electrodes, such as two-electrode systems or for multiplexed sensing applications. Much like LEGO bricks, these can be attached together to create an endless possibility of designs. As a proof of principle for this "LEGO-brick" concept, complete three-electrode systems have been developed by a number of different methods. The authors would like to stress that this is simply a proof of concept and that an endless number of designs are possible. Photographs, schematics, and SEMs of these different methods of combining devices have been shown in **Figure 2**. First, it is possible to stick multiple capped devices on top of each other using adhesives, see Figure 2A. Second, it is possible to build the devices up vertically by sputtering directly onto the capping layers, using masks to separate the different bond pads for the different layers, Figure 2B. Third, it is possible to design a mask in which the three electrodes are in the same 2D plane and simply separated from each other by the mask design, Figure 2C. The CVs of these devices, Figure S10 in the Supporting Information, show that there is a shift in the half-wave potential (from +0.175 to +0 V) when switching from a Ag/AgCl reference electrode to a sputtered Au pseudoreference electrode, as would be expected. Other than this, there is no difference in the obtained electrochemical signal, proving that functioning complete three-electrode systems can be produced by this "Lego-brick" method.

2.3. DNA Detection

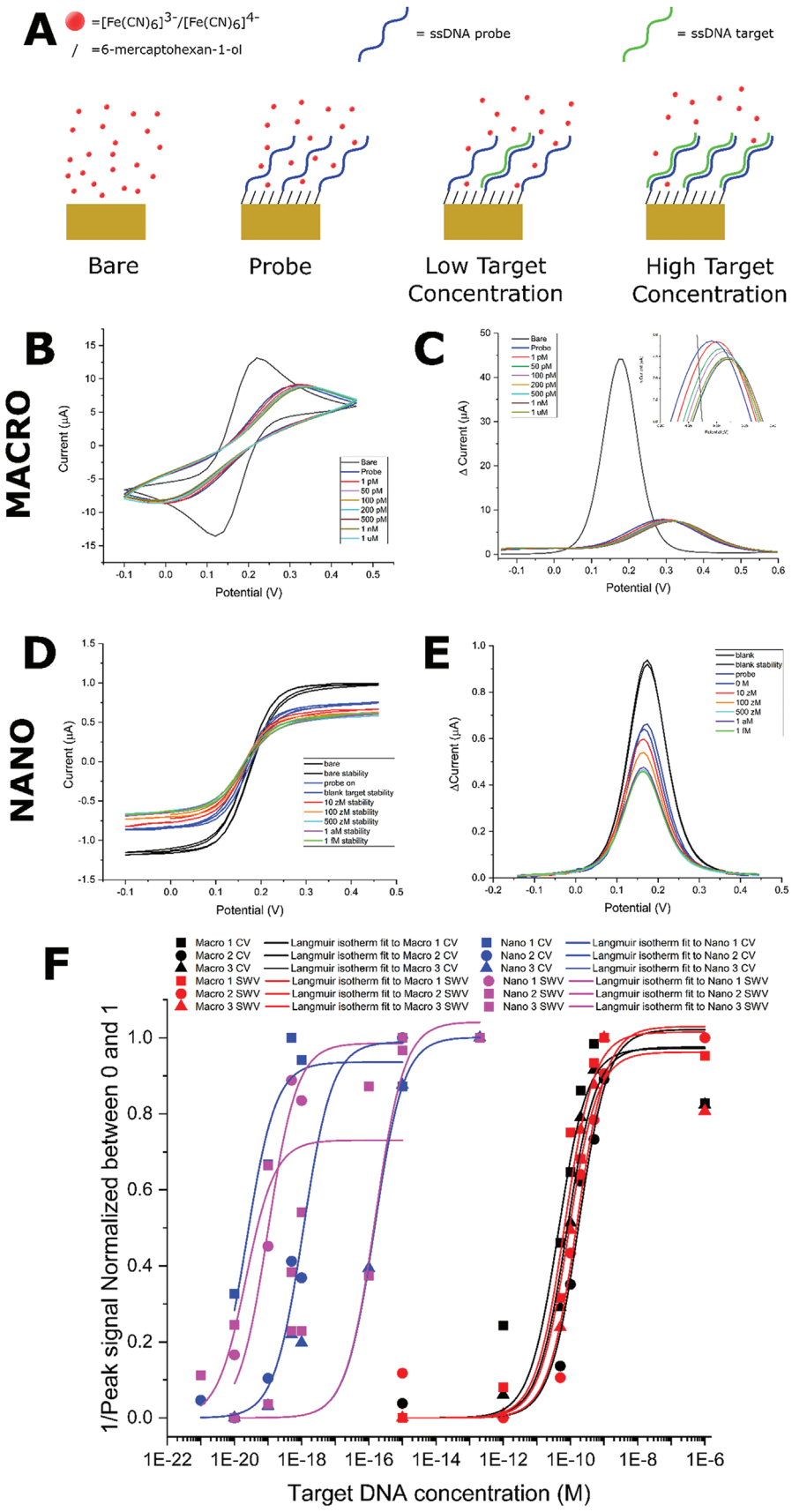
In order to assess the sensing performance of the **e**lectrodes, they were functionalized with an ssDNA probe for the detection of a DNA sequence specific to SARS-CoV-2. The authors would like to stress that this is a proof-of-concept experiment, intended to ascertain the performance of the nanoband electrodes and compare them to existing commercial electrodes. As such, it was deemed suitable to detect a synthetic complimentary DNA sequence rather than RNA from real samples and the authors wish to stress that no claims are being made that an amplification-free SARS-CoV-2 sensor has been developed. The mode of operation of the sensor is shown schematically in **Figure 3**. First, the electrochemical response of a clean (bare) electrode is measured in a solution of 5×10^{-3} M $K[Fe(CN)_6]^{3-}$ and 5×10^{-3} M $K[Fe(CN)_6]^{4-}$ in 1 × phosphate-buffered saline (PBS) with 10×10^{-3} M $MgCl_2$. Next, the electrodes were functionalized by the spontaneous formation of a mixed self-assembling monolayer from an aqueous solution containing 6-mercaptohexan-1-ol and a thiol-C6-modified ssDNA probe. This process takes a minimum of 2 h on macroscopic electrodes but was possible in less than 2 min on the nanoband electrodes. This is in agreement with previous publications and further evidences the nanoscale properties of these electrodes.[3] When placed back in the redox agent-containing solution and the electrochemistry was re-measured, there is a clear decrease in the limiting current, Figure 3. This is because the charge transfer at the electrode is impeded by the steric blocking of the redox molecules by the SAM film, as well as the electrostatic repulsion of the anionic Fe species by the negatively charged phosphate backbone of the DNA. A control experiment was run to assess the stability of the SAM over the timescale of an assay, Figure S11 in the Supporting Information, in this control experiment, the functionalized nanobands were dipped into solutions of DNA-free water. In the main experiment, the functionalized electrodes were first placed in a solution of deionized water and then left to sit in the measurement solution for 20 min to make sure the probe monolayer was also stable. After which, it was placed consecutively in solutions containing increasing concentrations of target DNA before being rinsed with, and measured in, the measurement solution. The washing was important to remove any nonspecifically bound DNA from the surface. As the target DNA sequence binds to the probe layer, it further impedes the charge transfer at the electrode surface causing a decrease in current that is proportional to the amount of target DNA bound to the surface.

The CV and square wave voltammetry data from these experiments on macro and nanoband electrodes are provided in Figure 3. The Langmuir isotherm was chosen as the simplest and most appropriate model to fit these data to and from the fits, the technical limit of detection (LoD) of the macroelectrodes was found to be $92.4 \times 10^{-12} \pm 30.4 \times 10^{-12}$ M. However, the performance of the nanoband electrodes is significantly different, showing a clear sensitivity enhancement with a LoD of $97.1 \times 10^{-21} \pm 23.7 \times 10^{-21}$ m (1 zM = $\times 10^{-21}$ M) obtained in one of the repeats. While these limits of detection are very low, there is evidence in the literature of other nanoelectrode and nanoelectrode ensembles exhibiting similar sensitivities, including for DNA detection.[39–42] Avogadro's number is 6.022×10^{23}, meaning that a 10×10^{-21} m solution will contain 6000 molecules per liter. Therefore, a 2 mL solution of target DNA (as was being used here) should theoretically contain 12 target DNA strands. This means that with an LoD of 97×10^{-21} m, as few as 117 molecules in the 2 mL sample can be detected. However, the authors would emphasize caution on this front, these target DNA concentrations were made up by serial dilutions and there is obviously an error introduced by the pipetting. Table S4 in the Supporting Information shows the error in the final DNA concentration when different pipetting errors are taken into account. Even a 1% error (which is low for even the best of pipettes) could result in significantly more (or less) DNA in the low target DNA concentrations than is quoted here. Therefore, the authors would like to emphasize that the sensitivity of these electrodes is thought to be in the low zM range, based on these data and are not claiming single molecule detection limits. There are also concerns about whether or not 20 min is sufficient for such low amounts of analyte to diffuse to the electrode surface and bind to

cross-section have also been provided. B) Sputtering directly onto the capping layers. i) A cleaned substrate, ii) is sputter coated with a nanometer thin Au coating through a mask that also patterns the contact pad, iii) it is then capped, iv–vi) before sputtering and capping are repeated, using different masks to separate the contact pads, vii) the devices are then cut to relieve the nanobands. It is possible to leave the top layer uncapped so when dipped in solution its area is much larger than the other electrodes, allowing it to be used as a counter electrode. ix) A photograph and x) cross-sectional schematics and xi) an SEM image of this type of device. C) 2D devices. i) A cleaned substrate is sputter coated ii) with Au through a mask that patterns separate devices on the substrate surface. These can then be iii) capped and iv) cut to relieve multiple electrodes with variable shapes and orientations in the same plane. v) Photographs and vi) cross-sectional schematics and vii) SEMs have been provided.

© 2023 The Authors. Small published by Wiley-VCH GmbH

16136829, 2023, 51, Downloaded from https://onlinelibrary.wiley.com/doi/10.1002/smll.202302136 by Spanish Cochrane National Provision (Ministerio de Sanidad), Wiley Online Library on [15/01/2024]. See the Terms and Conditions (https://onlinelibrary.wiley.com/terms-and-conditions) on Wiley Online Library for rules of use; OA articles are governed by the applicable Creative Commons License



© 2023 The Authors. Small published by Wiley-VCH GmbH

16136829, 2023, 51, Downloaded from https://onlinelibrary.wiley.com/doi/10.1002/smll.202302136 by Spanish Cochrane National Provision (Ministerio de Sanidad), Wiley Online Library on [15/01/2024]. See the Terms and Conditions (https://onlinelibrary.wiley.com/terms-and-conditions) on Wiley Online Library for rules of use; OA articles are governed by the applicable Creative Commons License

the probes. We propose that bulk solution movements, such as convection and the agitation of the solution when the electrodes are inserted by hand, account for there being a sufficient amount of probe target hybridization in the 20 min tested.

What is clear, however, is that the sensitivity of these nanoband electrodes is far superior to that of the macroelectrodes and comparable to the best results for nanoelectrodes reported in the literature.[40] The variation in the nanoelectrode signal, at first glance, appears to be greater than that of the macroelectrodes. However, it should be noted that the *x*-axis is logarithmic, and the pipetting errors are larger for the lower analyte concentrations, therefore the spread of the data cannot be solely attributed to variation in the electrodes which were previously shown to be very reproducible. The difficulty in reproducibly making the calibration solutions with such low concentrations means that it is not possible to obtain linear ranges from the data shown in Figure 3F. The only conclusions that can be drawn are that these nanoband electrodes are extremely sensitive, capable of detecting DNA down at low zM levels. Until methods of reproducibly making solutions with such low concentrations of analyte are developed, accurate calibration curves will be impossible to obtain.

3. Conclusions

Herein, we have reported the cleanroom-free fabrication of nanoband electrodes. The nanoscale nature of the electrodes has been proven electrochemically as well as by SEM and AFM. These devices are extremely cheap, with raw materials' cost of €0.01 per electrode and can be made immediately in most labs around the world using commonplace, low-cost equipment. The electrodes exhibit superior performance compared to conventional electrodes, not just in terms of cost, but they are easy to manufacture in customizable design motifs, require no cleaning, can be made out of a wide range of materials, and are extremely sensitive. In the proof-of-principle DNA sensor shown here, the nanoband electrodes were able to achieve low zM levels of detection; markedly better than the pM detection limits of the same system on a macroscopic electrode. We believe that given these advantages, this work and these electrodes have the potential to revolutionize the fields of electrochemistry and point-of-care sensing. The low LoDs of these devices means that they can be used to develop sensors for biomarkers present in samples at very low concentrations. Methods of making the electrodes suitable for real world sample analysis, such as microfluidics and antifouling strategies will be the focus of future work.

For decades now, commercial point-of-care biosensors have been limited to the detection of highly abundant biomarkers such as glucose, lactate, progesterone, and virions. It is hoped that the lower LODs of these cheap nanoband electrodes will kick start the development of biosensors for a wide range of low-concentration biomarkers. This could not only lead to the earlier diagnosis of diseases, when the biomarkers are less abundant, but also to the development of point-of-care devices for disease states with biomarkers too dilute to currently detect. This could include, but is not limited to, biomarkers that cross the blood brain barrier or cross the placenta from a fetal to a mother's bloodstream. Likewise, as has been shown by the detection of DNA here, it may be possible to replace PCR tests with amplification-free DNA sensors using this technology.

4. Experimental Section

Materials and Equipment: A Mini Sputter Coater (model SC7620, Quorum Technologies) and the gold sputter target were purchased from ANAME Instrumentación Científica (Madrid, Spain). The three substrates used were PET (thickness 75 µm), PEN (thickness 125 µm), and Dupont grade Kapton HN (thickness 75 µm), all were purchased from Goodfellow GmbH (Spain). The capping layers were 3 M Kapton tape 5413 (Digi-Key), Acrylic Varnish CRC – Clear Brilliant (RS Components Spain), and Fellowes Enhance 80 micron lamination sheets (Amazon, Spain). The cutting was performed with a flintronic A4 Paper Cutter (Amazon, Spain), scalpels, or surgical scissors purchased from VWR, Spain. Aluminum masks were made in house. A Graphtec ce6000-40 cutting plotter was used to fabricate masks out of the aforementioned Kapton that was also used as a substrate.

Potassium hexacyanoferrate (III) ($K_3[Fe(CN)_6]$) and potassium hexacyanoferrate (II) 3-hydrate ($K4[Fe(CN)6]\cdot 3H_2O$) were purchased from Panreac AppliChem. Tris(2-carboxyethyl)phosphine (TCEP), 2-mercaptohexanol, 2-propanol (IPA), acetone, and PBS, potassium nitrate (KNO_3), and magnesium chloride ($MgCl_2$) were purchased from Merck KGaA, Germany. Gold working electrodes (CH101), Ag/AgCl reference electrodes (CH111), and platinum wire counter electrodes (CH115) were purchased from CH instruments. Au/Au/Au screen-printed electrodes were purchased from DropSense, Spain. The 0.3 µm alumina low viscosity polishing slurry (ET034), 0.05 µm alumina low viscosity polishing slurry (ET033), micropolishing cloths (ET032), and glass polishing slides (ET031) were purchased from eDAQ (Poland). Concentrated sulfuric acid (96%, ITW, Spain) and hydrogen peroxide 50% (Sigma Aldrich, Spain) were used to make piranha solution for electrode cleaning. An Ovan Ultrasonic 3L bath was purchased from Ovan (Spain). All aqueous solutions were prepared using deionized water from a Milli-Q Advantage A10 Water Purification System with 0.22 µm filters MPGP04001 (18.2 MΩ cm, Merck-Millipore, Spain). The electrochemical measurements were carried out with a Metrohm Autolab PGSTAT12 with NOVA 2.1 software. All the data analysis was performed in the NOVA 2.1 software or Origin 2018, unless stated otherwise.

Nanoelectrode Fabrication—Sputtering: The chosen substrate (Kapton, PEN or PET) was cut into 6 cm x 6 cm squares with the cutting plotter. These dimensions were chosen to fit underneath the mask and inside the sputter coater. The mask pattern was created using AutoCAD software, version 2021 from Autodesk. The design was created with 0 mm strokes to generate a vector file. The Kapton masks were produced using a Graphtec ce6000-40 plotter, while the aluminum masks were machined using a Haas vf 1 CNC milling machine. The substrate was cleaned by soaking in acetone for 5 min, rinsed under a stream of IPA to remove the acetone before being completely immersed in a bath of IPA for another 5 min. Finally, the substrate was rinsed with ultrapure water. Note, poor cleaning can affect the adhesion of the sputtered metal to the substrate. The cleaned substrate and the mask were placed in the sputter coater with a preloaded Au sputter target. Vacuum was applied until a pressure <0.8 mbar was achieved. The chamber was flushed three times with Ar to remove any remaining oxygen. The Ar inlet was opened and a

Figure 3. A) Schematic illustration of how the DNA sensing mechanism works. B) Overlayed CVs of the DNA sensing system response to different target DNA concentrations on a macroelectrode. Overlayed with Square Wave Voltammetry (SWV) data from the experiments, shown in (C). The results of the same experiment, with lower DNA target concentrations on nanoband electrodes are shown in (D) and (E). The conditions for these experiments are set out in detail in the experimental section. F) The calibration curves from the macro and nanoelectrode repeats with corresponding fits to the Langmuir isotherm. The reciprocal of the peak signal was normalized between 0 and 1 prior to plotting and fitting.

© 2023 The Authors. Small published by Wiley-VCH GmbH

16136829, 2023, 51, Downloaded from https://onlinelibrary.wiley.com/doi/10.1002/smll.202302136 by Spanish Cochrane National Provision (Ministerio de Sanidad), Wiley Online Library on [15/01/2024]. See the Terms and Conditions (https://onlinelibrary.wiley.com/terms-and-conditions) on Wiley Online Library for rules of use; OA articles are governed by the applicable Creative Commons License

potential was applied to create the argon plasma and begin sputtering. By controlling the gas pressure in the chamber (with the inlet valve), the current could be altered, which determined the target metal deposition rate. In this project, a 10 mA current was chosen and a deposition rate of 5 nm min^{-1} was produced. The duration of the sputtering could then be used with this deposition rate to make devices any desired thickness. Once the sputtering process was finished, the chamber was vented and the substrate was removed, see the Supporting Information video.

Capping—Adhesive tape: The freshly sputtered device was fixed onto a flat surface. The tape was aligned and a small portion was stuck to the work surface to aid the alignment. The tape was then dragged across the surface of the device by hand, under constant pressure to avoid the formation of bubbles. The excess tape was removed and the devices were taken onto the next step.

Spray Coating: The device was fixed onto a flat surface. A plastic mask was used to define the area to be spray coated. The spray coating (in this project acrylic) was applied as per the manufacturer's instructions, by shaking vigorously before use and spraying from 20 cm above the device. The spray coating was repeated thrice to ensure a complete covering of the devices before they were left to dry under ambient conditions for 20 min prior to use.

Lamination: The freshly sputtered devices were placed on a sheet of paper. A pre-patterned lamination sheet (PET, with an ethylene vinyl acetate, EVA, inner coating) with pieces was cut out to leave exposed contact pads on the finished devices, was aligned and placed onto the devices. The ensemble was then run through a Lamigator IQ (Renz, Spain), to laminate the devices in a hot lamination process where the EVA acted as a melt adhesive.

Cutting: The different cutting methods investigated in this project were to cut with a scalpel, scissors, and a flintronic A4 paper cutter. The blades of each device were rinsed with IPA and dried with N_2 prior to each cut. After repeated use, the blades could get blunt and either needed to be replaced or sharpened. It is vital to have the capping layers facing away from the direction of travel of the blade to avoid any adhesive being dragged over the working area of the nanoband being created.

Scalpel Cutting: The devices were fixed face down (with tape) on a Model craft cutting mat (RS components, Spain). A clean scalpel was used to cut the devices by hand by applying as even and uniform a pressure as possible with the blade perpendicular to the mat in a single swift stroke using the markings on the cutting mat to guide the alignment of the cut.

Scissor Cutting: Microscopy (surgical) grade scissors were needed as conventional office scissors are not sharp enough for this application. The devices were placed face down with the region that was intended to be cut resting on the bottom blade of the scissors. The upper blade was closed quickly and smoothly keeping it as perpendicular to the device as possible.

Flintronic Paper Cutter: The devices were stuck face down on the cutter surface, using the alignment markings on the surface to ensure the blade was cutting as straight across the device as possible. The blade was pushed down and dragged through the device at a uniform speed and pressure. In this instance, it was held perpendicular to the device by the design of the tool.

Sheet Resistance of the Metals: The sheet resistances of the Au sputtered onto different substrates were measured using a Keithley DMM6500 multimeter in a 4-point probe mode. Pogo pins with a pressure of 120 g and a separation of 2.54 mm were used. As is required for determining the sheet resistance of thin layers, a correction factor of 4.53 and a geometric correction factor of 0.78 were used when performing these experiments.[43]

The e-beamed samples used as a control were sputtered onto a 4″ Kapton substrate using the same mask as was used in the sputter coater. 35 nm of Au was deposited through the mask onto the substrate using an ATC-8E Orion evaporator (AJA International Inc., USA).

AFM and SEM: The samples were mounted on SEM sample stubs using double sided conductive carbon tape (TED Pella, INC), these were then loaded into a Thermo Fisher (formerly FEI) Quanta 650 FEG ESEM for image acquisition using the backscatter electrons detector under low vacuum conditions. In all the figures presented, the electron beam intensity, working distance, and magnification were stated.

AFM images were obtained through Molecular Imaging's PicoPlus modular Scanning Probe Microscope (SPM) system in combination with the PicoScan Controller and magnetic MAC Mode. PicoView 1.20 software was used during data acquisition but the analysis and corrections were performed in Gwyddion 2.61.

Electrochemical Characterization: The electrodes were characterized by CV, square wave voltammetry, and electrochemical impedance spectroscopy. Unless stated otherwise, the bare electrodes were tested in solutions of 5×10^{-3} M potassium ferricyanide, 5×10^{-3} M potassium ferrocyanide, and 1x PBS versus a silver/silver chloride reference electrode and Pt wire counter electrode. CVs were run between −0.1 and + 0.45 V at a scan rate of 10 mV s^{-1}, for a total of four cycles. The square wave voltammetry was run in the same set up immediately after the CVs from −0.15 to +0.6 V versus the open circuit potential with a 9 mV step, a modulation amplitude of 20 mV, and a frequency of 2.5 Hz. The electrochemical impedance spectroscopy was run with a dc voltage equal to the measured open circuit potential, with a 10 mV sinusoidal AC voltage over a frequency range of 100 kHz to 0.1 Hz, recording 10 frequencies spread logarithmically per decade.

DNA Sensing: The DNA probe was a thiol tagged primer approved by the Centre for Disease Control (CDC) for the detection of SARS-CoV-2. The sequences were ordered from Merck (Spain) and were as follows:

Probe 5′- ACCCCGCATTACGTTTGGTGGACC-(C_6SH) - 3'

Target 5′- GGTCCACCAAACGTAATGCGGGGT - 3'

The electrodes were placed in an aqueous solution containing 30×10^{-6} M 6-mercaptohexanol (MCH), 150×10^{-6} M TCEP, and 1.5×10^{-6} M of the probe DNA. The macroelectrodes were left in this solution for the self-assembled monolayer to form for 2 h, whereas the nanoelectrodes were left for 2 min, prior to rinsing with a stream of water to remove physisorbed thiols.

Before and after probe film formation, the electrodes were placed in a solution of 1x PBS with 10×10^{-3} M $MgCl_2$, 5×10^{-3} M potassium hexacyanoferrate (III) and 5×10^{-3} M potassium hexacyanoferrate (II). CVs were run between −0.1 and + 0.45 V versus a Ag/AgCl reference electrode (macro) or Au pseudoreference electrode (nano) and Pt wire counter electrode, at a scan rate of 10 mV s^{-1}, for a total of four cycles. The square wave voltammetry was run in the same set up immediately after the CVs from −0.15 to +0.6 V versus the open circuit potential with a 9 mV step, a modulation amplitude of 20 mV, and a frequency of 2.5 Hz.

After the probe film was formed the functionalized electrodes were placed in solutions containing increasing concentrations of DNA target, for 20 min each. Between target incubations, the electrodes were placed in the measurement solution, left for 20 min, and the electrochemical measurements were repeated. The DNA target concentrations tested were differed for the macro and nanoelectrodes. For the macroelectrodes, the target DNA concentrations tested were: 0 M, 1×10^{-15}, 1×10^{-12}, 500×10^{-12}, 1×10^{-9}, 500×10^{-9}, and 1×10^{-6} M. For the nanoelectrodes, the target concentrations tested were 0 M, 10×10^{-21}, 100×10^{-21}, 500×10^{-21}, 1×10^{-18}, and 1×10^{-15} M.

A control experiment was run where the functionalized nanoelectrodes were placed in MQ water rather than the increasing DNA concentrations, for the same number of repeats. A second control was run where the functionalized electrodes were exposed to noncomplimentary DNA target sequences.

Lego-Brick Concept: The different fabrication methods for the different 2D stacking designs (Lego brick) assemblies of the nanoband electrodes are described below. In all these cases, the substrate cleaning, sputtering, and capping were performed as described above.

2D Design: A mask was made out of Kapton, see Figure S2B in the Supporting Information, in which three electrodes could be patterned on a single device, running parallel to one another down the length of the device. The three electrodes were able to be used as a working electrode, pseudoreference electrode, and counter electrode. In the mask shown in Figure S2B in the Supporting Information, the electrodes were designed to be the same size, 3 mm wide and 21 mm long with 1.5 mm separations between them.

© 2023 The Authors. Small published by Wiley-VCH GmbH

16136829, 2023, 51, Downloaded from https://onlinelibrary.wiley.com/doi/10.1002/smll.202302136 by Spanish Cochrane National Provision (Ministerio de Sanidad), Wiley Online Library on [15/01/2024]. See the Terms and Conditions (https://onlinelibrary.wiley.com/terms-and-conditions) on Wiley Online Library for rules of use; OA articles are governed by the applicable Creative Commons License

Lego-Brick Concept 1: In this method, the individual devices were capped with the acrylic spray. Multiple devices could be stacked on top of each other with the acrylic acting as an adhesive between them. In this system, each of the devices performed the function of a working, counter, or reference electrode. In these experiments, the acrylic was needed to be left for longer to dry (overnight) under ambient conditions. The connection pads of each device could be cut with scissors to allow easy connection after stacking.

Lego-Brick Concept 2: In this method, new electrodes were sputtered directly onto the capping layer of the underlying device. Three mask designs (Figure S2C, Supporting Information) were used, one for each layer. The masks were designed to isolate the connections of each layer in the final device. The final layer, sputtered to be the counter electrode, was not capped, so that when dipped into a solution, the electrode area would be far greater than that of the working electrode.

Supporting Information

Supporting Information is available from the Wiley Online Library or from the author.

Acknowledgements

ICN2 is funded by CERCA programme, Generalitat de Catalunya Grant SEV-2017-0706 funded by MCIN/AEI/ 10.13039/501100011033. Funding for this project was obtained from Grant PID2021-124795NB-I00 funded by MCIN/AEI/ 10.13039/501100011033 and by "ERDF A way of making Europe". V.A. acknowledges the support and funding by the Department of Science and Technology – Science Education Institute (DOST-SEI) of the Philippines. G.M. would like to express his gratitude to the Carolina Foundation for financial support through the scholarship "Doctorado 2020." G.M. acknowledges Universitat Autonoma de Barcelona (UAB) for the possibility of performing this work inside the framework of Chemistry PhD Programme. V.A. acknowledges Universitat Autonoma de Barcelona (UAB) for the possibility of performing this work inside the framework of Biotechnology PhD Programme.

Conflict of Interest

The authors have no competing interests to declare.

Author Contributions

G.M. and V.A. contributed equally to this work. G.M. and V.A. contributed equally to the acquisition and analysis of the data as well as the paper writing. A.P. conceived the original idea, supervised the acquisition of the data, acquired the data, analyzed the data, wrote the manuscript, and led the project throughout. A.M. supervised the project and contributed to drafting the paper.

Data Availability Statement

The data that support the findings of this study are available from the corresponding author upon reasonable request.

Keywords

biosensors, low cost, nanobands, nanoelectrodes, single molecule detection

Received: March 13, 2023
Revised: June 28, 2023
Published online: August 27, 2023

[1] G. Henihan, H. Schulze, D. K. Corrigan, G. Giraud, J. G. Terry, A. Hardie, C. J. Campbell, A. J. Walton, J. Crain, R. Pethig, K. E. Templeton, A. R. Mount, T. T. Bachmann, *Biosens. Bioelectron.* **2016**, *81*, 487.
[2] D. K. Corrigan, H. Schulze, G. Henihan, A. Hardie, I. Ciani, G. Giraud, J. G. Terry, A. J. Walton, R. Pethig, P. Ghazal, J. Crain, C. J. Campbell, K. E. Templeton, A. R. Mount, T. T. Bachmann, *Analyst* **2013**, *138*, 6997.
[3] A. Piper, D. K. Corrigan, A. R. Mount, *Electrochem. Sci. Adv.* **2021**, *2*, e2100077.
[4] A. Frumkin, A. Donde, *Z. Phys. Chem.* **1926**, *123*, 339.
[5] K. Kuribayashi, H. Matsumoto, H. Uda, Y. Komatsu, A. Nakano, S. Ikegami, *Jpn. J. Appl. Phys., Part 1* **1983**, *22*, 1828.
[6] D. Mandler, S. Kraus-Ophir, *J. Solid State Electrochem.* **2011**, *15*, 1535.
[7] D. H. Craston, C. P. Jones, D. E. Williams, N. Elmurr, *Talanta* **1991**, *38*, 17.
[8] N. Komuro, S. Takaki, K. Suzuki, D. Citterio, *Anal. Bioanal. Chem.* **2013**, *405*, 5785.
[9] Y. Sui, C. A. Zorman, *J. Electrochem. Soc.* **2020**, *167*, 037571.
[10] N. M. Hemed, A. Convertino, Y. Shacham-Diamand, *Sens. Actuators, B* **2018**, *259*, 809.
[11] R. K. Gupta, A. Periyakaruppan, M. Meyyappan, J. E. Koehne, *Biosens. Bioelectron.* **2014**, *59*, 112.
[12] B. C. Mallick, C. T. Hsieh, K. M. Yin, Y. A. Gandomi, K. T. Huang, *ECS J. Solid State Sci. Technol.* **2019**, *8*, N55.
[13] D. E. Presnov, I. V. Bozhev, A. V. Miakonkikh, S. G. Simakin, A. S. Trifonov, V. A. Krupenin, *J. Appl. Phys.* **2018**, *123*, 054503.
[14] N. Elfstrom, R. Juhasz, I. Sychugov, T. Engfeldt, A. E. Karlstrom, J. Linnros, *Nano Lett.* **2007**, *7*, 2608.
[15] A. Piper, A. Mount, *Electrochemical Characterisation of Microsquare Nanoband Edge Electrode (MNEE) Arrays and Their Use as Biosensors*, University of Edinburgh, Edinburgh **2017**.
[16] I. Kleps, A. Angelescu, R. Vasilco, D. Dascalu, *Biomed. Microdevices* **2001**, *3*, 29.
[17] A. Piper, B. Alston, D. Adams, A. R. Mount, *Faraday Discuss.* **2018**, *201*, 201.
[18] E. J. F. Dickinson, R. G. Compton, *J. Electroanal. Chem.* **2011**, *661*, 198.
[19] M. Silvestrini, L. Fruk, P. Ugo, *Biosens. Bioelectron.* **2013**, *40*, 265.
[20] H. L. Woodvine, D. A. R. Mount, *Development and Characterisation of Microelectrode and Nanoelectrode Systems*, The University of Edinburgh, Edinburgh **2011**.
[21] J. G. Terry, I. Schmueser, I. Underwood, D. K. Corrigan, N. J. Freeman, A. S. Bunting, A. R. Mount, A. J. Walton, *IET Nanobiotechnol.* **2013**, *7*, 125.
[22] N. Couniot, T. Vanzieleghem, J. Rasson, N. Van Overstraeten-Schlogel, O. Poncelet, J. Mahillon, L. A. Francis, D. Flandre, *Biosens. Bioelectron.* **2015**, *67*, 154.
[23] X. Zhu, Y. Qiao, X. Zhang, S. Zhang, X. Yin, J. Gu, Y. Chen, Z. Zhu, M. Li, Y. Shao, *Anal. Chem.* **2014**, *86*, 7001.
[24] D. W. M. Arrigan, *Analyst* **2004**, *129*, 1157.
[25] Y. Wang, J.-M. Noël, J. Velmurugan, W. Nogala, M. V. Mirkin, C. Lu, M. Guille Collignon, F. Lemaître, C. Amatore, *Proc. Natl. Acad. Sci. USA* **2012**, *109*, 11534.
[26] S. M. D. Watson, H. D. A. Mohamed, B. R. Horrocks, A. Houlton, *Nanoscale* **2013**, *5*, 5349.
[27] M. Schwartzkopf, G. Santoro, C. J. Brett, A. Rothkirch, O. Polonskyi, A. Hinz, E. Metwalli, Y. Yao, T. Strunskus, F. Faupel, P. Müller-Buschbaum, S. V. Roth, *ACS Appl. Mater. Interfaces* **2015**, *7*, 13547.
[28] M. Schwartzkopf, A. Hinz, O. Polonskyi, T. Strunskus, F. C. Lö, V. Kö, P. Mü Ller-Buschbaum, F. Faupel, S. V Roth, F. C. Löhrer, V. Körstgens,

© 2023 The Authors. Small published by Wiley-VCH GmbH

16136829, 2023, 51, Downloaded from https://onlinelibrary.wiley.com/doi/10.1002/smll.202302136 by Spanish Cochrane National Provision (Ministerio de Sanidad), Wiley Online Library on [15/01/2024]. See the Terms and Conditions (https://onlinelibrary.wiley.com/terms-and-conditions) on Wiley Online Library for rules of use; OA articles are governed by the applicable Creative Commons License

P. Müller-Buschbaum, F. Faupel, S. V. Roth, *ACS Appl. Mater. Interfaces* **2017**, *9*, 5629.
[29] C. S. Smith, C. M. Bowie, K. D. Song, H. Yoon, V. K. Varadan, W. K. Kim, *Proc. SPIE* **2011**, *7980*, 798011.
[30] R. B. Morris, D. J. Franta, H. S. White, *J. Phys. Chem.* **1987**, *91*, 3559.
[31] A. J. Bard, L. R. Faulkner, *Electrochemical Methods: Fundamentals and Applications*, Wiley, New York **1980**.
[32] H. L. Woodvine, J. G. Terry, A. J. Walton, A. R. Mount, *Analyst* **2010**, *135*, 1058.
[33] K. Ngamchuea, S. Eloul, K. Tschulik, R. G. Compton, *J. Solid State Electrochem.* **2014**, *18*, 3251.
[34] E. J. F. Dickinson, R. G. Compton, *J. Phys. Chem. C* **2009**, *113*, 17585.
[35] I. Schmueser, A. J. Walton, J. G. Terry, H. L. Woodvine, N. J. Freeman, A. R. Mount, *Faraday Discuss.* **2013**, *164*, 295.
[36] C. L. Alexander, B. Tribollet, M. E. Orazem, *Electrochim. Acta* **2015**, *173*, 416.
[37] E. F. Douglass Jr., P. F. Driscoll, D. Liu, N. A. Burnham, C. R. Lambert, W. G. McGimpsey, *Anal. Chem.* **2008**, *80*, 7670.
[38] P. Sun, M. V. Mirkin, *Anal. Chem.* **2006**, *78*, 6526.
[39] X. M. Bin, E. H. Sargent, S. O. Kelley, *Anal. Chem.* **2010**, *82*, 5928.
[40] R. Gasparac, B. J. Taft, M. A. Lapierre-Devlin, A. D. Lazareck, J. M. Xu, S. O. Kelley, *J. Am. Chem. Soc.* **2004**, *126*, 12270.
[41] I. Ciani, H. Schulze, D. K. Corrigan, G. Henihan, G. Giraud, J. G. Terry, A. J. Walton, R. Pethig, P. Ghazal, J. Crain, C. J. Campbell, T. T. Bachmann, A. R. Mount, *Biosens. Bioelectron.* **2012**, *31*, 413.
[42] A. P. Wettasinghe, N. Singh, C. L. Starcher, C. C. DiTusa, Z. Ishak-Boushaki, D. Kahanda, R. McMullen, E. A. Motea, J. D. Slinker, *ACS Sens.* **2021**, *6*, 2622.
[43] S. Yilmaz, *J. Semicond.* **2015**, *36*, 082001.
[44] G. Maroli, S. Boyeras, H. Giannetta, S. Pazos, J. Gak, A. R. Oliva, M. A. Volpe, P. M. Julian, F. Palumbo, *Frontiers in Electronics*, **2023** 3 https://doi.org/10.3389/felec.2022.1060197.

© 2023 The Authors. Small published by Wiley-VCH GmbH

16136829, 2023, 51, Downloaded from https://onlinelibrary.wiley.com/doi/10.1002/smll.202302136 by Spanish Cochrane National Provision (Ministerio de Sanidad), Wiley Online Library on [15/01/2024]. See the Terms and Conditions (https://onlinelibrary.wiley.com/terms-and-conditions) on Wiley Online Library for rules of use; OA articles are governed by the applicable Creative Commons License

Biosensors and Bioelectronics 260 (2024) 116421

Contents lists available at ScienceDirect

Biosensors and Bioelectronics

journal homepage: www.elsevier.com/locate/bios

Wearable, battery-free, wireless multiplexed printed sensors for heat stroke prevention with mussel-inspired bio-adhesive membranes

Gabriel Maroli [a,b], Giulio Rosati [a,**], Salvio Suárez-García [a,***], Daniel Bedmar-Romero [a], Robert Kobrin [a,c], Álvaro González-Laredo [a], Massimo Urban [a], Ruslan Alvárez-Diduk [a], Daniel Ruiz-Molina [a], Arben Merkoçi [a,d,*]

[a] Catalan Institute of Nanoscience and Nanotechnology, BIST, and CSIC, Edifici ICN2 Campus UAB, 08193, Bellaterra, Barcelona, Spain
[b] Instituto de Investigaciones en Ingeniería Eléctrica Alfredo Desages (IIIE), Universidad Nacional del Sur – CONICET, Argentina
[c] Joint Department of Biomedical Engineering, NC State & UNC Chapel Hill, USA
[d] Catalan Institution for Research and Advanced Studies (ICREA), Passeig de Lluís Companys, 23, Barcelona, 08010, Spain

ARTICLE INFO

Keywords:
Inkjet printing
Bio-adhesive membranes
Heat stroke
NFC
Silver nanoparticles
Wearables

ABSTRACT

Wearable technologies are becoming pervasive in our society, and their development continues to accelerate the untapped potential of continuous and ubiquitous sensing, coupled with big data analysis and interpretation, has only just begun to unfold. However, existing wearable devices are still bulky (mainly due to batteries and electronics) and have suboptimal skin contact. In this work, we propose a novel approach based on a sensor network produced through inkjet printing of nanofunctional inks onto a semipermeable substrate. This network enables real-time monitoring of critical physiological parameters, including temperature, humidity, and muscle contraction. Remarkably, our system operates under battery-free and wireless near-field communication (NFC) technology for data readout via smartphones. Moreover, two of the three sensors were integrated onto a naturally adhesive bioinspired membrane. This membrane, developed using an eco-friendly, high-throughput process, draws inspiration from the remarkable adhesive properties of mussel-inspired molecules. The resulting ultra-conformable membrane adheres effortlessly to the skin, ensuring reliable and continuous data collection. The urgency of effective monitoring systems cannot be overstated, especially in the context of rising heat stroke incidents attributed to climate change and high-risk occupations. Heat stroke manifests as elevated skin temperature, lack of sweating, and seizures. Swift intervention is crucial to prevent progression to coma or fatality. Therefore, our proposed system holds immense promise for the monitoring of these parameters on the field, benefiting both the general population and high-risk workers, such as firefighters.

1. Introduction

Heat stroke, a life-threatening condition, manifests in two distinct forms: classic heat stroke (CHS), due to passive heat exposure, and exertional heat stroke (EHS), linked to physical activity. CHS occurs at rest and affects mostly vulnerable populations, such as children left in sun-exposed closed vehicles and elderly populations during heat waves. On the other hand, EHS strikes athletes (both elite and recreational), military personnel, and individuals engaged in physically demanding occupations, often in hot environments. Moreover, EHS is characterized by significant central nervous system (CNS) dysfunction, hyperthermia, and organ/tissue damage (Laitano et al., 2019). When the CNS succumbs to temperatures exceeding 40.5 °C, symptoms escalate rapidly (Al Mahri and Bouchama, 2018). In this scenario, prompt diagnosis is crucial for offering an effective treatment, starting with lowering the patient's temperature and alerting the healthcare emergency system (McEntire et al., 2013; Kim et al., 2019). In a world facing escalating temperatures, especially during intense summers, wearable monitoring systems emerge as critical allies. Wearable devices have become ubiquitous, yet their sensor technologies often face sensor instability requiring frequent replacements. On the other side, electrochemical or electrical sensing, known for their direct, sensitive detection and cost-effectiveness, hold

* Corresponding author. Catalan Institute of Nanoscience and Nanotechnology, BIST, and CSIC, Edifici ICN2 Campus UAB, 08193, Bellaterra, Barcelona, Spain.
** Corresponding author.
*** Corresponding author.
E-mail addresses: giulio.rosati@icn2.cat (G. Rosati), salvio.suarez@icn2.cat (S. Suárez-García), arben.merkoci@icn2.cat (A. Merkoçi).

https://doi.org/10.1016/j.bios.2024.116421
Received 28 February 2024; Received in revised form 16 May 2024; Accepted 22 May 2024
Available online 27 May 2024
0956-5663/© 2024 The Authors. Published by Elsevier B.V. This is an open access article under the CC BY-NC license (http://creativecommons.org/licenses/by-nc/4.0/).

immense promise for targeted diagnostics and monitoring. These systems empower currently existing prevention mechanisms, enabling early alerts and rapid responses. In this context, a compelling use case is heat stroke prevention, crucial for the general public and high-intensity workers, such as firefighters.

Several pioneering efforts have aimed at early detection of heat stroke, yielding a spectrum of sensor-based solutions. In this sense, Momose et al., (2023) proposed an information system for EHS prevention based on a simple sweat ratemeter only. In the work of Chen et al., (2017) a multiparameter (multi-sensor) system analyzing galvanic skin response (GSR), body temperature, sweat, and heart rate was introduced. However, the system is battery-based, bulky, wired, and uncomfortable to wear. In a similar study, Pham et al., (2020) worked on the ongoing challenges of achieving an optimal balance between wearability and functionality but without managing a strong integration. Other interesting approaches to EHS and CHS prevention have focused on machine learning for an in-depth analysis of the vital signs (Shimazaki et al., 2022). Despite granting high stability, these bulky electronic components compromise the usability of the system during routine operations by workers or everyday life by individuals. A notable breakthrough came in the form of an earbud-type wearable system (Matsumoto et al., 2019). Equipped with temperature and sweat sensors, this system demonstrated promising results.

To devise a sensitive and precise heat stroke detection system, it's crucial to align symptoms with measurable skin values. The CDC website lists the following as the main symptoms of heat stroke: confusion, loss of consciousness, hot dry skin or profuse sweating, seizures, very high body temperature, death if treatment delayed. Of these, the first two are not related to physiological conditions. The third, the fourth, and the fifth are measurable with our device thanks to humidity sensing (both in the case of no sweating, i.e. low humidity and profuse sweating, i.e. high humidity), muscles contraction, and skin temperature sensing. For temperature sensing, one of the most common approaches requiring just a conductor is the use of a "meander" resistor (Ershad et al., 2020), which resistance varies with temperature due to mechanical dilation. For humidity sensing, interdigitated electrodes (IDE) are typically used in combination with a permeable membrane trapping humidity and therefore changing its dielectric properties (Barmpakos et al., 2020), such as resistance and capacitance. Regarding seizures detection with sEMG, (Baumgartner et al., 2021) proved that sEMG single channel measurements can be used to accurately identify seizures in epilepsy, extending the work of Conradsen et al., (2011). Djemal et al. also push forward the concept in 2023 (Djemal et al., 2023) using wearable (despite bulky and battery-based) single channel sensors with the same aim and proving their accuracy for the seizures detection. SEMG and muscle contraction can be easily measured as well simply using a couple of electrodes accurately placed along the muscle direction and measuring the action potential crossing them (Rosati et al., 2021). However, for these sensors to thrive in wearable applications, they must overcome connectivity challenges (power, readout, and connection to smartphones or other portable devices). Most published works showcase visually appealing devices but omit details on amplifier connections and data analyzers (often wired). Some progress includes wireless data transmission protocols, but these typically bulky modules require power sources like batteries or energy harvesters. The typical wireless data transmission protocols used for this purpose are (in descending order of power consumption and distance reached): wi-fi, low-power Bluetooth (Yang et al., 2022; Zhao et al., 2023), and near field communication (NFC). Notably, NFC does not need external power (i.e. batteries) as the reader powers the system through the data-reading antenna (Haerinia and Noghanian, 2019; Rossetti et al., 2024), for more details of the NFC functionality check the Supplementary Information.

Among techniques for fabricating battery-free wireless data transmission systems on flexible 2D substrates, printing emerges as a standout for its performance and features. Nanofunctional inks based on cost-effective silver nanoparticles can form highly conductive paths, allowing for the fabrication of electronic circuits, sensors, and antennas by inkjet printing (Yang et al., 2022; Maroli et al., 2023; Nalepa et al., 2024). Even consumer printers can be adapted for these applications, yielding low-cost, scalable disposable devices on plastic substrates (Rosati et al., 2022). While inkjet printing surpasses screen printing in terms of being maskless and wasteless, it may face issues like poor adhesion to the substrate and often requires post-treatments. Besides, the thinness of inkjet-printed layers (typically less than 1 μm) can affect conductivity and durability. On the other hand, hybrid contactless printing techniques like the one proposed by Voltera allow for on-demand deposition of conductive pastes by syringe-based deposition, making it suitable for fragile substrates.

In wearable technologies, the first crucial step is ensuring intimate skin-sensor contact. While various technologies address heat stroke symptom detection, the adhesive system that secures wearables to the skin remains pivotal. An innovative approach involves nature-inspired bioadhesive membranes, drawing inspiration from mussel-like materials widely used in biomedical applications (Barros et al., 2021). Observing the remarkable functions that characterize these living organisms (e.g., underwater adhesion), research has been focused on imitating those functions. Over the past years, it has been determined that catecholamine-based molecules are playing a crucial role in the chemical structure of adhesive proteins (Lee et al., 2006), leading to the development of synthetic materials through catecholamine polymerization (dopamine-like polymers). These catechol groups and polyphenolic molecules provide adhesive properties across a wide variety of surfaces even in aqueous environments (Saiz-Poseu et al., 2019), tissues (Ju et al., 2022) and skin (Sousa et al., 2018). When polymerized with amino-based ligands, the resulting membranes offer chemical versatility, high biocompatibility, and crucial skin conformability (Contreras-Pereda et al., 2024). Thus, these membranes serve a dual role: maintaining close skin contact for 2D flexible devices and acting as a platform for integrating electronic circuits and sensors via out-of-the-cleanroom and non-contact additive manufacturing techniques.

Hence, in this work, we explored the development of printed sensors on a polyethylene terephthalate (PET) with a semipermeable coating, and on nature-inspired membranes (Fig. 1). The aim was to create integrated circuits and NFC antennas for battery-free and wireless readout of a network of critical sensors crucial in heat stroke prevention (temperature, humidity and muscle contraction). The adhesive membrane was designed, drawing inspiration from mussel adhesion molecules. Commercially available reagents (pyrocatechol and hexamethylenediamine) were used, and their polymerization yielded structures inspired to those observed in mussels. We examined two integration approaches: integrating sensor circuits on the PET substrate with interconnected antennas and using the membranes to maintain skin contact, and alternatively, direct sensor and antenna printing onto the adhesive membranes. The advantages and disadvantages of inkjet printing and paste deposition using a Voltera printer were also evaluated. Finally, the whole platform has been validated both in a controlled lab environment and through *in vivo* testing on healthy volunteers during physical activity.

2. Materials and methods

2.1. Membranes fabrication and characterization

All reagents were purchased and used without further purification from Sigma-Aldrich (Madrid, Spain). Solvents were used as received without additional drying or degassing (Scharlab, Madrid, Spain). Type 1 ultrapure water from in-house Milli-Q® filtration systems (Millipore, Burlington, MA) was used in all experiments unless otherwise specified.

The synthesis of the bioinspired membranes was performed following the previously reported protocol (Contreras-Pereda et al., 2024) with the following modifications: the catechol-based molecule

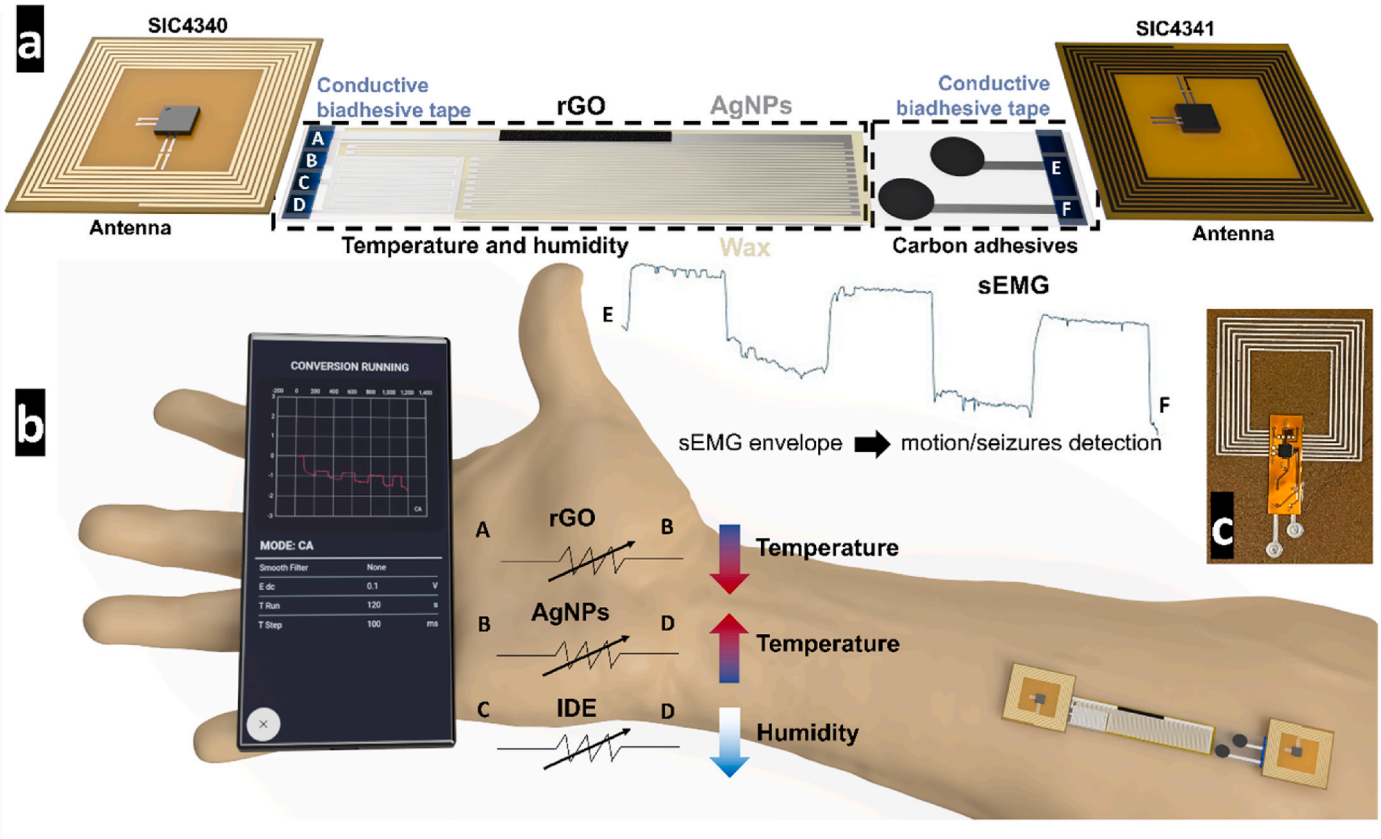


Fig. 1. a) Schematic of the sensor network. The rGO temperature sensor is connected between pads A and B and exhibits a decrease in resistance value with increasing temperature, as indicated by the arrows. The silver sensor between pads B and D exhibits an increase in resistance value with increasing temperature. The humidity sensor, consisting of a silver interdigitate, between pads C and D evaluates the change in conductivity of the substrate. As the humidity increases, the resistance decreases. The electrodes used for motion and seizure detection are located between pads E and F. b) Schematic of the sensor placement on the forearm. c) Picture of the electrodes and antenna directly printed on the bioadhesive membrane with the NFC chip.

used was benzene-1,2-diol (pyrocatechol, 10 mmol) and mixed with hexamethylenediamine (HMDA, 10 mmol).

Hyperion 2000 FTIR microscope (Bruker Optik, GmbH, Ettlingen, Germany) was used in reflection mode, which is equipped with a nitrogen-cooled mercury-cadmium-telluride (MCT) detector (InfraRed Associates, Inc., Stuart, FL, USA) using a 15× reflection objective, a gold mirror as reference and scanning for 30 min with a resolution of 4 cm^{-1}. For the analysis, the membranes were attached to a gold surface. All the data obtained was processed using the Opus version 7.2.139.1294 (Bruker) software.

Cell viability assay was performed using PrestoBlue™ cell viability kit (Invitrogen™) to evaluate the possible cytotoxic effects of the membranes in the NIH/3T3 cell line. Initially, a total of 5 × 10^4 cells/well with 100 μl medium were seeded in a 96-well plate (Falcon™ 353072, Fisher Scientific) and incubated at 37 °C for 24 h. Cells without membranes were used as controls, while membranes (cut in circular discs of 8 mm in diameter and UV sterilized) were incorporated into each well, followed by incubation at 37 °C for 24 h. Afterward, the membranes and medium were removed and 10 μl of PrestoBlue™ cell viability kit were added to each well following the manufacturer specifications and finally read (Victor3, PerkinElmer). In each plate, three replicates were done for each condition and a total of four repetitions (N = 4) were performed. Results were represented with OriginPro version 9.8.0.200 software.

Images obtained from SEM measurements were acquired on a scanning electron microscope (FEI Quanta 650 FEG, Thermo Fisher Scientific, Eindhoven, The Netherlands) in secondary electron mode with a beam voltage between 2 and 20 kV and chamber pressure of 10^{-5} Pa. The working distance was set at 10 mm and different amplifications were tested for final images. The samples were prepared by attaching the membranes on aluminum stubs. Before performing the analysis, the samples were metalized by depositing on the surface a thin Pt coating (5 nm) using a sputter coater (Leica EM ACE600).

2.2. Sensors network printing and stamping

For inkjet-printed devices, a commercial silver ink (Mitsubishi Paper Mills Silver Nano™ AgNP, NBSIJMU01) was loaded into a rechargeable cartridge and printed with an Epson XP15000 printer on the Mitsubishi Paper Mills special substrate (NB-TP-3GU100) and on the membrane as further detailed later. For the deposition of the screen printing pastes, the V-one dispenser/printer from Voltera (Canada) was used. The pastes Flex 2, Lot: GigglingGrouper and solder Paste T5, Lot: IcyInchworm, were purchased from Voltera. Flexible polyamide PCBs were fabricated by PCBWay, China. The 3M Electrically Conductive Adhesive Transfer Tape 9703 was purchased in Digikey. For the reduced graphene oxide (rGO) temperature sensor, Graphene oxide (GO) dispersions (1 wt%) were purchased from Graphenea (Spain). All reagents for the saturated solution (LiCl, $MgCl_2$, KCO_3, $NaNO_3$, NaCl, KCl, KNO_3) were purchased and used without further purification from Sigma-Aldrich. The digital multimeter Keithley DMM6500 was purchased in Farnell Components SL. The carbon conductive adhesives tabs 16084-1 tabs 16084-1 were purchased in Ted Pella, Inc.

For the fabrication of the sensor network on the Mitsubishi substrate, the silver trace layout was first printed twice with the Epson printer. This approach aimed to enhance conductivity by incorporating a higher volume of silver nanoparticles within the ink. In parallel, the Graphene Oxide (GO) was filtered and subsequently reduced by laser following the

steps previously reported (Scroccarello, 2023). Then, the trace of reduced Graphene Oxide (rGO) was transferred to the substrate by a press. Next, the carbon conductive adhesive tabs were placed on the silver circles reserved to be the electrodes. Finally, using 3M 9703 conductive tape, the flexible PCBs were attached to the connection pads. The fabrication steps can be seen in Fig. 2.

2.3. Smartphone readout

Near Field Communication (NFC) technology is a short-distance communication protocol, in the order of 5 cm, that operates at 13.56 MHz on ISO/IEC 18000-3 air interface and at rates ranging from 106 kbit/s to 424 kbit/s. NFC uses loop antennas, whose inductance value will be determined by the internal capacity of the chip to be used, in such a way that the resonance frequency between the designed antenna and the internal capacitor is 13.56 MHz. It is also possible to incorporate external capacitors to reduce the value of the desired inductance. In addition, the parasitic capacitance presented by the inductor must be taken into account. A compact model of the concentrated components of the inductor and the capacitance of the chip can be seen in Fig. S1. Based on this model, the resonance frequency of the antenna and chip set will be given by,

$$f_{resonance} = \frac{1}{2\pi\sqrt{L\left(C_{chip} + C_{parasitic}\right)}} \quad \text{(Eq. 1)}$$

Most of the chips for NFC communication have an internal capacitance of the order of 50 pF, and thus this will be the starting point for the design of the inductor. In particular, the chip used in this work from Silicon Craft has an internal capacitance of 51 pF. Using Eq. (1), and neglecting the parasitic capacitance of the inductor, the required inductance value will be calculated. With the inductance value determined, the inductor is designed geometrically (Maroli et al, 2021), the parasitic capacitance is obtained and the model is iteratively adjusted. As the first iteration step, the required inductance will be $L = 1/(2\pi f_{res})^2 C_{chip} = 2.75\ \mu H$. Another important parameter to take into account in this type of design is the series resistance that the inductor will have. Both its length, as well as the width and thickness of the traces will determine the resistance value. This parameter is very important as it will define the quality factor (Q) of the inductor, where $Q = \omega L/R$. The quality factor is entirely related to the distance at which our antenna will be able to transmit. This relationship can be seen in Ortego's work.

The SIC4340 integrated circuit, developed by Silicon Craft, exhibits remarkable versatility in its ability to measure resistance across a wide

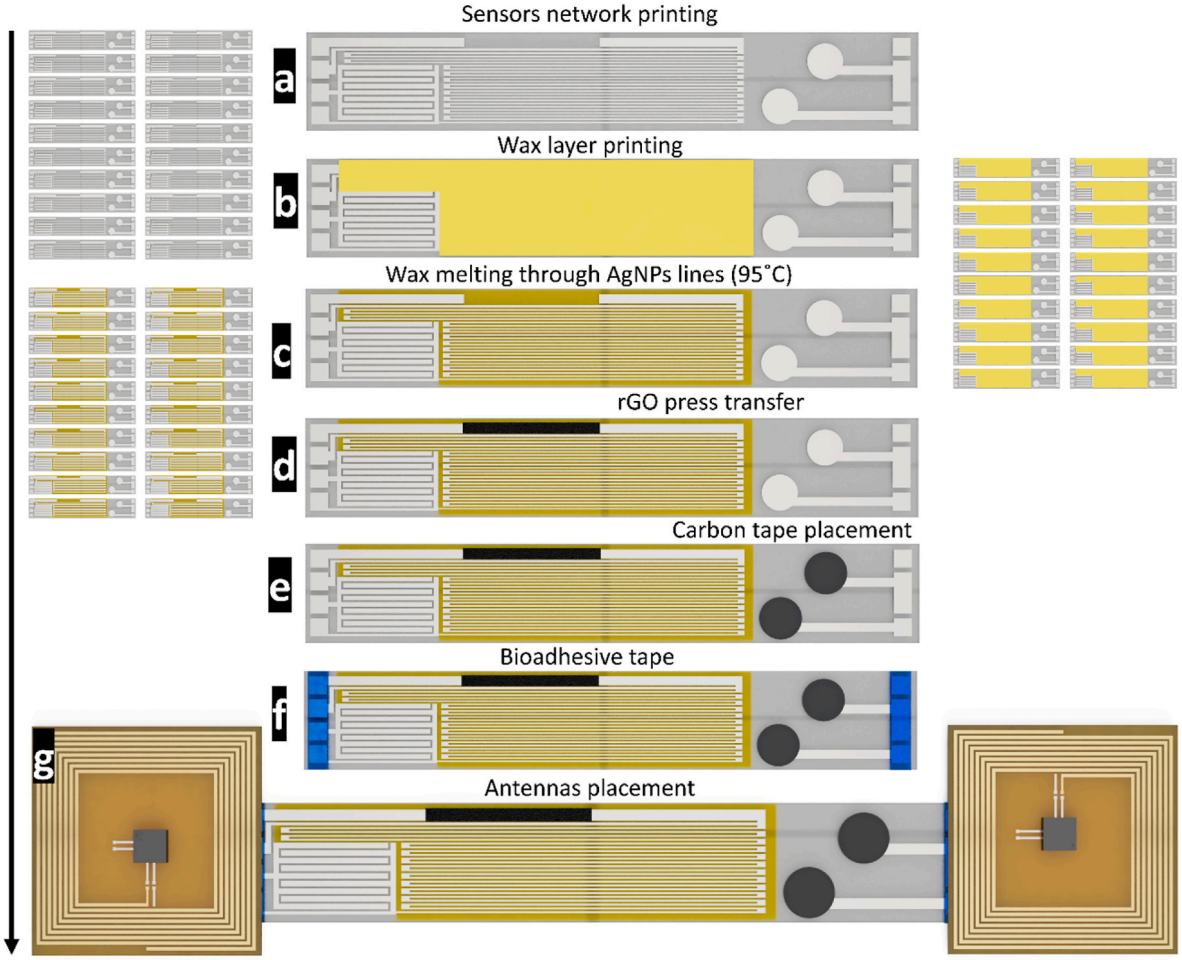


Fig. 2. Represented form top to bottom the fabrication steps of the inkjet-printed sensors network on Mitsubishi semi-permeable substrate and of its preparation for the temperature, humidity and simplified surface electromyography (ssEMG), measurements with the near-field communication (NFC) antennas. a) The sensor network is printed on the A4-sized Mitsubishi substrate. To enhance the conductivity of the traces, the design is printed twice. b) The wax printer is then employed to print a coating of wax, which adheres to the substrate and the silver traces. This step is also carried out in duplicate. c) To allow the wax to permeate the substrate and to remove it from the silver traces, the sensor is passed through a laminator, covering the devices with a sheet of paper. The wax diffuses into the substrate, and any excess is absorbed by the paper. d) In this step, the devices are cut and manipulated one by one. The reduced Graphene Oxide (rGO) sensor, previously reduced by laser, is transferred using a press. e) Carbon tape circles are placed on the printed electrodes. f) Anisotropic conductive tape is placed on the connection pads between the antennas and the device. g) Finally, the antennas are connected to the device.

spectrum. To ensure accurate measurements, it is essential to configure the bias current such that the voltage readings acquired by the chip fall within the range of 0.2 V–1.2 V. The resistance value can be derived using the formula R = Vsen/Isen, where Isen represents the bias current, which can be adjusted within the range of 1 μA–504 μA. However, it is important to note that setting the bias current below 10 μA may introduce significant errors, primarily attributed to the least significant bit (LSB). Consequently, we consider the valid range of current to be 10

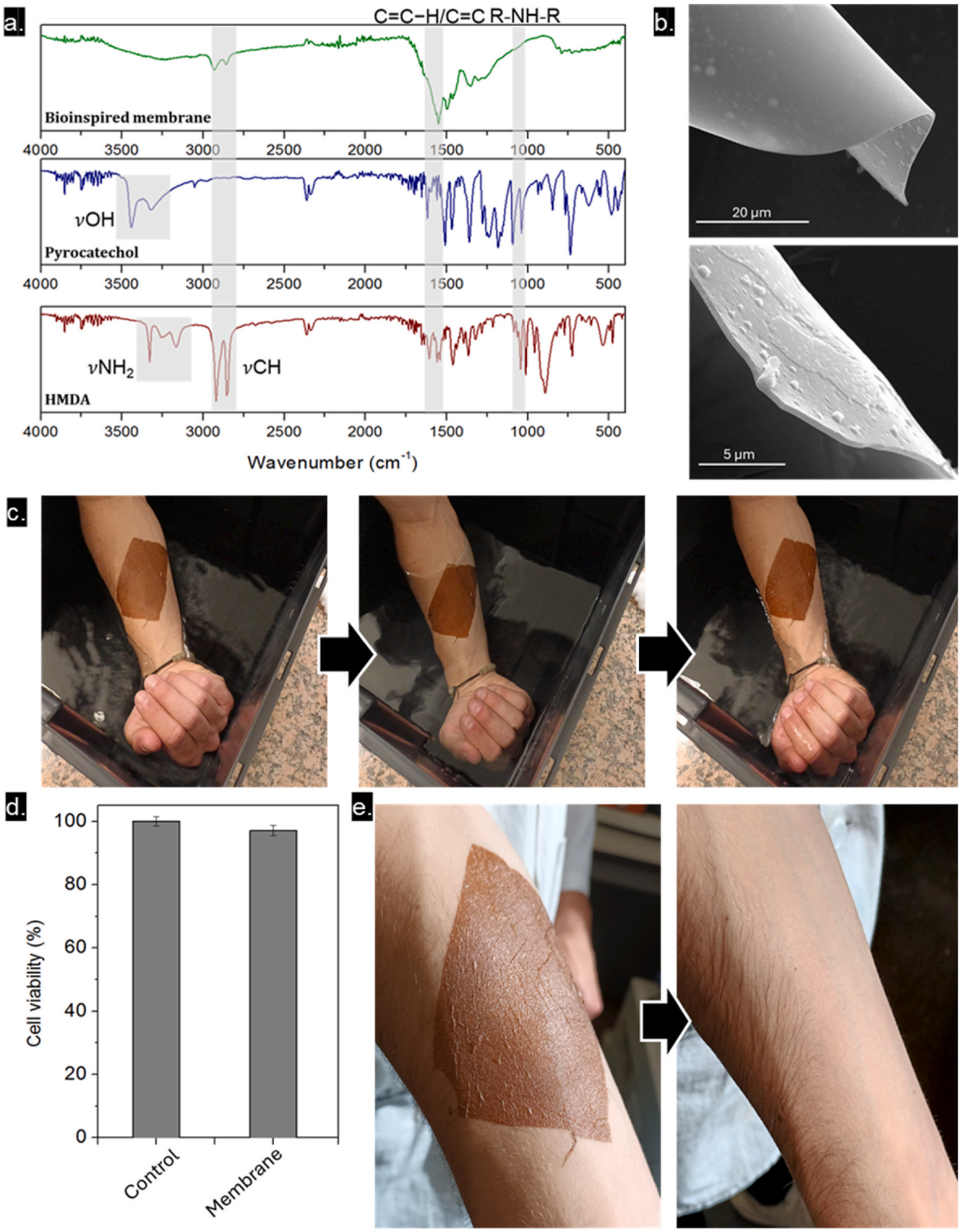


Fig. 3. Bioinspired membranes were characterized after their synthesis to corroborate the correct polymerization, adhesion and biocompatibility. a) FT-IR spectroscopy measurements corroborated the polymerization between pyrocatechol and hexamethylenediamine (HMDA) ligands for the formation of the membranes. b) Scanning electron microscopy (SEM) showed the formation of thin free-standing membranes. c) Water-resistant adhesion was demonstrated by subsequent cycles of water immersion of a membrane adhered directly to the skin of a volunteer. d) *In vitro* biocompatibility was studied in fibroblast cells (NIH/3T3), showing high cell viability, thus demonstrating the low toxicity of the membranes. e) The membrane conformability to the skin was excellent, ensuring intimate contact between the tissue and the device, which can be easily removed if needed without inducing any skin damage.

μA–504 μA, paired with a voltage range of 0.2 V–1.2 V.

Taking these constraints into account, we can establish the lower and upper resistance limits as follows: Rmin = 0.2V/500 μA = 400 Ω and Rmax = 1.2V/10 μA = 120 KΩ. This affords us the capability to detect resistance variations up to 300-fold when adapting the bias current for each measurement. Conversely, if the bias current remains fixed, the detectable variation is limited to a factor of 6.

Furthermore, it is noteworthy that the SIC4340 Chip features three channels. This allows for the adaptation of bias current values to create three distinct measurement ranges, thereby expanding the range of detectable variations to 216 times.

For muscle contraction measurements, simplified surface electromyography (ssEMG), the SIC4341 integrated circuit, also from Silicon Craft, was used. This integrated circuit is intended for electrochemical measurements, but since it can perform chronoamperometry, it is suitable for this application. Like a potentiostat, the chip has a connection for 3 electrodes, Working, Counter and Reference. However, the smartphone application provided by the manufacturer, gives the possibility to configure the system on 2 electrodes, only considering the Working and the Counter. This was the mode selected for the muscle contraction measurements. A voltage of 0.5 V, a run time of 300 s and a measurement interval of 100 ms were configured. To improve the connection between the printed pads and the skin, carbon conductive adhesive tabs were used. For the larger muscles such as the bicep and tricep, the scale of 20 μA was used, while for finger movement recording the scale selected was 2.5 μA.

3. Results and discussion

3.1. Membranes characterization

The membranes were synthesized following a straightforward methodology which allows for the formation of a bioinspired material based on catecholamines that imitates some of the properties found in mussels. In this case, pyrocatechol and HMDA ligands, which are commercially available, were used for their polymerization, obtaining a polydopamine-like structure inspired to those observed in mussels (Suárez-García et al., 2017). The analysis of the FT-IR spectra (Fig. 3a) corroborated the polymerization of the membrane. The broad band around 3250 cm^{-1}, corresponded to the stretching vibrations of hydroxyl (–OH) and amine ($–NH_2$) groups, whose peaks can be appreciated in the catechol derivatives and HMDA spectra, respectively. The peaks around 2850 cm^{-1} could be attributed to asymmetric and symmetric stretching vibrations of aliphatic carbons (C–H) of HMDA. The peak at 1700 cm^{-1} corresponds to quinones (C═O). Finally, the signal around 1500 cm^{-1} was attributed to C═C–H and C═C vibrations from the catecholic/quinonic rings of the catechol derivatives, while the peak at 1260 cm^{-1} belongs to a secondary amine binding an alkyl or an aromatic ring.

Besides, the SEM analysis of the membrane showed a submicrometer uniform thickness and a relatively flat surface (Fig. 3b). These morphological properties endow the membranes with ultra-conformable adaptability to the skin (Fig. 3c–e). Interestingly, the membranes showed great adhesion on the skin mainly due to the chemical structure previously discussed. The water-resistant adhesion was corroborated by immersing a membrane attached to the skin of a volunteer for severe cycles (Fig. 3c). The bioadhesive membrane developed allows for the direct adhesion of the device onto the skin, meeting two of the main requirements: i) it is capable of keeping the device in place for the required time, even in conditions of humidity and movement, and ii) it can be easily removed without causing pain or injury to the skin (**Supplementary Information videos SV1**). The needed adhesion is a compromise between resistance and adhesive capacity on the skin, as high adhesion could limit its application due to skin damage. In our case, we have achieved a balance by obtaining sufficient adhesion that allows the device to be supported on the skin in conditions of movement and humidity but that can also be easily removed at any time.

Finally, the *in vitro* biocompatibility of the membranes was corroborated, showing cell viability above 95% in fibroblast cells (Fig. 3d and Fig. S2). Similarly, the tests performed directly on *in vivo* skin have shown a high biocompatibility of the material without showing signs of inflammation, irritation, or erythema on the skin where the adhesive membrane was applied (Fig. 3e). As previously mentioned, the conformability of the membrane on the skin was excellent, perfectly adapting to the relief of the skin and facilitating the intimate adherence between the tissue and the membrane without causing any injury (Fig. 3e).

3.2. Humidity and temperature double sensing

In our research endeavor, we harnessed the capabilities of the SIC-4340 chip, which boasts three measuring channels. Within this framework, we strategically deployed three sensors: a humidity sensor alongside two temperature sensors, one with a negative coefficient and the other with a positive coefficient. The humidity sensor consists of an IDE sensor. Unlike conventional capacitance-based measurements, we focus on the resistance change of the Mitsubishi substrate as it absorbs humidity. To characterize this sensor, the IDEs were placed inside a plastic beaker, maintaining constant relative humidity as shown in Fig. S3. For that, saturated solutions of different salts (LiCl (11%), $MgCl_2$ (33%), KCO_3 (43%), $NaNO_3$(64%), NaCl (75%), KCl (84%) and KNO_3(94%)) were prepared. The resulting resistance changes were measured with a digital multimeter. Notably, the linear region of the calibration curve emerged at 11% RH and 33% RH, yielding resistance values exceeding 100 MOhm and 43 MOhm, respectively (Fig. 4a). At 94% RH, the sensor reached saturation, indicating that the Mitsubishi substrate was already wet or has absorbed as much water as it can. While the Mitsubishi substrate-based sensor leverages water absorption-induced conductivity changes, we encountered limitations when attempting to apply this concept to the bio-inspired membrane. Consequently, an alternative solution consisting of a sensor based on GO with Nafion was developed for the bio-inspired membrane. The composite was performed following the previously reported protocol (Yakoh et al., 2018) and as expected an exponential response was obtained (Fig. 4b), with the benefit that the resistance values were lower than those obtained for the interdigitated on Mitsubishi. Numerous humidity sensors exhibit sluggish responsiveness to humidity fluctuations due to the slow desorption of water from the sensor surface. However, one of the characteristics of heat stress is the absence of sweating, so having a fast-responding sensor is vitally important. To assess our sensor's reactivity, we conducted continuous resistance measurements while exposing the sensor to moist breath (Fig. 4c). The obtained results demonstrated the sensor's ability to restore its initial resistance value in less than a minute. The interesting feature of the Mitsubishi substrate trapping humidity may also be further exploited in a future work for the sensing and biosensing of metal ions and metabolites in sweat with appropriate normalization of the sweat rate (Yang et al., 2022; Rosati et al., 2018).

It is known the inherent temperature sensitivity of metals induces resistance changes, a phenomenon that extends to our humidity sensor crafted with silver ink. To mitigate this effect, temperature sensors of positive coefficient and negative coefficient were incorporated. The positive coefficient sensor consists of a silver-ink printed mender resistor, in the same way as the interdigitated one was printed. Silver traces are a porous material, exhibiting a resistivity approximately 10 times higher than bulk silver. Similarly, the thermal coefficient of the printed silver is different from its bulk counterpart. To quantify this, the resistor was exposed to various temperatures and its thermal coefficient was calculated using the equation $R = R_0 .(1 + \alpha \Delta T)$. Our findings revealed that the alpha value for printed silver was $\alpha = 1.91.10^{-3}$ (Fig. S4). Unlike metals, carbon-based materials such as rGO have a

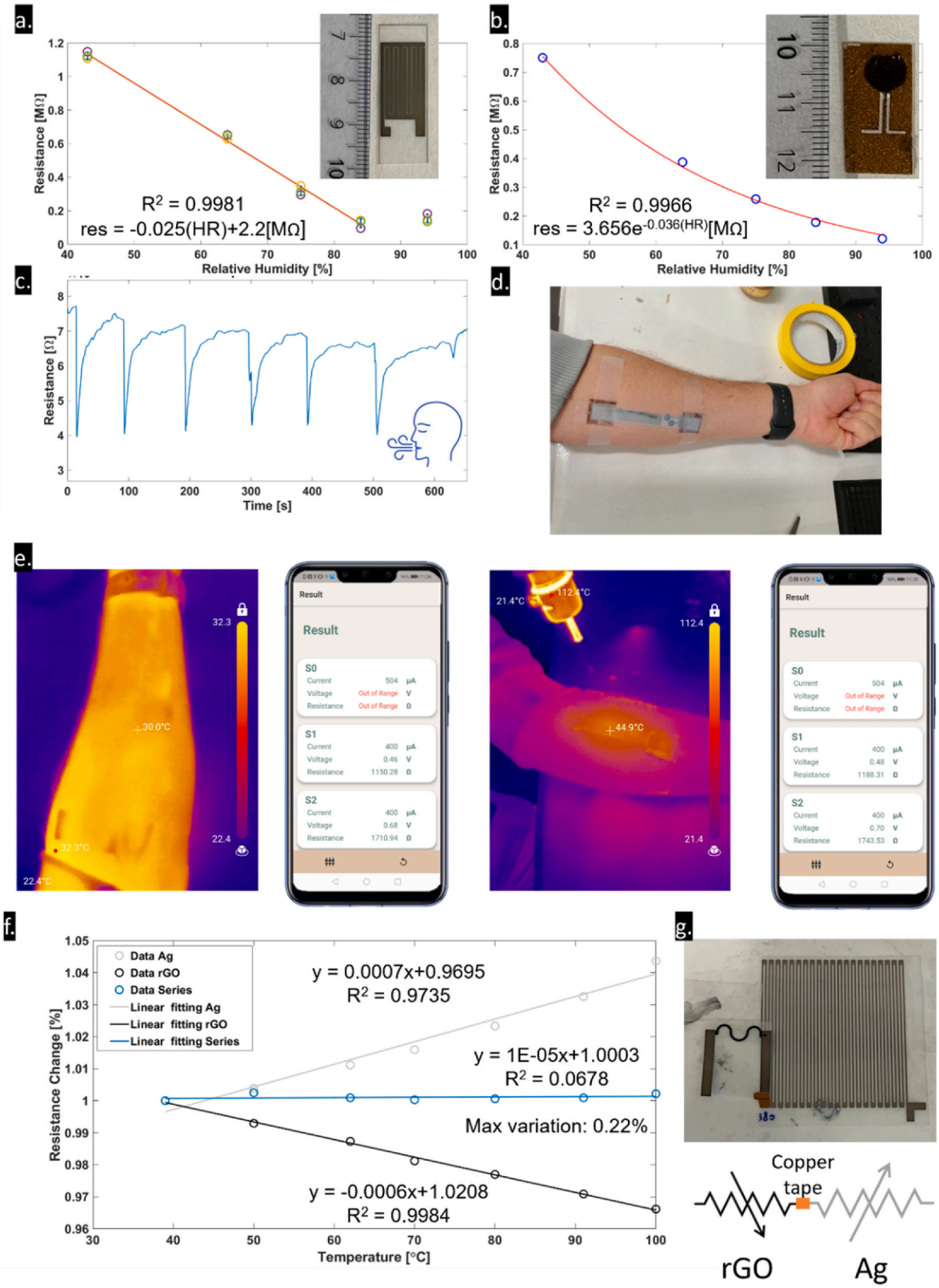


Fig. 4. a) Silver nanoparticles interdigitated electrode (IDE) humidity sensor inkjet-printed on semipermeable PET substrate. b) Comparison with a Nafion sensor on reduced graphene previously reported. c) Inkjet-printed humidity sensor response to breath and (d) illustration of the device positioning on skin for sweat detection and temperature sensing. e) Thermographs of the inkjet-printed device on the skin at room temperature and under hot air flushing for calibration. f) Calibration curves of the silver nanoparticles meander resistor and the rGO serpentine. g) Corresponding series of the two resistors.

negative thermal coefficient, which means that their resistance decreases as temperature rises. Fig. S4 shows different shapes of temperature sensors made with stamped rGO. From studying them at different temperatures, it was determined that their thermal coefficient is $\alpha = -5.8.10^{-4}$. These characteristics can be used to build flexible resistors that do not change their value with temperature. Fig. 4f and g show how by placing a silver printed resistor with a positive coefficient in series with a negative coefficient rGO stamped resistor it is possible to obtain a system whose resistance value becomes independent of temperature. In a practical temperature range (30–100 ^{O}C), the maximum recorded resistance variation was 0.22%. This negligible fluctuation renders our approach highly suitable for most applications. This innovative strategy was used in the construction of our wearable technology.

In our pursuit of effective wearable technology, we meticulously examine the performance of our sensors under real-world conditions. Specifically, we focused on temperature and humidity sensors, aiming to bridge the gap between laboratory-calibrated measurements and practical scenarios. For this, similar conditions to what a firefighter could be exposed to were mimicked, placing the sensor on the forearm and exposing it to hot air. Fig. 4e shows the thermal image of the arm with the sensor before and when exposed to heat as well as the values obtained with the smartphone by NFC. The initial value with the skin at 30 °C is 1150.28 Ω for sensor 1 (silver resistor), and 1710.94 Ω for sensor 2 (silver in series with rGO). After exposing the arm to the hot air, measurements were taken again obtaining 1188.31 Ω and 1743.53 Ω respectively. Taking the alpha values obtained during the characterization of the sensors, it is possible to estimate the temperature at:

$$T = \frac{\frac{R}{R_0} - 1}{\alpha} + T_0 = \frac{\frac{1188.31}{1150.28} - 1}{1.91x10^{-3}} + 30 = 47.33\ ^{\circ}\text{C}, \quad \text{(Eq. 2)}$$

The rGO resistor value was determined by the difference between channel 1 and channel 2, as the resistors were in series. The obtained values are 560.66 Ω and 555.22 Ω, respectively. Applying again the equation Eq 2. the temperature obtained by this sensor is 46.73 °C.

The calculated temperatures closely align with those obtained using a thermal camera. In both measurements, it is observed that sensor 1 indicates 'Out of Range', which means that the skin is dry. In scenarios where the skin is wet, such as during physical activity, the sensor would yield a value, impacting the overall temperature sensor readings. Notably, the reported value would be lower due to the influence of humidity. The issue is evident in the *in vivo* tests presented in Fig. S5. To address this issue of sweat absorption and its interference with resistance measurements, the temperature sensor area was coated with wax, allowing for a protective layer to prevent unwanted moisture effects (Fig. S6). Sensor readings were taken during *in vivo* tests (Fig. S7) to capture the skin's temperature upon application, which was measured at 31 °C with the thermal camera. Interestingly, once the membrane secured the sensor in place, a cooling effect was observed due to its moisture content. This effect led to a decrease in temperature of 7° in both temperature sensors and a significant change in the humidity sensor value. This was evidenced by a decrease in sensor resistance values and confirmed by thermal imaging. As the person began to move, their body temperature gradually increased, resulting in a subsequent increase in sensor readings reflecting this physiological change. The recorded temperatures were approximately 13° higher, or around 6° above the initial baseline temperature (Table S1). These dynamic responses to physiological changes underscore the intricate interplay between sensor placement, environmental conditions, and user activity. In addition to the *in vivo* test, the real-time response of the temperature sensor powered by NFC can be seen in the SV2 video.

3.3. Muscle contraction simplified sensing

Surface myography, a critical tool for monitoring muscle activity, typically involves the placement of two electrodes along the muscle fibers, complemented by a third ground electrode in an unaffected zone (generally near a joint). The resulting muscle action potential is then amplified and recorded over time with a sufficient sampling frequency to get all the information (typically with $f_s = 1$ KHz). Unfortunately, the conventional wired setup poses limitations, hindering natural movements, or requiring relatively bulky electronics next to the sensors. In our innovative approach, we repurpose the SIC4341 NFC chip, originally designed for simple electrochemical measurements (such as amperometry), to perform two-electrode recording of muscle action potentials.

The two electrodes were affixed to the skin utilizing conductive carbon tape. Notably, this tape exhibits a higher impedance compared to conventional conductive gels. However, these gels present two significant drawbacks for this specific application. Firstly, given the semi-permeable nature of our substrate, the gel tends to disperse across the substrate, thereby posing a risk of short-circuiting the electrodes. Secondly, these gels exhibit a capacitive response that can result in a phase shift of up to 40°. The gel behaves like a resistor-capacitor filter that enhances some frequencies and mitigates others, deforming the signal. In contrast, the carbon tape, while being tenfold more resistive than the gel, maintains a consistent value across varying frequencies and does not exhibit a capacitive component. A comparative analysis of these two connection modalities is presented in the tables and Figs. S8–S11.

The utilized setup enabled the direct quantification of currents linked to muscle contractions, facilitated by the NFC chip. This system, powered wirelessly, allowed for real-time, battery-free data acquisition via a smartphone. Despite the signal's limited frequency content owing to the device's relatively low sampling rate, and the signal's partial drift due to the lack of a ground electrode, the results shown in Fig. 5 unequivocally demonstrate the accurate detection of muscle contractions. We rigorously tested our system on various muscle groups. The testing was performed for the finger's extension muscles on the back of the forearm (Figure S12 and Fig. 5a) and for the triceps and biceps muscles in response to the extension (Fig. 5b) and contraction of the forearm (Fig. 5c), respectively. The red arrows denote the instances of action execution: finger movement, tricep contraction without load, and bicep contraction with load, respectively. Conversely, the light blue arrows represent the resting positions: fingers curled into a relaxed fist without exerting force, the tricep relaxed without weight resistance, and the extended arm position during the bicep exercise involving weightlifting (Fig. S13-**S14**). The results found so far prove that the system could be used for the detection of seizures, if accurately placed, which are a possible effect of heat stroke.

3.4. Direct printing on the membrane and advantages and disadvantages of inkjet and Voltera printing

Aiming for efficient wearable antennas, we encountered critical challenges during the fabrication process. Two different approaches were explored for printing the antenna on the bio-inspired membrane. Specifically, we investigated inkjet printing techniques and the capabilities of a Dimatix (Fujifilms DMP 2800 series) research-grade printer. Initially, an exploration into inkjet printing techniques was conducted, using an Epson XP15000 Consumer Printer (Fig. S15). However, a critical challenge emerged with the inherent need for these materials to be dry, resulting in their increased brittleness and fragility. The inherent risk to the printer's internal components, particularly the rollers and paper drive wheels, prompted us to seek alternative solutions. To mitigate this risk, we utilized the CD printing tool provided with the printer, allowing the substrate to remain flat with minimal movement. Nonetheless, this method presents a drawback: unlike conventional printing software that enables adjusting print quality based on Dots Per Inch (DPI) settings, the CD tool necessitates an image file. However, this image is compressed, resulting in significantly lower quality and compromised conductivity due to reduced deposition of silver ink. This limitation adversely impacts the final print quality. Although it was possible to print some patterns, printing with silver ink requires a

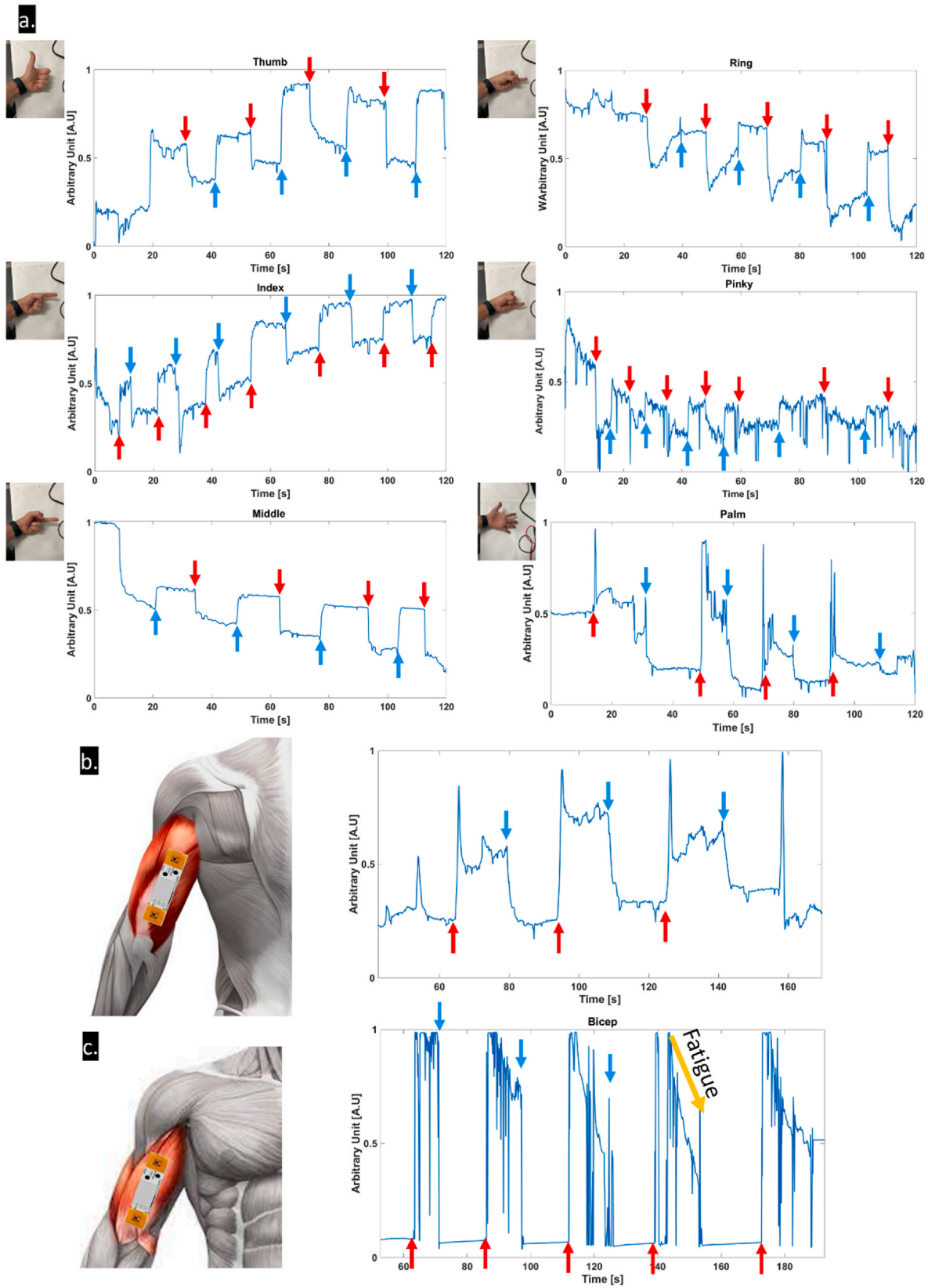


Fig. 5. a) Simplified surface electromyography (ssEMG) normalized measurement on the forearm for the detection of the fingers muscle contraction. b) SsEMG normalized measurements on the tricep muscle and (c) on the bicep muscle. The red arrows indicate the contraction and the blue ones the rest phases in all the plots.

subsequent sintering process at high temperatures to make the tracks conductive (Fig. S16) (Maroli et al., 2023). Regrettably, this process damaged the membranes and permanently adhered them to the CDs used as holders.

Having ruled out consumer printing, we explored the Dimatix (Fujifilms DMP 2800 series) printer. Among other parameters, this research-grade printer offers adjustable drop spacing and platform temperature during printing. In this case, we were able to print a functional antenna on the membrane, as shown in Fig. S17. However, this process proved tedious and time-consuming. To prevent any short circuits between antenna tracks, we restricted printing to a single nozzle. Additionally, to achieve good conductivity it was still necessary to apply the thermal sintering process, so it was not possible to remove the membrane from the sacrificial substrate, in this case PET, after the sintering process. It is for this last reason that the inkjet printing approach was discarded for printing directly on the membrane. Instead, a V-One printer from Voltera was used, which is a paste dispenser instead of printing inks. Printing with this system has two major advantages, the first is that the substrate is kept flat on a surface while the carriage that extrudes the silver paste moves over it. On the other hand, silver pastes, in addition to not requiring a sintering process, form a thicker and thus more conductive layer (Figs. S18 and S19 present SEM images of the printed traces), so it has been possible to design a smaller antenna than the one printed with inkjet ink. Resistance and inductance measurements of the Voltera printed antenna are shown in Fig. S20 and Fig. S21.

As shown in Fig. 6, the bio-inspired membrane was placed in a container with water and carefully lifted with a piece of PET. Next, the PET with the membrane is placed in the Voltera V-One, where the desired design loaded through the Gerber files was printed using silver paste. Once the antenna and contact pads were printed, the SIC-434X chip was placed. Due to the size of the chip pad, it was not easy to solder it directly onto the substrate. To overcome this limitation, we designed a small auxiliary PCB (25 mm long by 8 mm wide) to serve as an adapter. This auxiliary PCB not only facilitated chip attachment but

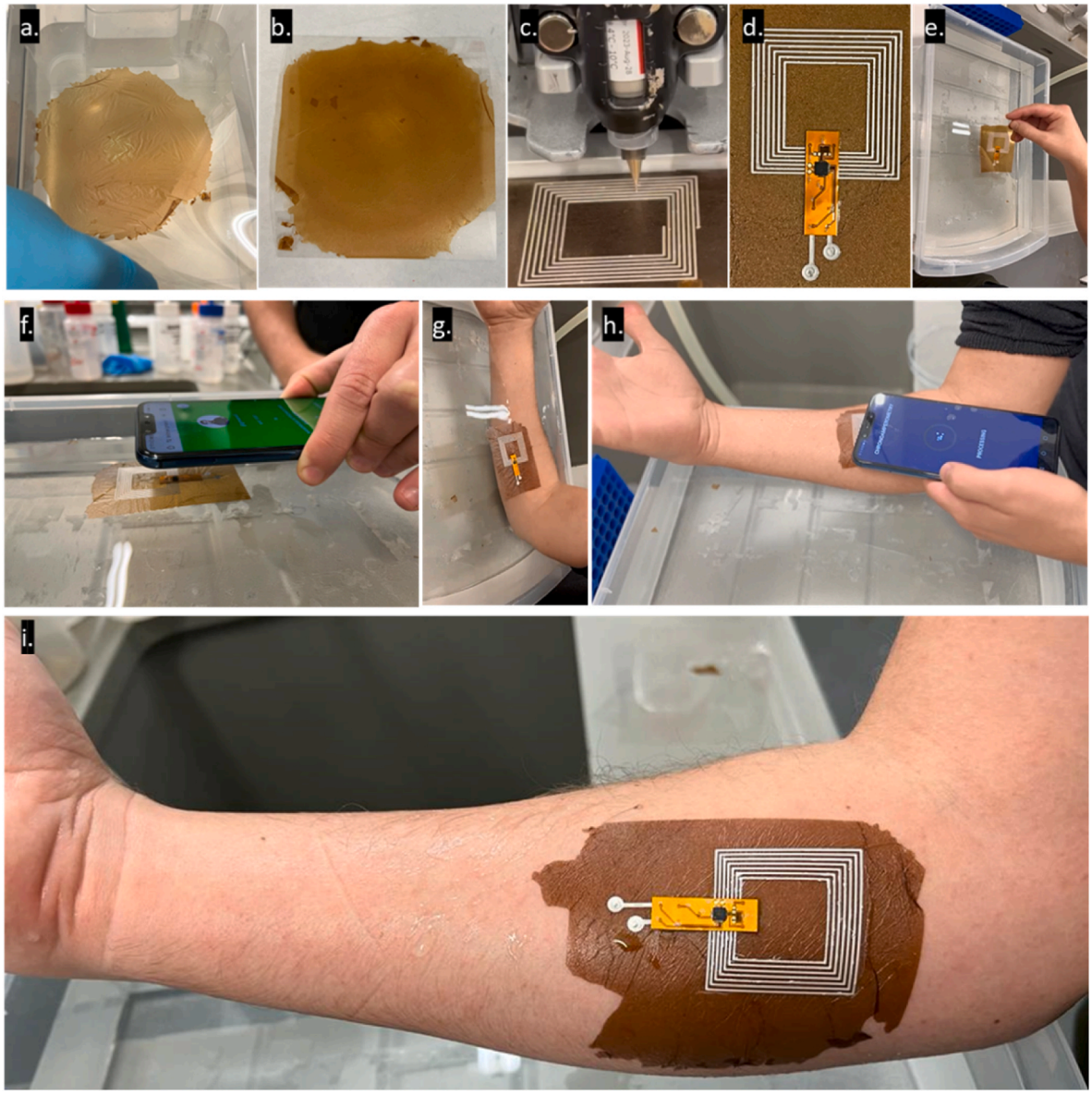


Fig. 6. Pictures of the fabrication phases of the printed sensorised bioadhesive membranes. a) Free-standing membrane on water. b) Transfer on the plastic temporary substrate for printing. c) Silver paste deposition with Voltera equipment to form the NFC antenna. d) Attachment of the flexible PCB integrating the NFC chip on the printed membrane. e) Release of the printed membrane from the temporary substrate. f) Testing of the NFC connection on the free-standing membrane on water. g) Adhesion of the membrane to the forearm skin. h) Testing of the NFC connection on the adhered membrane. i) Close-up of the printed membrane. The membrane has been placed with the antenna, chip and ssEMG contacts on top only for illustrative purposes.

also allowed for removal after device use. Moreover, it enabled reuse in new devices, employing Electrically Conductive Adhesive Transfer Tape (ECATT). This PCB was manufactured in flexible polyamide substrate, by the company PCB-Way (Fig. S22). The chip was soldered onto the PCB using Voltera's solder paste and then the flexible PCB and chip assembly were stuck to the membrane by employing a unique piece of ECATT, specifically the 3M Electrically Conductive Adhesive Transfer Tape 9703. This ECATT boasts anisotropic electrical conductivity, meaning it facilitates current flow exclusively through the thickness of the adhesive ('Z-axis') and not along its plane. This selective conductivity was achieved by embedding the adhesive matrix with conductive particles positioned to create point-to-point connections across the adhesive layer while maintaining electrical insulation laterally. This characteristic is particularly advantageous in preventing short circuits among the closely spaced pads and ensures reliable, targeted electrical connections. In order to detach the device from the PET, the device was again immersed tangentially in water (Fig. 6e). The system was then tested in water to verify that the membrane has not broken or that the PCB had not detached on contact with water (Fig. 6f). Next, the arm was then immersed in the water tank and the membrane stuck to the arm as it was taken out from the tank (Fig. 6g). Finally, the smartphone was brought close to the device for reading via NFC (Fig. 6h). All the steps of this process can be seen in detail in the **Supplementary Information video SV3**.

4. Conclusions

In this work, we have introduced a novel compact layout for an inkjet-printed wearable capable of measuring temperature, humidity (sweating), and muscle contractions. Crucially, this wearable can be powered and read with a smartphone via wireless NFC. Beyond this, we demonstrated the use of this methodology for the integration of sensors in bio-inspired and conformable membranes that imitates water-resistant adhesion observed in mussels. We have compared approaches of printing the sensors and antennas for the NFC readout on the membranes by inkjet printing and by the deposition of pastes using a Voltera printer, outlining the advantages and disadvantages of each strategy.

We have accurately designed the sensor network to reach the highest possible grade of integration for this type of fabrication method. In fact, we have: i) addressed the limitations of temperature sensing via a meander resistor by introducing an additional reduced graphene oxide resistor to compensate for the resistance change effect induced by bending, strain, or humidity variations; ii) taken advantage of the absorbent coating of the plastic substrate used for inkjet printing, enhancing humidity sensing with resistive IDE and iii) used simple amperometric measurements to measure the current associated with the muscle action potential, enabling surface electromyographic envelope identification related to muscle contraction. Finally, we have validated all the sensors with both laboratory-based and *in vivo* testing on a healthy volunteer performing physical exercise. This ensures the platform's reliability, effectively bridging the gap between wearability and precise monitoring.

All in all, these devices may become an important point for the prevention of life-risk emergency conditions such as both classic and exertional heat stroke. The multi-sensing capability and appropriate normalization algorithms, wireless connectivity and real-time connection, and natural movement compatibility are essential features of these prevention systems. Future directions will be focused on long-term reliability, robustness of such complex systems and cross-interference reduction remain critical areas for further exploration.

CRediT authorship contribution statement

Gabriel Maroli: Writing – review & editing, Writing – original draft, Methodology, Investigation, Formal analysis, Data curation, Conceptualization. **Giulio Rosati:** Writing – review & editing, Writing – original draft, Supervision, Funding acquisition, Conceptualization. **Salvio Suárez-García:** Writing – review & editing, Writing – original draft, Supervision, Project administration, Conceptualization. **Daniel Bedmar-Romero:** Methodology, Investigation. **Robert Kobrin:** Writing – review & editing, Methodology, Investigation. **Álvaro González-Laredo:** Methodology, Investigation. **Massimo Urban:** Methodology, Investigation. **Ruslan Alvárez-Diduk:** Writing – review & editing, Supervision. **Daniel Ruiz-Molina:** Writing – review & editing, Supervision, Resources, Funding acquisition. **Arben Merkoçi:** Supervision, Resources, Funding acquisition.

Declaration of competing interest

The authors declare that they have no known competing financial interests or personal relationships that could have appeared to influence the work reported in this paper.

Data availability

Data will be made available on request.

Acknowledgments

The ICN2 is funded by the CERCA programme/Generalitat de Catalunya. The ICN2 has been supported by the Severo Ochoa Centres of Excellence programme [SEV-2017-0706] and is currently supported by the Severo Ochoa Centres of Excellence programme, Grant CEX2021-001214-S, both funded by MICIU/AEI/10.13039/501100011033. The MIaSkin project has been funded by the ICN2 Severo Ochoa Seed Funding for Emerging Topics 2021 Program. This project has received funding from the European Union's Horizon 2020 research and innovation programme under grant agreement No 101008701. Views and opinions expressed are however those of the author(s) only and do not necessarily reflect those of the European Union. The European Union can not be held responsible for them. We acknowledge Departament de Recerca i Universitats of Generalitat de Catalunya for the grant 2021 SGR 01464. This work was supported by grantsPID2021-124795NB-I00 and PID2021-127983OB-C21 financed by MICIU/AEI/10.13039/501100011033 and ERDF "A way to make Europe". G.M. would like to express his gratitude to the Carolina Foundation for financial support through the scholarship "Doctorado 2020". G.M. acknowledges Universitat Autonoma de Barcelona (UAB) for the possibility of performing this work inside the framework of Chemistry PhD Programme. G.M. thanks Patricia Batista Deroco and Lei Zaho for their advice on the Dimatix printer. G.M. thanks Nerea de Mariscal i Molinas for her help in filming the S.I. video.

Appendix A. Supplementary data

Supplementary data to this article can be found online at https://doi.org/10.1016/j.bios.2024.116421.

References

Al Mahri, S., Bouchama, A., 2018. Chapter 32 – heatstroke. In: Romanovsky, A.A. (Ed.), Handbook of Clinical Neurology, vol. 157. Elsevier, pp. 531–545.
Barmpakos, D., et al., 2020. Microelectron. Eng. 225, 111266.
Barros, N.R., et al., 2021. Biomater. Sci. 9, 6653–6672.
Baumgartner, C., et al., 2021. Seizure. Eur. J. Epilepsy 86, 52–59.
Chen, S.-T., et al., 2017. Sensors 18, 17.
Conradsen, I., et al., 2011. Annu. Int. Conf. IEEE Eng. Med. Biol. Soc. 7715–7718.
Contreras-Pereda, N., et al., 2024. Mater. Today Chem. 35, 101855.
Djemal, A., et al., 2023. Bioengineering 10, 703.
Ershad, F., et al., 2020. Nat. Commun. 11, 3823.
Haerinia, M., Noghanian, S., 2019. Sensors 19, 1732.
Ju, J., et al., 2022. ACS Appl. Mater. Interfaces 14, 25115–25125.
Kim, S., et al., 2019. Ind. Health 57, 370–380.
Laitano, O., et al., 2019. J. Appl. Physiol. 127, 1338–1348.
Lee, H., et al., 2006. Proc. Natl. Acad. Sci. USA 103, 12999–13003.

Maroli, G., et al., 2021. Arg. Conf. on Electr. (CAE) 61–66.
Maroli, G., et al., 2023. Arg. Conf. on Electr. (CAE) 69–74.
Maroli, G., et al., 2023. Front. Electron. 3, 1060197.
Matsumoto, K., et al., 2019. 41st Ann. Int. Conf. Of the IEEE Eng. In: Med. And Biol. Soc. EMBC, pp. 7049–7055.
McEntire, S.J., et al., 2013. Prehosp. Emerg. Care 17, 241–260.
Momose, H., et al., 2023. Sci. Rep. 13, 416.
Nalepa, M., et al., 2024. Biosens. Bioelectron. 256, 116277.
Pham, S., et al., 2020. Sensors 20, 855.
Rosati, G., et al., 2022. Biosens. Bioelectron. 196, 113737.
Rosati, G., et al., 2021. Sci. Rep. 11, 14938.
Rosati, G., et al., 2018. Biosens. Bioelectron. 21, 54–64.
Rossetti, M., et al., 2024. Biosens. Bioelectron. 250, 116079.
Saiz-Poseu, J., et al., 2019. Angew. Chem. Int. 58, 696–714.
Scroccarello, A., et al., 2023. ACS Sens. 8, 598–609.
Shimazaki, T., et al., 2022. Sensors 22, 395.
Suárez-García, S., et al., 2017. Biomimetics 2, 22.
Sousa, M.P., et al., 2018. Biomater. Sci. 6, 1962–1975.
Yakoh, A., et al., 2018. ACS Appl. Mater. Interfaces 10 (24), 20775–20782.
Yang, Q., et al., 2022. Biosens. Bioelectron. 202, 114005.
Zhao, L., et al., 2023. ACS Appl. Mater. Interfaces 15, 9024–9033.